2001

Keyhole gas tungsten arc welding: a new process variant

Brian Laurence Jarvis
University of Wollongong

Keyhole Gas Tungsten Arc Welding:

a new process variant.

This photograph is an end-on view of keyhole GTAW on 8mm wall-thickness stainless steel pipe.

Certification

I, Brian Laurence (Laurie) Jarvis, declare that this thesis, submitted in fulfilment of the requirements for the award of Doctor of Philosophy, in the Department of Mechanical Engineering, University of Wollongong, is wholly my own work unless otherwise referenced or acknowledged. The document has not been submitted for qualifications at any other academic institution.

Brian Laurence Jarvis

15th July 2001.

Keyhole Gas Tungsten Arc Welding: a new process variant

By

Brian Laurence Jarvis

B.Sc. (Hons) Flinders University, 1975

Thesis

Submitted in fulfilment of the requirements
for the degree of Doctor of Philosophy in Mechanical Engineering,
Faculty of Engineering, University of Wollongong
June 2001.

Wollongong, New South Wales

Dedication

To my Mother and Father

Acknowledgements

I wish to thank my adviser and supervisor, Professor Michael West, for his support and direction during this investigation.

Special thanks are also due to my co-supervisor, colleague and friend, Dr Nasir Ahmed for laying the foundations for this work, and for his continued encouragement and support. Particular thanks are also extended to Ken Barton, who has played such a major role in the practical development of this process. Thanks are also extended to my many colleagues who have contributed in numerous ways.

This work has been made possible through the support and generosity of the CSIRO and the CRC for Welded Structures (formerly the CRC for Metals Welding and Joining)

Table of Contents

Table of Tables

Table of Figures

Nomenclature

All symbols used are explained in the text. The following is a list of those more commonly used.

A	Area
A_a	Area of arc impingement on the anode
A_d	Cross sectional area of the cathode emission region
A_e	Surface area of the cathode emission
E	Energy
F	Force
FAF	Fixed anode force
G	Plate thickness
H	Enthalpy
I	Current
J	Current density
K	Conductivity, mean curvature
P	Pressure
Q	Power input
R	Specified radius
R_a	Radius of anode region
R_e	Radius of emission region of the cathode
T	Temperature
V	Voltage
a, b	Constants
c	Heat capacity
g	Grams, acceleration due to gravity
h	Height
k	Arc force constant, thermal conductivity
r	Radius
s	Welding speed
t	Time
v	Velocity

w	Bead width (face and root)
x, y, z	Position coordinates
α	Thermal diffusivity, arc expansion ratio
ε	Emissivity
γ	Surface tension
η	Efficiency
ν	Viscosity
θ	Angle, half angle of the cathode taper
ρ	Density
σ	Electrical conductivity
ξ	Dimensionless distance from arc in direction of travel
Ω	Resistivity

Abstract

The topic of this thesis is the discovery and development of a robust 'keyhole mode' of the Gas Tungsten Arc Welding (GTAW) process. This process variant represents a significant departure from conventional fusion welding processes, and is not explicable by traditional models of keyhole formation and behaviour. To be specific, the well-known keyhole processes of plasma, laser and electron beam welding are dependent on the generation of significance ablation (or 'recoil') pressure. Furthermore, there has been an acceptance that this is an essential characteristic of all keyholes. The power densities associated with GTAW are known to be too low to achieve significant ablation, and consequently this process is regarded as incapable of conventional keyhole operation, unless the circumstances are exceptional. This thesis therefore challenges the established views on two counts:

- Keyholes welding is practical with existing GTAW technology; and
- Keyholes can be stable even in the absence of significant surface ablation.

Defence of these claims necessarily raises discussions ranging from the very practical aspects of work-place applications through to theoretical considerations such as the geometry of surfaces. While this work has endeavoured to address the various issues as they have arisen, emphasis has been placed on the development of a broad appreciation of the topic. It is acknowledged that in doing so it has failed to fully explore many of the areas that have been presented. For example, the relationship between GTAW keyhole surfaces and minimal surfaces may lead to fresh insights in weld pool mechanics. In practical terms such a study might lead to a much better appreciation of various forms of porosity, or potential control strategies based on the detection and interpretation of plasma or surface oscillations.

The work begins with an experimentally based exploration of the process before addressing the questions of keyhole stability, formation and the process dependencies. It is hoped this approach will provide an efficient means of presentation, and might provide fresh insights into the physics of gas tungsten arc welding.

1. Thesis

1.1. Objectives

1.1.1. Introduction

This research began with the generation of a transient keyhole mode of the high current gas tungsten arc welding (GTAW) process. Subsequent reproduction of this phenomenon confirmed its authenticity and encouraged a vision of a novel, high productivity GTAW process. The aim of this research was defined at that moment. It was:

> *'To understand the phenomenon and to realise its potential as a viable new GTAW process variant.'*

Although such goals can never be achieved in the strict sense, it is nevertheless contended that this work has been successful at both the fundamental and practical levels. In particular, the keyhole phenomenon, first observed under relatively extreme welding conditions, has been developed into a robust and highly productive welding process. In addition, the fundamental aspects of the process have been sufficiently well described to provide consistency with the observed behaviour, and quantitative interpretations of the critical process dependencies.

1.1.2. Thesis

The thesis underpinning this work can be simply stated:

GTAW can be operated in a keyhole mode to provide a process having some significant advantages over established welding methods.

1.1.3. Implications

The thesis stated above carries both theoretical and practical implications that must be addressed before it can be accepted.

The established view of keyhole welding is that it is restricted to a very high power density regime that is only reached by laser, electron beam, glow discharge and plasma arc processes (Lancaster, 1986). Indeed, with only few exceptions, (eg Norrish 1992) keyhole welding has attributed exclusively to these processes. The reason for this is that the formative mechanism for all reported keyhole processes is recoil pressure from surface ablation.

GTAW processes (with the possible exception of the dual shield variant) (Norrish, 1992) fall well short of the power densities needed for significant surface ablation. Therefore the claim that a conventional GTAW system can be operated in a keyhole mode challenges the established view on both theoretical and practical grounds. At a practical level, repeatable demonstration of the phenomenon would seem convincing enough. However, without a convincing explanation of how the phenomenon is produced the claim will remain on uncertain ground.

The second claim is that the resulting keyhole GTAW process has significant advantages over other welding technologies. The challenge here goes beyond demonstrating an advantage, such as a higher productivity or superior weld appearance when compared to an alternative welding method. In fact the sting is in the word 'process' because this carries the implications of controllability and adaptability. Without a clear understanding of what conditions are important to achieving a keyhole mode, and how the welding parameters should be altered to suit different applications, the technology would be of minimal practical interest.

1.2. Justification strategy

1.2.1. Justification criteria

It is proposed here that three criteria need to be satisfied to justify the thesis of this work. These are:

- The demonstration of process performance, robustness and practicality;
- The identification of the important process parameters and their means of influence;
- The provision of a sound theoretical model of the GTAW keyhole and its conditions for stability.

1.2.2. Outline

The issues just raised are at the core of the remainder of this work. However, the approach that has been chosen has been to structure the discussion to reflect a progressive understanding of the process rather than to provide a sequential response to the thesis. The course of that development is outlined below.

1. Review the established keyhole welding processes
2. Describe the development and performance of keyhole GTAW as a practical process
3. Examine the structure of a GTAW keyhole in detail
4. Describe the forces in high current arcs that lead to keyhole formation
5. Quantify the relationships between the welding conditions and keyhole behaviour
6. Review aspects of heat conduction, particularly with respect to impact on the keyhole GTAW process.

1.2.3. Detailed research intentions

The study begins with a review of the literature. The essential purpose of this review is to explore known keyhole phenomena in welding, examine the fundamental

processes involved in their formation and stability, and provide a context for the description of this GTAW variant.

In the following chapter attention will be directed to tracing the development of this new process from transient phenomenon to a well-controlled process. In the course of this work the influential process parameters will be identified and operating windows defined. The objective is to demonstrate that the process is practical and attractive, that it has significant advantages in some applications, that it is robust, and that it can be tailored to meet specific tasks.

However, no new process will be introduced into a fabrication shop unless the potential user can be confident of its benefits. Performance is crucial, and this requires the technology is well understood at a fundamental level, and process characteristics can be predicted even for untried conditions. The remaining chapters address these issues. Should the technology develop it is hoped that this work may provide the starting point.

The following chapters will draw together considerations from areas including arc physics, electromagnetic theory and heat flow. The aim will not be to develop comprehensive models, but rather to draw out some of the physical mechanisms that are essential to a practical appreciation of the phenomenon.

Chapter 4 will explore the essential aspects of keyhole behaviour, with the intention of developing a fundamental appreciation of the phenomenon, and identifying the mechanisms that set the operating limits for the process. The first issues to be taken up will be the operating windows and causes for process failure. This will be followed by a detailed look at weld metal displacement from the arc region, leading into a mathematical formulation of the GTAW keyhole. This section of the study will examine the forces acting on the keyhole in an attempt to identify both the reasons for its stability and the general characteristics of its dynamics. The roles of surface tension and arc forces will be prominent throughout these discussions

The arc force is presumed to be the only available mechanism for generating significant displacement of the weld pool. The broad aims of Chapter 5 are to provide a theoretical model of arc force, estimate its magnitude, and to determine the parameters

that influence it. The arc force will be examined both theoretically and through a series of experiments designed to measure its effects under a variety of welding conditions.

It is intended that the study of the arc force should lead naturally into the issues of chapter 6. This chapter will aim to investigate the roles specific arc characteristics play in regulating the keyhole process. The first objective of this section will be to review some of the extensive literature on welding arcs. The remainder of the discussion will draw on this material to extend the understanding of the GTAW process that has been developed in the preceding chapters. In particular, current, voltage, electrode geometry and shielding gas composition have been identified in the literature as exerting major influences on arc characteristics. Consequently it is appropriate to investigate their effects on keyhole formation through an examination of arc-keyhole interactions.

The final investigative chapter addresses the issue of heat flow in the weldment. It will be presented in three sections dealing with analytic models, approximations for high welding speeds, and the development of a series solution as a tool for approximating the fields associated with keyhole GTAW. These general results will be used to provide some insights into the thermal environments of GTAW keyholes. Convective heat flow will not be considered. In fact it might be argued that the very thin liquid films encountered in the leading portions of high current GTAW weld pools cannot support the significant temperature differences that drive such convective flows. It is recognised however, that convection is important under conditions where the liquid layer is of the order of a millimetre deep, such as under low current arcs and in the trailing regions of weld pools.

The final chapter will summarise the work done and the case for the thesis.

2. Literature Review - Deep Penetration Welding

2.1. Introduction

2.1.1. Power density in fusion welding

Welding requires energy, and this can be provided by several means. The most familiar of these is chemical combustion. Chemical reactions are widely used because of the simplicity and portability of the equipment. Examples include oxy-hydrogen and oxy-acetylene flame welding, and thermite processes. Alternatively, electric arcs are used to provide higher temperatures and greater control of the welding environment. There are many processes in this category, ranging over all the variants of manual metal arc (stick welding), gas metal arc (GMAW), gas tungsten arc (GTAW), and submerged arc welding (SAW). However, other energy sources are also used, including friction, kinetic energy (as in explosive welding) and particle beams.

Since all welding processes depend on fusing the metal surfaces, the power input per unit area is always a critical parameter. This is usually referred to as 'power density', and can be expressed in units of watts per square metre (W/m^2). It is convenient to use this parameter to divide the various fusion welding processes into two groups: conventional processes and high power density (HPD) processes. Quigley (Lancaster 1986) has suggested that the threshold for HPD welding be set at 10^{10} W/m^2. However, recognised HPD processes often operate below this value and a figure of 10^9 W/m^2 is probably more appropriate. Four processes can exceed this threshold - plasma (PAW), laser (LBW), electron beam (EBW) and glow discharge electron beam (GDEB) welding. The GDEB process will not be considered here. The conventional fusion welding processes have power densities between $3x10^6$ and 10^9 W/m^2. For illustration, an oxy-acetylene flame can reach a power density of about 10^7 W/m^2 whereas argon arc processes usually exceed 10^8 W/m^2 (Beesley, 1976).

The range of power density that can be usefully used for fusion welding can be given some context by considering the two extreme cases. At the lower boundary of $3x10^6$ W/m^2 the energy input barely keeps place with conductive losses to the surrounding

metal and minimal fusion takes place. The fraction of energy input producing the fusion is referred to as the 'melting efficiency' and will be discussed later. At the other extreme (greater than about 10^{13} W/m^2) vaporisation becomes so rapid that very little heat is able to flow into the substrate, and the effect is to produce a parallel sided hole straight through the material. The operating window for fusion welding therefore allows the power density to be varied by a factor of $3x10^6$, which is a very impressive range.

The division between conventional and HPD processes is not arbitrary. When the energy density approaches about 10^{10} W/m^2 forces generated by the recoil of vaporising weld metal become important, and provide a mechanism for the displacement of the molten material from the energy impingement zone. This displacement mechanism allows the beam to penetrate deeply into the metal through a small opening at the top of the weld pool. Welding under such conditions is appropriately known as 'keyhole' welding or simply 'keyholing.' The keyhole may typically be a couple of millimetres wide at the top and tens of millimetres deep.

Conventional arc processes do produce some metal vaporisation, but the rates are low and the resultant forces are insignificant in shaping the weld pool. Recoil-driven keyholes cannot occur. However, arc forces and droplet impact may distort the pool surface, and this can also lead to enhanced penetration. Nevertheless, it is unusual to find a situation where the weld has penetrated to a depth even equal to its width.

Accurate physical descriptions of all the above processes rely heavily on an understanding of the heat and fluid flows within the weld pool and the welding arc or beam. This is complex in arc welding because of the large number of effects that need to be considered. Surface tension, plasma shear, current flow and density variations (bouyancy), and also droplet impact in the case of GMAW, can influence flow within the weld pool. It may therefore appear that recoil-driven keyhole welding would be easier to describe since many of these factors are not present or can be ignored. However, the physics of a keyhole moving through liquid metal and maintaining itself through the pressure generated by the vaporising material is equally challenging, and its implementation is extremely difficult because of the very high degree of coupling between the various parameters.

2.1.2. Fluid flow in conventional arc welding

The first models of the fusion welding process were based entirely on conduction (Rosenthal 1941, Rosenthal 1946, Wells 1952, Christensen et al 1965), and were used to calculate thermal cycles. However, it was soon apparent that conduction alone could not explain the variety of outcomes observed, and convective effects had to be taken into account. This led to the appreciation of the strong influence of heat and fluid flow in weld pools on such things as penetration shape, solidification behaviour, microstructure, defect formation, distortion and stress.

According to Matsunawa (1992) active discussion of the role of weld metal flow began in the early 1960's. This received a considerable impetus in 1965 when Ishizaki demonstrated surface tension gradient-driven flow in paraffin (Matsunawa 1992). In a simple and elegant demonstration he dipped a hot soldering iron in wax and observed a strong radial outward flow across the puddle surface. The resulting penetration pattern was wide and shallow, and closely resembled what had been found in steel weldments. Similar results were obtained in other organic materials, but it was not until 1971 that Woods and Milner set up an experiment with a liquid metal (mercury) (Matsunawa 1992). Their results were disappointing: the effect was present when the mercury was under vacuum, but disappeared as soon as air was admitted. They attributed this to a gross reduction in surface tension due to oxygen contamination, and concluded that such flow was unlikely to occur within a welding environment. However, they did observe a flow of electromagnetic origin when they simulated a 'welding' current, and this became the subject of modelling activities for the remainder of the decade.

When a current flows through a conductor the induced magnetic field generates a compressive force on it, and this is appropriately known as magnetic pressure (Lorrain and Corson 1970). Furthermore, if the current is geometrically divergent a pressure gradient will be established along the conduction path. In cases where the conductor is a fluid this will result in a flow in the direction of reducing magnetic pressure. This has several implications for arc welding. As current enters the weld pool from the arc plasma it diverges strongly, promoting a flow radially inward across the surface of the pool (see Figure 2.1). The plasma will also be subject to a net acceleration towards either the electrode or weld pool, according to which has the lower surface current

density. Finally, if the electrode is a consumable wire then detachment of the droplet that forms at its tip can be either enhanced or retarded depending on whether the maximum current density occurs on the droplet surface or closer to the solid wire.

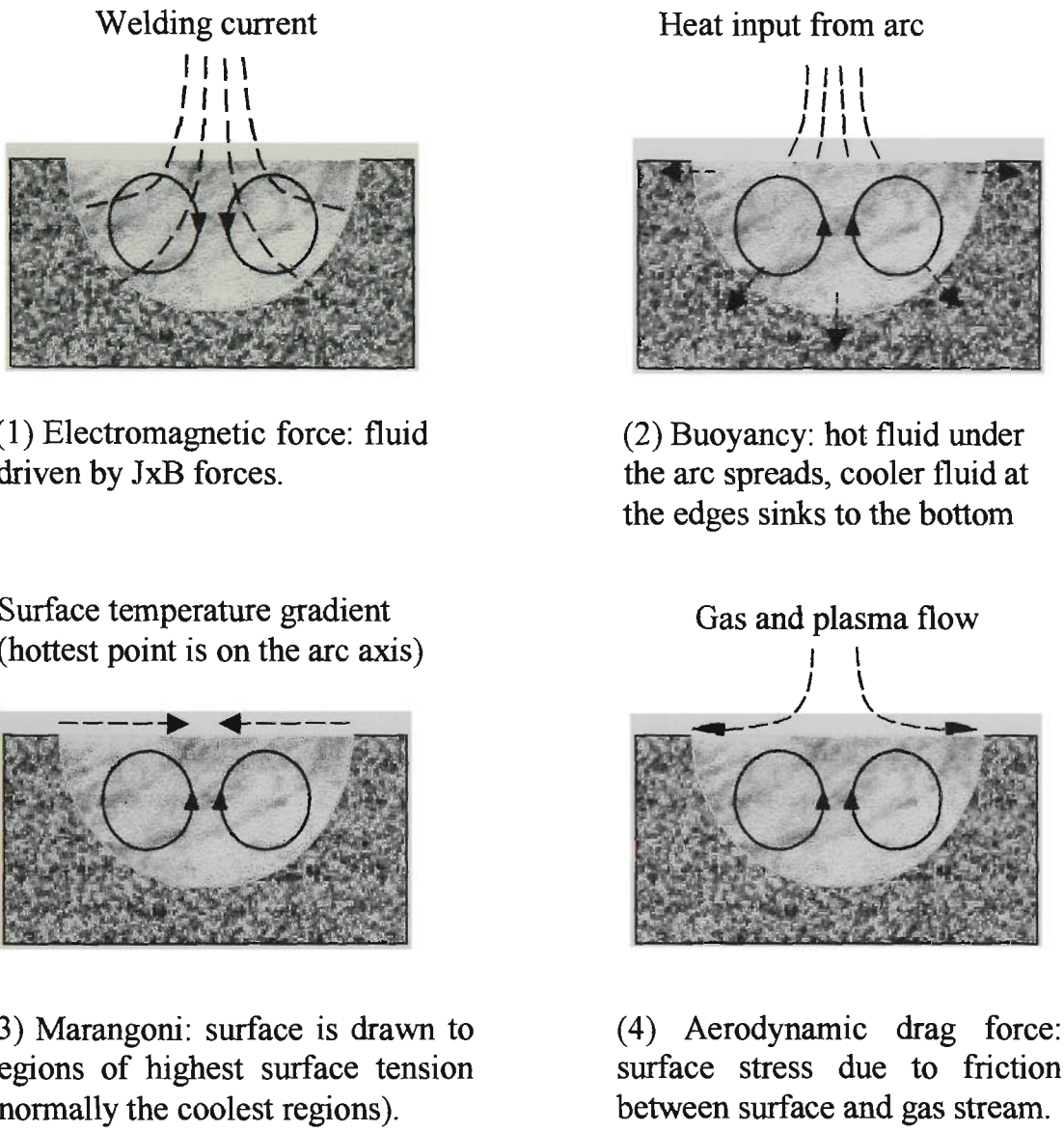

Figure 2.1. Flow directions induced by four possible motive forces in arc welding (Matsunawa 1992).

Surface tension driven flow was reconsidered when Heiple and Roper (1982) reported that surface-active elements such as sulphur, phosphorus and selenium had a dramatic effect on weld penetration in stainless steel. They proposed that these elements would lower the surface tension of the molten metal. Furthermore, they realised that these elements would be eliminated at higher temperatures. This raised the possibility that the

temperature coefficient of surface tension could become positive, (that is surface tension could increase with temperature under some circumstances), and reverse the direction of flow originally predicted by Ishizaki. This hypothesis was verified by Mills two years later in his studies with 304 and 316 stainless steels of varying sulphur content (Mills 1984). Subsequently surface tension was included with bouyancy and electromagnetic (Lorentz) forces in weld pool models. The flow resulting from gradients in surface tension is often referred to as Marangoni flow (Lancaster 1986).

Finally, as pointed out by Matsunawa (1992) plasma shear forces can also be important, and need to be accounted for in modelling efforts. The list of forces acting on a conventional arc weld pool therefore includes bouyancy, Lorentz, surface tension and aerodynamic drag (or plasma shear). Their effects on fluid flow are indicated in Figure 2.1. In addition, if metal transfer in present then the force resulting from droplet impact must also be considered. The bouyant and Lorentz forces are body forces because they act within the volume of the weld pool, whereas surface tension and aerodynamic drag are shear stresses that act on the surfaces.

2.2. Keyhole (Deep Penetration) Welding Processes

2.2.1. Electron Beam

In 1907 von Pirani suggested that electron beams should be used for thermal processing of materials when he took out a patent for electron beam melting (Meleka 1971). However, at that time the technology for generating and manipulating electron beams was just beginning, and it was not until after the developments required for oscilloscopes and electron microscopes during the 1920's and 1930's that the idea could be taken seriously.

The first electron beam processing unit was built by Suddeutsche Laboratorien Mosbach in 1949 (Steigerwald 1983). That device was portrayed as a precision heat source particularly suited to drilling small components such as watch bearings. Nevertheless, the 1952-licence agreement also covered its use for soldering, brazing

and welding (Vertrag Irving Rossi 1952). It was presumed that the beam would affect these latter processes in much the same way as a conventional flame or arc.

The true potential of the electron beam for welding was first demonstrated in 1958. At that time the American company Westinghouse was faced with the problem of welding zircaloy plates for use in nuclear submarines. Zircaloy is refractory and chemically very reactive, and consequently the idea of welding them in vacuo with an electron beam was proposed. A 2.5kW, 125kV German-built machine was available, and so an extensive investigation of the proposal was undertaken. Since the beam could easily bore through the 5mm plates it was decided to have the beam traverse the plates at various speeds. As the parameters were varied the transition from boring to electron beam welding was observed for the very first time (Steigerwald 1983).

Initially EBW was confined to the nuclear industry, but the aerospace, electronics and instrumentation industries were quick to appreciate its potential and began installing units as early as 1961 (Mekela 1971). Non-vacuum EBW was reported by Meier in 1963 (Meier 1963). Since that time the sophistication and power of the units has increased in line with demand. By the early 1980's commercial units were available with beam powers up to 100kW, and penetration of 200mm could be achieved (Steigerwald 1983). At that time, as now, welding of even thicker material was limited by the difficulties with the welding process rather than the generation of sufficient beam power.

One recent innovation however, has been to increase the beam voltage from a maximum of about 150kV to 500kV (Tomie, Abe and Arata 1990). Such high voltage beams are claimed to produce deeper, narrower keyholes than commercial equipment, and this offers considerable benefits. One of these is an enhanced ability to produce full penetration keyholes in the flat position. The flat position is the favoured welding position, but successful fully penetrating welding is dependent on the weld pool being held to the plate during solidification by surface tension. For this to occur the width of the root bead must be decreased as plate thickness is increased. Consequently the level of difficulty for this particular type of weld increases rapidly with plate thickness, and full penetration welding of thick plate (>50mm) is conducted in the horizontal position. However, the experimental 500kV device was used to complete full penetration flat

position welds in 105mm thick austenitic stainless steel, an accomplishment well beyond the capabilities of conventional equipment.

2.2.2. Plasma Arc

Plasma arc welding was introduced during the 1950's (Tomsic and Jackson 1974, Arata and Kobayashi 1985). It has generally been regarded as an extension of GTAW, the difference being that the arc is forced to pass through a small orifice that strips away the outer layers of conductive, ionised gas. This results in a much stronger plasma jet, and an increase in energy density. The process offers several advantages over conventional welding techniques, such as excellent root contour, higher welding speed and lower heat input (Tomsic and Jackson 1974). These attributes are a consequence of its ability to operate in a keyhole mode.

Plasma arc keyholing differs from LBW and EBW keyholing in that it is invariably fully penetrating. This is a consequence of the nature of the beam: being composed of atomic species it cannot be absorbed as electrons or photons, and so must be permitted to escape though the bottom of the keyhole. In addition the beam diameter is relatively large, resulting in a wide keyhole. In cases where the molten metal is supported solely by surface tension and backing gas pressure it will tend to sag much more noticeably than with the narrower LBW and EBW keyholes. Penetration under such circumstances is quite limited: Tomsic and Jackson (1974) have reported up to 6mm for stainless steels, while Woolcock and Ruck (1978) obtained 18mm penetration for titanium. The latter case was attributed to the higher surface tension and low density of titanium. Examples of operating conditions were: 86 amps at 22.5 volts and 165 mm/min travel speed for 6mm stainless steel, and 310 amps at 28 volts and 120 mm/min for 18 mm titanium plate. Greater penetrations have been obtained more recently, and Quigley (Lancaster 1986) has reported penetrations of 15mm in stainless steel. However, this relied on newer torch designs and in particular, metal support.

2.2.3. Laser Beam

The first laser was built and demonstrated by Maiman in 1960. A short time later Javan, Bennet and Herriot produced a continuous beam of about 20mW from the first gas laser

(Beesley 1976). The first CO_2 laser was demonstrated Patel in 1964 (Houldcroft 1991). These milestones stimulated a great amount of research activity, which rapidly led to a vast array of lasing mediums and device characteristics. Within ten years of Maiman and Javans' demonstrations high power cw lasers were being applied to industrial tasks, including welding. For example, in 1970 Coherent Radiation, a laser manufacturer, was reporting on the use of a 250W CO_2 laser for the welding of thin gauge materials (Webster 1970). While the capability of that machine was quite modest, the same article presented news of an experimental CO_2 unit of 4600W, claimed to be able to join 3mm thick stainless steel at 350mm/min. The same journal issue also carried an article on the use of an 1100W cw Nd:YAG laser (Staff report 1970). While neither this nor the 250W CO_2 laser had exhibited keyhole welding it was clear that the technology was developing rapidly.

Less than two years later Locke, Hoag and Hella (1972) published a comprehensive paper entitled 'Deep penetration welding with high power CO_2 lasers.' The lasers they had been using over the past year were producing beam powers of up to 20 kW. Their references cited experiments with a 30 kW device (Locke Hella and Westra 1971).

The work of Locke et al demonstrated that high-powered lasers were capable of true keyhole mode welding, and also highlighted the similarities to deep penetration EBW. They reported penetrations of up to 3/4 inch (19mm) with aspect ratios of 6 to 1 in stainless steel. The travel speed for that case was an impressive 50 in/min (1300 mm/min). A penetration of 12mm was obtained at twice this speed. Penetration was subsequently found to be very dependent on the nature of the test piece (Locke et al 1972). Thus for an arbitrary coupling efficiency of 30% Locke observed that 4kW was required for a 10mm penetration weld in stainless steel, 14kW for carbon steel, 16kW for aluminium and an estimate of greater than 60kW for copper.

One important difference between laser and electron beam welding is that the vapour escaping from the laser-induced keyhole interacts with the beam, and may even form an ionisation cloud above the work piece when the power exceeds about 8kW. This problem can be overcome by introducing an 'assist gas' to disperse the vapours and inhibit ionisation. Nevertheless Albright (1982) has reported instances where this plasma plume could be maintained in argon assist gas even after the work piece had

been removed, indicating a complete decoupling between the beam and plate. Helium has been found to be much more efficient than argon in suppressing the plume, and its use has resulted in better and more consistent penetration. The generation of plasma plumes is a characteristic of LBW, particularly when high-powered CO_2 lasers are used.

The two lasers commonly used in welding are CO_2 and Nd:YAG. Advocates of the Nd:YAG systems emphasise the ease of handling the output beam - its 1.06μm radiation can be focussed with glass lenses and transmitted through optical fibres. Also because the wavelength is much shorter than the 10.6μm of the CO_2 laser, the beam generally couples more efficiently to metal work pieces, and can be focussed to a smaller spot size if the beam power is low. It should be noted that the claim of smaller spot size may not hold for high powered Nd:YAG lasers since these tend to have relatively poor (multi-mode) beam quality. The commercial CO_2 lasers have the advantages of power and efficiency, and units with outputs of 20kW have been available since the early 1970's, whereas multi-kW Nd:YAG systems are still rare. Commercial Nd:YAG systems did not exceed 3 kW prior to 1995 (Wirth 1995). Output powers had been pushed to about 5kW by 1998.

Nevertheless, other laser systems are under investigation. For example, Houldcroft (1991) has cited an experimental CO system with an output of 6.7kW. Initial claims have suggested that its beam is far superior to the longer wavelength CO_2 laser, at least in cutting applications.

2.3. Beam-to-work-piece Coupling

2.3.1. Electron beam coupling

For deep penetration welding to occur the electron or laser beam must satisfy two conditions: firstly it must generate sufficient reaction pressure to form a keyhole, and secondly it must interact with the vapour filled cavity in such a manner that the system remains stable.

High-energy electrons (ie with energies of 10's of keV) have a very short wavelength in comparison to laser radiation, and interact by ionising and scattering from individual atoms and nuclei. Thus the interaction of the beam with the vapour is essentially the same as with the metal surface, given allowances are made for particle densities. According to Duley (1987) the electrons penetrate the metal surface to depths measured in tens of microns. He argues that since the particle density of the vapour in an electron beam keyhole is about five orders of magnitude smaller than in the metal (assuming the weld is carried out under vacuum), the characteristic depth of penetration in the vapour should be in the order of metres. In other words the interaction between the beam and the vapour is not significant. However, since the electrons carry their energy to well into the metal, sub-surface boiling will occur, resulting in violent reactions (Duley 1987) and explosions (Schebesta 1975) in the keyhole walls. As might be expected, when EBW is carried out at atmospheric pressure the attenuation in the keyhole becomes much greater. Resulting keyholes are wider and shallower than those produced under vacuum (Meier 1963).

One difficulty that EBW shares with conventional arc welding is susceptibility to magnetic fields. This can be problematic with deep penetration EBW because alignment along the full depth of the joint is critical, and deviations of the order of millimetres are sufficient to defect the joint. In one study Weber (1982) found that fields as small as one gauss existing between the gun and work-piece produced unacceptable deflections, and necessitated the provision of shielding. He also observed that the thermo-electric currents generated when joining dissimilar metals can also result in beam deflection and defective welds.

2.3.2. Laser beam coupling

LBW is normally conducted at atmospheric pressure, and in such circumstances the laser radiation interacts quite strongly with the gas in the keyhole. Coupling between the laser beam and the work-piece can be quite complex, and it is generally recognised that LBW keyhole welding is an inherently difficult and unstable process (Kristensen and Olsen 1992). For example, laser irradiation can result in a plasma plume that in turn shields the plate from further exposure, creating an unstable situation (Locke et al 1972, Albright 1982). In fact, while laser-material interactions are controllable within narrow

operating limits, chaotic phenomena can be observed in unconstrained systems (Lim and Chatwin 1994).

Experimental data from closed, or blind, keyholes have shown that deeper and more consistent penetration result when the plasma plume and vapour density is suppressed. The use of assist gas for plume suppression has already been noted. Plasma 'ignition' occurs above the keyhole in the region where the metal vapours and ambient gas mix. The plasma that is formed may have a temperature as high as 18000 K, and can be strongly absorbing to the laser radiation. However, there is some uncertainty regarding its penetration into the keyhole, and Duley has suggested that although it may reach into the mouth of the keyhole, it generally does not fill it or extend towards the tip. This view is not universally shared (eg Dowden et al, 1987).

In practical terms laser beams interact much more strongly with the channel products than do electron beams (Duley 1987), but this is in part due to the differences in gas densities within the keyholes. EBW welds made at atmospheric pressure, ie non-vacuum EBW, have profiles similar to LBW (Meier 1963), and laser welds made under vacuum produce the very high aspect ratios normally associated with conventional EBW (Arata, Abe and Oda 1984). In addition, Moon and Metzbower (1986) have examined the consequences of introducing metals with much higher vapour pressures into the keyholes. Their results clearly showed that the increased amount of vapour in the keyhole significantly reduced penetration.

Clean metal surfaces are highly reflective to the radiation from most lasers, and consequently absorption can be very low. Classical physics predicts that the absorption coefficient, A, is proportional to the square root of the DC conductivity divided by the wavelength of the incident radiation (Ireland 1989):

$$A = 0.0365\sqrt{\frac{\sigma}{\lambda}}$$

(σ is the resistivity in μohm-cm and λ is the wavelength in μm). A is in the range of 5-30% for most metals illuminated with 1.06μm radiation (ie from the Nd:YAG laser),

and a factor of about 3 smaller for radiation from CO_2 lasers. Some calculated values are presented in Table 2.1.

Table 2.1. Predicted absorption of a number of common metals (Ireland 1989).

Metal	**Absorption (%)**	
	10.6μm	*1.06μm*
Copper	1.5	4.6
Gold	1.7	5.4
Aluminium	1.9	6.0
Brass	3.0	9.5
Nickel	3.1	9.8
Iron	3.5	11.0
Steel alloys	4 – 10	10 – 30

This has given rise to concerns regarding the so-called 'reflection barrier' for CO_2 lasers (Albright 1982), and has been used as an argument for the use of shorter wavelength lasers (Ireland 1989). However, it is an argument that is often overused. For example, copper is renowned for being extremely difficult to process with any laser, yet it is more absorbing to the relatively short radiation of Nd:YAG lasers than steel is to that of CO_2 lasers. However, the latter combination is used routinely. In addition, experimentally determined absorption spectra often deviate significantly from the classical predictions, particularly at visible wavelengths. Again using copper for illustration, it is found that its absorption increases from about 5% to over 50% as the wavelength decreases from 1μm (1000nm) to 500nm (Kaye and Laby, 1966).

In any case high surface reflectivity breaks down if the laser beam is sufficiently powerful. Under such circumstances the surface heats due to a complex interaction with the light, and it is claimed that the absorptivity increases to about 50% (Albright 1982).In any case once a keyhole has developed any radiation entering it must undergo very many reflections before re-emerging, and hence the percentage of energy absorbed is usually very high. Albright (1982) has very effectively demonstrated this aspect of beam coupling. Normally a CO_2 laser operated at 250W is not capable of penetration welding, but he was able to achieve this by forming the output into pulses, each commencing with a high intensity spike. Each initial spike temporarily reduced the

surface reflectivity of the metal, allowing the relatively low intensity radiation that followed to be efficiently coupled to the weld zone. The technique also produced another benefit: the pulsed beam tended to change the direction of the solidification front, thus disrupting the centre-line solidification plane.

Stability within the keyhole is achieved through a balance of surface tension and hydrostatic forces against excess pressure and the recoil due to ablation (Andrews and Atthey 1976, Giedt 1982). Giedt (1982) considered the situation in EBW, and expressed the net pressure in a keyhole at an arbitrary depth, y, as

$$P = \frac{\gamma}{r_y} + \rho g y$$

and at the tip of the keyhole (depth h) as

$$P = \frac{\gamma}{r_b} + \rho g h$$

In these equations r_y and r_b are the radii of the keyhole at y and the cavity tip, respectively, ρ is the metal density and γ is the surface tension. This simple model has been used to generate estimates of the keyhole wall temperature, given the radius and the relationship between the metal temperature and vapour pressure. If correct the model should have general applicability. Experimental data for LBW keyholes in AISI 304 stainless steel have shown the vapour pressure to be approximately $2\text{-}3 \times 10^{-3}$ bar, implying surface temperatures of 2200°C (Duley 1987). This agrees with calculations on volume loss due to evaporation, and suggests metal vapour densities of between 3×10^{16} and 3×10^{17} atoms /cm^3 under typical welding conditions (Duley 1987).

2.3.3. Laser-matter interactions

The relationship between vapour pressure and wall temperature only applies when all the beam energy is absorbed directly in the keyhole walls. This may be a good approximation in some cases, but the experimental evidence already presented indicates that there are two processes operating: direct absorption at the keyhole walls, and coupling through the heated vapours and plasma. It has even been suggested (Ireland

1989) that the absorption of radiation in the vapour and plasma plume may increase process efficiency. The proposed mechanisms are the absorption and re-emission of radiation at shorter wavelengths, and thermal conduction to the channel walls. Dowden et al (Dowden, Postacioglu, Davis and Kapadia 1987, Dowden, Kapadia and Postacioglu 1989) have developed models that explore this as the dominant coupling mechanism, and found such models to be self-consistent. In fact their results agreed well with some experimentally determined profiles. To further illustrate the range of possibilities, the condition that little or no beam energy is directly absorbed by the metal walls is also plausible in some situations, such as with fully penetrating or low speed welds.

It is at this point that one begins to appreciate the difficulties involved in modelling laser-matter interactions. This area has attracted a great deal of effort, as evidenced by the recent review of Ocana (1994) that cites over 100 references. In general these papers are presented as fundamental studies and not identified by searches of welding-oriented databases.

According to Ocana quite precise knowledge of the physical processes occurring in laser-matter interactions is now available. The problem is that many of the processes are so complex that characterisation with respect to practical experience is extremely difficult. In particular, the appearance of vapour and plasma during irradiation definitely excludes any possibility of a 'linear' approach to the problem. In his words "The laser flux is itself modified by the apparition of these phases" (Ocana 1994). One could add that the keyhole chemistry and geometry also modify the laser flux, vapour and plasma densities.

At power levels below 10^{10} W/m^2 conduction may be sufficient to prevent any surface transformations, but above this value melting and evaporation will occur. (It is useful to note that a 1 kW laser focussed to an area of 0.1mm square would deliver a power density of 10^{11} W/m^2). Ocana has noted that very short duration exposures at power levels up to 10^{12} W/m^2 generally produce vapour, whereas higher power densities result in plasma formation. Laser irradiation can generate plasma through a process known as optical break-down. In any vapour there will inevitably be the occasional free electron. If the laser radiation is intense enough the associated electric fields will accelerate these

electrons sufficiently between collisions that they cause further ionisation. This condition results in an avalanche of charge-carrier formation and the vapour is rapidly converted to highly ionised and absorbing plasma. This break-down process is enhanced by easily ionised species, which accounts for the replacement of argon with helium as an assist gas since argon has a lower ionisation potential than helium.

The threshold for breakdown is lowered if the vapour temperature is increased or the frequency of the radiation is reduced (Ocana 1994). Thus if the irradiance is continuous a positive feedback of energy absorption may result. Experimentally it is found that break-down under CO_2 laser illumination can occur at about 10^{11} W/m^2 whereas the higher frequency Nd:YAG radiation needs a power density approaching 10^{12} W/m^2. If the power level exceeds 10^{13} W/m^2 high-temperature plasma will always form, irrespective of the characteristics of the material being irradiated.

Whenever a plasma forms it will be subject to rapid pressure rises, and hence expansion. As it expands much of it will escape from the path of the beam, and rapidly extinguish. Only that portion which expands in the direction of the beam will be sustained, and this gives the appearance of the plasma being confined by it. This phenomenon is known as a laser-supported absorption wave. Other related waves are laser-supported combustion and laser-supported detonation waves (Ocana 1994).

2.4. Keyhole Models

The EBW and LBW energy couples to the work-piece directly by absorption in the keyhole walls, and indirectly through absorption in the keyhole vapour and plasma. This gives rise to a variety of observations that would be in conflict if only one mechanism were operative. These include the observation of 'cool' vapour within the body of keyholes (Duley 1987), the better performance claimed for Nd:YAG lasers over CO_2 lasers of the same power (Ireland 1989), and the decreased aspect ratio for keyholes in non-vacuum in comparison to vacuum environments. To date the transport of energy and momentum via the keyhole plasma remains a topic of research (Dowden et al 1987, Ocana 1994 and Kroos, Gratzke and Simon 1993). A comprehensive model is needed, and that model will need to address effects due to heat conduction, and

plasma sheath and pre-sheath effects governing the transport of the ionisation and kinetic energy of plasma ions (Kroos, Gratzke and Simon 1993).

2.4.1. Conduction Models

A common approach to the modelling of welding processes, at least since the work of Rosenthal (Rosenthal 1942, Rosenthal 1946) has been to consider heat conduction only. This can be defended because ultimately it is the thermal cycle that determines the various microstructural and mechanical properties of the joint. However, one criticism that has often been raised in relation to these models has been the assumption that the thermal properties of the material are not temperature dependent. To the contrary, the thermal properties of metals are strongly dependent on temperature and, for example, include various phase changes. Heat conduction problems that include phase changes are referred to as 'Stefan problems.' Although the importance of this objection is still somewhat unclear, the inclusion of non-linear properties is readily accomplished now due to the availability of computers capable of calculating high precision numerical solutions.

A second and more fundamental objection has been the contrived nature of the initial heat distribution required to simulate the process. This difficulty is a direct consequence of the choice to neglect convection (fluid flow). Despite this, conduction models have much to commend them, and are actively being researched today (Painter et al 1993).

An important early contribution to the description of keyhole welding was a paper presented by Swift-Hook and Gick (Swift-Hook and Gick 1973). They modelled the keyhole as a line heat source, and concerned themselves only with the heat flow. Two dimensionless parameters were derived - X, a normalised power per unit depth, and Y, a normalised melting width. Y is a function of X, and was presented as a simple curve, the position of which varied with the coupling efficiency (see also Appendix A1). This description was found to be valid for all available data - from both EBW and LBW. The relationship between X and Y indicated that there was a theoretical maximum melting efficiency, 48%, and that this did not correspond with the highest penetration. The melting efficiency can be defined as the amount of energy required to melt a unit volume of metal in isolation divided by the energy required to generate the same

amount of fusion in the welding situation. This result showed that efforts to increase efficiency beyond this level were futile, and in any case efficiency was won at the expense of penetration. It was argued that the latter was usually more important. These results were useful for predicting the laser power required for a specified penetration, but did not offer any insight as to how the penetration of a given process might be improved. For example, LBW required about 1000kW/m penetration in steel whereas EBW required only 150kW/m.

This type of description has been extended and refined by various researchers since 1973. For example, Giedt (1981) presented a study of EBW keyholes that included photographic evidence for the elliptical shape of the vapour channel. This led him to propose a model that treated the heat source as an elliptical cylinder. Miyazaki and Giedt (1982) presented an analytic treatment of this model the following year. It gave reasonable predictions of penetration as a function of beam power in partial penetration welds, and efficiency for full penetration welds.

In early 1988 Steen, Dowden, Davis and Kapadia (Steen et al 1988) modified the line source model proposed by Swift-Hook and Gick by adding a point source at the surface. The addition was motivated by the observation that laser keyholes often had a pronounced broadening, or 'nail-head' near the surface. This work was soon followed by a more general treatment where the heat distribution along the keyhole axis was allowed to vary (Akhter et al 1989). For example it could take the form of several distinct point sources. This approach allowed the construction of heat distributions that reproduce observed fusion profiles, and so could be used to generate the temperature fields outside the fusion zone, and provide some insight as to how the power absorption varied with depth within the keyhole. Several examples of keyholes through lap joints were presented, and the source-fitting technique showed that heat concentrations occurred at positions corresponding to the plate surfaces, namely at the top of the keyhole and at a depth corresponding to the interface between the two plates. As the authors pointed out, the approach can be readily extended for cases where the complete three-dimensional fusion surface can be obtained. A method was suggested for obtaining such surface data.

These descriptions, as well as the non-dimensional parametric approach of Bibby, Goldak and Shing (Bibby et al 1985) are powerful because they are simple to apply, and relate directly to one of the most important practical consequences of welding - the thermal cycle. They thus constitute powerful investigative tools. However, they are usually seen as having only limited predictive function because the required input must be obtained from completed welds rather than the physical properties of the beam and material. Nevertheless, given the appropriate input the predictions can be expected to be more accurate than those of more fundamental models.

2.4.2. Fundamental models

Three years after the work of Swift-Hook and Gick, Andrews and Atthey (Andrews and Atthey 1976) provided one of the first physically based descriptions of a slow-moving keyhole. The requirement of low speed corresponded to the neglect of certain aspects of heat flow. The paper was not only important for its content, but also because it is regarded as the pioneering effort that introduced the topic of keyhole modelling to the wider scientific community (Kapadia and Dowden 1994). The model described a keyhole where the driving force was the recoil pressure generated by ablation of material from the keyhole walls. In the first instance this was balanced against the hydrostatic pressure of the molten metal and subsequently the consequences of introducing surface tension were discussed. Solutions for cases without surface tension were readily obtained, but contained a singularity at the tip. Surface tension removed this singularity, and reduced the predicted penetration by a factor of about three, but required numerical techniques for solution. Surface tension was thus recognised as a dominating force in keyhole welding.

Since the early 1980's a group at the University of Essex in the U.K. has been a major contributor to the theoretical description of keyhole behaviour. For example, in 1983 Dowden et al presented an analytic model for fluid flow (Dowden, Davis and Kapadia 1983). The model was constructed in two dimensions, and explored the consequences of a variety of temperature-viscosity relationships. This work was later treated numerically (Davis, Kapadia and Dowden 1985) using a technique known as the 'method of lines.' The models showed down-stream displacement of the solid-liquid boundary, and gave minimum power requirements. The form of the temperature-

viscosity relationship was found to be relatively insignificant. Surface tension effects were neglected.

In subsequent works the group has considered liquid flow in the axial direction (Postacioglu et al 1987) driven by pressure gradients, and the dynamics of vapour flow at medium welding speeds (Dowden et al 1991). In the latter paper they showed that shocks could form at the keyhole entrance, and at the exit if it is fully penetrating. In all cases relevant equations were presented and sophisticated mathematical techniques used for their treatments.

In 1985 Wei and Giedt (Wei and Giedt 1985) produced a two dimensional model in which the flow around a keyhole was driven by surface tension variation with temperature. In their description the keyhole was supported by vapour pressure, but actual temperature and velocity distributions were determined from a self-convergent finite difference method. Surface tension was assumed to vary linearly with temperature:

$$\gamma = \gamma_m + C_\gamma (T - T_m)$$

where γ is surface tension, γ_m is its value at the melting temperature, C_γ is a constant (-4.0 $x10^{-3}$ N/m°C for iron), T is temperature, and T_m the melting temperature. The significance of their work was that it showed that the surface tension gradient induced flow (ie Marangoni flow) could be a dominating factor in keyholes. Calculations based on the properties of iron predicted a keyhole where the liquid was only fractions of a millimetre thick at the front, and reached a velocity of almost 300mm/sec. as it streamed around the sides. They also noted that the bottom of the keyhole was known to be hotter than the top and therefore axial flow should be expected. Finally, variations in vapour pressure within the cavity were predicted, and it was argued that these would become much more significant if flow velocities were reduced. Consequently it was postulated that variation in vapour pressure could provide the driving force in materials where the temperature coefficient of surface tension was either very small or positive. In such circumstances flow rates would be expected to be relatively low, and the liquid layer at the front of the cavity would be relatively thick.

Not all subsequent models have been as supportive of the role of Marangoni flow. A comprehensive numerical model developed by Lambrakos el al (Lambrakos, Metzbower, Dunn and Moore 1992) concluded that the presence of the keyhole represented a geometric constraint on fluid flow, and this was always the dominating influence on fluid convection. Their work demonstrated the power of numerical simulations since they were able to include the temperature dependence of properties including surface tension, viscosity and specific heat. Other important observations were that the welding process consisted of time-dependent structures even in the steady state, and that there were many spatially-fine structures embedded in much courser structures.

While the findings of Lambrakos et al were important, one of the underlying assumptions was that the keyhole surface could be defined by the temperature-of-vaporisation isotherm. This effectively prohibited the development of a gradient in surface tension, and therefore Marangoni flow. A later paper by Kroos et al (Kroos, Gratzke and Simon 1993) treated a fully penetrating keyhole, and allowed the surface and its temperature to adjust self-consistently subject to balances in energy and between ablation pressure and surface tension. Results for this model contradicted previous assumptions: the keyhole was wider than the diameter of the beam by a factor of at least 1.7, and the surface temperature was up to 100K above the evaporation temperature. Also a minimum laser beam power of 790 W/mm was predicted for steel. Marangoni flow was not investigated, but it was the opinion of the authors that under the conditions described in the model it would play only a minor role.

2.4.3. Dynamic behaviour

The majority of modelling approaches have concerned themselves with 'steady-state' keyholes (Kroos, Gratzke, Vicanek and Simon 1993). However, in practice it is found that keyhole welding is an unstable process that can be very difficult to control (Kristensen and Olsen 1992). According to Kroos "the keyhole is never found in an entirely stationary state."

In a 1973 study of electron beam welding defects Arata (Arata Terai and Matsuda 1973) identified six types of defects (excluding cracking) that were attributed to the

dynamics within the keyhole. He characterised three types of porosity, depending on position and structure, as well as 'spiking', 'cold shut', and 'unmelted lump.' These are illustrated in Figure 2.2. Only the AR porosity defect was specifically related to the type of beam (it was suggested that it was due to arcing within the electron gun), and consequently the remaining defects could be expected to occur in laser beam welding as well. The experiments were conducted on a range of materials including carbon steel and austenitic stainless steel. Porosity defects increased significantly with increasing oxygen and nitrogen contents of the two steels respectively.

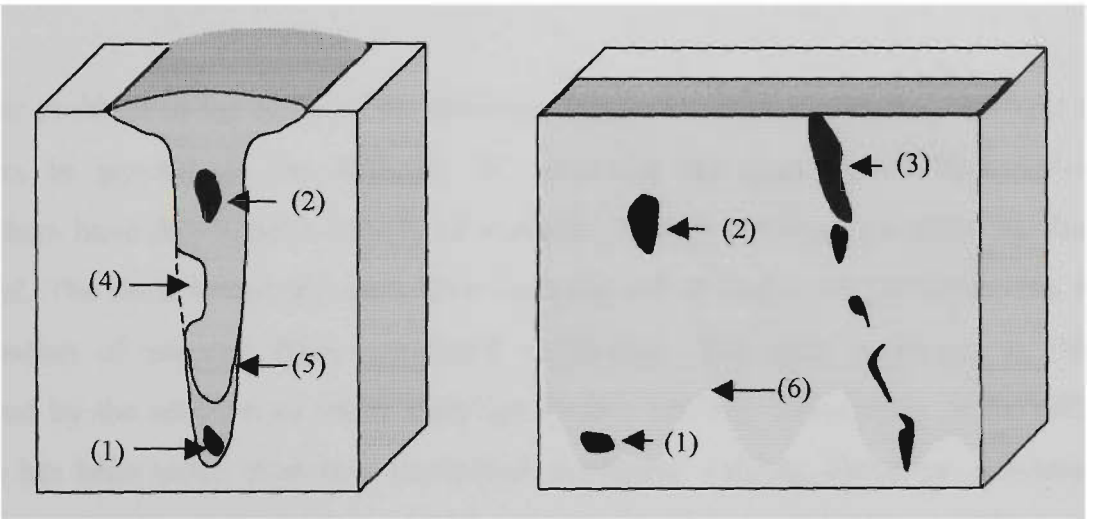

Figure 2.2. Schematic illustration of various macroscopic weld defects. (1) R-porosity, (2) A-Porosity(3) AR-Porosity, (4) Unmelted lump, (5) Cold shut and (6) Spiking (Arata, Terai and Masuda 1973).

Arata has also investigated the dynamic behaviour in laser keyholes (Arata et al 1977, Arata, Abe and Oda 1983) and reported some unexpected results. In particular he observed disturbances travelling parallel to the keyhole axis along both the leading and trailing edges. He concluded that any irregularity in the leading surface would grow rapidly and be propelled to the bottom of the keyhole due to both the directed nature of the beam and its rapid attenuation with depth. The amplification of irregularities on the leading surface, and the resulting high velocity flow has been confirmed by direct observation of electron beam welding (Metcalfe and Quigley 1975). However, according to Postacioglu et al, an axial pressure gradient develops in steady state keyholes and this will power flow parallel to the beam (Postacioglu et al 1987) even in the absence of the mechanism Arata has described.

The liquid metal to the front of the keyhole is usually very thin, and hence moves at high velocity. At the rear, however, the molten region is much thicker and slower moving. Because of this associated disturbances and oscillations can grow to relatively large amplitudes and destabilise the keyhole, resulting in numerous defects including channel closure. As expected a quantitative description of the dynamics would be very difficult because the system is clearly non-linear. Arata has however, offered a qualitative description that has been useful in demonstrating the complexity of the situation (Arata et al 1977).

A major problem in the study of the dynamic behaviour within keyholes, and perhaps keyholes in general, is the difficulty of observing the phenomena. Nevertheless, researchers have developed a variety of methods through which information has been obtained. The most frequently used have been the use of high-speed cameras, and the examination of sections from completed weldments. The latter technique is often enhanced by the addition of tracer materials during welding. Monitoring of the efflux plasma has been noted elsewhere in relation to plasma welding. However, Kristensen and Olsen (1992) have looked at oscillations in the plasma plume of laser welding. The finding that the oscillations are in the audio range has prompted Kroos et al to suggest the use of acoustic pick-ups, although their use has not been noted in the literature. The most direct observations have been made by Arata, and in his work he has provided examples of x-radiography, x-ray fluorescence (for electron beam welding only), and the use of transparent materials. The last method has only been used with laser welds because of the conductivity requirements with plasma and electron beam. He has used water and a variety of glasses, but his best results have been obtained with soda glass.

Mathematical treatments found in the literature were by Kristensen and Olsen (1992), Kroos et al (1993), and Lim and Chatwin (1994). Kristensen looked at the response of a keyhole to changes in laser power both theoretically and experimentally. The paper reported that oscillations in beam power induced in-phase oscillations in the plasma and keyhole at low average power levels, but reported a phase reversal as average power was increased. This corresponded to the striking of a resonance in the trailing section of the keyhole, with resultant large amplitude radial oscillations. They demonstrated that these resonances could be initiated by step changes in beam power.

The work of Kroos et al (1993) was entirely theoretical, and resulted in the development of a mathematical description of radial oscillations in a highly idealised keyhole. One interesting finding was that keyholes have a closing time τ of about 0.1 ms:

$$\tau \approx \sqrt{\frac{\rho r^3}{\gamma}}$$

where r is the keyhole radius, ρ is the liquid density and γ is the surface tension. Other results were that the oscillation frequency is of the order of 400 Hz, and that there is a minimum power per unit depth of keyhole required to prevent spontaneous closure. The estimation of the keyhole closing time is particularly relevant to pulsed laser welding applications.

Laser-matter interactions are inherently non-linear and difficult to control, and Lim and Chatwin (1994) have formalised this by proving the existence of chaos in such systems. The behaviour can be described by what are known as 'Poincare-Birkhoff-Smale horseshoes', and they proposed that optimal control parameters can be obtained by exploiting this fact.

2.5. Plasma arc keyholes

2.5.1. Process characteristics

In 1974 Tomsic and Jackson (Tomsic and Jackson 1974) published a study of the parameters responsible for keyhole behaviour in plasma arc welding. Although the study was carried out on type AISI 304 stainless steel, the authors considered the results to be of general applicability. The article provided a good practical understanding of the process and gave a necessary basis for the development of control systems. The parameters identified were: heat input, current, arc length, travel speed and orifice flow rate. The authors showed how the various parameters interacted and how the operating window could be affected by factors such as plate thickness and joint fit-up. For example, if fit-up is very good the bottom width of the keyhole may be very small, and

is limited only by the requirement for full penetration. However, if it is poor, the bottom width must be increased to ensure full fusion. This in turn increases the chances of humping and undercut, while the larger exit hole also reduces process efficiency.

Studies such as that of Tomsic and Jackson emphasise the importance of control of the keyhole geometry in plasma welding. While full penetration is essential, the penalties for excessive heat or gas flow, which include undercut, humping, and unacceptable cooling times, must be avoided. A practical means of monitoring penetration was seen as desirable, and the approach suggested by Metcalfe and Quigley (1975) presented a simple solution. Their work showed that relatively simple monitoring of the luminosity of the efflux plasma (the plasma escaping through the bottom of the keyhole) was sufficient to provide the required information. In fact, not only could it indicate whether penetration was complete or not, but also revealed the occurrence of instabilities associated with the keyhole, and excessive keyhole exit diameter. The authors provided a mathematical analysis that described the various conditions they had observed.

It is not always easy or practical to observe the efflux plasma, and front side detection would be of much greater value. Martinez et al reported success in this area in 1992, at least with respect to the welding of aluminium alloys (Martinez, Marques, McClure and Nunes 1992). Their strategy was to look for the presence of hydrogen emissions in the optical spectrum of the plasma. They monitored the ratio of the intensities of the 656nm hydrogen line to the 696nm argon line, and found an abrupt decrease whenever the keyhole became open. Further experiments showed that the change was a result of a decrease in the effects of atmospheric contamination as the keyhole entered into a fully penetrating mode. They concluded that this was a result of the contaminant being flushed through the open keyhole, and thus more effectively removed from the visible portion of the arc. The technique should be applicable to any metal, although the approach does not quantify the degree of opening, and would be sensitive to torch design and environmental conditions.

2.5.2. Variable polarity plasma arc welding

While the maintenance of an open and stable keyhole is a fundamental problem, material-specific difficulties have been a major concern. Plasma keyhole welding is

particularly suited to metals of low density, and therefore its potential for the welding of aluminium and its alloys was recognised very quickly. However, the impediment to its successful application in this area has been due to the tenacity of the oxide layer that forms on these materials. This problem also occurs with conventional GTAW, but in that case was overcome by the development of alternating current welding technology. Alternating the polarity of the welding current is effective because when the plate surface takes on a negative voltage with respect to the plasma it attracts and is bombarded by positive ions, and the oxide is removed by sputtering. This polarity cannot be maintained indefinitely, however, because the heat generated in the electrode is excessive, while little is transferred to the work piece. In practice the polarity is switched rapidly, typically at mains frequency.

Unfortunately the same technique failed when applied to plasma keyhole welding of aluminium. It was not until Tomsic and Barhorst introduced a much more versatile power supply and experimented with the waveforms that high quality keyhole welding was achieved. In particular they were able to experiment with a non-symmetric square wave for which they could independently vary the amplitude and duration of the current for each polarity. High quality performance was achieved, but was found to depend critically on producing sufficient cleaning action during the electrode-positive segment of the cycle. It was found experimentally that this could be achieved with short, large amplitude pulses for the cleaning phase, and much longer, lower amplitude pulses for providing the energy to maintain the keyhole. The best settings were dependent on many factors including type of material. They used the term 'variable polarity plasma arc' (VPPA) to illustrate this point.

2.5.3. Enhanced plasma arcs

Plasma arc welding is characterised by a constricted arc, and there is a clear incentive to enhance this effect. Arata has given this topic considerable attention since the early seventies. In his development of what he described as a 'point arc' (Arata and Inoue 1974) he illustrated two additional means of constriction. Normally the plasma arc is constricted by forcing it through a small orifice. Arata has developed a torch where an additional orifice was formed by jets of cold gas flowing in the reverse direction. The gas wall was arranged in such a way that the flow had a substantial tangential

component. This produced two effects: a thermal pinch and a stripping action whereby the outer conductive thermal sheath and plasma flame were blown away. Energy density was increased substantially because of the much smaller cross section of the plasma.

In later work Arata increased the tangential velocity of the gas wall to in excess of 150 m/sec (Arata and Kobayashi 1983). In such systems the pressure at the centre of the vortex drops below 100 Torr, producing a narrow, partially evacuated gas tunnel surrounded by a high velocity gas wall at or above atmospheric pressure. In a description of one device he referred to a plasma jet with a diameter of 2.5mm carrying 400 amps. Such devices are capable of very high power, perhaps extending into the megawatt range (Arata and Kobayashi 1985). However, the application of these devices to welding is unclear, and the only example reported was with the point arc process.

2.5.4. Fluid flow in VPPA weldments

Fluid flow specific to plasma arc keyholes has not attracted significant attention in the literature. This is most likely because the particular vehicle for energy delivery to a keyhole (eg laser, plasma or electron beam) is of minor concern in comparison to the difficulties involved in modelling a generalised flow behaviour. Nevertheless interesting research has been done, and a good example is the work of Walsh and Nunes (Walsh and Nunes 1989). Their work not only investigated the various forces responsible for generating flow in VPPA welding of aluminium plate, but also illustrated a variety of experimental techniques of importance.

The work was carried out on 2219 aluminium plate of up to 12mm in thickness. Experimental tools used included high-speed cinematography, the addition of a wide range of oxides, halides and sulphates, and the introduction of tracers in the form of filler material (Walsh and Nunes 1989). What emerged was a detailed qualitative description of a plasma arc keyhole in aluminium.

The keyholes they observed were between 4 and 5 mm in diameter. Most of the heat was delivered to the leading edge, which also corresponded to the direction of the plasma flow and the location of the anode spot. The liquid metal was less than 0.5mm

thick in this region, and remained thin, though less uniform, around the forward half of the keyhole. The trailing region of the keyhole was characterised by a much thicker, croissant-shaped fluid pool, the thickness of which increases slightly with depth. Fluid motion in this region was dominated by Marangoni flow. They were able to estimate that at a welding current of 250 amps the contributions to fluid velocity were approximately:

Bouyant force	-	5 mm/sec
Lorentz force	-	100 mm/sec
Marangoni force	-	1250 mm/sec.

The surface temperature of the pool was estimated from the behaviour of some of the chemical additions to be between 1000 and 1200° C, and the Peclet number in the range of 10 to 70. This signified that heat transfer was predominantly via convection rather than conduction (Walsh and Nunes 1989).

Among their numerous observations they reported that oxygen concentrations as low as 10 ppm were detrimental, causing the keyhole to expand and become unstable. One reason was because it reduced the surface tension, but they also found that it altered the electrical conditions in the plasma such that the arc voltage increased and more heat was delivered to the pool. The resultant increase in pool volume caused sagging and additional instabilities to develop (Walsh and Nunes 1989).

3. A practical appraisal of keyhole GTAW

3.1. Introduction

3.1.1. Background

Keyhole welding processes are those in which energy is delivered directly to the joint faces via a relatively small 'hole' punched through the plate surface (front face). The keyhole is the resultant cavity extending across the joint faces. The formation of a keyhole permits relatively efficient delivery of energy to the joint faces when compared to conduction from the surface. However, the two liquid metal streams flowing around the keyhole as it traverses the joint must coalesce without loss of material in the trailing regions of the weld pool. This constraint distinguishes the process from cutting.

The energy for welding may be delivered by a laser or electron beam or by a current-carrying jet of plasma as in PAW. Keyhole formation is dependent on an increase in pressure in the interaction region. This pressure is provided by the recoil from ablating material in LBW and EBW (Lancaster 1986, Andrews and Atthey 1976, Matsunawa et al, 1998), whereas for a significant portion of the pressure results from the mechanical impact of the jet in PAW (Lancaster 1986).

Keyholes cannot form if the resultant pressure is too low to force the molten metal away from the beam (or arc) axis. In such cases the heat is conducted to the lower portions of the joint in what is referred to as "melt-in mode" welding. Melt-in mode welding is familiar from processes such as oxy-acetylene and the various forms of electric arc welding. As might be expected, keyhole welding requires greater precision in fit-up and parameter control than do the more commonly used processes.

PAW keyholes differ from those generated with lasers or electron beams in that they must be 'open' to allow the venting of the arc gases. This means that the keyhole must extend all the way through the plate. The plasma escaping from the bottom of the keyhole is referred to as the 'efflux' plasma. PAW has been regarded as the only arc

welding process typically operated in a keyhole mode (AWS Welding Handbook). Indeed, it is frequently contrasted with gas tungsten arc welding (GTAW) where the keyholing capability of PAW is seen as its primary advantage (ASM Handbook, Vol 6, Halmoy 1994). Nevertheless there have been descriptions of successful keyhole welding using modified GTAW equipment in the dual-gas GTAW process (Norrish 1992), although wider use has not been reported. The disadvantages of PAW in comparison to GTAW include higher capital costs, increased sensitivity to variations in the process parameters, added torch complexity, and increased maintenance. The complexity of PAW compared to GTAW technology is often seen as a liability in production situations, where GTAW is regarded as being particularly reliable and reproducible.

GTAW is a precision welding method that has been used for many years to produce high quality joints in a wide variety of materials. It is a clean process because fume generation is very low, and generally no fluxes are required. It may be operated manually at lower welding currents to weld relatively thin materials, but requires careful V- or X-type edge preparation for thicker sections. This in turn usually necessitates the addition of filler material and multiple passes to complete the joint, leading to significantly increased joint completion times.

As an alternative, the GTAW process may be automated and operated in a high current mode (ie >300 amps) to induce displacement of the weld pool. This results in greater penetration, and can be used for joints between square-edged sections. This process variant is sometimes referred to as high current, buried arc, or immersed arc GTAW. It is generally operated with direct current and with the electrode as the cathode because this polarity provides the greater efficiency in energy delivery to the weldment. Examples of the high current GTAW process are presented in Figure 3.1.

In its normal, or melt-in, mode the high current GTAW process forms a relatively deep weld pool through the combined effects of high heat input and weld pool displacement. The displacement is due to arc pressure, and results in a crater, or cavity, under the arc. In some situations there are advantages to having the electrode tip projecting within this cavity, and in that case the arc is referred to as being submerged, or buried. The puddle may sometimes be made deep enough to achieve

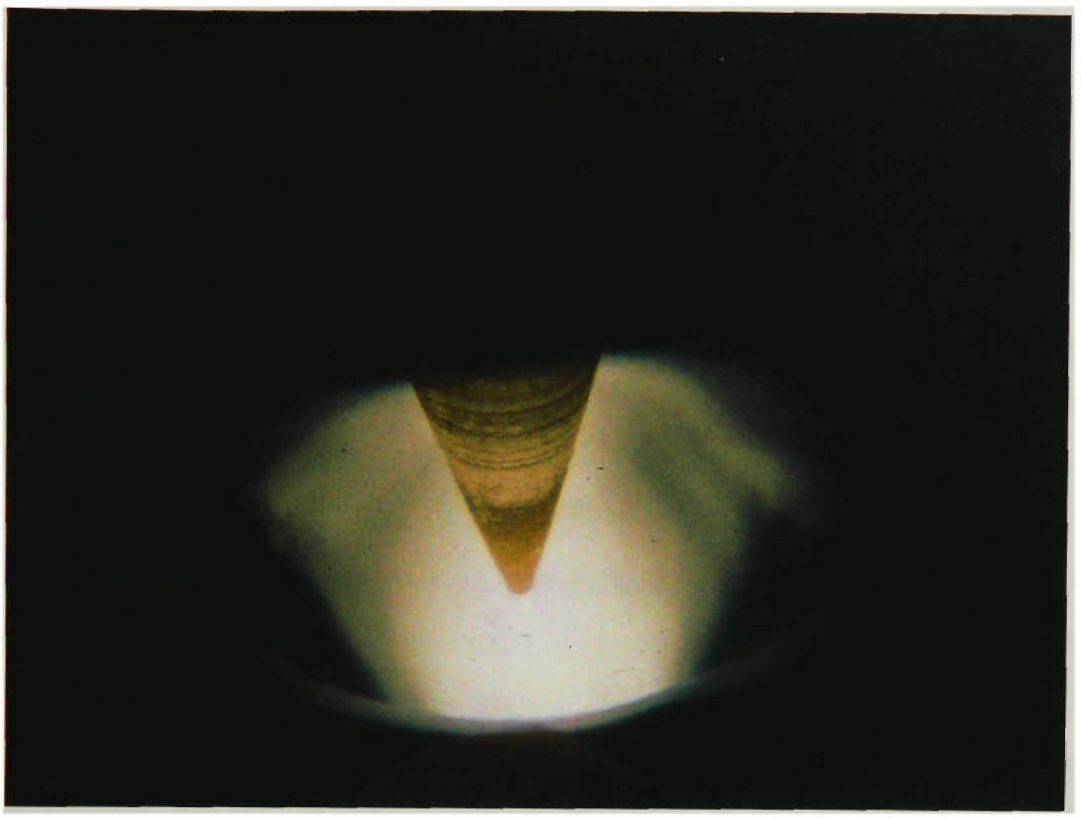

(a)

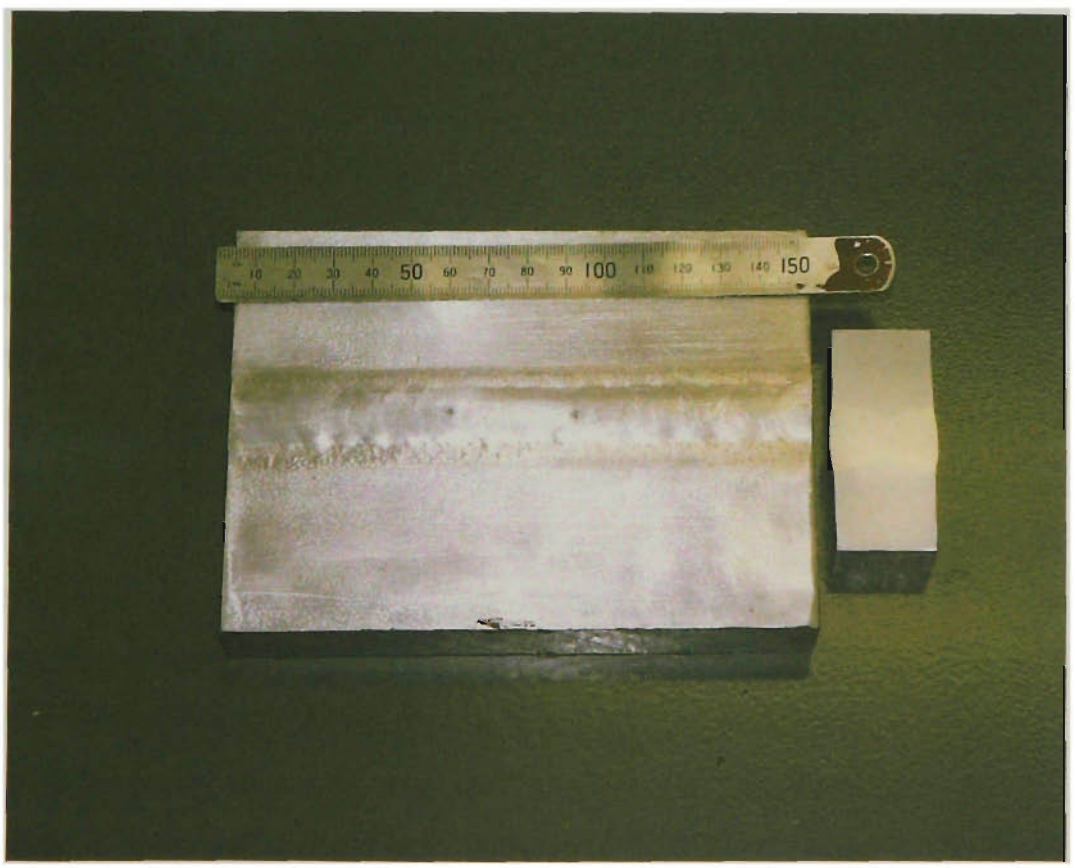

(b)

Figure 3.1. Close-up of the high current GTAW process (a) showing pool displacement, and (b) sample welds on 25mm AA5083 plate.

'full penetration', but this requires backing bars or other devices to support the liquid metal until it freezes.

Despite some compliance with the definition suggested above, this mode of welding has not been regarded as constituting a keyhole. Likely points of distinction are that the opening is not considered to be small (the width of the cavity is generally significantly greater than its depth), and the puddle must be supported if full penetration is achieved.

In practice the degree of penetration can be difficult to control, especially if the weld is not fully penetrating. In addition a defect known as hollow bead may be a problem at currents over 350 amps, and the process may become violently unstable above about 500 amps. The latter two difficulties are related to the generation of high arc pressures. Hollow-tipped electrodes have been developed as one means of reducing arc pressure and thereby alleviating these problems (Yamauchi et al 1981).

3.1.2. Keyhole mode GTAW

The keyhole variant of the GTAW process can be regarded as an alternative solution to these problems. More specifically, the development and application of a keyhole mode of the GTAW process encompasses the central thesis of this research. Since this particular mode of GTAW does not appear in the literature, it is presented as a novel process variant. As such it has already gained significant industrial credibility, and is therefore taken to constitute a potentially valuable addition to welding technology.

In the keyhole mode the arc pressure is deliberately increased to the point where it becomes possible to push the cavity to the bottom of the pool. The keyhole forms when there is sufficient heat input to melt through the plate, because at this point the bottom of the cavity breaks through the root face of the weldment and the arc gases can escape. The arc pressure must derive from Lorentz forces acting on the arc plasma since the power density of GTAW is too low to generate an appreciable recoil pressure (Lancaster 1986). Thus GTAW keyholes owe their formation to electromagnetically driven arc jets, as opposed to recoil pressure in the cases of laser

and electron beam keyholes, and a combination of recoil and stagnation pressure for plasma arc keyholes.

For the weld to be completed the keyhole must close behind the arc, and this places a number of constraints on the process parameters. However, since the keyhole extends across the entire width of the joint face welds are completed in a single pass. Also, because the gas flow is much less obstructed than in the melt-in mode weld pool turbulence and porosity are rare. This can be contrasted with high current GTAW, where pool turbulence, hollow bead defects and worm-hole porosity are familiar problems. (The latter defect can also be produced if there is an incomplete transition to the keyhole mode as may occur with thicker (>7mm) plate. Completing the transition, for example by increasing the welding current, eliminates the problem). The process is illustrated in Figure 3.2.

Keyhole mode GTAW is intended as an automated welding process for the flat position (also known as down-hand) welding of ferrous and non-ferrous alloys in the thickness range of about 3 to 12mm. Applications could include the welding of large flat sheets, and vessel and pipes that can be rotated under the arc. The physical mechanisms that underscore the process make it ideally suited to materials of relatively low thermal conductivity, such as stainless steels and titanium. Typically fabricator of these more expensive materials demand high weld quality and appearance. The keyhole mode GTAW process provides the quality of GTAW with a productivity that is very competitive with conventional submerged arc and gas metal arc welding. In addition it has the advantages of a minimal requirement for filler material, the acceptance of square edge plate preparation, and of being a single pass process. Typical examples of performance include the welding of 12mm AISI 304 at 300mm/min in a single pass, 8mm AISI 304 at 500mm/min and 3mm 3CR12 at 1000mm/min.

(a)

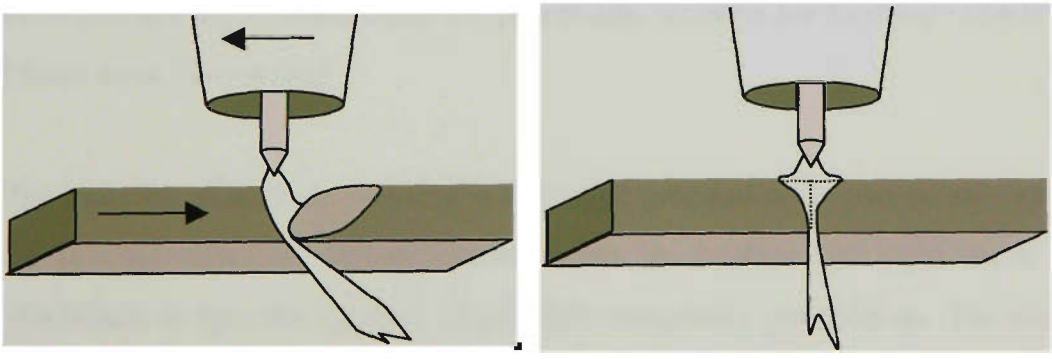

(b)

Figure 3.2. Side-on view of keyhole welding of 8mm wall-thickness AISI 304 pipe (a) and a schematic of the process.

3.2. Equipment

The process can be operated using commercial equipment intended for use with high current GTAW. Essentially this means a DC constant current power source, a wire feed unit, and a high current welding torch. The process is operated with the torch electrode at a negative potential with respect to the work-piece (DCEN polarity), and must be automated.

It is essential that the torch performs reliably and consistently when operated in the range of 300 to 800 amps. The torches used during this work were of a patented CSIRO design intended for high current GTAW (CSIRO 1995). The significant features of these torches are a continuous current rating in excess of 1000 amps, and a water-cooling system that includes the torch barrel and shroud. The comprehensive cooling is important for achieving a stable and reproducible arc over the entire current range, due mainly to the stabilisation of the temperature gradients in the tungsten electrode. The torch can accept electrodes of 2.4, 3.2 4.0, 4.8 and 6.4mm diameter. In this work rare-earth doped electrodes of between 3.2 and 6.4mm diameter were used. In most cases a trailing shroud was fitted to protect the solidifying weld metal from oxidation. The trailing shroud was approximately 30mm wide by 100mm long. Other commercial torches are available that are potentially suitable for keyhole GTAW, but none of these have been tested.

One of the benefits of keyhole welding is that edge preparation is particularly simple. Since the process relies on self-generated forces to displace the weld metal it is usually sufficient to provide squared edges with reasonably good fit-up. The process has been used successfully with edges prepared in a variety of ways, including plasma cutting, shearing, guillotining and machining. However, for most laboratory experimentation samples were either welded bead-on-plate or the edges were machined.

In some instances filler wire was introduced. This was used either to reduce undercut, compensate for joint gap, provide some additional reinforcement or to modify the microstructure of the weld metal. The wire was fed from the leading side of the torch

to avoid complications with the trailing shroud. It was found most convenient to introduce the wire at a small but non-critical angle to the work piece (eg 30°), and to have the delivery tube pivoted and spring-loaded so that the wire always pressed against the plate surface. This guaranteed that during operation the wire was always in contact with the leading edge of the weld pool cavity as it entered the arc. The arrangement minimised and stabilised interference with the arc, and wire feed speeds of up to 5.4 m/min (equal to 2.9kg/hr) were used successfully. A schematic of the arrangement is shown in Figure 3.3.

Two commercial power supplies were used during the laboratory studies, and there was no evidence to suggest that the choice of supply was a significant factor in the process. The initial work was conducted with an inverter supply with a capacity of 600 amps. Later work required an increased current capacity and for that a 1000 amp SCR-based power source was used. The torch was operated with DC electrode negative (DCEN) polarity at all times. Current and voltage were measured with a CSIRO welding monitor. When possible the voltage was measured between the top of the torch and the work-bench, thus avoiding the inclusion of unwanted voltage drops in the readings.

The keyhole mode relies on the arc gases being able to escape from the underside of the plate (the root face). When this side of the plate could be seen the appearance of the highly luminous efflux plasma signalled the onset of keyhole mode. Observation was made easier by constructing a metal box with two glass sides and a longitudinal slit some 60mm wide in the top. This provided good viewing of the underside of the plate while still permitting the use of inert backing gases when required. In practice a backing channel of 10mm wide by at least 6mm deep was required for currents up to 500 amps, but its depth needed be increased to about 20mm for higher currents. Throughout this work keyhole mode was detected and controlled directly by the operator. Visual observations were augmented by videography when thicker materials were being studied.

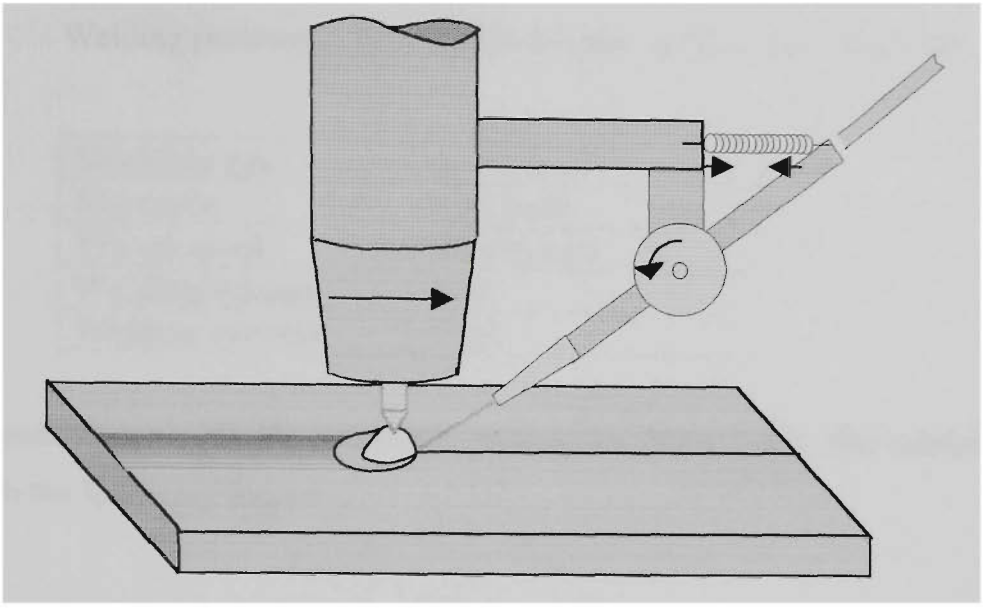

Figure 3.3. Schematic of wire delivery system showing how wire is pressed against the lip of the crater.

3.3. Process parameters

3.3.1. Introduction

The first successful generation of a GTAW keyhole was achieved on 5.1mm SAF 2205 duplex stainless steel. The conditions were estimated after gathering data on the heat input required for full penetration for various travel speeds. The parameters used for this first keyhole weld are presented in Table 3.1.

The removal of backing plates, and any other obstruction that would interfere with venting of the arc gases through the weldment was crucial to achieving the keyhole mode. Furthermore a fortunate combination of other parameters (gas composition, material properties and plate thickness) played a major role in this initial success. In fact, this particular set of conditions subsequently was found to be only marginally sufficient to sustain the keyhole. For example, the first attempts to reproduce this welding mode were unsuccessful due to a slight increase in the thickness of replacement material. Also the beneficial influence of the nitrogen in the shielding gas was not at first appreciated. The nitrogen had been incorporated as an austenite stabiliser and its effects on the physical properties of the arc had not been considered.

Table 3.1. Welding parameters first used to keyhole weld 5.1mm SAF2205.

Shielding gas	Ar-10He-2N
Electrode	3.2-Ce-60
Travel speed	500mm/min
Welding voltage	12.0
Welding current	630A

For convenience and brevity electrode parameters have been abbreviated and presented in the following format:

Diameter – elemental addition – tip angle

The electrode diameter is given in millimetres, the elemental addition is the element added to stabilise the electrode and the tip angle is the included angle of the tip in degrees. Thus 3.2-Ce-60 refers to a 3.2mm ceriated tungsten electrode ground to a 60° included angle. Similarly gas compositions are presented as:

Predominant gas – percentage and symbol of second gas – etc.

As an example, Ar-10He-2N refers to a gas mixture containing argon with 10% helium and 2% nitrogen.

3.3.2. Threshold current

Once repeatability had been achieved an experimental program to determine an operating window and process sensitivity to welding variables was established. One of the most important dependent variables for process characterisation was the minimum welding current needed to initiate a keyhole, and much of the subsequent work involved determining the relationship between this minimum current and other welding parameters. This minimum necessary current was termed the 'threshold current'.

Increasing the current above the threshold tended to degrade the weld quality by increasing the tendency for undercut, as shown in Table 3.2. This trend has been verified for other materials and thicknesses. It must be appreciated however, that undercut is only one of many quality considerations, and therefore operating at current levels close to the threshold does not necessarily constitute good welding practice. Furthermore, undercut is sensitive to many factors in addition to current.

Table 3.2 An indication of the effect of welding current on visual appearance (5.6mm SAF 2205, 13.0V and 450mm/min travel speed)

Current *(amps)*	**Appearance** *(visual assessment)*
530	Good
540	Good
550	Undercut, heavy underside bead
560	Severe undercut, excessive underside bead

3.3.3. Experimental schedule

The initial investigation was made using 5.6mm SAF 2205. This work included examining the influence of travel speed, voltage, gas composition, and electrode geometry on the threshold current. The results helped establish a practical appreciation of the process and how it could be controlled. Once these experiments had been completed the process was applied to other materials. Many other variables having a significant impact on the process were encountered in this stage. Material characteristics including thermal conductivity, density, surface tension and sample thickness were influential. New materials also introduced new constraints, particularly in the area of shielding gas composition. These results were used first to build up a qualitative description of the process, and subsequently, with extension, to support the development of more fundamental, quantitative models of essential aspects of the behaviour.

3.3.4. Travel speed

Varying the travel speed had different consequences depending on the nature and thickness of the materials. However, in all cases there was a minimum operating speed below which the weld pool collapsed through the plate. This limit was found to decrease with increasing plate thickness and decreasing thermal conductivity. As an example, the 5.6mm SAF 2205 had a minimum keyhole mode speed of between 300 and 350mm/min, whereas for 12mm AISI 304 the speed was about 175mm/min. Similarly thicker weldments exhibited a lower maximum welding speed than thinner ones. These limits were dependent on the arc characteristics as well as the weldment properties.

3.3.5. Voltage

Voltage also was an important factor in weld performance. For example, in one set of experiments on 5.6mm SAF 2205, keyhole welding proved impossible with voltages below 11.3 volts. The threshold current was in excess of 620 amps at this setting, but dropped to a constant 510 amps above 14 volts. Moreover, the decrease in threshold current was largely restricted to the range between about 12 and 13 volts. Consequently operation within this transition region was very sensitive to parameter variations and gave unpredictable results. This behaviour is illustrated in Figure 3.4. Evidently the voltage in the initial demonstration was at the edge of this transition.

The welding of the much thicker 12mm AISI 304 was also influenced by voltage. In this case there was a range of voltage over which the keyhole could be controlled, but there was a definite optimum for the particular set of welding conditions. The effects were recorded in terms of the degree of difficulty the operator experienced in maintaining the keyhole. These particular results, shown in Table 3.3, were obtained using a travel speed of 300mm/min, a shielding gas of argon with 10% added nitrogen, and an electrode tip of 45°. Current settings were accurate to within ±5 amps.

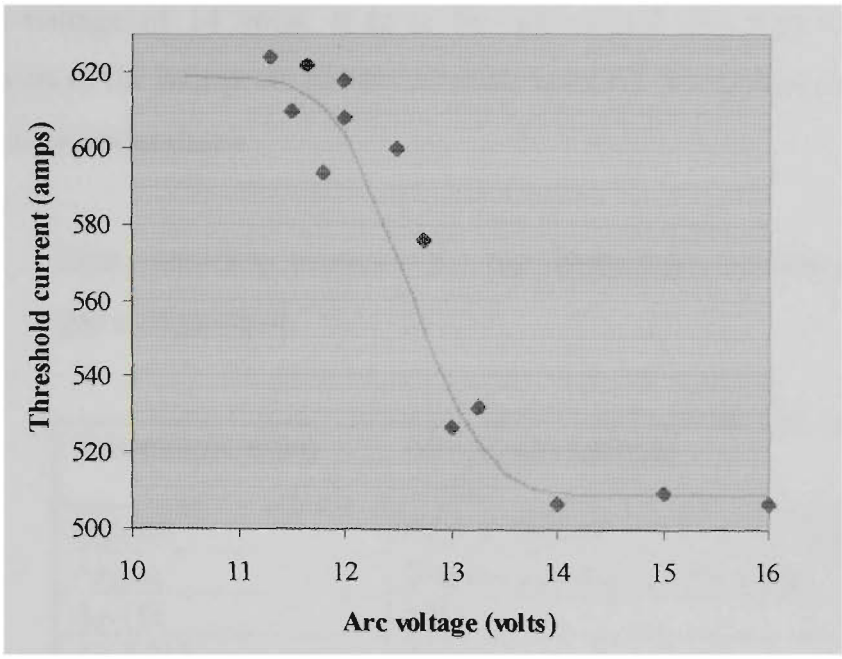

Figure 3.4 Threshold current for keyhole mode as a function of voltage for 5.1mm SAF 2205.

Table 3.3. The effect of arc voltage on keyhole formation in 12mm austenitic stainless steel.

Arc voltage *(volts)*	**Current** *(amps)*	**Degree of difficulty**
15	750	very difficult
16	730	difficult
17	700	comfortable
18	680	becoming harder
19	650	difficult

3.3.6. Shielding gas

Since the shielding gas regulates the transport of energy and momentum in GTAW variations in its composition had the potential to influence the threshold current. Taking pure argon as the reference, the addition of helium increased the threshold current, whereas additions of nitrogen or hydrogen reduced it. The effects could be very significant as the data in Table 3.4 show. It can be seen that the threshold current in pure argon was more than 40% higher than with the Ar-10N mixture. The data is

taken from experimentation on 5.6mm SAF 2205, with a travel speed of 450mm/min, and an arc voltage of 14 volts. It is to be appreciated that while the addition of diatomic gases to the mix promotes the keyhole process, this option is constrained by metallurgical considerations.

Table 3.4. Data providing evidence for the dependence of threshold current on gas composition.

Gas composition	**Threshold current** *(amps)*
Helium	Pool collapsed at 520 amps; no keyhole
Argon	Did not keyhole to 600 amps
Ar-1H	528
Ar-3.2H	486
Ar-10He-2N	513
Ar-3.5N	475
Ar-5H-5N	457
Ar-10N	435
He-25N	Unstable and did not keyhole.

3.3.7. Electrode geometry

The last set of variables easily altered were those determining the electrode geometry. Only conical tips were used during the investigation, and the two parameters investigated were the included angle of the tip, and the electrode diameter. Both increasing the electrode diameter and reducing the included angle of the tip reduced the threshold current significantly, with reduction of the included angle of the tip providing the greater effect. For example, the threshold current for a 90° tip was almost 40% greater than for a 45° tip for experiments using a 3.2mm ceriated electrode on 5.6mm SAF 2205. Almost half of this variation occurred between the angles of 45° and 60°. Changing the electrode diameter from 6.4 to 3.2mm increased the threshold current by about 13% for the same material.

3.3.8. Combined effects of gas and electrode geometry: 5.6mm SAF 2205

Repeated experiments also confirmed cumulative nature of the influences of gas mixture, electrode diameter, and tip angle. For illustration, combination of a 4.8-Ce-45 electrode with Ar-10He-2N gas, welding speed of 450mm/min and 14 volts across the arc developed a keyhole through 5.6mm SAF 2205 at 407 amps. This compared to 510 amps with the original electrode, and 630 amps in the initial demonstration at 12 volts and 500mm/min on 5.1mm material. The threshold current was further reduced to 377 amps with Ar-10N shielding gas.

3.3.9. Material

As the range of materials was extended from the original 5 and 6mm duplex stainless steel the influence of plate thickness and other physical properties became progressively more evident. For example, considerable experimentation was required before the process could be applied successfully to 12mm AISI 304 stainless steel, suggesting that material thickness was an important factor. In fact the process failed when applied to even thicker sections of AISI 304. The process could not be repeated with either 12mm C-Mn structural steel or 3CR12 stainless steel. This variation in performance was attributed to differences in thermal conductivity, since austenitic and ferritic steels have otherwise very similar physical properties. Specifically, austenitic stainless steels have quite low thermal conductivity in comparison to ferritic steels. In addition materials with significantly greater thermal conductivity than steel, such as aluminium and copper alloys, were found to be highly resistant to keyhole mode GTAW. Issues relating to the influence of thermal properties are discussed in more detail in Chapter 6.

Further investigation with C-Mn structural steel showed that the keyhole stability was critically sensitive to rust on the root surface of the plate. When heavy oxidation was present the mechanism supporting the weld pools tended to fail, and large pendent drops of molten metal formed along the weld, even on plate only 4mm thick. However, pre-weld surface cleaning dramatically reduced the problem, and material to at least 8mm thickness could be welded comfortably. In contrast to various ferrous applications, parameters were readily found for 13.8mm titanium plate (Grade 2

commercially pure titanium), and the process was stable over a wide operating window. In this case the material density was the most significant physical difference between the materials. The underlying mechanism in both these situations would appear to be related to surface tension, and this is discussed in Chapter 4.

Problems relating to material thickness were also evident as the thickness was decreased. Typically ferrous materials less than about 3mm thick could not be keyhole welded. This appeared to be related to difficulties in reducing the bead width. It was evident that there was a lower limit to the welding speed that could be used, and this limiting value increased as the thickness decreased. In any case the difficulty was of more theoretical than practical relevance since the melt-in mode is entirely satisfactory for plate less than 3mm thick.

3.3.10. Other variables: wire feed, flow-rate and the influence of cross flow.

Three other factors that were thought might influence the keyhole mode were the shielding gas flow rate, wire feed rate and the constricting action of a gas flow across the arc.

The effect of flow rate was examined by varying it between 10 and 50 litres per minute with other conditions held constant. No discernible change to the threshold current was observed.

Table 3.5. Data providing evidence for the dependence of threshold current on wire feed rate.

Wire feed *(mm/min)*	**Current** *(amps)*
2030	536
1070	496
300	492
0	475

On the other hand the wire feed rate did affect the threshold current, as the following results show (see Table 3.5). Conditions used were Ar-3.5N shielding gas, a 3.2-Ce-60 electrode, 14V across the torch and a travel speed of 450mm/min. The filler wire was 1.2mm diameter 309L.

Directing a gas flow across the arc was anticipated to strip off the outer layers of the plasma, effectively applying a strong thermal pinch to the arc and thereby constricting it. Several attempts were made to test this, but uncertainty was introduced because of the pick-up of outside air, and recurrent damage to the gas manifold directing the flow. The results below support a significant effect, but a more carefully designed shielding gas manifold would have been required to reliably quantify the effect. Conditions used were a 4.0-Ce-60 electrode, arc voltage of 14V, travel speed of 450mm/min, and an argon shielding gas. An additional gas outlet directed argon forward from the trailing shroud. This flow rate was varied. Indicative results are presented in Table 3.6.

Table 3.6. Data providing evidence for the dependence of threshold current on thermal pinching.

Cross flow rate *(l/ min)*	**Current** *(amps)*
0	470
2	445
4	435

3.4. Process performance and operating windows

3.4.1. Joint qualification

In general, welded joints must conform to certain nationally recognised standards. These standards are written with considerations given to the material, its intended application, and the welding process being used. Conventional practice usually involves the development of a specific set of welding parameters, known as a 'welding procedure' or 'schedule', for a given application. Sample weldments made

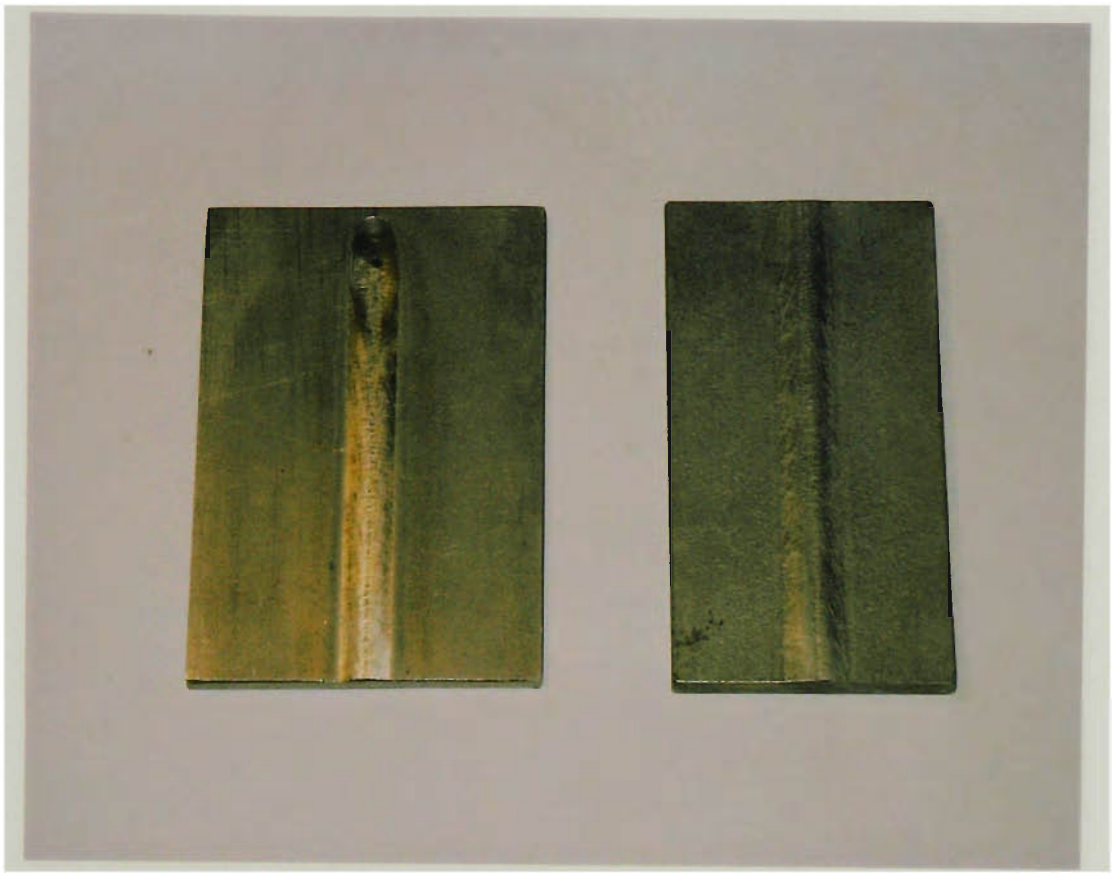

(a)

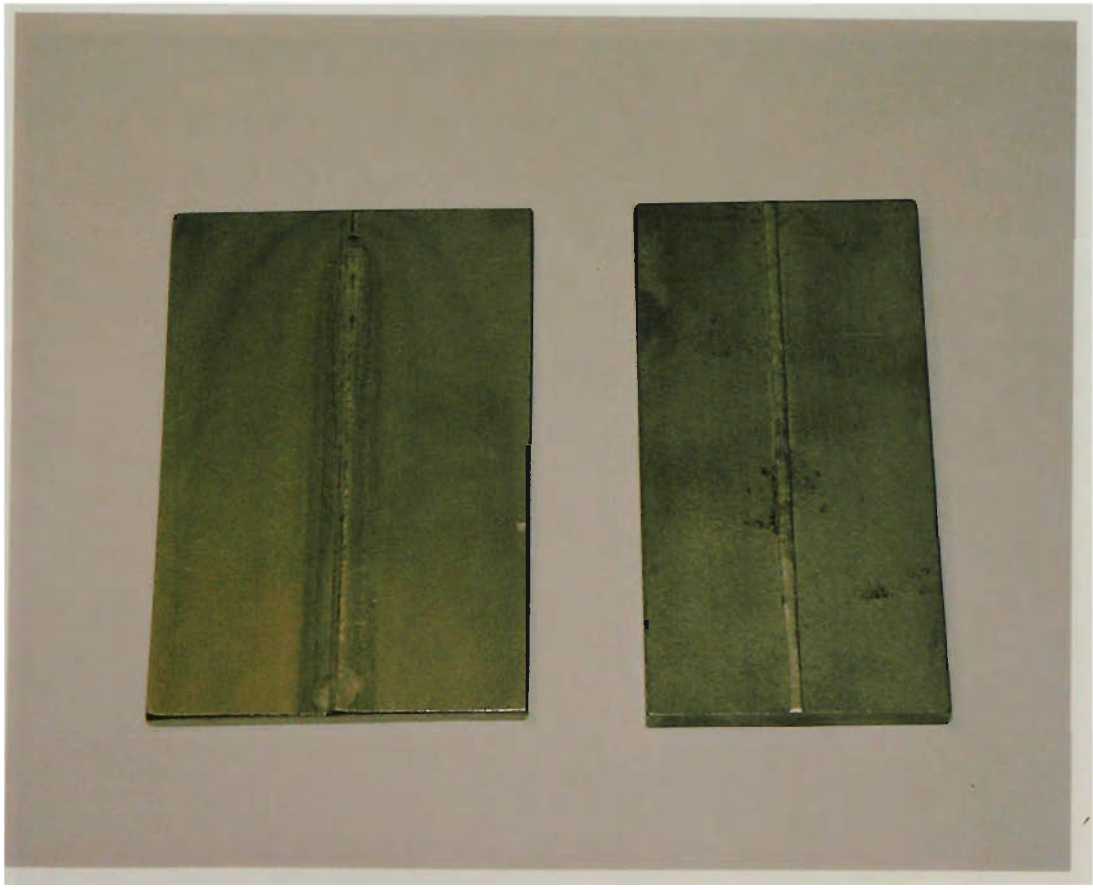

(b)

Figure 3.5. Keyhole GTA welding examples for 4mm AISI 316 (left) and 6.4mm C-Mn steel showing (a) front face beads and (b) root beads.

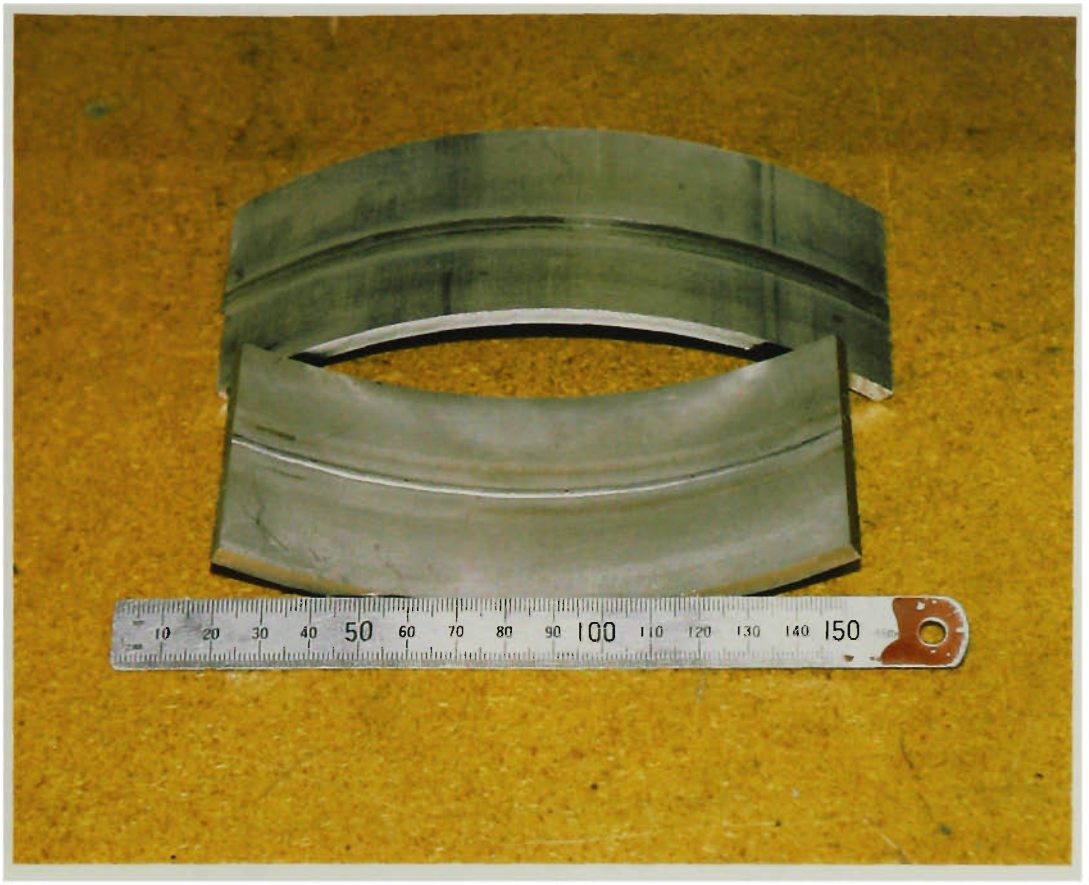

(a)

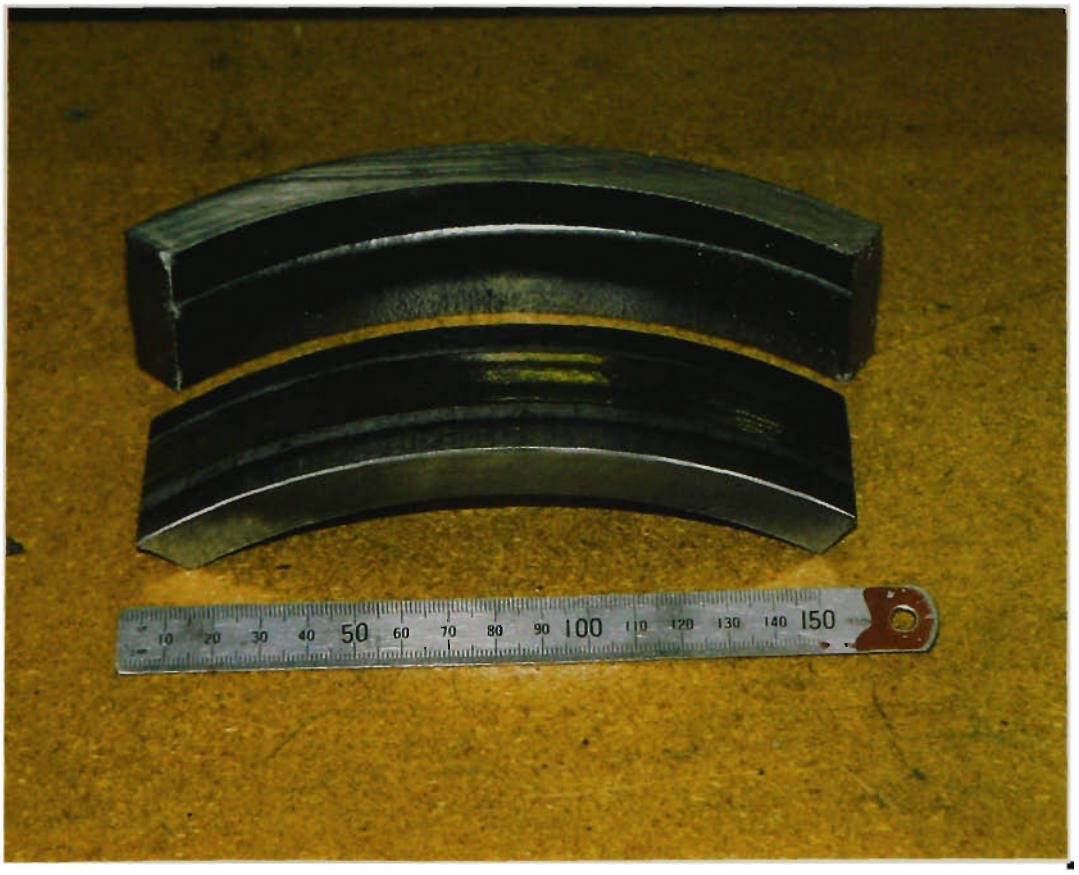

(b)

Figure 3.6. Internal and external beads for keyhole GTA welding of pipe. (a) 4mm wall thickness AISI 304 and (b) 14mm wall thickness G2 titanium.

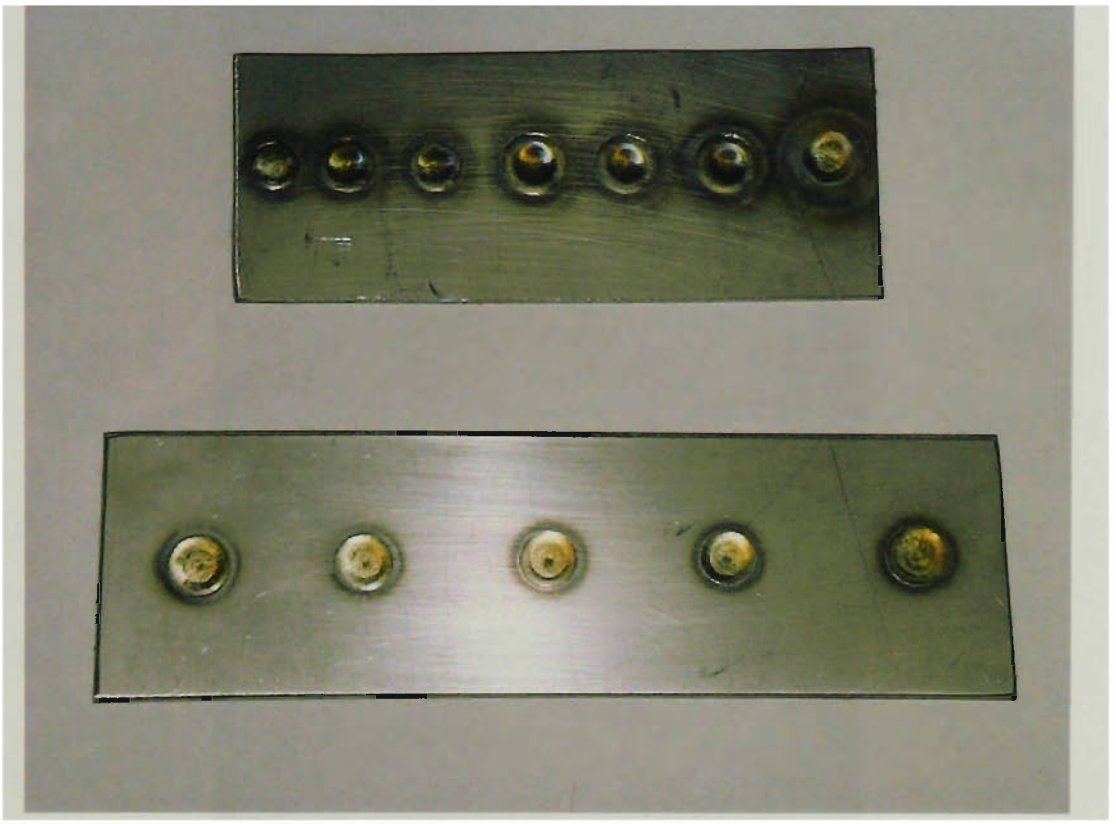

(a)

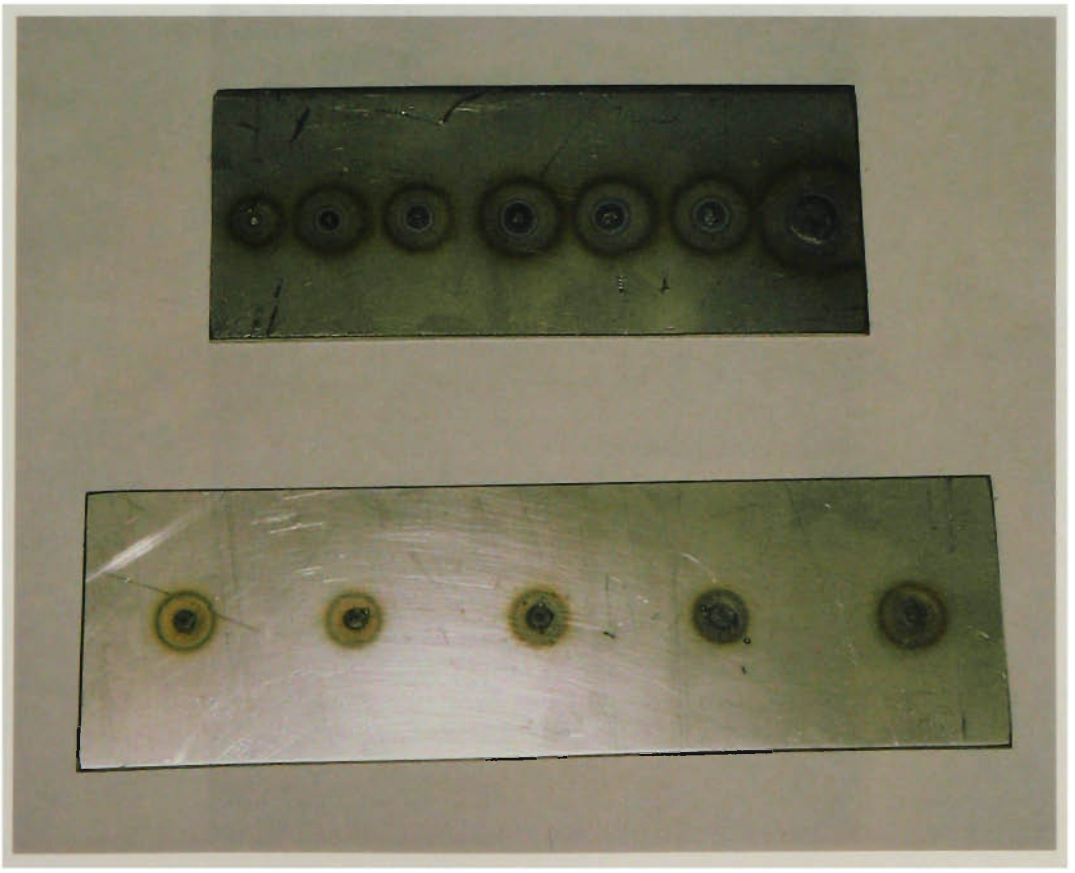

(b)

Figure 3.7. Keyhole GTAW process used for 'one-sided spot welding' of two 1.2mm AISI 316 sheets. (a) front face and (b) root face.

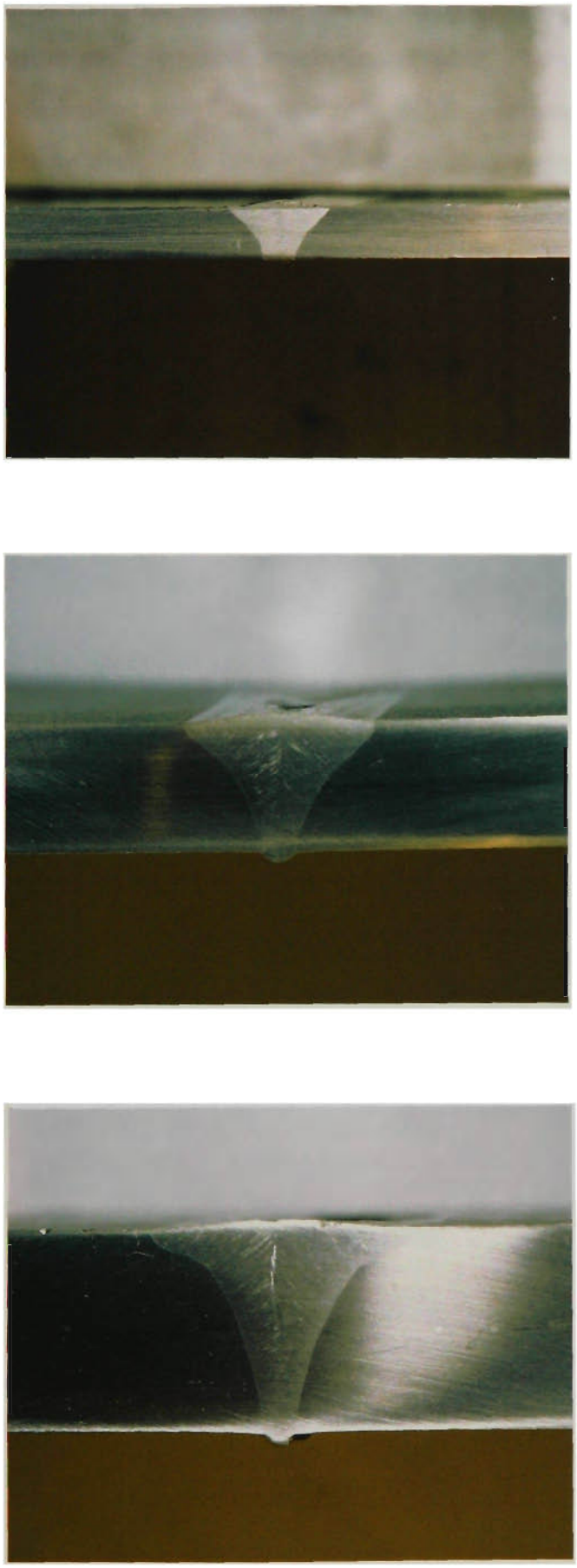

Figure 3.8. Fusion profiles for (from top) 3mm, 8mm and 12mm AISI 304 stainless steel.

according to this procedure are then qualified to the relevant standards. This process can be time consuming and expensive, but is an important component in safeguarding the integrity of welded structures. Clearly a new welding process variant would be of little value if it were incapable of being used to produce weldments of the required standard. On the other hand it is not realistic to generate an exhaustive set of procedures to prove the merits of a welding process. With this in mind the generation and qualification of keyhole mode GTAW procedures for the list of weldments indicated in the Table 3.7 represents a reasonable demonstration of performance. All joints were prepared as simple square-butts with no root gap. The austenitic stainless steel plates were welded using an Ar-5H shielding gas, the pipe was welded using an argon-hydrogen-helium mixture, and the other joints were made using pure argon shielding.

Table 3.7. Instances for which keyhole GTAW procedures have been developed and qualified.

Material	**Standards applied**	**Results**
3mm AISI304	AS 3992-1998, ASME IX-1998 ASTM A262, AS 1554.66*	Complied
3mm AISI 316L	AS 3992-1998, ASME IX-1998 ASTM A262, AS 1554.66*	Complied
3mm 3CR12	AS 1554-1994 Part 6.	Complied
4mm AISI304	AS 3992-1998, ASME IX-1998 ASTM A262, AS 1554.66*	Complied
4mm AISI 316L	AS 3992-1998, ASME IX-1998 ASTM A262, AS 1554.66*	Complied
4mm 3CR12	AS 1554-1994 Part 6.	Complied
6mm AISI304	AS 3992-1998, ASME IX-1998 ASTM A262, AS 1554.66*	Complied
8mm AISI 304	AS 3992-1998, ASME IX-1998 ASTM A262, AS 1554.66*	Complied
8mm AISI 304 pipe	AS 3992-1998, ASME IX-1998 ASTM A262, AS 1554.66*	Complied
10mm AISI316L	AS 3992-1998, ASME IX-1998 ASTM A262, AS 1554.66*	Complied
13mm G.2Titanium	AS 2205-1997	Complied

* AS 1554.6 Appendix F relates to the percentage of delta ferrite in the weld metal. Recommended levels vary according to the intended application. See Appendix A for details.

For further clarification CSIRO metallurgist Mr D. Viano has provided a detailed assessment of the results for the AISI304 and AISI 316L samples listed in Table 3.7. This assessment is included in entirety in Appendix A. The weld quality of the titanium plate was also carefully scrutinised because any single pass procedure for this thickness of the material would be of significant commercial interest. The results of that study have been presented by Lathabai and Jarvis (Lathabai and Jarvis, 2001).

Examples of keyhole welds in different materials and thicknesses are provided in Figures 3.5, 3.6 and 3.7. A series of etched cross sections are shown in Figure 3.8.

3.4.2. Operational windows

The procedures referred to in Table 3.7 include an extensive coverage of austenitic stainless steel plates (ie AISI 304 and 316L). In fact this group of procedures were all developed using the same shielding gas, electrode type and electrode geometry. This provided a good basis for an examination of an operational window. To do this further trials were made in which the travel speed was varied and the resultant process characteristics examined for each thickness. The trial was further extended with the inclusion of 12mm AISI 304. This was the thickest plate of that type available, and was known to be close to the edge of the operating window for that material. In these trials the electrode-to-work gap was fixed rather than voltage. The 'gap' parameter represents an alternative to arc voltage, and is often the easier of the two to control in a production environment. The particular gap values were those used for the corresponding procedure, and were not varied. Consequently the resultant speed-thickness operating window can be taken as being indicative of the general process behaviour, but with the qualification that specific details are subject to the selection of the set points of the independent variables identified in the preceding section. Relevant data are presented in Table 3.8 and illustrated graphically in Figure 3.9.

Table 3.8. An example of a speed-thickness operating window for austenitic stainless steel.

Thickness *(mm)*	Minimum speed *(mm/min)*	Tendency	Optimum speed *(mm/min)*	Tendency	Maximum speed *(mm/min)*
3	550	Slumping	700 – 1500	Undercut	Not found
4	325	Slumping	400 – 800	Undercut	Not found
6	250	Slumping	350 – 700	Undercut	Not found
8	225	Slumping	300 – 550	Undercut	700
10	200	Slumping	250 – 450	Collapse	500
12	175	Slumping	225 – 375	Collapse	400

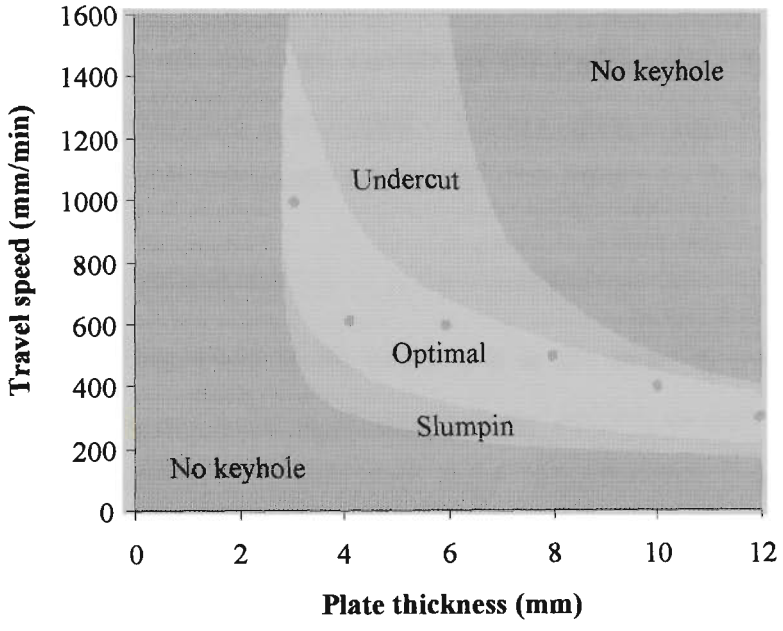

Figure 3.9. Approximated speed vs thickness operating window for keyhole mode GTAW of AISI304. Details are based on the data in Table 3.8.

Summarising these observations:

- Welding speed must be decreased as sample thickness increases.
- Keyhole failure corresponds to failure of the pool support mechanism.
- Visual appearance deteriorates near the edges of the operational window.
- Plates less than about 6mm potentially have very high welding speeds, but presently limited by undercut.
- The process is tolerant to travel speed variations (for the examples cited).

3.4.3. Application to pipe

As presently developed the keyhole GTAW process is intended for use in the flat position. This is a significant limitation, but the range of application can be extended considerably when weldment manipulation is an option. One example is in the welding of pipes that can be rotated under a stationary welding head. This is often the preferred practice with other fusion welding processes because it requires the minimum variation in welding parameters and produces the best joint quality.

Girth welding of rotated pipes with the keyhole GTAW process has been shown to be effective and to have the potential to produce high quality joints (for example see Table 3.7). The attractive features of this application (other than those already mentioned for plate) are the high quality of the surface and internal beads, and the guarantee of full penetration (see Figure 3.6 and Figure 3.10). However, the transition from plate to pipe does introduce additional constraints to those associated with flat plate.

The most obvious constraint to be overcome is the need to overlap the start of the weld and then terminate without generating any defects or leaving a crater. Limited experience has provided evidence that these requirements may not be difficult to achieve. It is the nature of the process that it produces a minimum of reinforcement, and this is an advantage when overlapping the weld because it implies a minimal change in the apparent joint thickness. In any case the only welding parameter normally varied is the welding current, and appropriate settings or adjustments can be verified visually.

The start of the weld produces slight excess in reinforcement compared to the remainder of the weld due to an initial displacement of material from the weld zone, and this adds to the effect of increased thickness. On the other hand much of the heat of the process will remain in the joint (unless the pipe is very large) and this constitutes a sometimes considerable degree of preheat. The two effects drive the required welding current in opposite directions, and the net adjustment is unpredictable, but usually small. In the limited number of trials conducted it has been the experience that the weld will continue to perform adequately even if the current is

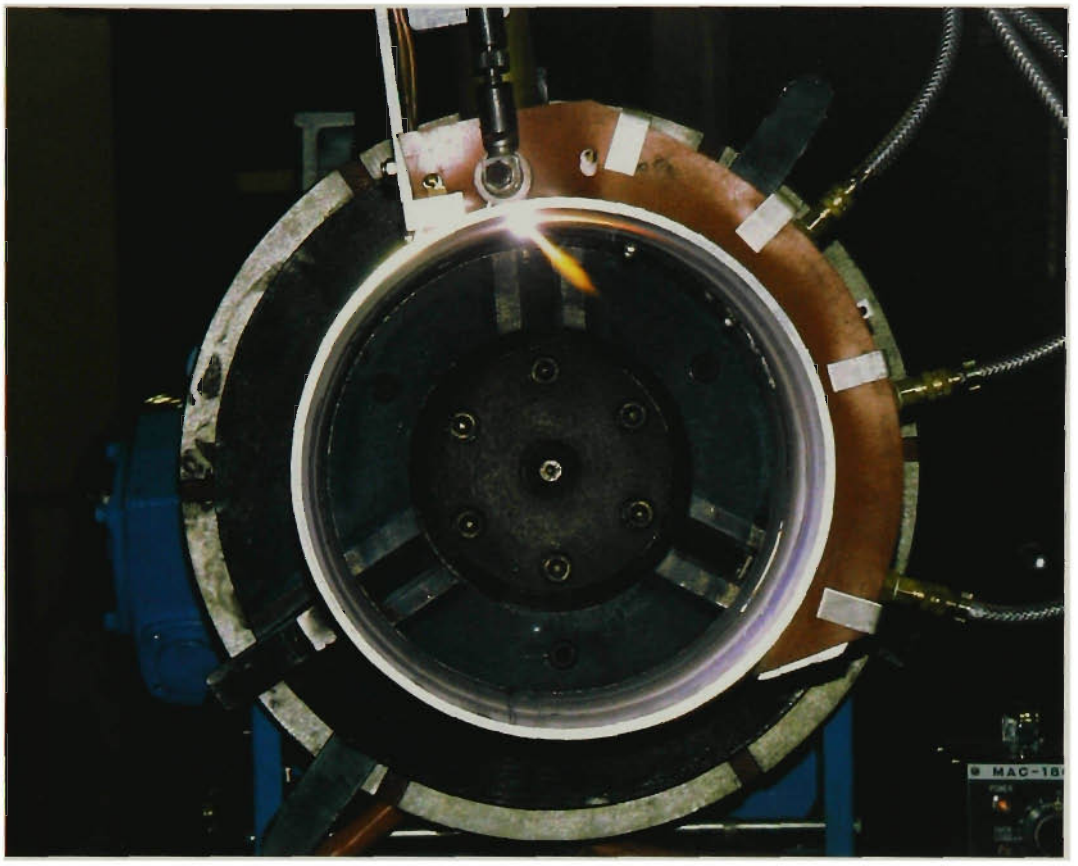

(a)

(b)

Figure 3.10. Experimental shielding trials for keyhole GTAW of pipe (a) and 8mm wall thickness AISI 316 pipe welded without additional shielding (b).

kept constant. Nevertheless, it is expected that the self-pre-heating effect will place a lower limit to pipe diameter. This limit would be anticipated to be dependent on wall thickness and material characteristics.

Weld termination can result in defects including porosity, underfill and burn-through. Porosity commonly occurs if the current is reduced below the threshold while the pipe rotation is continued. Ramping down the welding current while the pipe rotation is maintained is therefore a poor strategy for ending the weld. It may be surmised that the porosity forms as the keyhole closes, blocking the passage of the arc gases. A more successful strategy has been to simultaneously stop the rotation and ramp down the current. This technique maintains a shrinking weld pool, and provides time for any gas pores to rise to the surface and be eliminated. There is however, a need to regulate the rate at which the current is reduced because there is a danger of over heating and burning through the pipe. This termination process must incorporate filler addition for crater fill, even if the filler wire is not used for the remainder of the joint. Numerous manually controlled terminations support the view that the required parameter settings have broad tolerances.

Another issue to be addressed in pipe welding is the generation of worm-hole porosity. This is seldom found in welding of plate material, but may occur in pipes with wall-thicknesses exceeding about 6mm. Details of this phenomenon will be discussed elsewhere, but essentially it has been associated with partial choking of the keyhole exit. Apparently, at least for thicker walls (eg 7.1mm) the keyhole does not need to be completely closed to generate this porosity. Furthermore, no indicative behaviour, such as wavering of flickering, has been identified in the efflux plasma. In fact the visual indicator that this porosity might be forming appears to be the presence of a steeply angled jet emerging from the trailing side of the keyhole entrance. This jet can be detected electronically. The porosity problem is easily overcome by increasing the current, and values of 5% to 10% above the threshold can be anticipated. The different behaviour between pipe and plate could be due to the normal practice of welding slightly 'down-hill' on pipe to achieve the best bead profile. This could increase the tendency of the pool to become unstable and move forward, restricting the gas flow. The severity of the porosity may be influenced but not eliminated by varying other factors including torch angle, welding position and gas composition.

These findings provide a forceful reminder that the presence of a strong efflux plasma jet is not a guarantee good weld quality.

3.4.4. Process extensions.

Undoubtedly further study would identify new areas where this technology might find application, and the various ways in which it may be adapted to meet more demanding tasks than those already discussed. One application that has been identified is the welding of lap joints. All keyhole-welding processes have the characteristic that they do not rely on careful joint preparation, and generally the more tightly the two edges butt together the better. In development work it is common to work without joints (ie bead-on-plate) as the introduction of a tight butt joint has very little affect on the parameters. Consequently keyhole-mode welding is very well suited to lap joints. This holds true for the keyhole GTAW process as well, as has been verified in numerous trials. This is certainly one area where further development and assessment would appear to have merit. Initial experimentation has not uncovered any new difficulties, suggesting that the existing knowledge may be sufficient to support many such applications. If this were to be the case then sheet materials as thin as 1.5mm could be successfully joined with welding speeds in excess of 1000mm/min. This area also raises the issue of joining dissimilar materials, and could potentially be of some value in this regard.

Another major issue with keyhole welding is the limitations on maximum joint thickness. In this respect keyhole GTAW is comparable to PAW for the materials on which it can be applied. This suggests that both processes are limited by the same failure mechanisms. In any case strategies adopted for PAW may be suitable for keyhole GTAW as well. One strategy has been to prepare thick joints as shown in Figure 3.11 (Halmoy 1994). Normally the first pass is made with PAW, and the final filling runs could be completed with GMAW for example. The keyhole GTAW process could well duplicate this approach, but with the option of simply reverting to the melt-in high current mode to complete the filling runs.

Other areas that might be addressed in the future include welding out of position, and extending the range of materials that can be used. Both areas are expected to be

challenging. For example the small variation from the flat position applied to pipe welding has already highlighted problems with resultant bead shape and pool stability. The same difficulties are encountered with other keyhole processes and may be viewed as being of a fundamental nature. Extending the range of materials is certainly possible by following the PAW route. However, the development of new shielding gas mixtures and electrode materials together with a move away from constant DC supplies may also generate many new possibilities.

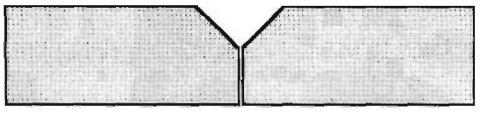

(a)

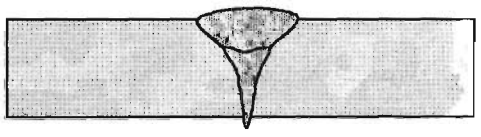

(b)

Figure 3.11. Schematic of joint preparation (a) and run layer pattern (b) for PAW of thick plate.

3.4.5. Competitiveness

The competitive advantage of one process over another is always an issue for fabricators, but it is usually only determined within the context of the particular application. Every process in use today must have some characteristic features that the fabricator finds attractive. These include versatility, cost, user experience, established reputation, technical support and product requirements, among many others. Consequently it is more appropriate to present the process characteristics so that

assessment can be made with respect to specific requirements. The main characteristics of the keyhole GTAW process are:

- It is an automated, flat position welding process
- Joints are completed in a single pass
- It requires only square butt edge preparation.
- It has a minimal requirement for filler materials.
- Welding speeds can exceed 500mm/min for materials of 6.4mm and under.
- It can be applied to materials, such as AISI 304 and titanium, to 12mm thick.
- Equipment cost is similar to that of GMAW and significantly less than PAW.
- It operates in a full penetration mode.
- It is relatively robust with respect to setting up and operating windows.
- It will accept limited variations in joint fit-up (eg guillotined edges).
- Joint quality is very high as is characteristic of other GTAW processes.

The potential savings of the process are highlighted with the comparison between the welding effort required to join two 12mm AISI304 plates using a keyhole and a conventional GTAW approach. These are presented in Table 3.9. The respective weld bead cross-sections are shown in Figure 3.12. For this exercise the parameters for the conventional GTAW procedure were based on recommended values provided in the AWS Handbook, and the procedure was automated.

Table 3.9. Comparison of welding procedures for keyhole and conventional GTAW for 12mm AISI 304 plate.

Welding Parameter	**Conventional GTAW**	**Keyhole GTAW**
Joint preparation	Double-V	Square butt
Number of passes	7	1
Filler material / metre of weldment	1000g	50g
Welding current	320 amps	690 amps
Welding speed	200 mm/min.	300 mm/min.
Total arc-on time / metre of weldment	35 minutes	3 minutes 20 seconds

(a)

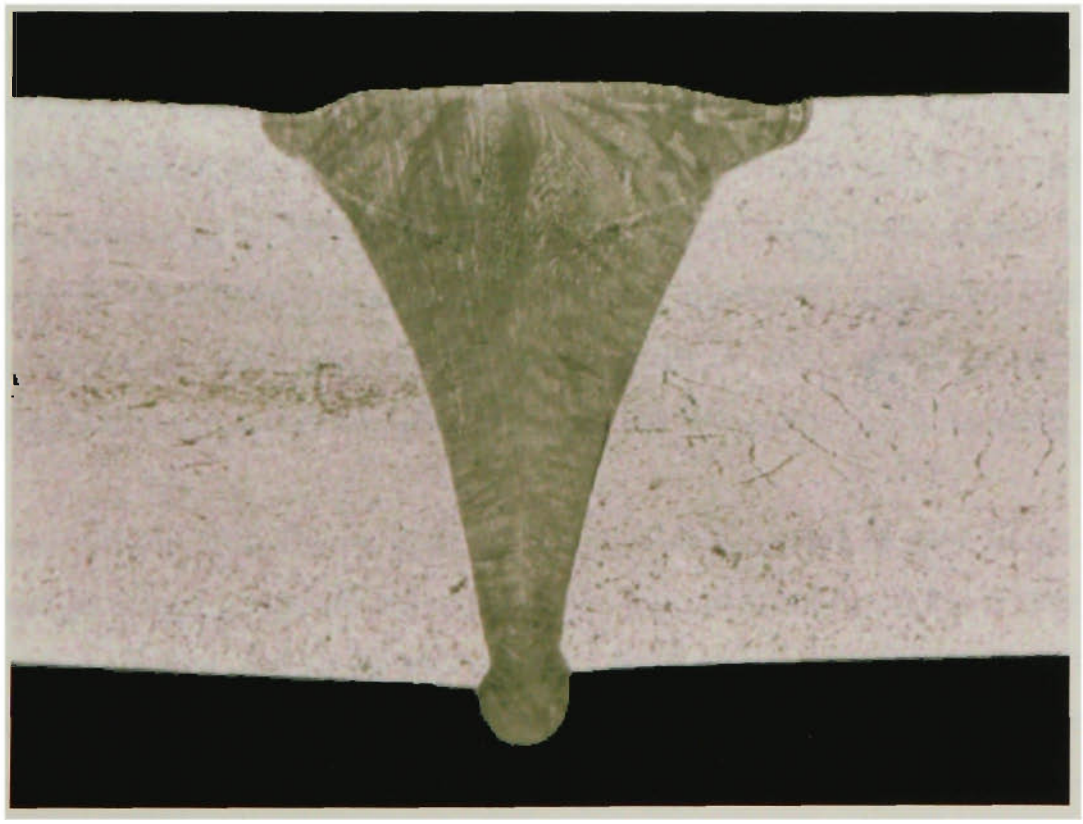

(b)

Figure 3.12. Comparative weld bead profiles for (a) a conventional (seven pass) GTA and (b) single pass keyhole GTA weld of 12 mm AISI 304 plate.

4. The role of surface tension in keyhole behaviour.

4.1. Surface tension in relation to keyhole failure.

4.1.1. 2-D verses 3-D geometries

In general keyholes produced during welding are unstable, highly dynamic structures. In contrast however, the GTAW keyhole is quite robust, and at currents over about 350 amps it is often much more stable than the alternative GTAW melt-in mode. As illustration, when the process was photographed during trials on pipe a relatively clear reflection of the interior of the torch was visible in the trailing pool, despite a welding current in excess of 400 amps. One such image is presented in Figure 4.1.

In developing models of welding keyholes it is usual to regard the keyhole as entirely surrounded by liquid, and then exploring the conditions under which there is no net pressure difference across the surface. The balance usually considered in high power density keyhole welding includes the pressures arising from the depth of liquid metal, ρgh, surface tension, γ/r, and the recoil pressure of material ablating from the surface. In these expressions ρ is the liquid density, g the acceleration due to gravity, h the height of the liquid head, γ the surface tension and r the keyhole radius. The first two terms, hydrostatic (ρgh) and surface tension pressure, are regarded as acting to collapse the keyhole, and so must be balanced by the ablation or 'recoil' pressure.

However, GTAW keyholes are not easily reconciled with these models. In the first instance gas tungsten arcs are not regarded as being sufficiently intense to generate appreciable ablation, and so the role of recoil pressure is not significant (Lancaster 1986). Furthermore, unlike plasma arc welding, there are no gas-dynamic forces generated independently of the arc. Consequently the perception gained from the literature (eg Lancaster 1986, AWS Welding Handbook 1991) is that the GTAW process should not produce keyhole welds.

The solution to this dilemma is found by reassessing the term for surface tension. Laser and electron beam keyholes have large aspect ratios (ratio of depth to width),

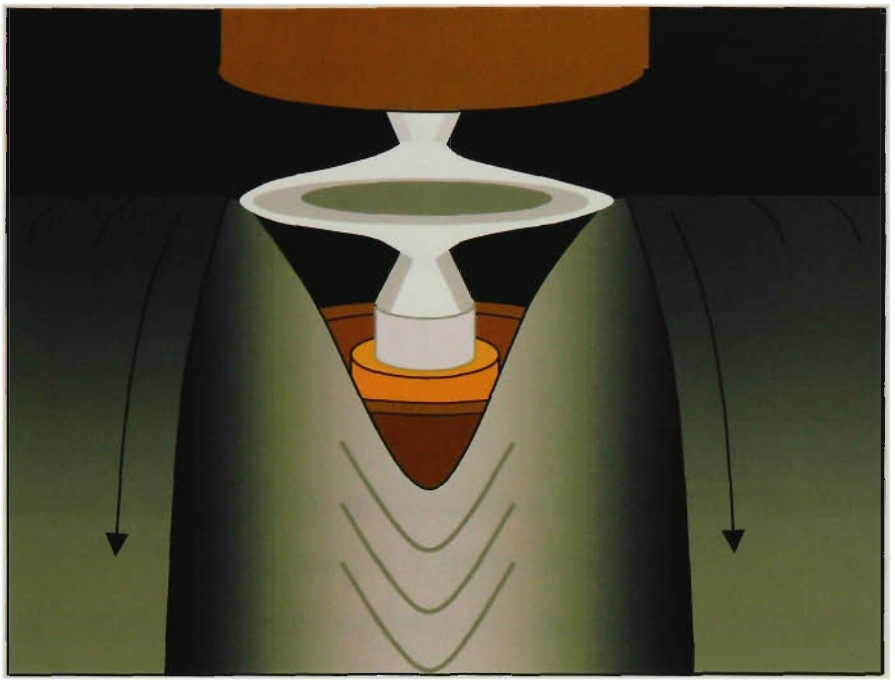

(a)

(b)

Figure 4.1. Reflection of the arc, electrode, contact tip and shroud in the tail of **(a)** an ideal weld pool and **(b)** an actual welding application. The reflection in (b) indicates a very stable, tranquil pool. (Keyhole GTAW of 8mm wall thickness stainless steel pipe).

and values exceeding 10:1 are not unusual. Such high aspect ratio keyholes are approximately cylindrical, and this is the reason for the two-parameter, or 2-D, expression for the pressure due to surface tension (γ/r). However, standard texts (eg Champion and Davy 1947) show that the change in pressure, P, across a liquid surface due to the surface tension is related to the surface curvature, and can be written

$$P = \gamma\left(\frac{1}{r_1}+\frac{1}{r_2}\right) \tag{4.2}$$

In this expression r_1 and r_2 are the principal radii of curvature. This can be referred to as the 3-D equation. Evidently the 2-D expression applies if one of the two radii can be ignored, as in high aspect ratio keyholes. For example if $r_1 << r_2$ then

$$\frac{1}{r_1}+\frac{1}{r_2} \cong \frac{1}{r_1}$$

And

$$P \cong \frac{\gamma}{r_1}$$

or simply

$$P = \frac{\gamma}{r}$$

The distinction between the 2-D and 3-D expressions is that the 3-D expression has two radii of curvature. Importantly the two radii need not be of the same sign. For illustration, if the liquid exhibits a convex surface then the pressure is higher inside the liquid than outside it and vis-a-versa if the surface is concave. However, it is also possible for a surface to be concave along one axis and convex along another, that is, to have saddle points. The resultant pressure-change across the surface then may be positive, negative or zero. This possibility is illustrated in Figure 4.2.

For convenience take the two principal axes of a keyhole such that the two curvatures are taken around the axis (the radial plane), and in the axial plane, respectively. Then for all open keyholes the two curvatures will be of opposing sign (see Figure 4.3). For high aspect ratio keyholes the curvature in the radial plane dominates, and so the surface tension always acts to collapse the keyhole. However, as the aspect ratio

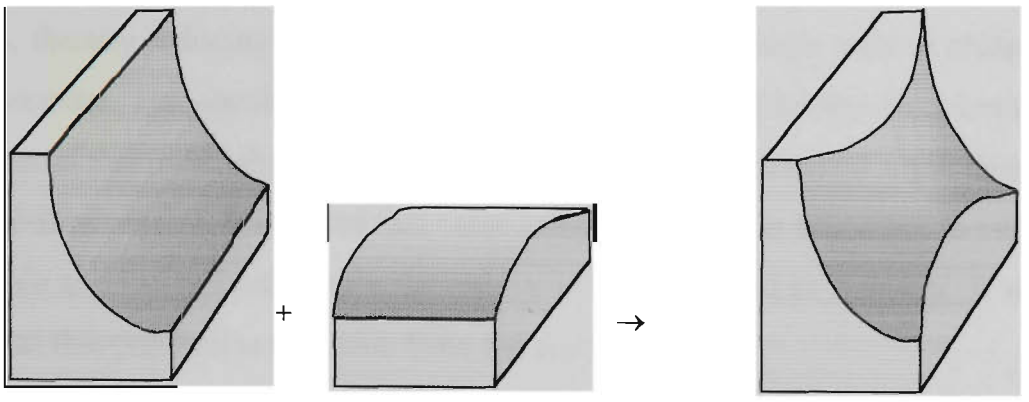

Figure 4.2. Illustration of how surfaces of arbitrary curvature can be constructed.

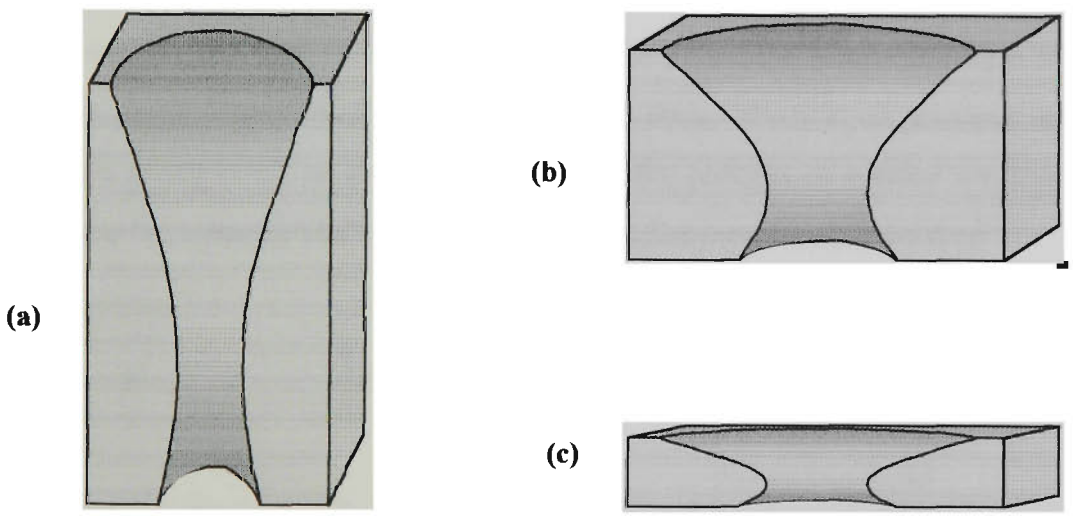

Figure 4.3. Schematic illustration of how the keyhole curvature varies with changes in the two radii of curvature identified in the text. In this sequence the radial curvature dominates in (a), tending to collapse the keyhole, curvature approaches zero in (b), and becomes negative (axial curvature dominates) in (c).

decreases the axial curvature increases, and it acts to open the keyhole. If the aspect ratio becomes small enough the axial curvature will dominate and the keyhole will widen. It is proposed that the two curvatures are approximately equal in GTAW keyholes, thereby reducing the need for additional pressure terms such as ablation or vapour pressure. This would counter the established argument against their formation. It is a tenet of this thesis that GTAW keyholes can only be understood when described within a 3-D geometry. It is noted that some internal pressure is necessary to establish the keyhole and maintain it against the inflow of fresh material as it moves. It will be argued that this pressure is available from the arc forces.

4.1.2. Aspects of surface tension

At this point the issue of surface curvature needs further clarification. In the above, reference has been made to the 'principal' axes of curvature without proper definition. In fact, principal axes may be chosen arbitrarily provided only that they are orthogonal and tangent to the surface at the chosen point. This is due to result from geometry that states that "at any point on any surface the sum of the reciprocals of the radii of curvature in any two mutually perpendicular sections is constant" (Grimsehl 1947). Furthermore, the sum of the two reciprocals is called the mean curvature of the surface at that point. If this result is applied to (4.1) then, "the normal pressure due to surface tension at any point on a surface is equal to the product of surface tension and mean curvature" (Grimsehl 1947). That is, if K signifies mean curvature then

$$K = \frac{1}{r_1} + \frac{1}{r_2} \tag{4.2}$$

where r_1 and r_2 are the radii of curvature in any two mutually perpendicular section, and

$$P = \gamma K \tag{4.3}$$

Another aspect of liquid surfaces concerns the 'angle of contact'. When a liquid, a solid and a gas are simultaneously in contact and in equilibrium the liquid surface will

make a characteristic angle of contact with the other two media. The angle, illustrated in Figure 4.4, is called the angle of contact.

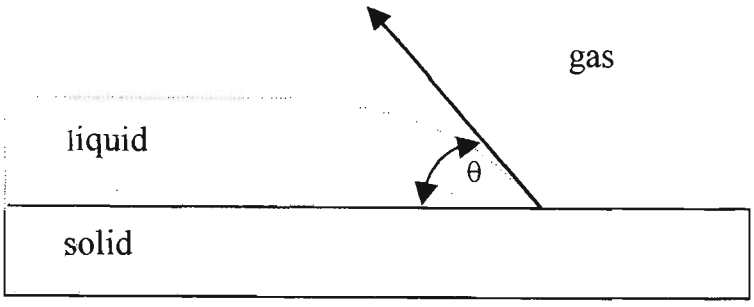

Figure 4.4. A schematic diagram illustrating the concept of the 'angle of contact'.

To determine the angle of contact three surface tensions must be identified. These are the surface tension of the liquid in contact with the gas, γ_{lg}, that of the solid-liquid interface γ_{sl}, and that of the solid-gas interface, γ_{sg}. It can be shown that the resultant angle of contact, θ, is given by

$$\cos\theta = \frac{\gamma_{sg} + \gamma_{sl}}{\gamma_{lg}} \tag{4.4}$$

This is an important relation to consider when describing the boundary conditions between, for example, a puddle of liquid metal on a solid metal substrate.

Further to the above, it is known from thermodynamics that the solid and liquid phases of a material have the same surface tensions at the material's melting point (Chalmers 1953). Therefore, in the case of a liquid metal in contact with its solid phase $\gamma_{sg} = \gamma_{lg}$, and $\gamma_{sl} = 0$. Reference to (4.4) shows that the angle of contact must be zero for this special case. It will be assumed that this condition holds, in the absence of additional forces on the surface, around the edges of weld pools.

4.1.3. Keyhole failure in thick plate

Keyholes in thicker plates (e.g. 8mm to 12mm) can fail by having the molten metal in the weld pool escape through the keyhole root. This type of failure was a major obstacle during the initial welding trials on 12mm AISI 304 plate. In that work failure took either of two forms, depending on whether or not an oxygen-free backing gas was used. In each case enhancement of the effect resulted in the cutting of the plate. Although these alternate modes of failure were less important than the underlying mechanism, they did provide clues to that mechanism, and will be discussed for this reason. An example of each failure type is shown in Figure 4.5.

In the first instance the welding was conducted without a protective backing gas, and the liquid drained from the rear of the keyhole exit forming 'stalactites.' This mode was cyclic. Whenever the weld pool depth built up to a critical level the closure mechanism failed and almost the entire contents of the pool drained out. The keyhole was then restored and the cycle repeated. However, when oxygen was excluded from the root face or a ferritic stainless (3CR12) or structural (C-Mn) steel was substituted for the AISI 304, the liquid metal at the root of the weld pool would coalesce into large pendant drops. These sometimes grew large enough to drip from the plate. After many trials with different materials it was concluded that stalactite formation was very uncommon, and the pendant drop was the normal mode of failure.

The effect of oxygen on keyhole failure in 12mm AISI 304 was qualified by conducting several experiments with changing conditions applied to the root face of the plate. The following behaviour was observed:

- Keyholes with air backing could be maintained up to a travel speed of about 420mm/minute. Failure involved the formation of heavily oxidised stalactites.
- Keyholes with argon or nitrogen backing were stable to only about 320mm/min. Failure involved formation of pendent drops.
- Keyholes with argon-hydrogen backing were stable to about 420mm/min. Failure involved formation of pendent drops.

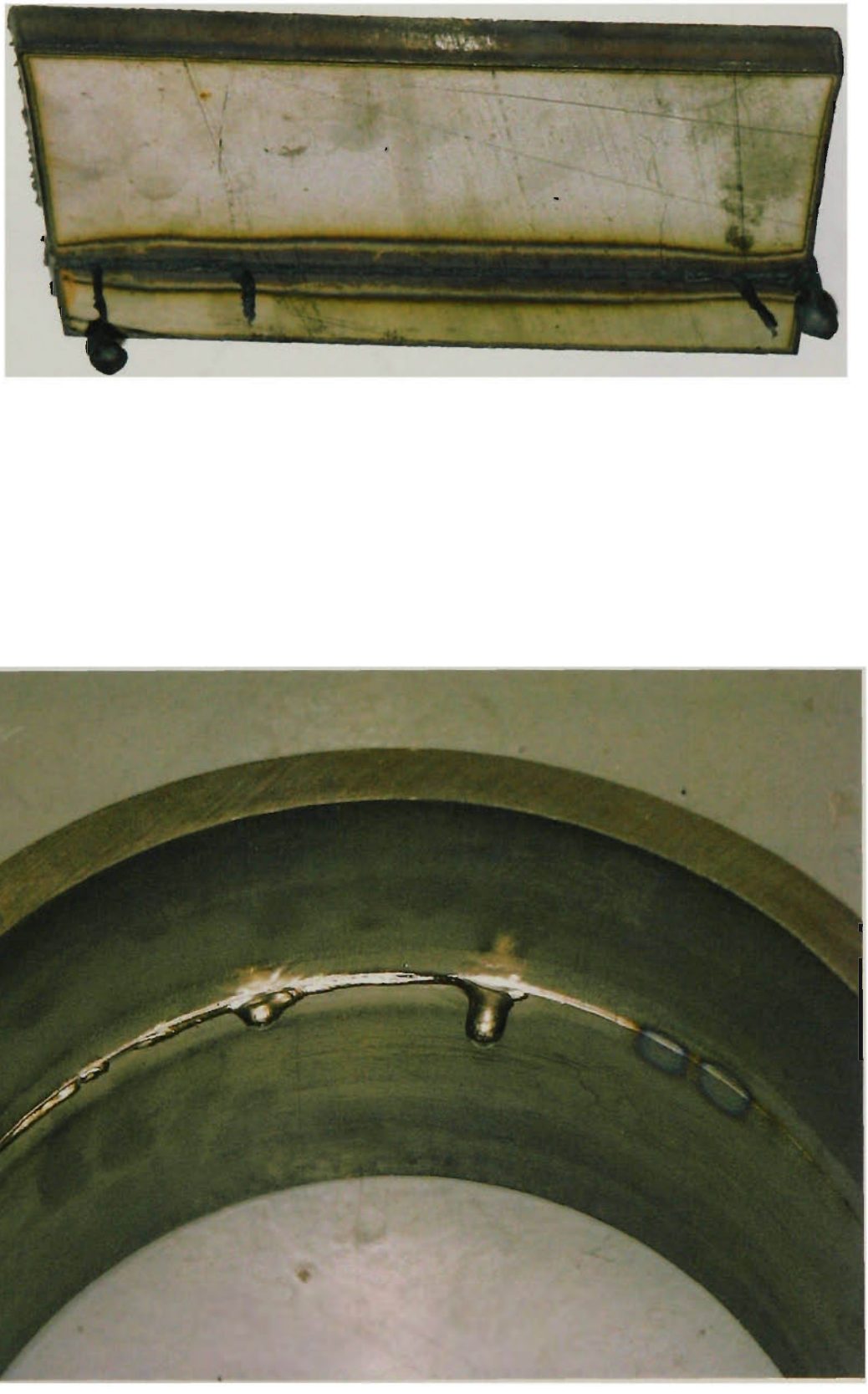

Figure 4.5. Photographs showing the unusual 'stalactite' failure (upper) and more common pendent drop failure (lower) in keyhole welding of thick sections.

The general behaviour of the system can be understood by considering the surface tension acting on the trailing puddle on the root face. For argument, let the liquid portion of the root bead have an effective width w and length s, as in Figure 4.6.

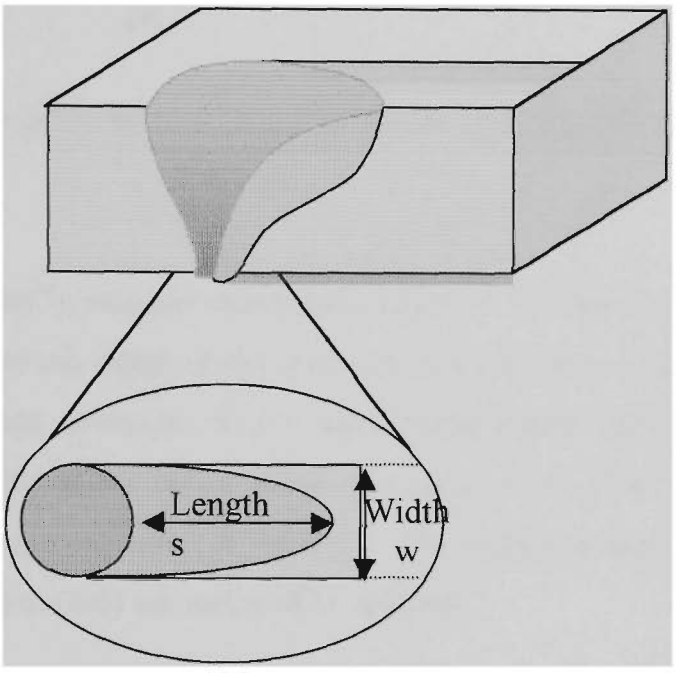

Figure 4.6. Schematic illustrating the geometry of the root bead for a keyhole weld.

Assume that the lowest maximum radii of curvature of this bead are r_a and r_b where r_a = w/2 and r_b = s. The minimum value of the mean curvature occurring anywhere on the root bead, K_R, is then given by

$$K_r = \frac{1}{r_a} + \frac{1}{r_b} \tag{4.5}$$

Since any expansion of the surface will reduce the curvature, the maximum pressure required to rupture the surface is given by substituting K_R in (4.3):

$$P = \gamma K_R$$

This pressure can be supplied by the head of liquid metal, depth, *h*, and density ρ

$$P = \rho g h$$

Consequently the maximum depth that can be supported by surface tension is

$$h = \frac{\gamma K_R}{\rho g} \tag{4.6}$$

The allowable depth h given by (4.6) must be greater than the plate thickness, G, if the process is to work.

To test this experimentally measurements were taken of the base dimensions of the AISI 304 stalactites and the depth of the pool before the failures occurred. This data was used to determine whether or not the model could describe the failure mechanism. The density of the liquid metal was taken to be 7000 kg/m^3 (Iida and Guthrie 1993). Results are presented in Table 4.1. The predicted values for h based on a least-squares-error fit to (4.6) are included in the table.

Table 4.1. Conditions applying at failure for keyholes in 12mm AISI304.

Measured r_a *(mm)*	**Measured r_b** *(mm)*	**K_R** *($1/r_a + 1/r_b$)*	**Measured depth** *(mm)*	**Predicted depth** *(mm)*
1.5	2	1.17	12	11.5
2	3	0.83	8	8.2
1.5	2.5	1.07	12	10.5
1.3	2	1.27	12	12.5
1.5	3	1.00	9	9.8
1.5	2.5	1.07	10	10.5

Regression (least squares error) of the data assuming the form of (4.6) gave a correlation (r^2) of 0.76 and indicated an effective surface tension, γ, of about 0.7 N/m.

$$h = 9.836 K_R$$

This value is quite low, but since the root face of the plate was exposed to air the surface tension would have been reduced significantly by absorption of oxygen. (The surface was black from oxidation). Furthermore, the model makes no allowance for

dynamic effects, and it is certainly plausible that these triggered failure of the weld pool before the theoretical maximum depth was obtained. In any case, the results are consistent with the simple model that has been proposed.

Even in inert atmospheres the surface tension of iron is reduced by surface-active elements such as the oxygen and sulphur commonly present in the metal, and values of around 1N/m are anticipated (Lancaster 1986). Given that, in inert atmospheres, the root beads were typically about 4mm wide at failure and taking s to be slightly longer at 6mm, this value of surface tension would support a stainless steel pool no more than 11.9mm deep. Again the result is consistent with the experimental evidence.

Finally the unusual behaviour of AISI 304 compared to 3CR12 and C-Mn steel, in the presence of air backing, can be explained by the progressive formation of a coherent, refractory Cr_2O_3 skin (m.p. 2265°C) that supports the rear sections of the puddle. The concentration of chromium in AISI 304 is much higher than in 3CR12, (and there is virtually no chromium in C-Mn steel) and is sufficient to form a protective film at normal temperatures. Therefore, if the pool is to rupture in an oxidising environment it will do so close to the keyhole exit where the skin has not yet cohered. Such systems have enhanced stability due to the effective reduction of the weld pool length. However, as the oxygen content is decreased the formation of the skin will be suppressed, and the pool will fail more easily. Finally, if oxygen can be removed even from the surface metal the surface tension will be increased, and the pool will again become more resistant to rupture. This degree of oxygen removal requires the action of a reducing gas, hence the addition of 2% hydrogen was found to be beneficial.

The preceding discussion highlights that the choice of backing gas can exert a major and sometimes unexpected influence on process performance. This is a factor that should not be overlooked during the development of welding procedures.

4.1.4. Travel speed

The qualitative effect of travel speed can be deduced from the preceding argument regarding support of the weld pool. Reference to the derivation of (4.6) indicates that the weld pool will be supported by surface tension provided

$$\frac{G}{K_R} \leq \frac{\gamma}{\rho g} \tag{4.7}$$

Wells (1952) has shown that the pool length, and hence r_b, increases with pool width, $2r_a$, and travel speed. Therefore let $r_b = Vr_a$ where V always increases with travel speed and

$$V \to 1 \quad as\ travel\ speed \to 0$$
$$V \to \infty\ as\ travel\ speed \to \infty$$

Then

$$K_R = \frac{1}{r_a}\left(1+\frac{1}{V}\right)$$

and

$$\frac{G}{K_R} = \frac{Gr_a}{1+\frac{1}{V}}$$

It follows that a maximum value of G/K_R corresponds to a maximum in Gr_a. Consequently there is a maximum permitted value of Gr_a for any given welding speed, and this value decreases as welding speed (and therefore V) increases. This can be made apparent by substitution into (4.7), giving

$$Gr_a \leq \frac{\gamma}{\rho g}\left(1+\frac{1}{V}\right)$$

The worst scenario for weld pool support, that is r_b is large relative to r_a, corresponds to the situation of relatively high welding speeds. In that case the pool will be supported provided

$$Gr_a \leq \frac{\gamma}{\rho g}$$

In other words the keyhole will always be stable (with respect to dripping from the plate) if $Gr_a \leq \gamma/\rho g$. However, if Gr_a exceeds this value then V, and hence the travel speed, must be limited to maintain stability. Evaluation for stainless steel, assuming a root bead radius of 2mm (γ = 1N/m, $\rho = 7x10^3 kg/m^3$, g = 9.8m/s) indicates that the critical plate thickness is about 7.3mm. This is thicker than the duplex and super duplex (SAF 2507) stainless steel plates used in the initial studies, and is consistent with the finding that there was no observed maximum travel speed for those plates. However, it is significantly less than the 12mm thickness of the AISI 304, indicating that in that case stability should have been strongly dependent on travel speed, as was observed to be the case.

4.1.5. A first rule for keyhole stability

The preceding argument may be extended further to provide a practical criterion for the GTAW keyhole. Firstly, the worst situation for rupture of the root surface of the pool is that r_b is very large. In the limiting case of high welding speed the pool will be supported provided

$$\rho g G \leq \frac{\gamma}{r_a}$$

Now consider the case where r_b is a minimum. It is assumed that r_b cannot be smaller than r_a because this would imply a greater temperature gradient to the rear of the pool than perpendicular to it. For this case the maximum pressure that can be supported is $2\gamma/r_a$, and the pool will always collapse if

$$\rho g G > \frac{2\gamma}{r_a}$$

In other words the keyhole will always be stable if $Gr_a \leq \gamma/\rho g$, and will always collapse if $Gr_a > 2\gamma/\rho g$.

These relations can be used to establish the viability of a keyhole process by comparing the product of two weld pool dimensions to a parameter dependent only on the material properties. Since it is more usual to refer to root bead width (w) than radius, the relations will be presented in terms of the former. In this case $w = 2r_a$, and Gw is the product of the root bead width and the plate thickness. The resultant regimes are:

$Gw \leq 2\gamma/\rho g$	The pool will be supported.
$2\gamma/\rho g < Gw \leq 4\gamma/\rho g$	Stability is dependent on the value of r_b, and will fail above some critical value of welding speed.
$Gw > 4\gamma/\rho g$	The process will always fail. (4.8)

As an example this criterion may be applied to 12mm plate, assuming a surface tension of 1N/m and a liquid density of 7000kg/m^3 (ie typical of stainless steel). In that case the pool will be stable at all speeds if the root bead width is less than about 2.4mm, but would not be stable at any speed if the width reaches 4.8mm. More generally, if these physical constants are used the 'critical' value of Gw for stainless steel is found to be about 28mm^2, and the weld pool condition is as shown in Table 4.2.

Table 4.2. Operating regimes for AISI 304 predicted from the first stability rule.

Root bead width x plate thickness, Gw (mm^2)		
< 28	*28 – 56*	*> 56*
Pool supported	Pool stability decreases with increasing travel speed	Pool collapses

4.1.6. Control limitations.

The constraint on the maximum value of Gw still allows any thickness of plate to be welded provided the root bead width is made sufficiently small. In reality however, the maximum plate thickness is limited. One reason for this is that the venting of the

arc gases imposes some restrictions on the relative areas of the keyhole entrance and exit. This will be discussed in Chapter 6. Another reason is that the welding parameter tolerances decrease with plate thickness. The following scaling argument is presented to illustrate this constraint. Three assumptions are made (see Figure 4.7 for details):

(1) The cross-sectional area of the fusion zone is proportional to the heat input.
(2) The fusion zone width increases uniformly with heat input.
(3) All GTAW keyholes have the same taper.

The conditions under which the first assumption is valid have been determined by Wells (1952), and are approximately satisfied by this process. The second assumption is conservative because typically the width at the root of the keyhole would increase more rapidly than at the front face, further increasing the risk of failure. The final assumption is introduced temporarily for clarity. The implications of its relaxation will be considered later.

The minimum fused area in this model corresponds to the keyhole converging to a point on the bottom surface of the plate. For simplicity the model represents the keyhole profile as being a (truncated) isosceles triangle as in Figure 4.7, but in fact the argument is valid for arbitrary profiles. By assumption (2) increasing the heat input increases the fused area by Gw where G is the plate thickness and w is the width of the root bead, as before. However, it has been established in (4.8) that the weld pool will collapse if the product Gw exceeds some critical value. In other words the maximum allowed change in fused area is independent of plate thickness. Applying assumption (1), the allowable change in heat input, $2\Delta Q$, is also independent of plate thickness.

Let the 'level of control' be defined as the allowed change in heat input divided by the actual heat input (Q_0), that is $2\Delta Q/Q$. By assumption (1) and (3), Q_0 is proportional to the square of the plate thickness since the minimum fused area is $G^2 \tan\theta$. Furthermore since $2\Delta Q$ is independent of plate thickness, the required level of control is inversely proportional to G^2.

$$\frac{2\Delta Q}{Q_0} \approx \frac{1}{G^2} \tag{4.9}$$

This result has significant implications. For example, suppose stable keyholes occur in 5mm plate for currents between 380 and 480 amps. The required level of control is then 24%, assuming that the welding current is the only variable that influences heat input. However, according to (4.9) this reduces to 4% for 12mm thick material, and to 1.5% at 20mm thickness. Furthermore, if heat input is also proportional to voltage (Q ~ IV), then the level of control of Q is approximately $\Delta I/I + \Delta V/V$. In this case if each of these variables could be controlled to 2% the maximum thickness for keyhole welding AISI 304 plate would be 12mm.

Variations in joint thickness are also important. For example, suppose that the welding parameters have been fixed and the joint thickness varies by a small fraction such that $G \rightarrow G(1+\delta)$, where $\delta = \Delta G/G$. The required heat input then changes from Q to $Q(1 +2\delta +\delta^2)$. Since δ is small this is approximately $Q(1+2\delta)$. But it has been established that if the variation in Q exceeds ΔQ the keyhole will fail. Hence the requirement

$$2\delta Q < \Delta Q$$

or

$$\frac{\Delta G}{G} < \frac{\Delta Q}{2Q} \tag{4.10}$$

This states that the allowable percentage variation in joint thickness is half the allowable percentage variation in heat input. In the example of the 12mm thick plate it was estimated that the heat input should not vary by more than 4%. For that same case the joint thickness would need to be constant to within 2%, or 0.24mm. These results suggest that active (feedback) control of the welding parameters will be increasingly attractive as plate thickness is increased.

At this point it is appropriate to consider relaxing the constraints imposed by assumptions (2) and (3). Removing (3) allows the fusion profile, and hence Q, to be

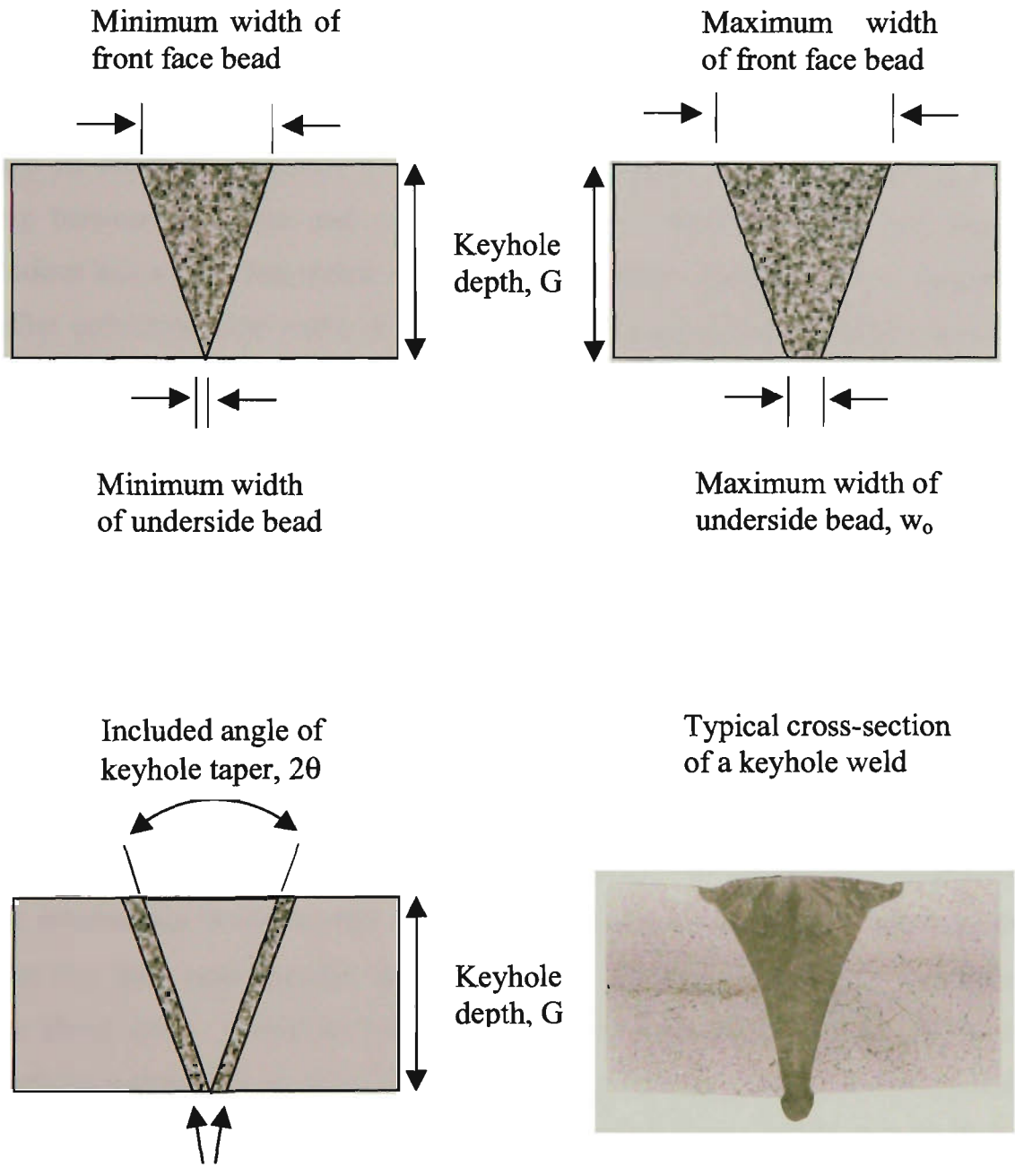

Figure 4.7. Diagrams illustrating how the cross-sectional area of a keyhole profile might change with increasing heat input. Included is a macrograph of a keyhole weld on 12mm AISI 304.

varied independently of plate thickness. However, as long as (2) is still valid ΔQ does not change. Therefore the required level of control will be relaxed if Q can be decreased, and there will be a definite control advantage to be gained by minimising the threshold current. In addition, it is likely that the keyhole taper will become sharper as the plate thickness is increased (for example heat is transported more slowly between the front and root faces) and this will also make the control limitations less severe than indicated by the simple model. Assumption (2) anticipates a further correction. The width of the keyhole root tends to increase faster than the width at the front face, but this effect decreases with increasing plate thickness (see Chapter 6 for detailed discussion of heat flow). Again this suggests that the control requirements for thick plates may be overestimated. Despite these qualifications however, the model is helpful in understanding the difficulties arising when plate thickness is increased. Furthermore, its predictions are accurate enough to guide the practical development of welding procedures.

4.1.7. Keyhole failure in thin plate

The 'first stability rule' for keyhole GTAW does not provide a complete appreciation of the relationship between plate thickness and pool stability. To the contrary, the process also fails quite abruptly for stainless steel plates as the thickness is reduced below about 3mm. Intuitively this appears to be associated with an increasing difficulty in maintaining an attractive (eg ~1:1) keyhole aspect ratio. However, a wide root bead would not lead to a failure through the mechanism already discussed. For example, according to the data in Table 4.2 a 3mm plate should support a root bead up to 10mm wide, whereas typical widths range between about 2 to 4mm. The implication is that there is an alternative failure mechanism.

Failed welds in thin plate are reminiscent of thermally cut thin sheet where the liquid metal is drawn to beads along the sides of the seam and there is no closure of the keyhole. Consequently the proposed failure mode can be visualised as the weld puddle being split lengthwise, or 'unzipped', with the two halves drawing themselves up against the respective sides of the weld seem. Photographs of failed keyhole-welding samples are presented in Figure 4.8. The proposed process is illustrated in Figure 4.9.

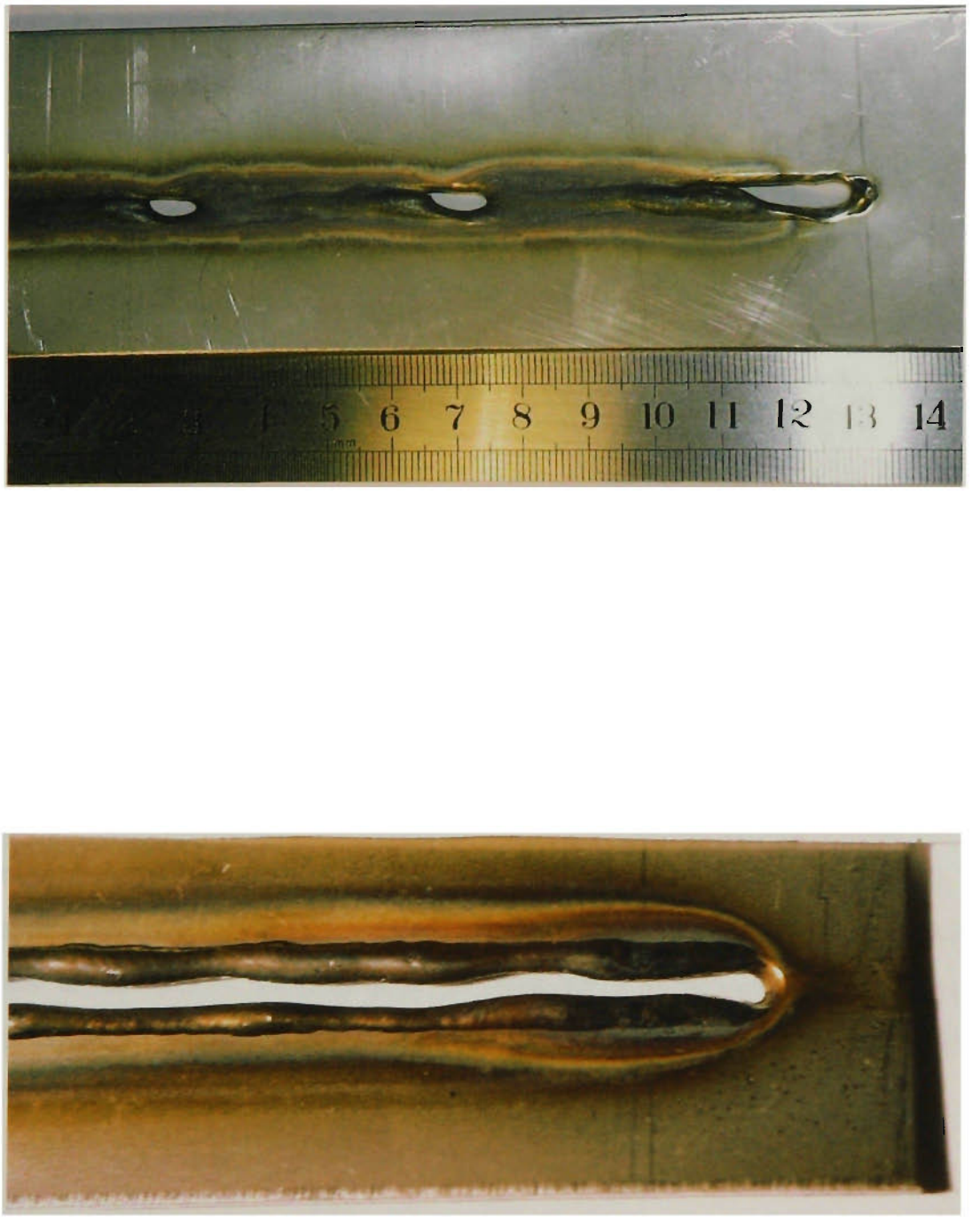

Figure 4.8. Examples of partial (upper) and complete (lower) keyhole failure in thin plate due to 'unzipping'.

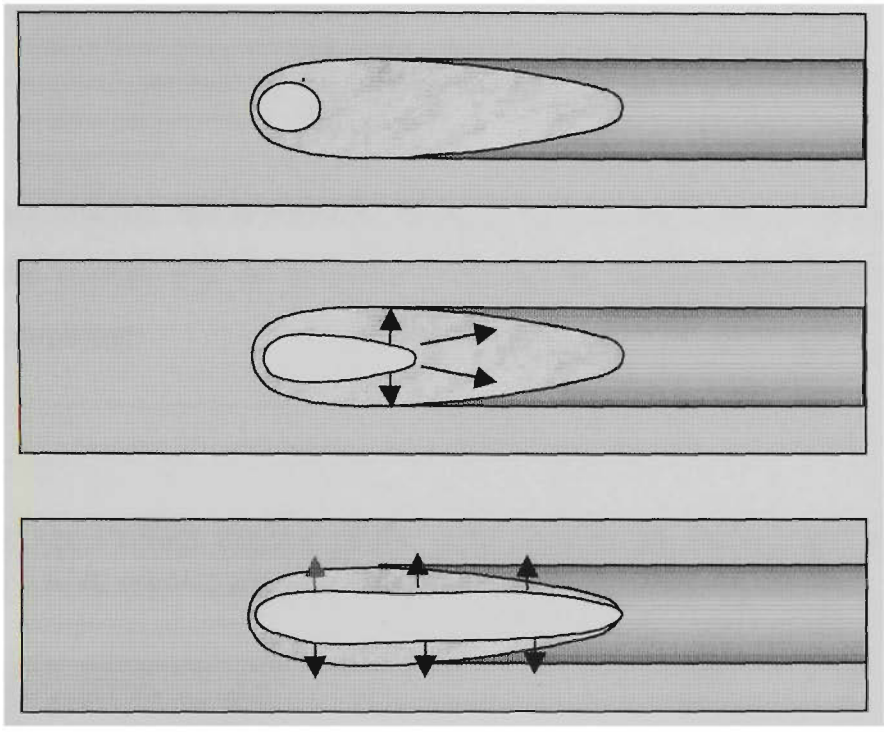

Figure 4.9. These schematics illustrate the proposed 'unzipping' failure of a keyhole in thin plate.

This possibility can be explored by examining the energy changes associated with an incremental unzipping, as perhaps due to some random fluctuation. The system will be unstable and unzipping will continue if an incremental rupture releases energy. Whether or not this is the case may be determined by examining the associated change in surface area of the puddle, since surface area (A) and surface energy (S) are related:

$$S = \gamma A$$

Although it is not immediately evident, the change in surface energy may be positive, negative or perhaps zero. On the one hand the unzipping will destroy surface because the opening extends towards the tail of the pool, while on the other hand new surface is created along the length of the opening (see Figure 4.9). Physically the system will be stable against unzipping if the net change in surface energy is positive because this constitutes a restoring force:

$$F = -\frac{dS}{dx}$$

$$= -\gamma \frac{dA}{dx}$$

(γ is the surface tension, but is numerically equal to the coefficient of surface energy). Conversely the system will be unstable if energy is released, and in this case the rupture will propagate.

Retraction of the trailing surface of the weld pool by an incremental distance δx (exagerated, a to b) creates an area δH, and destroys an area δW:

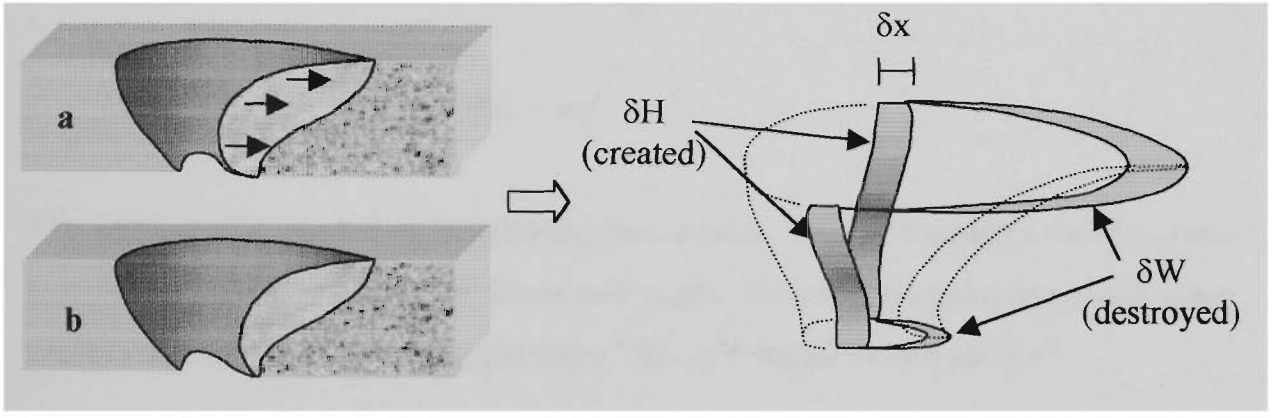

Figure 4.10. Schematic diagram indicating the changes in liquid surface area due to an incremental unzipping of the weld pool.

4.1.8. A second rule for keyhole stability.

To estimate the conditions under which the rupture will propagate it is necessary to specify the net change in surface area for an incremental δx lengthening of the keyhole opening. To facilitate this the change in surface area will be resolved into two components, δW and δH, as shown in Figure 4.10.

The surface area destroyed by an incremental lengthening of the opening, δW, is dependent on the curvature of the face and root weld beads. For simplicity, the respective bead profiles will be assumed to be flat. Any other bead profile would

involve a greater surface area per unit length, and increase the energy release. Therefore the energy associated with the destroyed area δS_W is at least

$$\delta S_W = -\gamma \delta W$$

where

$$\delta W = -(w_f + w_r)\, \delta x$$

and w_f and w_r are the width of the front face and root beads respectively. For completeness this incremental release of energy can be equated to the component of force promoting the unzipping, F_o,

$$F_0 = Lim_{x \to 0} - \gamma \frac{\delta W}{\delta x}$$

$$= -\gamma (w_f + w_r)$$

The surface area created in lengthening the opening, δH, is dependent on the cross-sectional profile of the keyhole. Since this is also unknown the calculation will again assume that the profiles are straight lines. This is illustrated in Figure 4.11.

For this approximation the keyhole sidewalls are of length L, where

$$L^2 = G^2 + \tfrac{1}{4} (w_f - w_r)^2$$

If the keyhole opening is unzipped by δx then δH be $2L\delta x$, and the component of force acting to close the rupture, F_c is then $2\gamma L$. The net change in surface energy will be zero if the two forces, F_o and F_c balance. Equating these two terms gives

$$2L = w_f + w_r \qquad (4.11)$$

Substituting for L

$$\sqrt{4G^2 + (w_f - w_r)^2} \quad = \quad w_f + w_r$$

Squaring both sides gives

$$4G^2 + (w_f - w_r)^2 \quad = \quad (w_f + w_r)^2$$

After expanding and rearranging the result is

$$G \quad = \quad \sqrt{w_f w_r} \tag{4.12}$$

This is the critical condition; if $\sqrt{(w_f w_r)} > G$ then there will be an overall decrease in surface energy and the pool will unzip. On the other hand, if $\sqrt{(w_f w_r)} < G$ the unzipping will not proceed. Qualitatively, the result is not unexpected: the puddle width should be (roughly) less than the plate thickness.

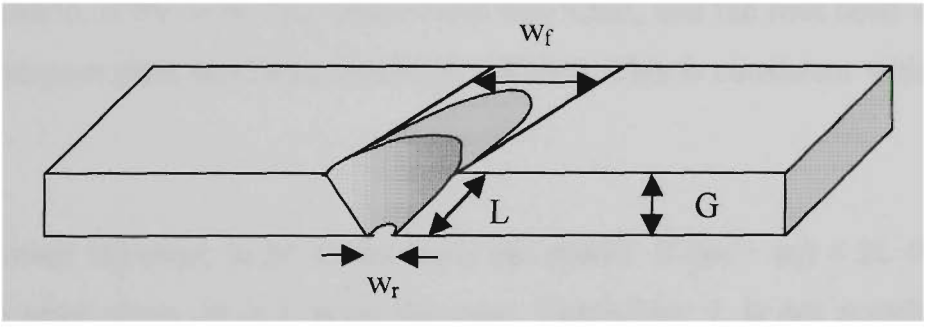

Figure 4.11. Keyhole cross sections for the two cases examined for unzipping.

4.1.9. Failure characteristics

An important physical characteristic of the unzipping mechanism is its sudden onset. This suggests that the assumption implicit in the preceding argument, namely that the pool is most resistant to unzipping when in its normal keyhole state, is true. However, a more detailed analysis would be needed to confirm or refute this claim. In the first instance it is not clear how, or to what extent, the two terms, δW and δH, change as the rupture develops. On the other hand it must be remembered that the liquid pool is

of quite limited extent, and the process need proceed only a very small distance before the cavity encounters a portion of the solidification boundary. Once this happens the rupture becomes 'frozen in', again changing the dynamics of the system. Finally, the rupture of the keyhole will allow much freer venting of the arc gases, reducing the transfer of heat and momentum from the arc to the weldment. These quantities are fundamental to keyhole formation, and this coupling further complicates the problem. What is important however, is the point at which failure begins rather than the details of how the failure evolves. For example, even if the transition to the unzipped mode is not stable the weld will still be totally unacceptable (see Figure 4.8).

Although the above model uses some obvious approximations to the relevant profiles, it does provide a practical indication as to when this failure mode may be anticipated. For example, if the top and bottom bead widths were equal the minimum plate thickness would be the same as the bead width. If the minimum bead width was say 4mm, then that would correspond to the minimum plate thickness that could be welded. However, the face and root bead widths are not usually equal. In a more realistic scenario, if the front face bead width was 4mm, and the root bead was 2mm, then the minimum plate thickness would be 2.83mm. This is consistent with common experience.

There is another inference to be drawn from this model. If $(w_f + w_r) < 2L$ then either the keyhole must close up or L must decrease. Decreasing L is not possible in this model unless the liquid peels away from the front and possibly root faces. Such an eventuality could provide a mechanism for the generating undercut. The implication is that the tendency for undercutting will increase as the weld pool becomes narrower. Consequently the control advantages associated with a reduction in threshold current (and therefore bead width) are won at the cost of an increased risk of undercut.

Whether or not undercut occurs, whenever $(w_f + w_r) < 2L$ there will be a force acting to draw the trailing surface of the pool towards the centre (this is what is meant by F_c). This constitutes a reduction in pressure in the trailing portion of the pool, and so acts to draw liquid to it. This 'pumping' action is important in understanding the dynamics of the pool, and will be addressed in the following sections.

4.2. Displacement of metal in the GTAW keyhole

4.2.1. Deficit

GMAW and high current GTAW passes commonly end with a 'termination' crater. In fact modern GMAW power sources often have a built-in 'crater-fill' function to rectify this phenomenon. Termination craters are also found at the end of keyhole GTAW runs. These craters often retain the basic characteristics of the keyhole when the welding current has been switched off abruptly.

Before discussing this phenomenon some terminology must be introduced to avoid confusion. The term 'cavity' will be used to refer to the solid-liquid interface of the weld pool. The liquid metal filling the cavity constitutes the weld pool, or simply 'pool'. The pool surface is the exposed surface of the weld pool. The depression bounded by the pool surface and the original plate surface is the crater.

The presence of a termination crater is proof that a particular weld pool contained insufficient liquid to fill its own cavity. This simple observation implies that the liquid does not simply pile up to the sides and rear of the pool under the influence of the arc force, but is actually lost into the weld bead. Weld pools in this condition will be referred to as its being 'deficient'. Accordingly, the deficit is the volume of metal displaced from the weld pool. Examples of several keyhole GTAW craters are shown in Figure 4.12. The distinction between full and deficient weld pools is illustrated schematically in Figure 4.13.

One important property of the weld pool deficit is that it must be conserved when the arc is abruptly extinguished. This is despite the fact that the actual surface geometry may change considerably between ceasing of the arc and solidification. Therefore, the deficit may be determined by abruptly terminating the weld and measuring the volume of the resultant crater.

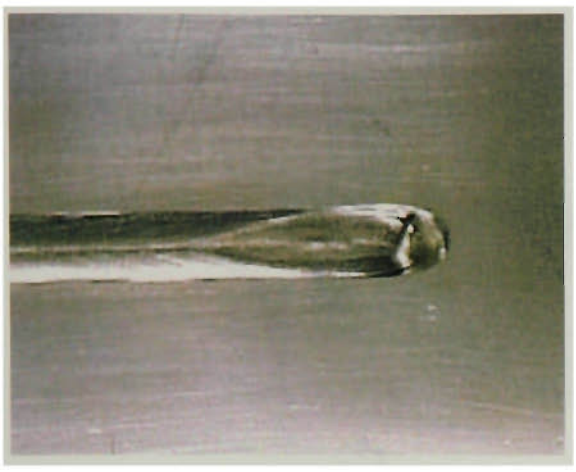

(a)

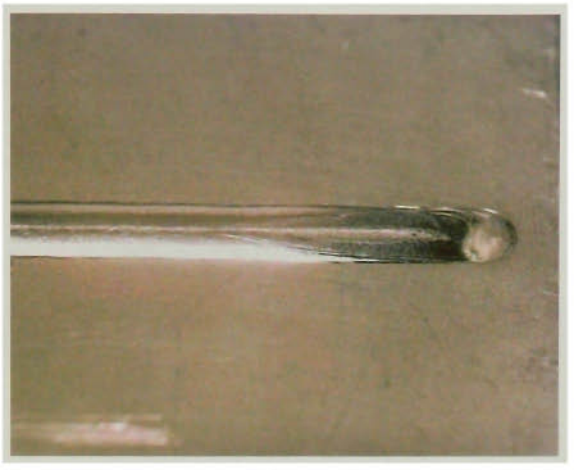

(b)

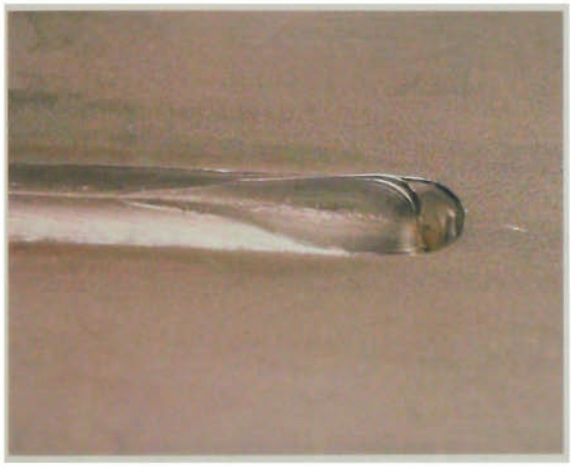

(c)

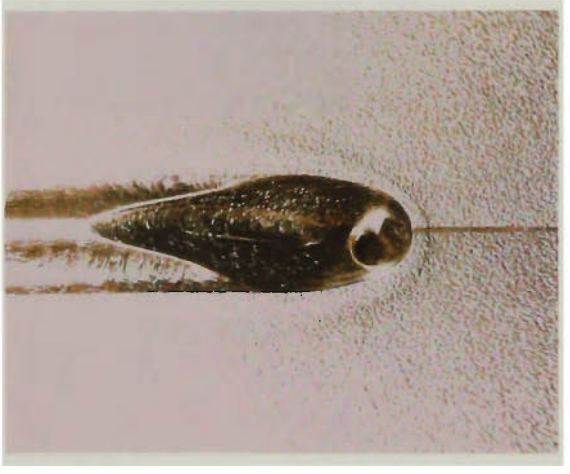

(d)

(e)

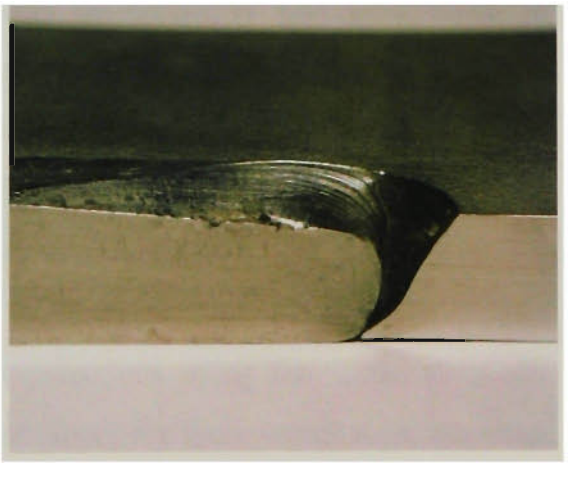

(f)

Figure 4.12. Examples of craters from keyhole GTA welds. (a) two 1.2mm stainless steel plates (lap joint), (b) 3mm stainless steel, (c) 8mm stainless steel, (d) 13mm titanium, (e) 12mm stainless steel, (f) cross-section through (e).

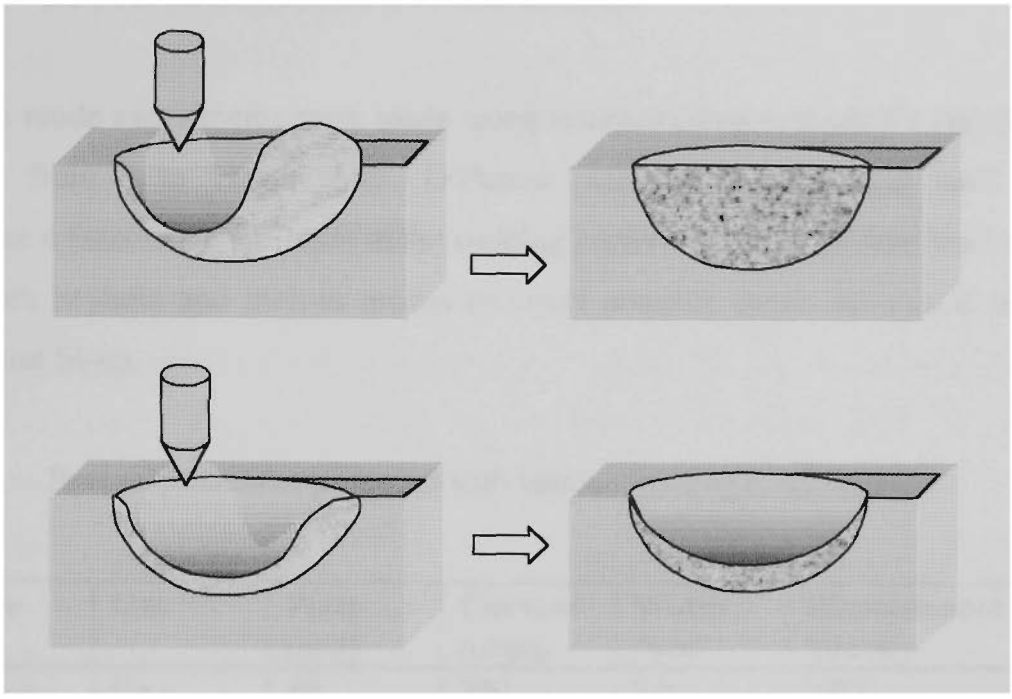

Figure 4.13. Schematic illustrating the concept of full (upper) and deficient (lower) weld pools before and after removal of the arc.

4.2.2. Experimental method and results

The conservation of deficit provides one measure of the state of the weld pool during the welding process. Therefore an experimental investigation was undertaken to measure the deficit associated with various welding conditions, including both the melt-in and keyhole modes. In all, 18 termination craters were produced and examined. The experiments included both keyhole and melt-in mode GTAW passes, the latter being made with both argon and helium shielding gases.

Each of the melt-in mode experiments was carried out using the same electrode geometry, welding speed and plate material. Test pieces for these welds were cut from a bar of 75mm x 10mm AISI 304 stainless steel. The pieces were each about 200mm long. A welding speed of 300mm/min provided adequate time for the correct current to be established and thoroughly stabilised during each weld. The 6.4mm lanthanated electrode was re-ground with a 60° included angle, and the arc gap was adjusted to 1mm between each weld. Welds were carried out with both argon and helium

shielding gas. The welding current was varied between limits imposed by the onset of either arc or weld pool instabilities, or electrode damage.

The keyhole mode experiments were made using established procedures for stainless steel plates from 3 to 12mm thick. Different plate thicknesses were used to accommodate a reasonable variation in the welding current. The welds were bead-on-plate for both keyhole and melt-in modes to avoid possible errors associated with imperfect joint fit-up.

Table 4.3. Pool displacement produced with various welding conditions.

Mode	**Gas**	**Plate** *(mm)*	**Current** *(amps)*	**Width** *(mm)*	**Displacement** *(grams)*
Melt-in	He	10	200	8.0	0.053
Melt-in	He	10	230	7.8	0.035
Melt-in	He	10	260	8.6	0.079
Melt-in	He	10	290	9.1	0.097
Melt-in	He	10	320	9.4	0.070
Melt-in	He	10	390	11.3	0.220
Melt-in	He	10	425	11.9	0.351
Melt-in	He	10	470	12.4	3.822
Melt-in	Ar	10	120	5.3	0.018
Melt-in	Ar	10	170	8.0	0.097
Melt-in	Ar	10	240	9.3	0.228
Melt-in	Ar	10	255	7.3	0.457
Melt-in	Ar	10	320	7.9	0.598
Keyhole	Ar-5H	3	375	6.0	0.34
Keyhole	Ar-5H	4	345	6.0	0.48
Keyhole	Ar-5H	6	435	8.5	1.10
Keyhole	Ar-5H	8	575	11.8	2.15
Keyhole	Ar-5H	10	600	10.7	2.37
Keyhole	Ar-5H	12	580	14.1	3.25

After the welds had been completed the section containing the termination crater of each weld was cut from each plate. Crater displacements were then determined from the weight of wax required to restore the original level over the crater. Weights were measured to an accuracy of ±0.5mg. The ratio of density of the wax to that of the steel was determined by comparing equal volumes of each: a sample was weighed, several blind holes were drilled in it and it was re-weighed, and finally these holes were filled with wax and the sample weighed a third time. Because of the differing densities of

wax and stainless steel the accuracy of the final estimate for displacement was nearer to ±5mg. The deficits (displaced volumes) were inferred assuming a stainless steel density of 7.8g/cm^3. Results from the 12 melt-in mode and 6 keyhole mode samples are presented in Table 4.3.

4.2.3. Forces required maintaining a deficit

The information gained from the measurements was sufficient to estimate upper limits to the arc forces involved in each instance. The arc force is known to have a quadratic dependence on current ($F = kI^2$ where k is an 'arc force constant'). The value of k is dependent on the current distribution in the arc (Converti, 1981), but values of the order of 20 x 10^{-6} grams weight/amp^2 are anticipated (Adonyi-Bucurdiu 1989). Arc forces are discussed in detail in Chapter 5.

The following simple model was developed to introduce the topic and to provide an initial insight into the relationships between deficit, arc force and surface tension. More detailed descriptions will be discussed in the following section. The main assumption made was that:

- The surface depression can be approximated as a spherical section, with volume equal to the deficit.

To estimate the force due to surface tension let the pool surface meet the plate surface at an angle θ, as shown in Figure 4.14. The vertical component of the surface tension per unit length of the boundary, dT, is

$$dT = \gamma \sin\theta$$

If r is the pool radius the total restoring force, T, is

$$T = 2\pi r \gamma \sin\theta \qquad (4.13)$$

If γ is taken as 1N/m, and w (= 2r) is the pool width in millimetres, then

$$T \approx 0.32w \sin\theta \quad \text{(grams weight)}$$

The surface tension therefore produces a maximum restoring force of 0.32w grams when the surface is perpendicular to the plate surface around the rim of the pool.

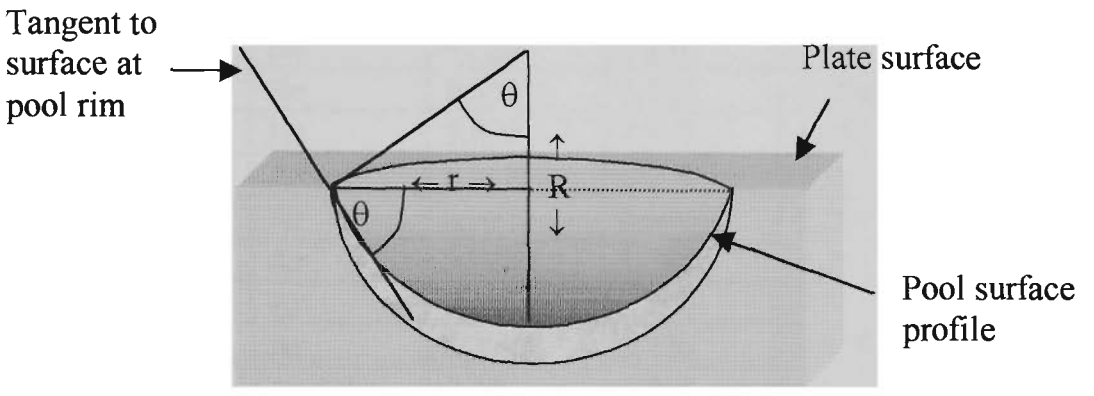

Figure 4.14. The identification of the variables used in estimating the maximum force due to surface tension.

An expression for the volume of the depression is needed in order to estimate sinθ in (4.13). This volume can be expressed as the difference between the volume of the portion of the sphere, radius R, subtended by the angle θ and the volume of the regular cone with slant height R and subtended by the same angle:

$$V = \frac{2\pi R^3(1-\cos\theta)}{3} - \frac{\pi R^3 \sin^2\theta\cos\theta}{3}$$

Rearranging and noting that R = r/sinθ leads to

$$V = \frac{\pi r^3\left(2-2\cos\theta-\sin^2\theta\cos\theta\right)}{3\sin^3\theta} \qquad (4.14)$$

Table 4.4. A comparison of forces associated with weld pool deficits.

Mode	Gas	B Force *(grams)*	T Force *(grams)*	Sin θ	10^6x k (g/A^2)
Melt-in	He	0.053	0.384	0.150	10.9
Melt-in	He	0.035	0.267	0.107	5.7
Melt-in	He	0.079	0.493	0.179	8.5
Melt-in	He	0.097	0.540	0.185	7.5
Melt-in	He	0.070	0.368	0.122	4.3
Melt-in	He	0.220	0.791	0.218	6.6
Melt-in	He	0.351	1.122	0.294	8.1
Melt-in	He	3.822	3.975	1.000	35.3
Melt-in	Ar	0.018	0.296	0.174	21.6
Melt-in	Ar	0.097	0.690	0.269	27.3
Melt-in	Ar	0.228	1.165	0.391	24.1
Melt-in	Ar	0.457	2.226	0.951	41.2
Melt-in	Ar	0.598	2.426	0.958	29.5
Keyhole	Ar-5H	0.34	1.913	0.995	16.0
Keyhole	Ar-5H	0.48	1.923	1.000	20.2
Keyhole	Ar-5H	1.10	2.725	1.000	20.2
Keyhole	Ar-5H	2.15	3.679	0.972	17.6
Keyhole	Ar-5H	2.37	3.430	1.000	16.1
Keyhole	Ar-5H	3.25	4.286	0.948	22.3

Given V and r, (4.14) can be solved numerically for θ or sinθ. It is noted that the force associated with the deficit is the buoyant force (B), and is numerically equal to the displacement. Results are presented in Table 4.4. Calculated values of k are included, based on the proposed balance between arc force (kI^2), B and T:

$$kI^2 = B+T$$

4.2.4. Discussion of displacement results

The data show that the forces necessary to maintain the deficits are consistent with reasonable estimates of the arc force alone. Consequently there is no evidence to justify a search for additional forces.

One very significant feature of the melt-in mode data is an abrupt switching from a shallow to a deeply penetrating crater as the current is increased. This is demonstrated most clearly in the helium trials where the deficit increased by more than 1000% as the

current was increased from 425 to 470 amps. The same phenomenon was observed with argon: the deficit doubled as the current was increased from 240 to 255. This transition from shallow to deep penetration was so strong, and occurred so abruptly that it could be regarded as a switching between two distinct welding regimes. It is also important because the deeply penetrating crater is an obvious precursor to the formation of a keyhole. The abruptness of the transitions can be appreciated from the graphical presentation of Figure 4.15 and the images in Figure 4.16.

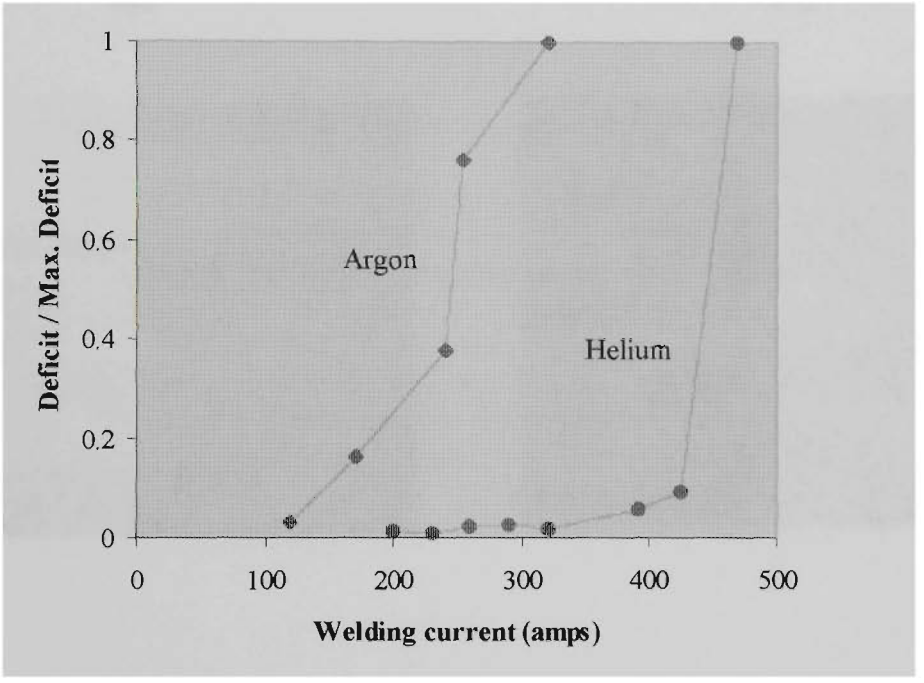

Figure 4.15. Variation in (dimensionless) deficit with current for melt-in mode GTAW.

The reason for the transition relates to the behaviour of the forces F (the arc force), T and B (the buoyant force associated with the weight of the displaced). Although T is dependent on both the contact angle and the pool radius, its maximum value (when $\sin\theta = 1$) increases linearly with pool radius. If B is temporarily ignored, the arc force will be balanced by surface tension provided

$$2\pi r\gamma \geq kI^2 \tag{4.15}$$

and

$$\frac{r}{I^2} \geq const. \tag{4.16}$$

(a)

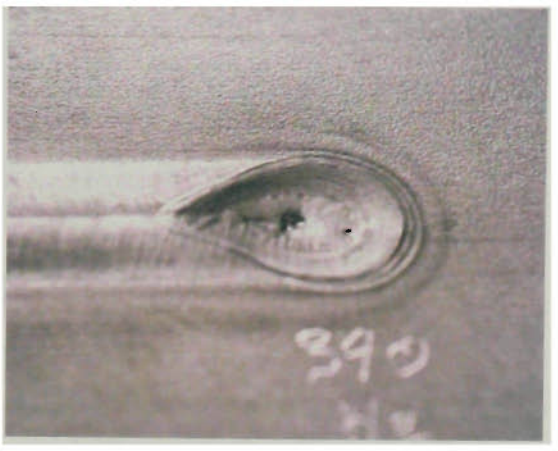

(b)

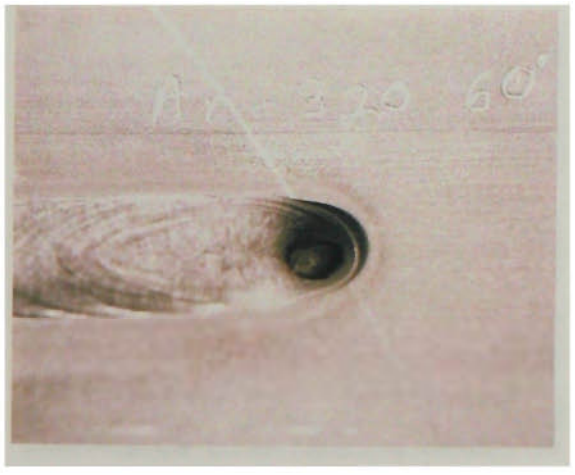

(e)

(f)

Figure 4.16a. Examples of variations in deficit (crater volume) with increasing current. (a) 240A, (c) 255A, and (e) 320A in argon: (b) 390A, (d) 425A and (f) 490A in helium.

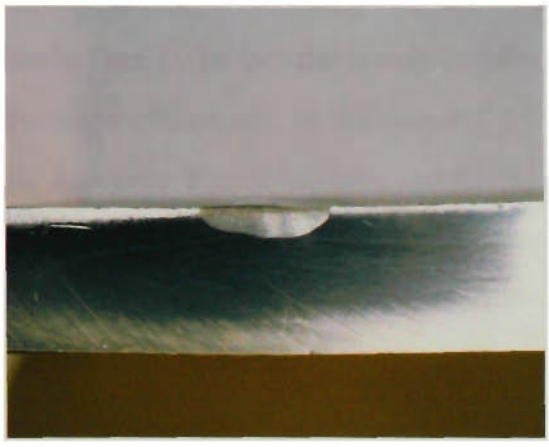

(a)

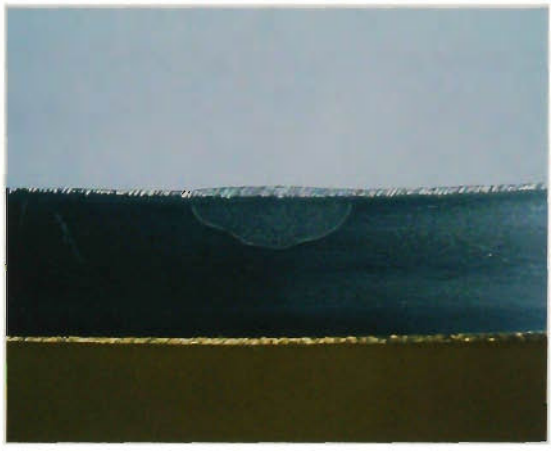

(b)

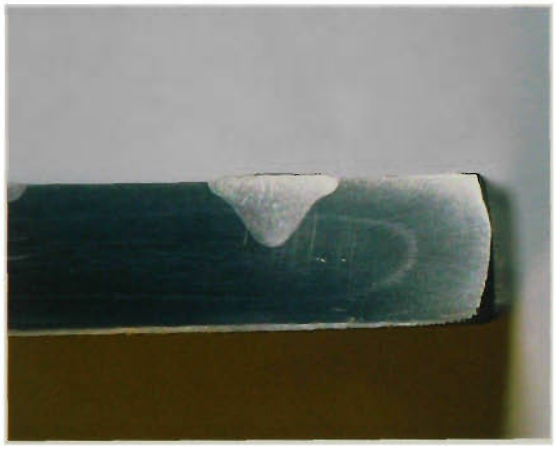

(c)

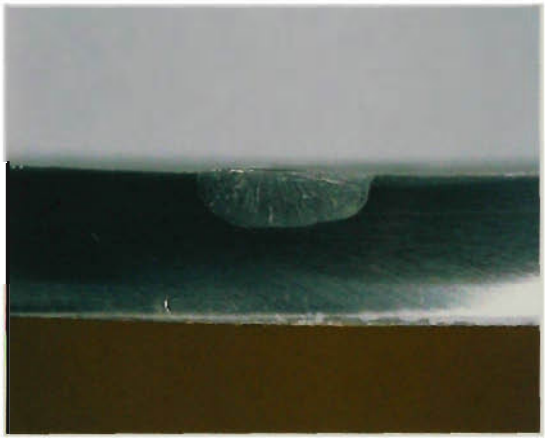

(d)

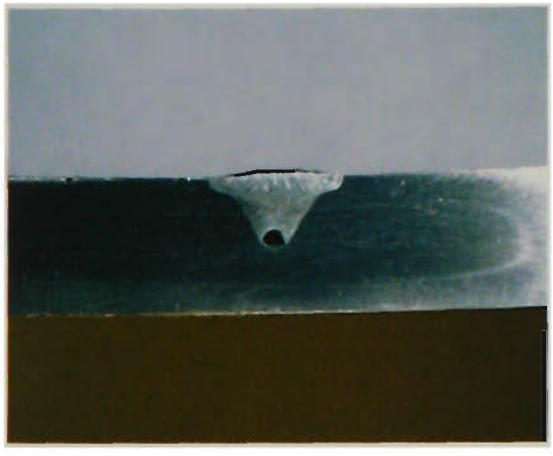

(e)

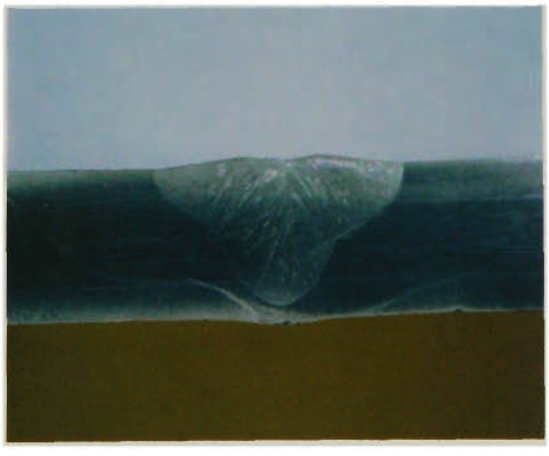

(f)

Figure 4.16b. Fusion profiles for the samples presented in Figure 16a. (a) 240A, (c) 255A, and (e) 320A in argon. (b) 390A, (d) 425A and (f) 490A in helium.

The condition (4.16) cannot be satisfied for all currents because r changes much more slowly than I^2. In fact the anode current density often tends towards a constant value, as discussed elsewhere, in which case $I \sim r^2$. Consequently although T may dominate at low currents F will always overwhelm it as the current is increased. B must then balance the excess arc force and so the deficit and the penetration will increase rapidly. The two regimes can therefore be classified as surface tension dominated and buoyancy-dominated.

As an example, suppose that the anode current density is approximately constant (as modelled by Converti, 1981). Then the pool radius, r, will vary as the square root of the current I:

$$r = r_0\sqrt{I}$$

where r_0 is a constant that characterises the spread of the arc current. The maximum restoring force that can be generated by the surface tension is exceeded when

$$kI^2 > 2\pi\gamma r_0\sqrt{I}$$

which reduces to

$$I > \left(\frac{2\pi\gamma r_0}{k}\right)^{\frac{2}{3}}$$

It is significant that the critical current increases for decreasing arc force constant (k) and increasing spread of the arc, as indicated by the value of r_0. It is also recalled that helium is a poor choice of shielding gas for keyhole welding, and is associated with diffuse arcs. It is not surprising then that the transition current was found to be much higher in helium than in argon. Furthermore, if k is set to 20×10^{-6} g/amp^2 (Adonyi-Bucurdiu, 1989) and the anode current density is 4 amps/mm^2 (from Table 4.3) then the transition current predicted by this 'proto-model' is found to be 434 amps.

4.2.5. Characteristics of the transition

The transition from T to B regimes is characterised by a sudden increase in penetration and deficit. In the model of Figure 4.14 it is also signalled by the angle between the pool and the plate surface reaching 90°. In practice the transition may occur before the latter condition is achieved. This can be seen from the example in Figure 4.17. To understand why this happens the surface curvature must be considered in a little more detail.

The important contribution of the preceding model is equation (4.13). This equation describes the vertical component of the restoring force exerted by the surface at a radius r. Although to this point it has only been applied at the rim of the pool, it is equally valid at all radii across the surface (assuming still that the discussion is restricted to axi-symmetric weld pools). Therefore, if the net downward force acting on the surface enclosed by the radius r is F(r) then for equilibrium

$$2\pi r \gamma \sin\theta = F(r)$$

or

$$\sin\theta = \frac{F(r)}{2\pi\gamma r} \tag{4.17}$$

Alternatively sinθ can be obtained from the net pressure distribution, P(r), since

$$F(r) = \int_0^r P(r')2\pi r' dr' \tag{4.18}$$

As an example, suppose the pressure distribution is parabolic, ie

$$P(r) = \alpha(R^2 - r^2) \tag{4.19}$$

where R is the radius of the pool and α is a constant. Then applying (4.18)

$$F(r) = \frac{\pi\alpha}{2}\left(2r^2R^2 - r^4\right)$$

and

$$\sin\theta = \frac{\alpha}{4\gamma}\left(2rR^2 - r^3\right) \tag{4.20}$$

Evidently, sinθ need not reach its maximum at the rim. For example, differentiating (4.20) shows that sinθ has a maximum value when r = √(2/3) R (≈ 0.816 R). This is almost 20% inside the pool boundary. Consequently the maximum arc force that can be sustained by surface tension alone can be less than the theoretical maximum 2πrγ, depending on how the force is distributed. A series of curves depicting surface profiles satisfying (4.20) are presented in Figure 4.17.

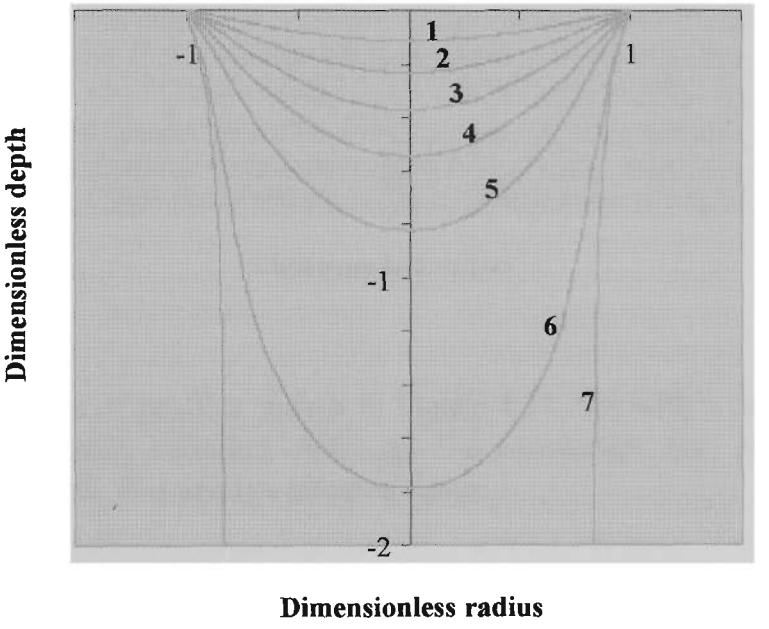

Figure 4.17. Depiction of weld pool profiles predicted from (4.20) (surface tension only). Arc force has been successively incremented by 0.15 units, beginning at 0.15. Penetration goes to infinity for arc forces exceeding 0.92.

Equation (4.17) is valid whether or not buoyancy is considered because F(r) is the net downward force acting on the surface. However, it is difficult to include buoyancy explicitly (as a function of r) due to the coupling between displacement and curvature: the displaced volume is dependent on the surface curvature, and the curvature is dependent on the weight of fluid being displaced. Nevertheless, it is not difficult to take an iterative approach to obtaining a solution. For example, a first approximation made

assuming no buoyant force (B(r)) can be used to estimate the displacement profile, and hence a first approximation to B(r). The process is then repeated with F(r) replaced with F(r) – B(r). This method was used in generating the curves shown in Figure 4.18. The curvature of the pool surface will be considered in greater detail in the next section.

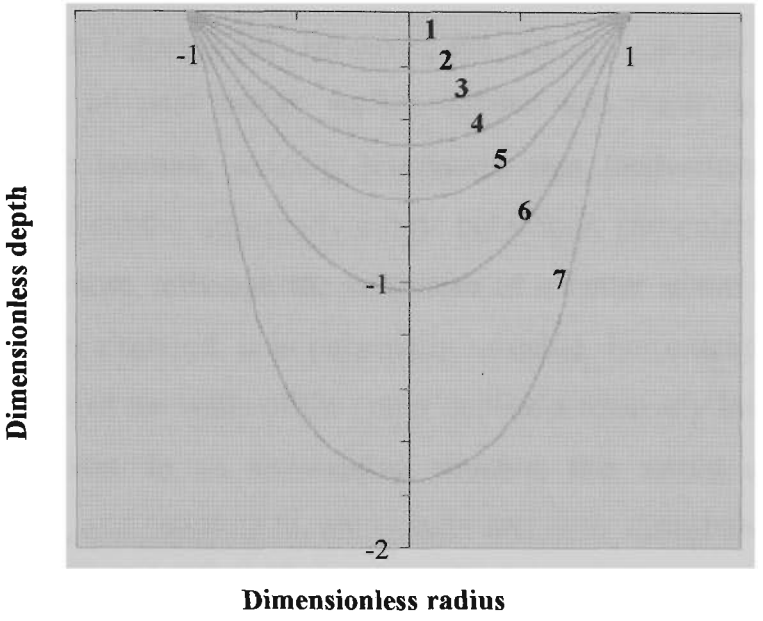

Figure 4.18. Series of profiles shown in Figure 4.17, but with a contribution due to buoyancy included. Although the penetration may still exhibits rapid growth, it is always remains finite.

The preceding discussion can be summarised with a graphical illustration of how the displaced volume changes with increasing arc force. To begin, the buoyant force is proportional to the displacement. Therefore the relationship between displacement and the arc force necessary to overcome buoyancy is a family of straight lines of slope $(1/\rho g)$. On the other hand, if only surface tension is considered then the displaced volume increases asymptotically as the arc force approaches (approximately) $2\pi r\gamma$. The position of the asymptote moves to the right (ie the maximum arc force increases) as either the surface tension or the pool radius is increased. However, increases in surface tension and pool radius are not equivalent. Certainly, if the arc force is fixed then increasing either the surface tension or pool radius reduces the surface curvature. In the case of surface tension this equates directly to a reduction in displacement. However, in the case of increasing pool radius, the reduction in surface curvature is

countered by an increasing pool area. As a result increasing surface tension is the more effective in reducing the displacement. These various relationships are illustrated in Figure 4.19.

The resultant force-displacement curve is obtained by summing the respective force components required for each given displacement. All resultant curves exhibit a transition region (see Figure 4.20). However, the size and position of the transition region is dependent on pool radius, surface tension and metal density. This is of practical importance because welding procedures that inadvertently fall into this transition region will exhibit apparently erratic behaviour, particularly with respect to penetration. Furthermore, although the behaviour of a crater in the buoyancy-limited domain has not been explored, it is potentially unstable. For example, the low axial curvature along most of the walls of the crater implies a relatively low resistance to its bending along its axis. In an arc-welding situation this would correspond to an increased sensitivity, and coupling to, arc wander and other disturbances in the plasma flow. Similarly it has interesting implications for laser-induced keyholes. Fortunately axial curvature is restored (and becomes negative) with the formation of an open keyhole. Consequently GTAW keyholes are quite stable, although the pool may have to pass through an unstable regime before the keyhole is formed.

In concluding it should be mentioned that all of the discussion is dependent on there being sufficient liquid in the cavity to sustain the required surface distortion. It cannot be assumed that this will always be the case. One only has to consider the situation of a given arc being applied to a plate with increasing travel speed. While the arc force remains constant throughout the experiment the molten volume can be made arbitrarily small. This indicates that there is at least a third regime wherein the surface profile is constrained by the pool cavity.

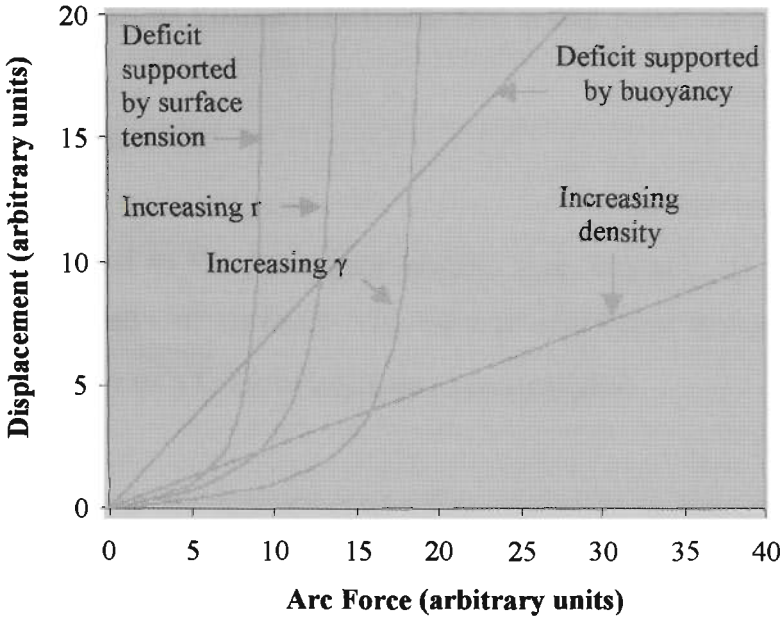

Figure 4.19. Qualitative depiction of the relationships between deficit and arc force (arbitrary units) arising from independent considerations of surface

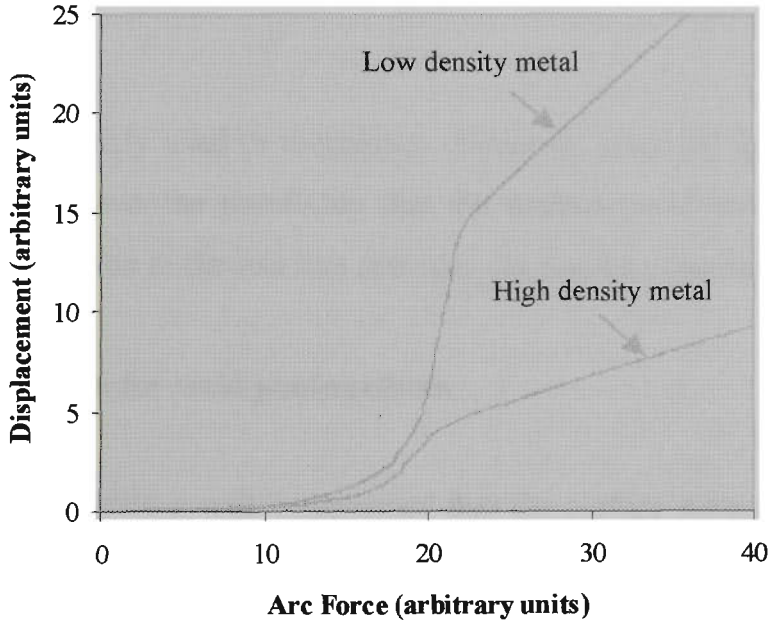

Figure 4.20. Qualitative depiction of possible resultant relationship between deficit and arc force obtained by summing the independent contributions of surface tension and buoyancy illustrated in Figure 4.19.

4.3. Mathematical considerations for weld pool surfaces

4.3.1. Introduction

The model presented in the preceding section is an example of a class of problems involving the geometry of surfaces. This section will begin the process of describing the surface geometry of a GTAW keyhole in more detail.

A general approach to the derivation of a free surface is to require that the energy (E) associated with the surface is at a local minimum:

$$\nabla E = 0 \tag{4.20}$$

This implies that there is no net force (F) acting anywhere over the surface since

$$\nabla E = -F$$

This criterion is widely used in mechanics. However, since all local minima satisfy this condition it allows the possibility that the surface could have several different stable states in addition to the one that provides the absolute minimum energy.

4.3.2. The equation for weld pool surfaces

To begin this discussion it will be assumed that the surface geometry results from a balance between an externally applied (arc) force, hydrostatic pressure in the liquid metal and surface tension. The forces acting on the surface due to fluid flow will not be included explicitly at this point. The surface will be described alternately in rectangular and cylindrical coordinates. In either case z will be taken as the vertical coordinate, with z equal to zero at the plate surface and decreasing towards the base of the pool.

The pressure change across the surface due to surface curvature is given by (4.3), and is γK. If K is positive the resultant pressure acts to collapse the cavity. The pressure due to the head of liquid metal is $-\rho gz$, where ρ is the density of the liquid metal and g

is the acceleration due to gravity. If this pressure is positive (as it is below the plate surface) it also acts to close the cavity. Finally, the arc pressure, $P_a(r, \phi, z)$ (or $P_a(x,y,z)$), must be included. If this pressure is positive it acts to expand the cavity. Consequently the required balance is

$$\gamma(r,\phi,z)K(r,\phi,z)-\rho gz-P_a(r,\phi,z) \quad = \quad 0$$

or (4.21)

$$\gamma(x,y,z)K(x,y,z)-\rho gz-P_a(x,y,z) \quad = \quad 0$$

Both the surface tension and the arc pressure are expected to vary over the surface, but their exact behaviour cannot be predicted a priori. The arc pressure arises from the momentum transfer between the arc gases and the weld pool, and is therefore coupled to the surface geometry. Similarly the surface tension is temperature (and composition) dependent, and therefore is also coupled to the surface geometry. These couplings make (4.21) properly soluble only as a member of a set of simultaneous partial differential equations. Since the purpose of this discussion is to understand some of the more general implications of (4.21) with respect to weld pool behaviour, it will be assumed that γ is constant over the surface and that P can be specified independently of the surface shape:

$$\gamma K(r,\phi,z)-\rho gz-P_a(r,\phi,z) \quad = \quad 0$$

or (4.22)

$$\gamma K(x,y,z)-\rho gz-P_a(x,y,z) \quad = \quad 0$$

Typically this is a second order partial differential equation. This equation, together with appropriately chosen boundary conditions, specifies the weld pool surface.

K can be expressed relatively succinctly in rectangular coordinates for a surface in space. Specifically, if K is the mean curvature of a surface at a point, and K_1 and K_2 are the principle curvatures at the point, then

$$K \quad = \quad K_1+K_2$$

and

$$K = \frac{r(1+q^2)-2pqs+t(1+p^2)}{(1+p^2+q^2)^{3/2}} \qquad (4.23)$$

where $p=\frac{\partial z}{\partial x}$, $q=\frac{\partial z}{\partial y}$, $r=\frac{\partial^2 z}{\partial x^2}$, $s=\frac{\partial^2 z}{\partial x \partial y}$ *and* $t=\frac{\partial^2 z}{\partial y^2}$

(Clegg, 1968). It is of some interest that if the forces other than surface tension are set to zero (or sum to zero) then (4.22) becomes

$$K = 0$$

or, in rectangular coordinates

$$r(1 + q^2) - 2pqs + t(1 + p^2) = 0$$

This is the celebrated differential equation that a free surface z = z(x, y) must satisfy. In fact this is the 'solution' to one of the most famous problems in differential geometry – namely that of describing the surface of minimal area (the minimal surface) spanning any closed loop in space. This particular problem is associated with Plateau, a Belgium physicist (1801 – 1883) who made an extensive study of such surfaces (Clegg, 1968).

Although K must be specified explicitly if a surface is to be determined, it is to be appreciated that (4.23) is a special case of the more general (4.21). In addition, various deductions follow directly from (4.21). For example, for the case of melt-in mode puddles it is inevitable that $K \geq 0$ at the bottom of the crater. It follows that the absolute minimum peak arc pressure required to generate a crater of depth z is ρgz. Since it is presumed that the melt-in crater must extend to the root face before a keyhole can be established, the generation of a keyhole must be preceded by the provision of this minimum peak pressure. The estimation of arc pressure will be considered in Chapter 5 and the implications of a minimum peak pressure will be discussed in Chapter 6.

4.3.3. Equation for axi-symmetric weld pools

The simplest useful approximation to a weld pool is one that has axial symmetry (ie no angular dependence). This is most directly dealt with in cylindrical coordinates. The expression for the curvature can be obtained from (4.23), but it is simpler to derive it directly using the methods of the calculus of variations. Specifically an equation describing a minimal surface will be developed and compared to (4.22). The intent is to subsequently identify the component for the curvature.

For directness consider a surface arising from only two influences: gravity and surface tension. To do this one first specifies the energy associated with the formation of a circular element of the cavity, radius r, thickness dz at a position z below the plate surface. There are two energy components associated with this disc: dE_s, which is the energy to create the surface area around its edge and dE_g, the energy required to remove the material from the disc to the surface. Writing z′ for dz/dr, z″ for d^2z/dr^2, r′ for dr/dz, etc, these components are:

$$\begin{aligned} dE_s &= 2\pi\gamma r\sqrt{1+r'^2}\,dz \\ &= 2\pi\gamma r\sqrt{1+z'^2}\,dr \end{aligned}$$

and

$$\begin{aligned} dE_g &= -\rho g\pi r^2 z\,dz \\ &= -\rho g\pi r^2 z\,z'\,dr \end{aligned} \qquad (4.24)$$

The energy is the sum of the various contributions:

$$dE = dE_s + dE_g + \ldots$$

thus

$$dE = \left(2\pi\gamma r\sqrt{1+z'^2} - \rho g\pi r^2 z\,z'\right)dr$$

and the total energy of the cavity is given by integration over r. This relationship has the form

$$E = \int F(r, z, z')dr$$

The condition for an extremum is provided by the Euler-Lagrange equation (Clegg, 1968):

$$\frac{d}{dr}\left(\frac{\partial F}{\partial z'}\right) - \frac{\partial F}{\partial z} = 0$$

Interpreting

$$F = 2\pi\gamma r\sqrt{1+z'^2} - \rho g\pi r^2 z z'$$

Then

$$\frac{\partial F}{\partial z'} = \frac{2\pi\gamma r}{\sqrt{1+z'^2}} - \rho g\pi r^2 z$$

$$\frac{d}{dr}\left(\frac{\partial F}{\partial z'}\right) = \frac{d}{dr}\left(\frac{2\pi\gamma r}{\sqrt{1+z'^2}}\right) - 2\rho g\pi r - \frac{1}{2}\rho g\pi r^2 z'$$

and

$$\frac{\partial F}{\partial z} = -\pi\rho g r^2 z'$$

Substitution into the Euler-Lagrange equation and dividing through by 2π gives

$$\frac{d}{dr}\left(\frac{\gamma r}{\sqrt{1+z'^2}}\right) - \rho g r z = 0$$

Writing this equation in the form (for $r \neq 0$)

$$\frac{1}{r}\frac{d}{dr}\left(\frac{\gamma r z'}{\sqrt{1+z'^2}}\right) - \rho g z = 0$$

allows the terms to be identified as pressures (since ρgz is a pressure). Referring to (4.22) we have

$$\gamma K = \frac{1}{r}\frac{d}{dr}\left(\frac{\gamma r z'}{\sqrt{1+z'^2}}\right)$$

Therefore the mean curvature for an axi-symmetric surface is

$$K = \frac{1}{r}\frac{d}{dr}\left(\frac{r z'}{\sqrt{1+z'^2}}\right)$$

$$= \frac{z'}{r\sqrt{1+z'^2}} + \frac{z''}{\left(1+z'^2\right)^{3/2}} \qquad (4.25)$$

Therefore we can write (4.22) for the axi-symmetric case as

$$\frac{1}{r}\frac{d}{dr}\left(\frac{\gamma r z'}{\sqrt{1+z'^2}}\right) - \rho g z - P_a(r,z) = 0 \qquad (4.26)$$

Now $z''/(1 + z'^2)^{3/2}$ is familiar as the expression for curvature in two dimensions, and can be associated with a curve on the surface in question generated by the polar angle ϕ = constant. We therefore identify the two terms as the normal curvatures of two orthogonal curves on the surface (M. do Carmo, 1976), with $z'/r\sqrt{(1 + z'^2)}$ being the curve generated by holding z = constant.

Equation (4.25) was derived with r as the independent variable. In some instances it may be preferable to have z as the independent variable. For example, this avoids the problem of possible infinities in z'. The curvature can be found in exactly the same manner as presented above, beginning with the alternate forms for dE_s and dE_g provided in (4.24). Carrying out this process gives the result:

$$K = \frac{1}{r}\left(\frac{d}{dz}\frac{rr'}{\sqrt{1+r'^2}} - \sqrt{1+r^2}\right)$$

$$= \frac{rr'' - r'^2 - 1}{r\left(1+r'^2\right)^{3/2}} \qquad (4.25')$$

And

$$\frac{\gamma}{r}\left(\frac{d}{dz}\frac{rr'}{\sqrt{1+r'^2}} - \sqrt{1+r'^2}\right) - \rho g z - P_a(r,z) = 0 \qquad (4.26')$$

4.3.4. Solutions for axi-symmetric weld pools

Before attempting to solve any specific cases of (4.26) it will be convenient to combine the two pressure terms, ρgz and P_a(r,z) into a single term that will be the mismatch between the two terms, or equivalently, the resultant pressure acting on the surface. Calling this term P(r,z), (4.26) can be shortened:

$$P(r,z) = \rho g z + P_a(r,z)$$

and

$$\frac{d}{dr}\left(\frac{\gamma r z'}{\sqrt{1+z'^2}}\right) = r\,P(r,z)$$

This can be integrated to give

$$\frac{rz'}{\sqrt{1+z'^2}} = \frac{1}{\gamma}\int r\,P(r,z)\,dr$$

$$= u(r) + c$$

where $$u(r) = \frac{1}{\gamma}\int r\,P(r,z)\,dr \qquad (4.27)$$

Solving for z',

$$z' = \frac{u(r)+c}{\sqrt{r^2-(u(r)+c)^2}} \tag{4.28}$$

from which z may be obtained by integration. We now consider some specific cases of this equation.

1. P(r) = 0

If the arc and hydrostatic pressures balance then u(r) = 0 and

$$z' = \frac{c}{\sqrt{(r^2-c^2)}}$$

If c = 0 the solution is z = constant. This corresponds to a flat weld pool, and is of little interest. However, if c ≠ 0 then the solution is

$$z = c\cosh^{-1}\left(\frac{r}{c}\right)+d$$

where d is another constant of integration. Rearranging to make r the dependent variable:

$$r = c\cosh\left(\frac{z-d}{c}\right)$$

This is the equation of a catenary. Catenaries are familiar from many natural situations. The analogy appropriate for this particular example would be a soap film drawn between two coaxial wire loops (see Figure 4.21). This solution is of fundamental importance to the discussion because it represents a stable keyhole surface, although admittedly under quite artificial conditions.

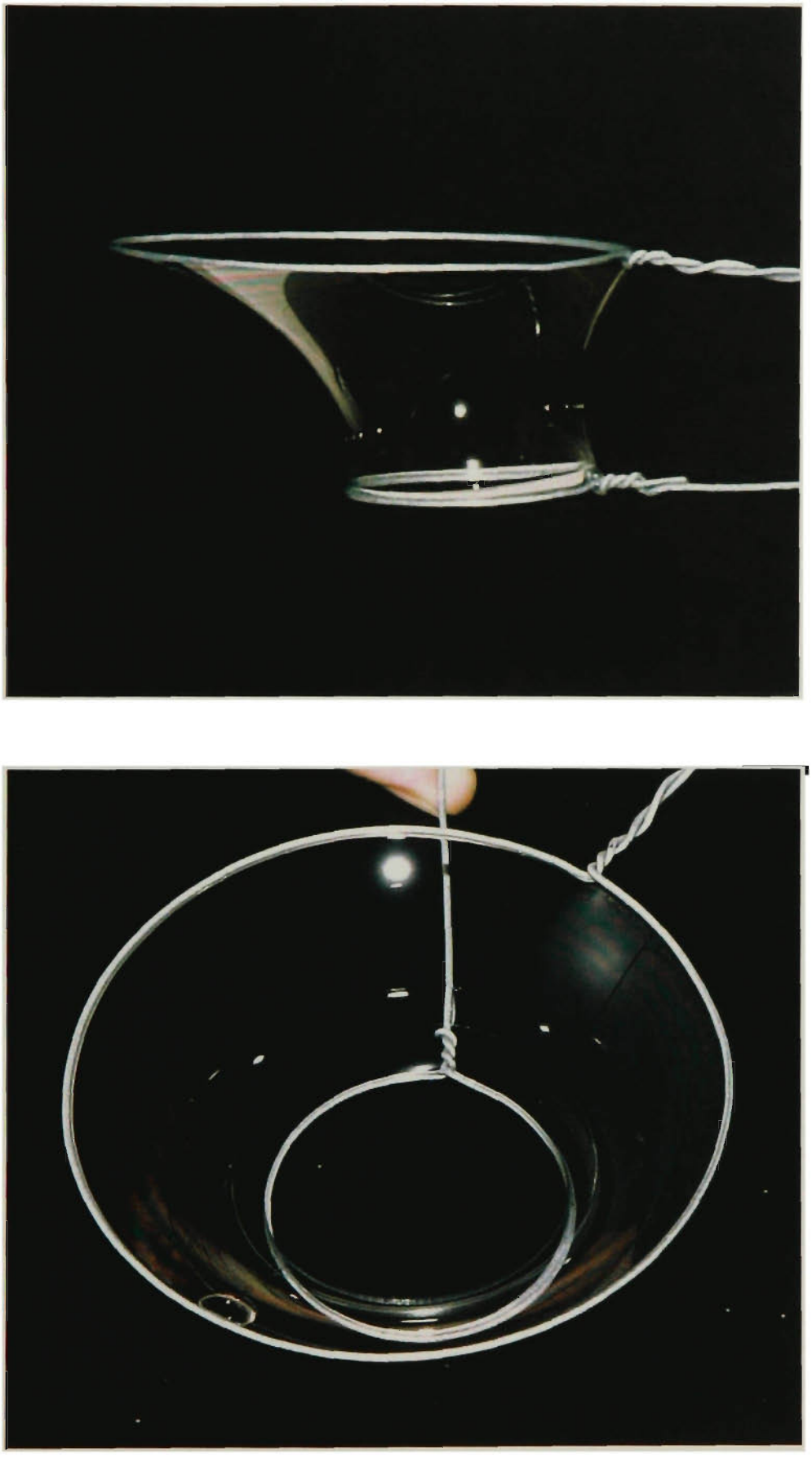

Figure 4.21. Soap and water films drawn to form minimal surfaces to illustrate the source of GTAW keyhole stability.

Case 2. $P(r) = \alpha(R^2 - r^2)$

This choice of arc pressure distribution corresponds to that used in Section 4.2.5 (4.19). In that discussion use was made of the variable $\sin\theta$, which was defined from Figure 4.14. The variable $\sin\theta$ can also be expressed in terms of differentials:

$$\sin\theta = \frac{dz}{\sqrt{dr^2 + dz^2}}$$

$$= \frac{dz}{dr\sqrt{1+\left(\frac{dz}{dr}\right)^2}}$$

$$= \frac{z'}{\sqrt{1+z'^2}} \qquad (4.29)$$

Substitution of this variable into (4.27), conducting the integral there indicated and dividing through by r gives the equation

$$\sin\theta = \frac{\alpha}{4\gamma}\left(2rR^2 - r^3\right) + \frac{c}{r} \qquad (4.30)$$

where a and c are constants. This is (4.20) with the added term c/r. The reason for the absence of the c/r term in the earlier model was the restriction to the melt-in mode puddle. For that situation the surface must pass through r=0, and symmetry demands that at that position $\sin\theta = 0$. This boundary condition is only satisfied by setting $c = 0$. Consequently the melt-in mode crater (4.20) is a special case of (4.30), and is only one of the possible solutions.

The melt-in mode solution may be determined by setting $c = 0$ in (4.28). First one must determine u(r):

$$u(r) = \frac{1}{\gamma}\int rP(r)\,dr$$

$$= \frac{\alpha}{4\gamma}\left(2r^2R^2 - r^4\right)$$

and then substitute into (4.28). Putting a = (α/4γ),

$$z' = \frac{a(2rR^2 - r^3)}{\sqrt{1+a^2(2rR^2 - r^3)}} \qquad (4.31)$$

This can be solved numerically to give the result obtained previously. As expected:

$$z' \to \infty \qquad as \qquad a^2(2rR^2 - r^3) \to 1$$

and

$$z' = \max \qquad when \quad r = \sqrt{\frac{2}{3}}R$$

4.3.5. Numerical verification

It is now quite clear that solutions to (4.26) include 'keyhole' topologies. However, it remains to be shown that such solutions can occur for the parameter values likely under welding conditions. In order to accomplish this (4.26′) should be presented in a more convenient form for numerical solution, and typical values for the relevant parameters must be estimated.

Recalling (4.26′):

$$\frac{\gamma}{r}\frac{d}{dz}\left(\frac{rr'}{\sqrt{1+r'^2}}\right) - \frac{\gamma}{r}\sqrt{1+r'^2} - \rho g z - P_a(r,z) = 0$$

This can be rearranged to read:

$$\frac{rr' - r'^2 - 1}{r(1+r'^2)^{3/2}} - \frac{\rho g}{\gamma}\left(z + \frac{P_a(r,z)}{\rho g}\right) = 0$$

The term $P_a/\rho g$ will be denoted as W(r,z). W(r,z) has the dimensions of length, (ie the pressure is given in terms of depth of liquid metal) and one would expect that if the plate has a thickness G then the maximum value of W will be of the order of G.

Given the dimensions of the observed keyholes it will be convenient to specify parameter values in the CGS system. The following values are typical:

γ	=	10^3 dynes/cm
ρ	=	7 g/cm^3
g	=	980 cm/s^2
r	~	0 to 1
z	~	0 to 1
G	~	1
W(r,z)	~	0 to 1

Using these values the term $\rho g/\gamma$ would have a value of 6.86. As an illustration, if the arc pressure has a parabolic distribution, with a value equal to 1 cm of liquid metal on the axis and zero at 1cm radius, then

$$W(r,z) = 1 - r^2$$

And the equation to be solved would be

$$\frac{rr' - r'^2 - 1}{r(1+r'^2)^{3/2}} - 6.86(z + 1 - r^2) = 0$$

Numerical solutions for a variety of pressure distributions and choices of material properties are presented in Figures 4.22 to 4.25.

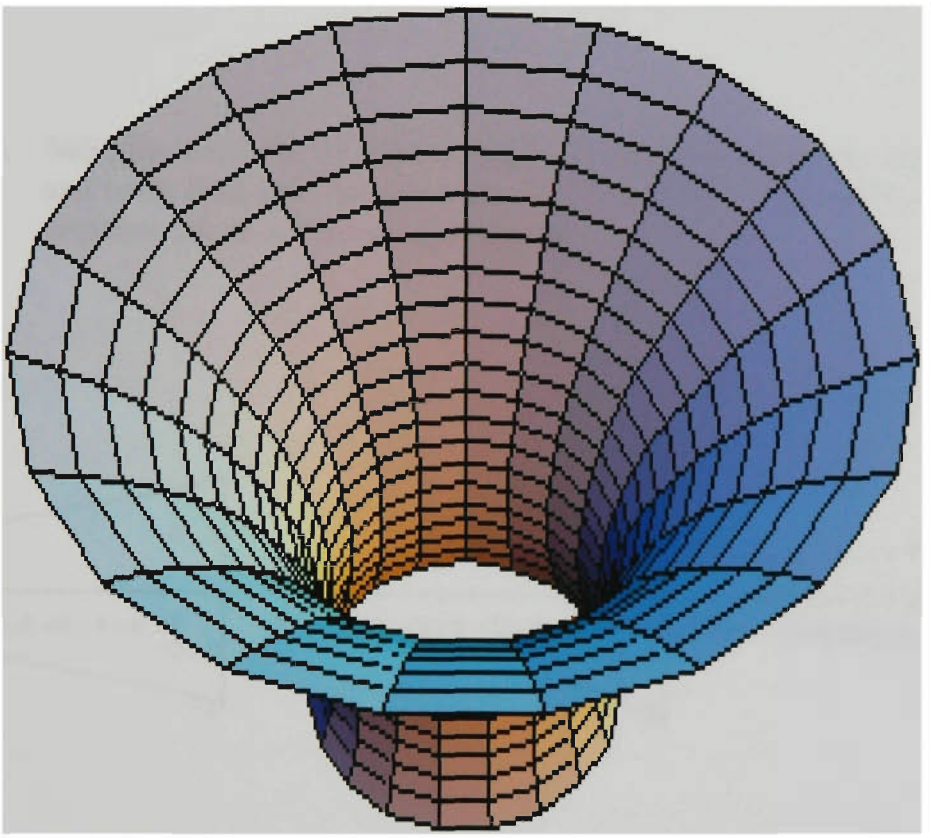

Figure 4.22. A cartenoid. This is an example of a minimal surface, and represents the principles of the GTAW keyhole stability. It would only be realised in a stationary keyhole if the arc pressure were such as to balance the hydrostatic pressure over the depth of the keyhole.

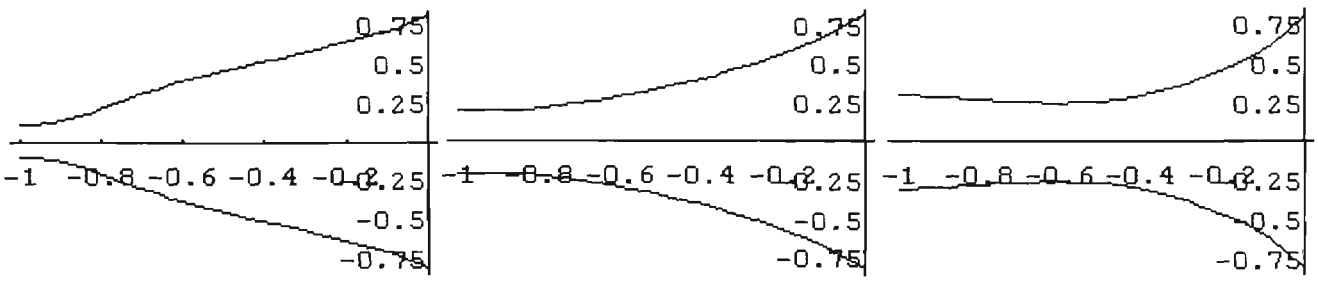

Figure 4.23. Solutions to (4.26) for 10mm stainless steel. Root openings 2mm, 4mm and 6mm diameter. Arc pressure = 0.5 P_0 (1/ (r^2 + 0.1), where P_0 is the pressure due to 10mm of liquid metal.

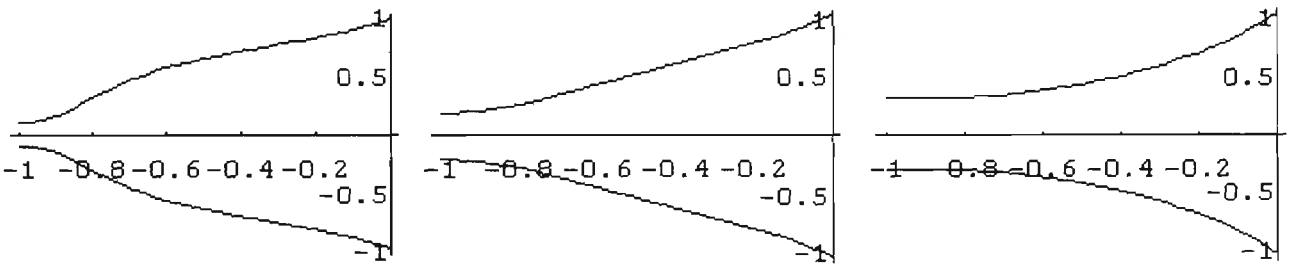

Figure 4.24. Solutions to (4.26) for 10mm stainless steel. Root openings 2mm, 4mm and 6mm diameter. Arc pressure = P_0 (1/ (r^2 + 0.1), where P_0 is the pressure due to 10mm of liquid metal (compare with Figure 4.23)

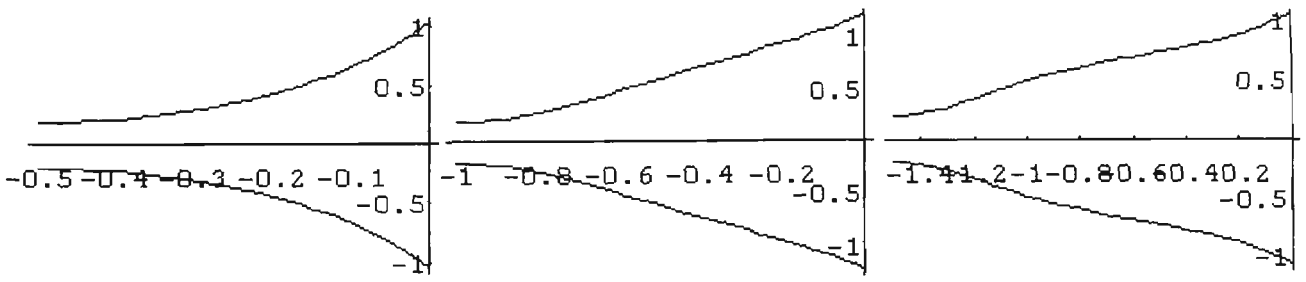

Figure 4.25. Solutions to (4.26) for 5, 10 and 15mm titanium. Root openings are all 4mm diameter. Arc pressure = P_0 (1/ (r^2 + 0.1), where P_0 is the pressure due to the plate depth of liquid metal.

The examples presented in the figures (Figures 4.22 to 4.25) serve to illustrate the plausibility of keyhole solutions. There is clearly much more that needs to be done before such solutions can be presented as realistic approximations to actual physical situations. Nevertheless, it is encouraging to find that keyhole solutions do appear to exist over a broad range of conditions, and particularly, that these conditions are within the anticipated range of the welding conditions under consideration.

An obvious issue to be addressed is the choice of boundary conditions. In the examples presented the choice has been to set the walls to vertical (r'(z) to zero) at the root face. This is not unrealistic because the temperature gradient will also be approximately perpendicular to the root face. More importantly, this is a good approximation to the reality, especially for thicker plates. Similarly the width of the opening is not known precisely, but the radius is typically between one and two millimetres in welding samples.

Another critical factor is to provide a convincing estimate of the arc pressure acting over the surface. In Chapter 5 arc pressure will be discussed in some detail. The important point to be made here, however, is that the arc pressure has two components. The first of these is a static pressure due to magnetic compression. The second is a dynamic pressure associated with the flow of the gases. This second term is realised when the flow is halted, or at least changed in some way (hence the term stagnation pressure). It is evident then that although its maximum value might be specified independently of the pool, the resultant pressure exerted on the pool surface is strongly coupled to the surface geometry. All that can be stateed here is that keyhole solutions occur even when the applied arc pressure is allowed to vary significantly. Further work is required in this area, but while it is anticipated that this would be very useful in developing a much deeper understanding of the pool surface, it is not expected that it would compromise the results already presented. The particular benefits of such a study may well be in a much-improved understanding of the transition between the deep penetrating non-keyhole, and the fully penetrating keyhole, states. The issue of this transition will be taken up again in the next section, and also in Chapter 6.

4.3.6. Moving weld pools

Any practical model of the weld pool surface must include the effects of travel speed. Since the progression of the puddle involves continuous energy and fluid flow through it the system is assumed to tend to a steady state and not a true equilibrium. A first step towards describing this situation is to reconsider the generation of a deficit.

The following terminology will be used when necessary. The crater intersects the front and possibly the root faces of the plate forming two closed curves μ and λ respectively. Physically μ and λ are the rims of the weld pool. It is common in welding discussions to resolve regions of the pool and its boundaries into 'leading' and 'trailing' portions. Loosely, the dividing line corresponds to the maximum width of the appropriate boundary. Leading edges and faces are then associated with the fusion front, whereas the trailing edge constitutes a solidification front. The subscripts 'l' or 't' will be used to identify the respective region when required.

As the arc moves forward parent metal melts and enters the weld pool at the leading face of the cavity, and solidifies into the trailing weld bead. In order to maintain a steady state the rate at which material enters the pool must equal the rate at which it is frozen into the weld bead. If these two rates differ over some time interval then the deficit will change, and therefore so will the weld bead cross sectional area. A very common example of this is seen at the beginning of any high current GTAW weld pass because the deficit begins as zero, and increases over the initial section of the weld. During this interval the metal transferred to the weld bead must be greater than that entering the pool, and hence the bead will have excess reinforcement. Similarly if the deficit reduces at some position the resulting reinforcement will also be reduced until the correction is completed.

It is inevitable that there will be some level of fluctuation between fusion and freezing rates and hence deficit, even for constant welding conditions. However, to maintain a steady state the deficit must return to a constant value when averaged over these random fluctuations. This raises the issue of a mechanism to restore the deficit to a particular value.

Consider the curves μ and λ formed between the liquid surface and the plate faces. The vertical positions of μ_l and λ_l are fixed by the plate surfaces, and therefore cannot change. However, μ_t and λ_t do have some freedom to move over time. This freedom is provided by the continuous reconstruction of these boundaries by the solidification of fresh material. In other words the bead profile can change because the solidification front is moving into a liquid rather than solid medium.

If the trailing edge of the pool intersects the surface at a non-zero angle (measured in the direction of motion) then the rate of solidification will be affected. It will increase if the adjacent liquid rises above the rim and decrease if it falls away. This constitutes a negative feedback that acts to maintain the surface in the vicinity of the rim level with the weld bead. The mechanism therefore regulates the deficit. It is important to realise that this mechanism operates only in the direction of welding (ie the x-axis). The angle at which the surface meets the rim, measured in the y-direction and relative to the plane of the plate, can remain non-zero because the solidification front has no component of motion in the y-direction. This allows the transverse profile of the bead to be curved. In summary, for steady state conditions the pool surface at the trailing edge is always tangent to the adjacent solidified metal, regardless of the direction of measurement. Moreover, this tangent is parallel to the plate surface when taken in the welding direction.

In a steady state condition the internal fluid pressure must drive the fluid to the rear of the pool and support the trailing surface at the level required for a uniform solidification rate. Furthermore, the flow must exactly match the fusion rate. Since the flow must overcome viscous, inertial and gravitational forces the pressure in the leading portion of the pool must be greater than it is in the trailing region. Any fluctuations from this steady state condition will be reflected in the deficit and frozen into the weld bead as ripples or other irregularities.

4.3.7. The effects of flow on the surfaces

Equations (4.21) and (4.22) were generated with the assumption of no flow. Consequently the pressures due to surface curvature and arc forces were balanced

against hydrostatic pressure (ie ρgh) alone. However, since the liquid metal must flow around the keyhole if the weld is to progress along the plate, the eventual consideration of flow is inevitable.

Fluid flow in welding is usually modelled numerically, beginning with an appropriate set of differential equations and sufficient boundary conditions to mathematically define the system. For example, the equations would include conservation of mass (continuity) conservation of momentum (Navier-Stokes), conservation of energy and possibly conservation of charge. Solutions then involve the determination of numerical representations that simultaneously satisfy these equations and the various boundary conditions. The form of the Navier-Stokes equation hints at the complexity of this task:

$$\rho\frac{dv}{dt} = -\nabla P + (\nabla \cdot \eta\nabla)v + J \times B + \rho g$$

(η is the fluid viscosity and v is its velocity). If viscosity is treated as a constant the equation would be

$$\rho\frac{dv}{dt} = -\nabla P + \eta\nabla^2 v + J \times B + \rho g$$

This equation cannot be solved without also determining the current distribution in the arc and the metal, the shape of the fusion surface, and so on. The important point for this discussion however, is that this equation includes a pressure gradient, ∇P, in addition to hydrostatic pressure. The impact for the present description of the surface is that the hydrostatic term ρgh generally will not represent the pressure in the liquid, and hence application the surface equations in their current form will not guarantee a zero pressure change across the surface. Clearly the solution to this is to replace the hydrostatic term with the total pressure in the liquid at the surface, P_{NS}. The 'NS' subscript has been included to indicate that this term is obtained from the solution of the Navier-Stokes equation. The equation describing the surface with fluid flow is then

$$\gamma K - P_{NS} - P_a = 0 \qquad (4.32)$$

This cannot be solved independently of the Navier-Stokes equation, and vis-a-versa.

Some appreciation for the dynamics of this relationship can be gained by considering just two mechanisms through which the passage of the arc induces flow in the liquid metal.

Progression of the fusion/solidification surface

Let the solution for the surface that gives a minimum energy for no flow of material serve as a reference. Now suppose the fusion front (ie the cavity) is incremented in the welding direction. If the liquid surface were to remain stationary with respect to the plate then its overall geometry would change due to the inclusion of formerly solid surface at the leading edge, and loss of previously liquid surface at the trailing edge. This would increase the surface energy because the original surface was at an energy minimum. This energy change would induce a restoring force ($F = -\nabla E$) that would be manifest as a pressure differential. This in turn would then give rise to a material flow. In other words the surface energy of the pool stiffens the surface and causes it to hold its shape and position relative to the moving weld pool rims, μ and λ. It is interesting that this driving mechanism operates independently of and in addition to arc forces and surface tension gradients. Arc forces and surface tension gradients are well-known contributors to liquid metal flow.

Displacement of the arc

The arc may also contribute to an asymmetry in the pressure distribution over the surface. Given that the arc is localised in space the pressure distribution must have a radial dependence. It follows that a simple displacement between the arc and pool axes could increase the arc pressure over the leading surface. In fact it is an intuitive expectation that the arc will encroach upon the leading edge as the travel speed increases, effectively squeezing the liquid metal against the still-solid face. This is what happens when the necessary adjustment in surface curvature is prevented by the cavity wall. Since the arc is not a rigid structure the reaction will deflect it towards the

trailing edge. This is exactly what is observed in practice (as shown in the opening photograph of this thesis, for example). For keyhole welding the angle and stability of the efflux plasma may be used as a gauge of the process performance.

4.3.8. Numerical simulation of the process

At the present time the practical execution of a numerical model of this process would be very challenging. The difficulties arise in a variety of areas. For example, the fact that the problem deals with a free surface is already difficult to treat, especially when the curvatures are significant (Mendez and Eagar 1998). It is obvious from the discussions already presented that surface curvature plays a crucial role in the stability and the dynamics of the process. However, the real difficulty results from the extensive, strong couplings that exist between the various quantities involved in the process. The interaction between the surface curvature and the fluid flow has already been highlighted. Moreover, Choo et al (Choo, Szekely and Westhoff, 1990) have shown that even moderate surface deformation impacts on the current and heat flux distributions, and cannot be modelled independently of the arc. This is further compounded by the knowledge that the surface tension and viscosity are temperature dependent, and the finding of Choo et al and Mendez and Eagar that plasma shear is likely to be the dominating force in high current GTAW processes. Finally, Mendez has also shown that the layer of liquid metal in the leading portion of high current GTAW cavities can be very thin, and this introduces a massive degree of asymmetry in the flow characteristics that cannot be captured in stationary models. In short, the problem cannot be reasonably reduced into smaller components but must be solved in its entirety. This implies a 3-D model incorporating the arc, moving weld pool, and a highly curved free surface.

4.4. Keyholes from a geometric perspective

4.4.1. Surface types.

The surface of a keyhole differs fundamentally from that of a melt-in mode weld pool because it has a hole through it, in much the fashion of a 'doughnut'. This reference to

an obvious topological distinction introduces a geometric perspective that may yield further insight into this welding process. Such topological transitions are not normally encountered in other arc welding processes.

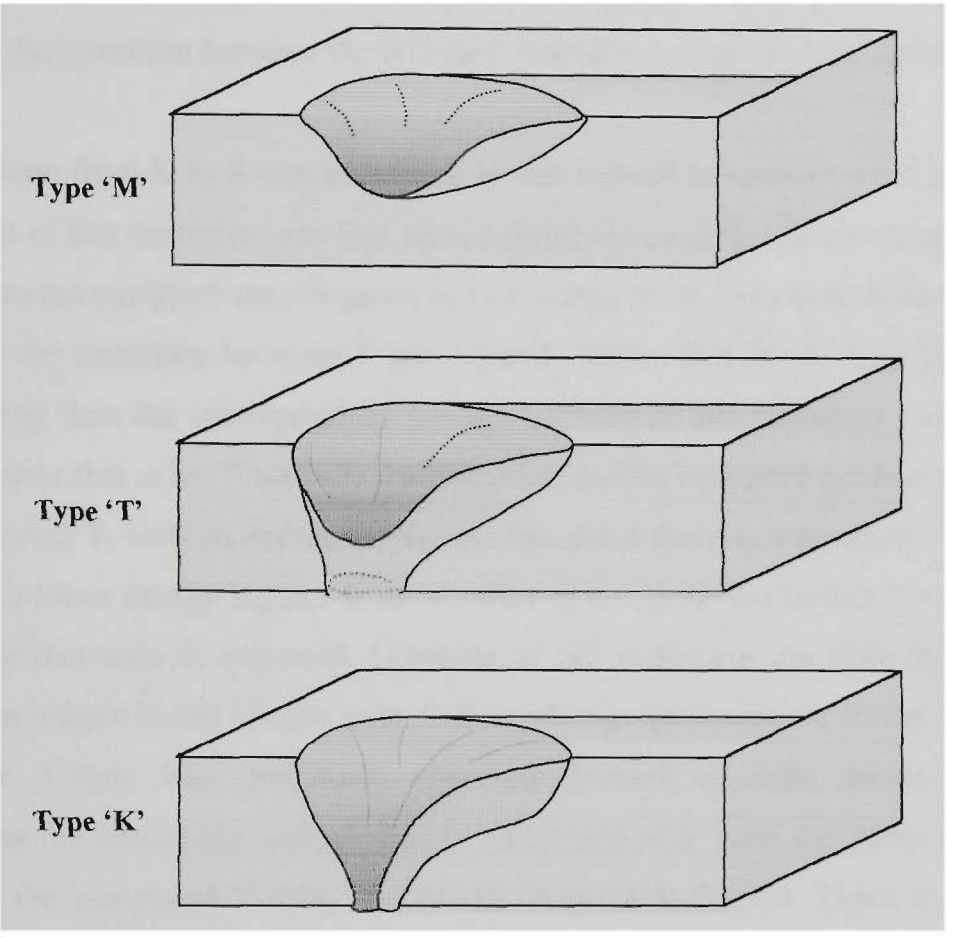

Figure 4.26. Illustration of three surface topologies that can occur during high current GTAW.

Weld pool surfaces can take different forms, such as a simple depression or an open keyhole. To distinguish these a simple depression associated with melt-in mode welding will be identified as a type 'M', while an open keyhole will be a type 'K' surface. The unzipped surface discussed previously constitutes another class, type 'Z'. It is anticipated that a keyhole will develop from an M surface as the current increases, possibly passing through an intermediate, fully penetrating state where there are unconnected liquid surfaces on both the front and root faces. This will be identified as a type 'T' surface. 'M', 'K' and 'T' surfaces are illustrated in Figure 4.26.

4.4.2. Transitions and hysteresis

Since the various pool surfaces are free surfaces their respective energies will be at local minima. As more energy is added a pool will expand in a more or less predictable way that might be calculated by standard mathematical techniques. However, the transition between the different geometries is much more interesting.

The transition from K to Z was examined in some detail in sections 4.1.7 and 4.1.8. One aspect of this transition was that once a threshold condition was reached and the transition to the unzipped state began it went to completion. This same behaviour also applies to the transition between T and K, and implies that the K-state provided a lower energy than the corresponding T-state. Looking at this transition sequentially, the conditions that drive T towards the transition can be increased gradually to some threshold level T_t with an energy $E_T(T_t)$. At this point there is a transition to the K-state with a lower energy $E_K(K_t)$. If the conditions are increased further the energy of the K-state increases as expected. However, if the conditions are now reduced the system can remain in the K-state even if the welding conditions are in the regions in which the T-state was previously observed. Indeed, if there are no random fluctuations the conditions will need to be decreased to at least the point where the energy of the associated T-state, E_T, would be equal to $E_K(K_t)$. There is even the possibility that the K-state may remain stable as the conditions are driven further from the threshold T_t. This is because the surface distortions follow different paths in evolving from T to K, and K to T, with each path presenting its own energy barrier. This is illustrated in Figure 4.27.

What is being described is hysteresis, where the conditions required to produce a transition in one direction differ to those required for the reverse transition. The primary requirement for hysteresis is that two alternative states or surface configurations are possible under the same set of welding input conditions. It is then possible to have the system remain in a higher 'meta-stable' state until an appropriate trigger is provided. The trigger could be a particular mode of surface vibration, or fluctuation in input conditions, for example.

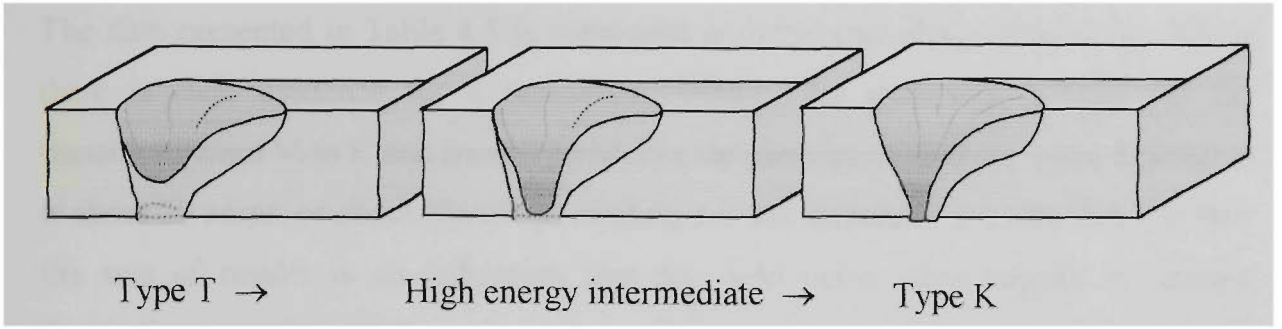

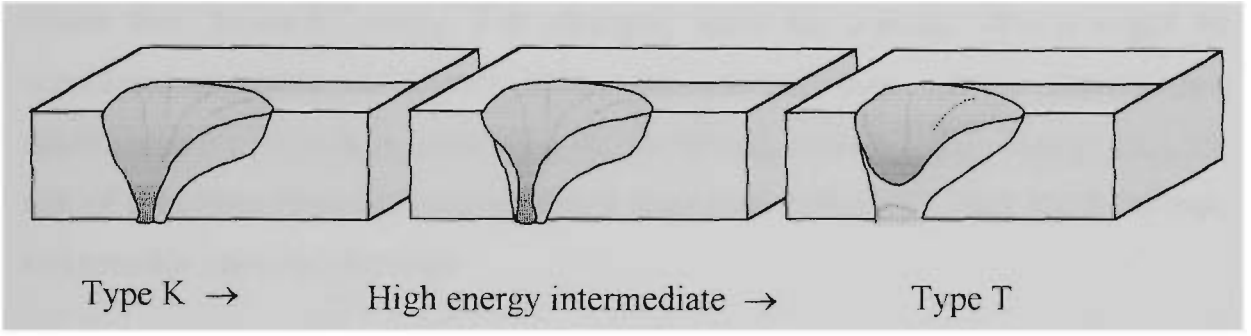

Figure 4.27. Illustration of how surface transformations may be separated by higher energy intermediate states

4.4.3. Hysteresis in the M-K transition

Hysteresis has been observed in the transitions between melt-in and keyhole modes in the keyhole GTAW process. For example, during the course of experiments designed to examine some aspects of the efflux plasma, the threshold currents (for the transitions M-K and K-M) were measured. Results are presented in Table 4.3. Each weld was made on 6mm AISI 304 stainless steel plate using an Ar-5H shielding gas and a welding speed of 450mm/minute. Significant features of the experimental conditions were that each set of determinations were made within single weld runs, and the welding conditions included constant arc length, as opposed to constant voltage. (This latter condition was a consequence of the equipment used and invalidated comparisons of the absolute threshold levels for the different electrode geometries reported elsewhere). In practical welding applications control of arc length can be provided by mechanical means, and although far less precise than arc voltage control it is more reliable and easier to implement.

The data presented in Table 4.5 is consistent with the preceding discussions. Firstly there is clear evidence for a separation between the threshold currents for the transitions from M to K and from K to M. For the conditions used the mean difference is about 20 amps, or about 5% of the welding current. Secondly, the variability within the sets of results is an indication that the weld pools were subject to random fluctuations capable of triggering the transitions. Practical implications are that the keyhole mode welding current should be established with due care to avoid operation within this 'bi-stable' range. For example, there are reasons why it might be considered desirable to operate below the true threshold current (having first establishing the keyhole by exceeding the threshold). However, this strategy runs the risk of a random disturbance triggering a transition to the then more stable M-state and possibly rejecting the weld.

Table 4.5. Examples of threshold currents for transitions between melt-in and keyhole modes.

Tip angle *(2θ°)*	**Sequential threshold currents** *(amps)*						**Av. Threshold** *(amps)*	
	M→K	K→M	M→K	K→M	M→K	K→M	M→K	K→M
20	360	360	365	345			363	353
30	360	360	360	350	360	340	360	350
40	350	320	345	320			348	320
50	350	320	360				355	320
60	370	345	375	345			373	345
70	380	375					380	375
80	400	390	430				415	390

4.4.4. More surfaces and porosity

The recognition of M, T and K surfaces raises the possibility of surfaces with more than one opening. It turns out that this may be possible. One example is the formation of certain types of porosity. Given that a K-type surface can be of lower energy than an M-type, it is plausible that an opening could be made through the liquid to the cavity, and be stabilised by its subsequent 'freezing-in'. This possibility is illustrated for an M-type surface in Figure 4.28. The resultant surface is almost identical to a K-type surface. There is no apparent reason why this cannot occur for keyhole surfaces

as well. In fact elongated gas pores have been observed in some keyhole welds on pipe. This issue is important because it offers a mechanism whereby pores developing in the weld pool can be stabilised and incorporated into the weld metal.

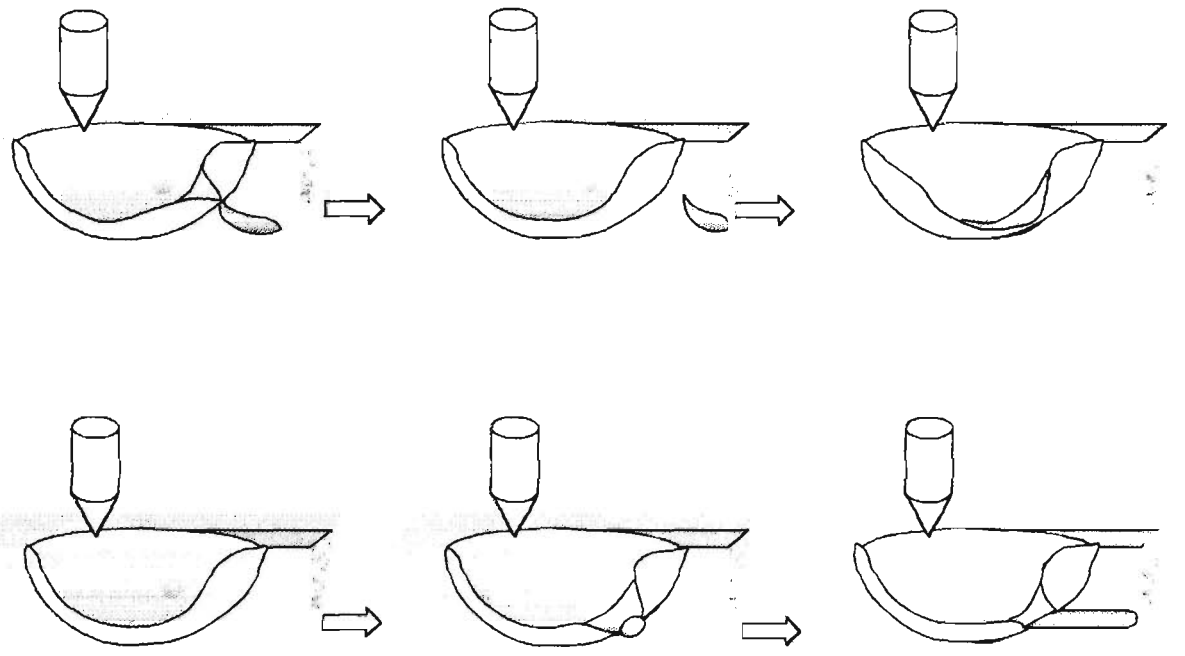

Figure 4.28. Illustration of a speculative unstable transition from an M-type surface to one generating worm holes (upper) and to a stable state generating tunnel porosity (lower).

4.4.5. Undercut

A frequently encountered limitation for many welding processes is the onset of undercut at the edges of the weld bead. This also might be a natural consequence of surface geometry.

In an earlier discussion it was argued that the net force exerted on the pool surface must be supported by the generation of a non-zero contact angle around the pool boundary. This force has a maximum value (per unit length) when the surface is perpendicular to the face of the plate. It has also been argued (4.3.1) that the bead profile cannot change in response to the y-component of the contact angle. The

resultant bead profile therefore is a projection of the contact angle around the trailing edge of the pool. However, the angle made between the plate and pool surfaces at the point where the pool reaches its maximum width is particularly significant because this is the angle the resultant bead makes with the plate. The pool surface need not be tangent to the adjacent material at this point because that metal had not solidified from the pool.

It might be supposed that the weld bead would always make a 'negative' angle to the plate since the pool surface is initially depressed. Fortunately this is not the case, and there are several reasons for this. These include the possible addition of filler material, and transverse shrinkage of the joint, which both increase the effective volume of material available to fill the cavity. However, the most significant factor is that the maximum width of the pool usually occurs behind the arc (see Figure 4.12). It can only be presumed that this 'delayed' widening is due to the convective transfer of heat from the arc to the tail of the pool via the superheated liquid metal. As this effect weakens and fails the contact angle can be expected to become increasingly negative as it reflects conditions closer to the arc. It is entirely possible for this angle to equal 90°, giving rise to the undercut defect.

This scenario is supported by macrographs of various weld beads. It is quite normal for keyhole GTAW cross-sections to give the impression of having resulted from two, as opposed to a single, weld pass. Effectively the superheated liquid being pumped into the tail of the pool acts as a second heat source. As the visible evidence for this mechanism decreases the conditions required for undercut are being approached.

The solution to undercut is therefore to increase the heat deposited into the tail of the pool to the extent required to ensure that the maximum pool width occurs in an area where the pool surface is relatively undistorted. This leads into considerations of heat flow, a topic dealt with in Chapter 7.

5. Displacement forces in GTAW.

5.1. A mathematical model for arc forces.

5.1.1. Arc force fundamentals.

The preceding discussions, particularly within the literature review, suggest that an arc force rather than recoil pressure is responsible for the initial formation of the GTAW keyhole. An analysis of this force is therefore a necessary component in developing an understanding of the process.

As the welding current in GTAW is increased there is a progressive displacement of the weld pool from the arc impingement area. The weld pool displacement is associated with the 'strength' of the arc, and is the result of an 'arc force' (see Figure 5.1). Correspondingly, the distribution of the arc force over the pool surface is expressed in terms of 'arc pressure'. These two qualitative descriptions are tentatively presented as initial definitions of arc force and arc pressure, respectively.

Surface depression in GTAW becomes significant when the welding current exceeds about 250 amps, at least when argon is the shielding gas (Lin and Eagar 1985 and Section 4.2). The development of this depression, or crater, could be used to define the transition from the conventional to the 'high current' GTAW regime. Alternate names for the high current regime include buried arc, sub-surface arc and immersed arc GTAW (Adonyi et al, 1992).

Goryachev and Zelenin (1964) appear to have been the first to exploit the arc-induced pool displacement in the form of a high current GTAW process. However, within a year Liptak had used it successfully to weld aluminium plate up to 32 mm thick (Liptak 1965). Since these early reports the process has been improved and applied to various other materials, including stainless and low alloy steels, and magnesium alloys (Nesterov et al 1987). Unfortunately the application of high current GTAW has been limited by the need for accurate control of the welding conditions. This need arises because the weld quality is highly sensitive to the magnitude and distribution of the arc

force, and these characteristics can only be controlled indirectly by virtue of their coupling to other process parameters.

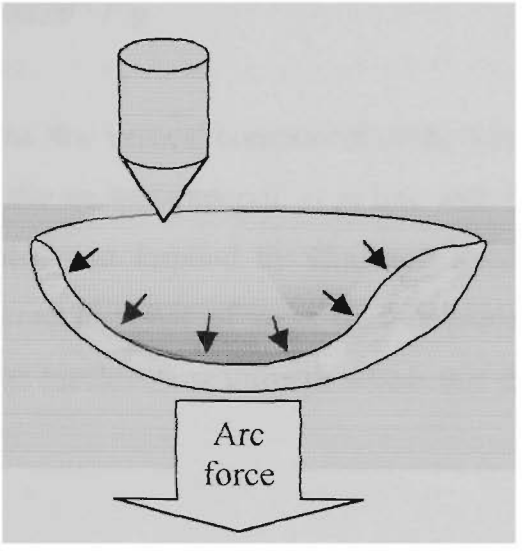

Figure 5.1. Arc force equals the vertical component of the force required to generate the pool displacement.

It is immediately evidently that the arc force is dependent on the magnitude of the welding current. Indeed, dimensional arguments can be used to show that arc force must vary with the square of the current, given the assumption that it derives from electromagnetic interactions (Viano et al, 1993). Alternatively, considering the magnitudes of the appropriate vectors only, one has

$$F \propto IB$$

but

$$B \propto \mu I$$

hence

$$F \propto \mu I^2 = kI^2 \qquad (5.1)$$

where F is the arc force, μ is the magnetic permeability, I is current, B is the magnetic field strength, and k is a constant. In the following discussions it will be convenient to refer to forces in units of grams (g); it is to be understood that this means grams weight. A force of one gram (weight) is equal to approximately 9.8×10^{-3} N.

If arc forces are invoked to explain the weld pool displacements reported on in Section 4.2 then the vertical component, F, of this force must be of the order of

$$F \approx 3x10^{-5} I^2 g$$

The definition of the arc force as 'the vertical component of the force acting on the weld pool to cause displacement of the molten material' is in line with the definition offered by Choo et al (1990), and also that implied by Guu and Rokhlin (1992). Such a definition deals with the observable result of weld pool displacement, and does not distinguish between the various mechanisms through which this displacement may be brought about.

5.1.2. An historical perspective

Accurate measurements of the vertical forces on the weld pool are difficult to make because the welding current generates forces throughout the welding circuit, including within the weld pool and the surrounding plate. One approach that has been used widely has been to measure the force acting on the work piece during welding (F_{total}) and then to repeat the measurement at the same current but with the arc short-circuited (F_{sc}). This latter condition is achieved by arranging to have the electrode tip dipping into a puddle of liquid gallium that substitutes for the weld pool. The assumption is that the force exerted by the arc is equal to the difference between the two measurements.

$$F = F_{Total} - F_{sc} \tag{5.2}$$

This strategy has been challenged on numerous occasions. The first to do so was Erokhin (1979) after he had tried to reconcile the findings of over thirty separate research groups. He observed that short-circuit corrections introduced an unacceptable degree of inconsistency into the results, and proceeded to argue for a redefinition of arc force which included volumetric forces within the weld pool. An invalidation of the short-circuit correction technique would imply that the arc force was dependent on weld pool geometry

At about this time Savage et al (1979) postulated three separate components to the arc force: the electromagnetic (IxB) force, the plasma jet force, and the electron impingement force. Again, if all these components were significant, the short-circuit correction strategy would be invalid. As it happened, the group's resultant experimental data suggested a linear relationship between current and 'total arc force,' and contradicted the available theoretical and experimental evidence. Consequently when Burleigh and Eagar (1983) produced new data showing the expected quadratic dependence of force on current, and confirming in detail the earlier theoretical work of Converti (1981), many assumed that the question of measurement strategy had been resolved. Since Burleigh and Eagar had made use of short-circuit corrections the method was continued and used in defining arc force, even though those researchers had stressed their concern had only been with the plasma jet.

Burleigh and Eagar had been attempting to measure the stagnation force of the arc jet. This related to the accepted model of force balance within the cavity: "In GTAW the force generating the cavity is the stagnation pressure of the plasma jet, while the forces opposing this pressure are due to the hydrostatic pressure of the liquid and to surface tension" (Lancaster, 1986). This balance has been described mathematically as:

$$P_s = \frac{2\gamma}{R} + \rho g h$$

P_s being the stagnation pressure of the plasma jet, ρ the density of the liquid, γ its surface tension, h the depth of penetration and R the radius of curvature.

In 1990 Choo et al again raised arguments paralleling those of Erokhin (1979), suggesting that the pool shape may affect the nature of the arc, and vice-versa. They defined arc force as "the stress imposed upon the free [weld pool] surface to deform it."

Despite growing unease the practice of making short circuit corrections has continued (Adonyi et al, 1992; Guu and Roklin, 1992). However, inconsistencies have now become more evident, as highlighted by the work of Guu and Rokhlin (Guu and Roklin 1992, Roklin and Guu 1993). In their first paper (December 1992), they detailed

measurements of arc force, using short-circuit corrections. Yet more recently (August 1993) they concluded that the measured plasma jet force was only about 20% of what was required to explain the pool displacement, and that "... electromagnetic and hydrodynamic forces must be taken into account to explain the measured levels of surface depression".

The view adopted here is that the discrepancy between the measured arc forces and the pool displacement can be resolved because the experimental technique involving short-circuit corrections is flawed, as has been suggested by Erokin and Choo. For example, when Erokin argued against the use of short-circuit measurements he concluded that k should have a value of between about 3 and 6 x 10^{-5} I^2 grams. This is in line with the data presented for argon arcs in Table 4.4.

5.1.3. General formulation of a model of arc force

Arc forces result from Lorentz driven flow within the arc gases. The Lorentz force per unit volume is JxB + ρ_eE where J is current density, B the magnetic field strength, E the electric field strength, and ρ_e the charge density. Since ρ_e is zero almost everywhere within an arc, the Lorentz force will be entirely magnetically induced.

Each element of the arc fluid is accelerated in proportion to the net force acting on it:

$$\rho\frac{dv}{dt} \quad = \quad \rho\left(\frac{\partial v}{\partial t} + v\cdot\nabla v\right) \quad = \quad (\textit{net force per unit volume})$$

where ρ is the (incompressible) fluid density, v its velocity and t is time. The net force per unit volume in an arc will include the Lorentz term JxB, the pressure gradient - ∇P, and a 'diffusion' term that accounts for viscous damping, $\eta\nabla^2$ v. The resultant equation is a modified Navier Stokes equation for an incompressible fluid, and reads:

$$\rho\frac{\partial v}{\partial t} \quad = \quad -\rho v\cdot\nabla v - \nabla P + J\,x\,B + \eta\nabla^2 v \qquad (5.3)$$

Solving this equation for an arc is a formidable challenge since the parameters are strongly coupled, rendering the system non-linear. For example, an increase in current density in a selected region will increase the heat generated and therefore the local temperature. The temperature rise then generates changes in the plasma density, viscosity and electrical conductivity. These changes further affect the current distribution, completing the coupling. In general several different equations must be satisfied simultaneously, and numerical methods must be used for their solution. The work of Zhu, Lowke and Morrow (1992) provides a comprehensive treatment of this problem. For example, they argued that, in addition to the couplings mentioned above, the current density distribution at the cathode had a major influence on the resulting arc properties through its impact on convective flow. This dependency arises because the convective flow is driven by magnetic pinch pressure that in turn is a function of the current distribution, particularly at the cathode. Therefore a unified solution for a free burning arc must involve the simultaneous description of the cathode and cathode sheath behaviour as well as the arc itself. (See also the discussion in Section 4.3.6).

Such a detailed solution is not required for the present purposes. Rather, it is more appropriate first to seek an approximation that can serve as a practical tool for estimating the resultant forces on the weld pool without describing the local conditions within the arc. One way to address this requirement is to ignore viscosity, as did Converti (1981). The influence of viscosity will be noted subsequently.

5.1.4. The Converti model.

Converti (1981) treated the arc as a truncated cone with the welding current, I, flowing between the two ends, smaller radius R_e and larger radius R_a. This geometry is illustrated in Figure 5.2. With the assumption that the current density is constant over any chosen radial cross section, the net force normal to the larger end was found to be

$$F = \frac{\mu I^2}{8\pi}\left(1+2\ln\frac{R_a}{R_e}\right) \qquad (5.4)$$

If R_e is taken as the radius of the emitting area on the electrode tip, and R_a as the arc radius at the anode (ie weld pool), then R_a/R_e is known as the arc expansion ratio.

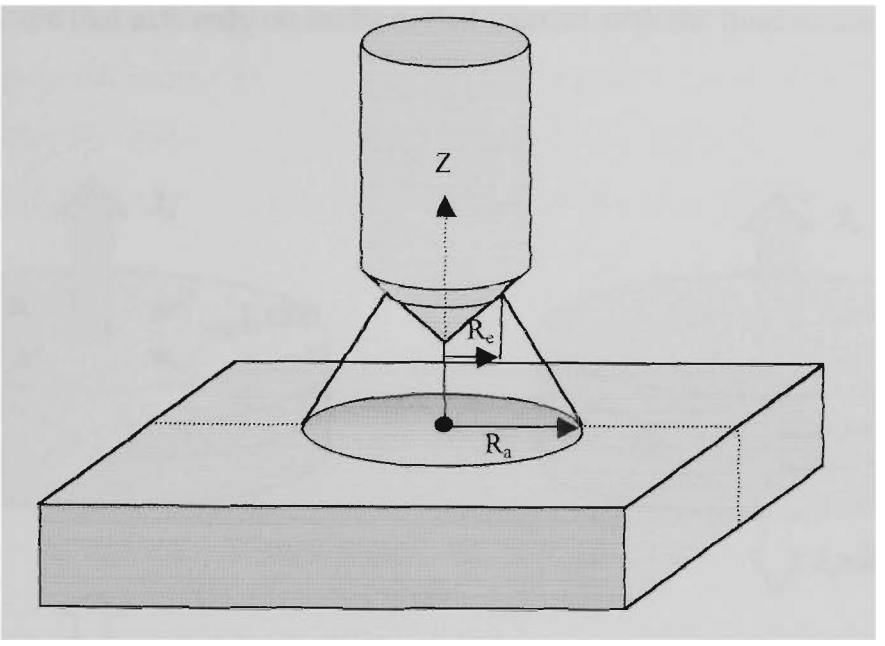

Figure 5.2 This schematic illustrates the geometry used in the Converti model.

5.1.5. Limitations of the Converti model.

The result obtained by Converti is important because it provides a means of estimating the magnitude of the arc force, and also identifies the main dependent variables. In particular, his model implies that the arc force can be affected either by changing the current or by changing the ratio R_a/R_e. Therefore, any influence that causes a change in either R_e or R_a at a given current must affect the resultant arc force. However, this result was determined for the idealised conditions of a uniform current density within a well-defined conical arc. It is important to know the sensitivity of his result to departures from these idealised conditions.

Converti identified two components contributing to the net arc force, both due to interactions between the arc current and its self-induced magnetic field. Current flowing through an arc generates a circumferential magnetic field, $B_\theta(r)$, perpendicular to both the axial and radial vectors. Consequently both axial and radial components of the arc current will interact with this field to give rise to forces. The axial component (J_z x B_θ) generates a compressive or pinch force while radial component (J_r x B_θ) results in an axially directed force. These two forces give rise to a radial pressure gradient and a fluid

flow (the plasma jet), respectively (see Figure 5.3). The fluid flow contributes a dynamic pressure that acts only on surfaces that interact with the fluid stream.

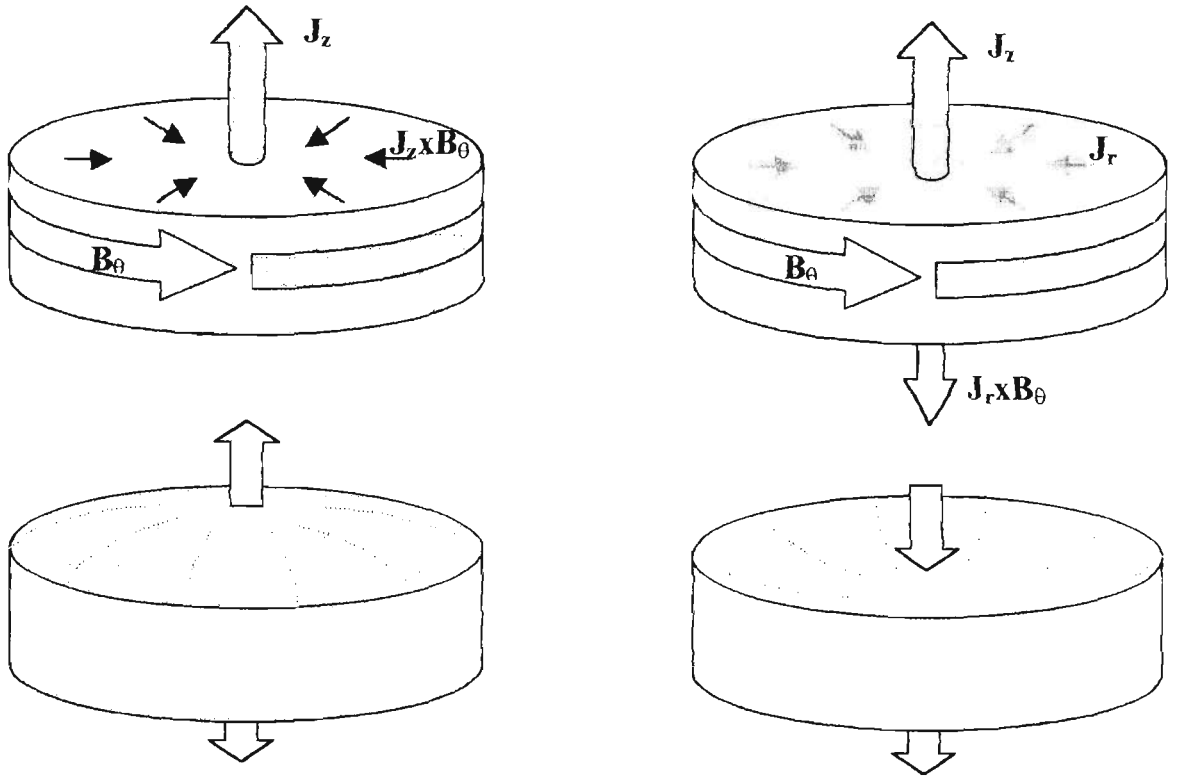

(a) J_zxB_θ radially pinches the plasma gas and squeezes it against the electrodes at each end of the arc.

(b) J_rxB_θ accelerates the plasma axially in the direction of reducing J_Z. This contributes a dynamic pressure, $\frac{1}{2}\rho v^2$.

Figure 5.3. These diagrams illustration the two electromagnetic interactions contributing to the arc force.

5.1.6. Force due to radial stress

When a current is passed through a conductor it interacts with its own magnetic field, subjecting the conductor to a compressive force or 'magnetic pinch'. In a fluid, such as the arc plasma, this radial stress must be balanced by an increase in internal pressure. It is this pressure acting over the surface of the weld pool that constitutes one component of the arc force (Figure 5.3(a)).

To quantify this component of the arc force consider a cross section through the arc, radius 'r', in a plane perpendicular to the arc axis. Allow this disc to be bounded by an annulus with a thickness 'dr' (see Figure 5.4). Further, assume that the current enclosed within the radius 'r' can be described by a differentiable function of the radius, say 'I(r)', and that the current flowing through the annulus is dI(r).

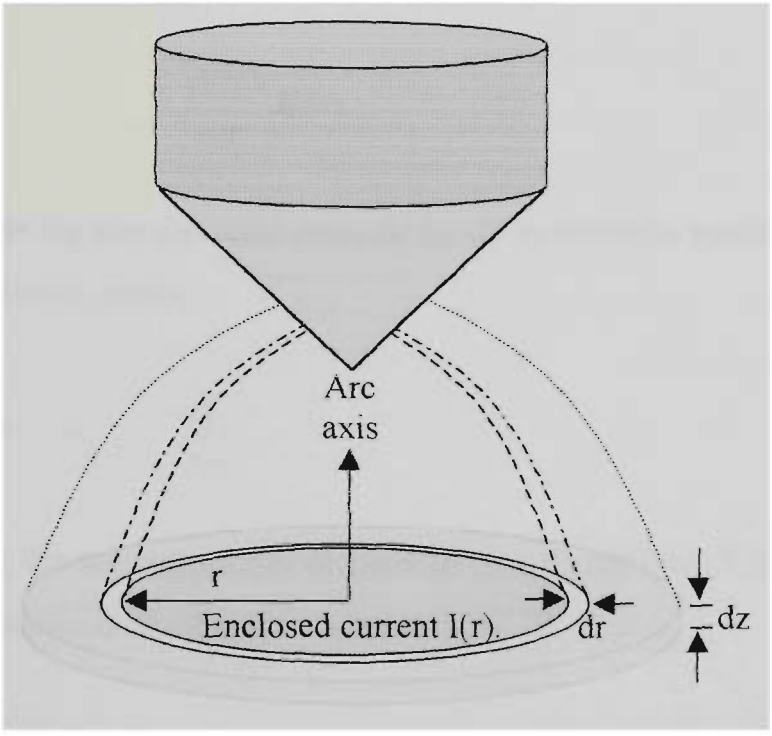

Figure 5.4. Schematic illustrating the parameters used in calculating the Lorentz forces in an arc.

The current flowing through the annulus is also given by its area ($2\pi rdr$) multiplied by the current density J(r). Since $2\pi rJ(r)dr$ can also be written as [dI(r)/dr]dr the current through the annular region can be expressed in any of the following ways:

$$dI(r) = \frac{dI(r)}{dr}dr = 2\pi rJ(r)dr$$

This axially-directed current interacts with the circumferential component of the magnetic field, $B_\theta(r)$, induced by the enclosed current I(r), to contribute an incremental compressive force df per unit height. This force df is directed radially towards the arc axis (see Figure 5.3(a)).

$$df = dI(r) x B_\theta(r)$$

where

$$B_\theta(r) = \frac{\mu I(r)}{2\pi r}$$

Since the current and the magnetic field are perpendicular,

$$df = \frac{\mu I(r)}{2\pi r} dI(r)$$

The pressure inside the annulus must increase by dP to maintain equilibrium against this added compression, where

$$dP = \frac{df}{2\pi r}$$

As a consequence, the net incremental increase dF in the total force F pressing on the face of the cross-sectional disc (eg the electrode) is $\pi r^2 dP$. That is

$$dF = \pi r^2 \, dP$$

$$= \frac{r}{2} df$$

The total (pinch) force pressing on a cross-sectional face is obtained by integrating dF over the current distribution:

$$F = \int_0^{I_0} \frac{\mu I(r)}{4\pi} dI(r)$$

whence

$$F = \frac{\mu I_0^2}{8\pi} \qquad (5.5)$$

This is the first term in Converti's expression for arc force. However, this derivation shows that this component of the arc force is independent of arc geometry and current distribution, provided both remain axially symmetric.

5.1.7. Force due to geometric divergence of current.

If the current within the arc is geometrically divergent it will have a radial component, I_r. This component will also interact with $B_\theta(r)$ to produce a force, $I_r \times B_\theta$, in the axial (z) direction. Since the magnetic field and the radial component of the current are perpendicular, the net force is the product of their respective magnitudes, and is parallel to the arc axis and in the direction of increasing arc radius. This force is balanced by the acceleration of the arc gases. The resultant pressure (stagnation pressure) acting over the electrode surface is dependent on the degree to which the surface impedes the flow.

Again assume an axially symmetric arc conducting a current I_0 enclosed by radius R_e at z = e and R_a at z = a. Consider two closely spaced surfaces, extending from the z=e to the z=a planes. Let these surfaces be symmetric about the z-axis, and everywhere aligned with the current flow. Because of these conditions any loop around the inner surface encloses a fixed current, I, and any loop around the outer surface encloses a similarly fixed current, I+dI. The separation between the surfaces is such that dI is infinitesimal. For convenience refer to the region bounded by these two surfaces as a shell. Then the strength of the magnetic field on the shell, at height z, is

$$B_\theta(r) = \frac{\mu I}{2\pi r(z)}$$

where r(z) is the radius of the shell at z. The radial component of the shell current is

$$dI_r = dI\left(\frac{dr(z)}{dz}\right)dz$$

The force exerted on this shell between z = e and z = a is then

$$dF = dI \int_{r(e)}^{r(a)} B_\theta(r)dr$$

$$= dI \int_{r(e)}^{r(a)} \frac{\mu I}{2\pi r} dr$$

$$dF = \frac{\mu I}{2\pi}(\ln r(a) - \ln r(e))dI$$

This equation indicates that the net increment in force is dependent on the enclosed current, and the radii of the shell at its ends. Since it is independent of the vertical profile of the shell, approximation by a truncated cone is unnecessary. The shell could equally well have the shape of a bell or hourglass, for example.

The total force due to the expansion is found by integrating dF over either I or r:

$$F = \int_0^{I_0} \frac{\mu I(r,a)}{2\pi} \ln r \, dr - \int_0^{I_0} \frac{\mu I(r,e)}{2\pi} \ln r \, dr$$

$$= \int_0^{R_a} \frac{\mu I(r,a)}{2\pi} \frac{dI(r,a)}{dr} \ln r \, dr - \int_0^{R_e} \frac{\mu I(r,e)}{2\pi} \frac{dI(r,e)}{dr} \ln r \, dr$$

This cannot be evaluated without knowing the current distributions at the anode and cathode emission region. However, attempting to integrate by parts gives

$$F = \frac{\mu}{4\pi} I^2(r,a) \ln r \Big|_0^{R_a} - \frac{\mu}{4\pi} \int_0^{R_a} \frac{I^2(r,a)}{r} dr$$

$$- \frac{\mu}{4\pi} I^2(r,e) \ln r \Big|_0^{R_e} + \frac{\mu}{4\pi} \int_0^{R_e} \frac{I^2(r,e)}{r} dr$$

Which, on evaluation gives

$$F = \frac{\mu I_0^2}{4\pi}\ln\left(\frac{R_a}{R_e}\right)+\int_0^{R_a}\frac{\mu I^2(r,e)}{4\pi r}dr-\int_0^{R_a}\frac{\mu I^2(r,a)}{4\pi r}dr \qquad (5.6)$$

Converti proposed that the net force on the weld pool is the sum of the $J_z x B_\theta$ and $J_r x B_\theta$ components (ie (5.5 and (5.6)). Therefore an arc of axial symmetry but otherwise arbitrary current distribution should generate an arc force of

$$F = \frac{\mu I_0^2}{8\pi}\left(1+2\ln\left(\frac{R_a}{R_e}\right)\right)+\int_0^{R_e}\frac{\mu I^2(r,e)}{4\pi r}dr-\int_0^{R_a}\frac{\mu I^2(r,a)}{4\pi r}dr \qquad (5.7)$$

5.1.8. The Converti model as a special case of (5.7)

Converti's model of an arc is a truncated cone with a uniform radial current distribution. This requires $I(r,e) = I_0(r/R_e)^2$, and $I(r,a) = I_0(r/R_a)^2$. These may be substituted into (5.7). However, it is readily seen that the integrals are equal:

$$\int_0^{R_e}\frac{\mu I^2(r,e)}{4\pi r}dr = \frac{\mu I_0^2}{4\pi R_e^4}\int_0^{R_e} r^3\,dr$$

$$= \frac{\mu I_0^2}{16\pi}$$

and

$$\int_0^{R_a}\frac{\mu I^2(r,a)}{4\pi r}dr = \frac{\mu I_0^2}{4\pi R_a^4}\int_0^{R_a} r^3\,dr$$

$$= \frac{\mu I_0^2}{16\pi}$$

Consequently the integral terms cancel, leaving Converti's result

$$F = \frac{\mu I_0^2}{8\pi}(1+2\ln\alpha)$$

Where α is the arc expansion ratio R_a/R_e.

5.1.9. Current redistribution due to surface depression at the anode

Of course there appears to be no imperative for the current density to be uniform over the arc impingement area. Indeed, there are some situations where the current density at the anode is relatively low, or even zero, on the arc axis. For example, during keyhole welding the metal along the arc axis is completely displaced, and hence the current density must go to zero. Off-axis peaks in current density have also been predicted to occur in melt-in mode GTAW when the pool surface becomes significantly distorted (Choo et al, 1990). These scenarios are illustrated in Figure 5.5.

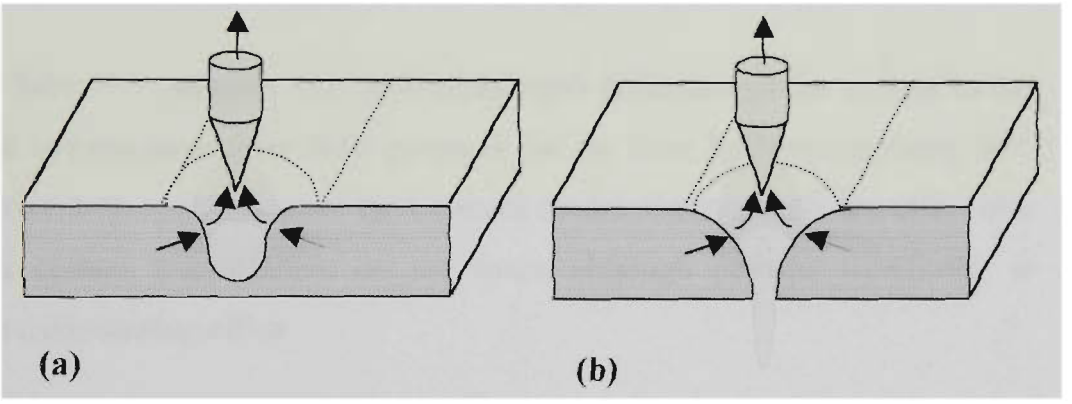

Figure 5.5. Schematic illustrating concentration of current at the rim of the arc impingement area for high current (a) and keyhole (b) GTAW pool surfaces. The arrows indicate current flow.

The consequences of a redistribution of current can be simulated by considering a current distribution of the form

$$I = I_0\left(\frac{r}{R_a}\right)^n \qquad for\ r \le R_a$$

If n = 2 then the current density is constant, as in the Converti model. However, if n is made larger the model describes a current distribution increasingly concentrated towards the boundary $r = R_a$. Assuming a constant current density over the cathode emission area, as before, and substituting in (5.7) gives

$$F = \frac{\mu I_0^2}{8\pi}(1+2\ln\alpha)+\frac{\mu I_0^2}{4\pi R_e^4}\int_0^{R_e} r^3\,dr-\frac{\mu I_0^2}{4\pi R_a^n}\int_0^{R_a} r^{n-1}\,dr$$

$$= \frac{\mu I_0^2}{8\pi}\left(1+\frac{1}{2}-\frac{1}{n}+2\ln\alpha\right)$$

As the current becomes increasingly concentrated at the periphery of the arc impingement area (that is n is made very large) the force approaches

$$F = \frac{\mu I_0^2}{8\pi}\left(\frac{3}{2}+2\ln\alpha\right) \qquad (5.8)$$

Reference to Table 5.1 indicates that such an extreme deflection of the current to the rim of the arc impingement zone only increases the arc force by between about 10% and 15% relative to the predictions of the Converti model. Consequently the effect of a more modest current redistribution on arc force, although perhaps significant, is unlikely to be a dominating effect.

For completeness the arc force associated with a current concentrating around the arc axis should also be considered. In doing so, however, one is confronted by the experimental fact that the current density is a maximum at the cathode emission region under normal welding conditions. Therefore the most concentrated anode current distribution will at best approach one corresponding to zero arc expansion. The arc force for this limiting case can be written directly; it is the pinch force alone, namely

$$F_{\min} = \frac{\mu I_0^2}{8\pi}$$

5.1.10. Estimation of arc force values

If the Converti model (5.4) is used to estimate arc force and F is required in grams, then

$$F = 5.1x10^{-6} I^2 \left(1+2\ln\left(\frac{R_a}{R_e}\right)\right) grams \qquad (5.9)$$

Any evaluation of (5.9) requires knowledge of the ratio R_a/R_e, or equivalently the anode and cathode current densities. To begin, consider the conditions at the cathode.

Various authors have provided data indicating that the current density at the cathode tip is relatively constant over the emission region (Savage et al 1965, Cram 1983, and John Locke private communication). This is consistent with the fact that the evaporation of electrons constitutes a very strong cooling effect, thereby reducing temperature gradients over the emitting surface. Measured values for cathode current densities vary slightly around about 150 A/mm^2, depending on electrode composition (Matsuda et al 1990), and welding current (Adonyi 1989).

The essentially constant current density over the cathode emission region is useful, but it must be combined with considerations of the tip geometry if it is to be related to R_c.

Let the cathode tip be conical with an included angle of 2θ, as in Figure 5.5. Further, let h represent the slant height of the emitting region of the tip. The emitting area A_e then corresponds to the surface of a right circular cone with a base radius $R_e = h \sin\theta$:

$$A_e = \pi R_e h$$

$$= \frac{\pi R_e^2}{\sin\theta}$$

ie

$$A_e = \frac{A_d}{\sin\theta} \qquad (5.10)$$

In (5.10) A_d is the cross-sectional area of the emitting region of the cathode, that is, the base area of the cone shown in Figure 5.6.

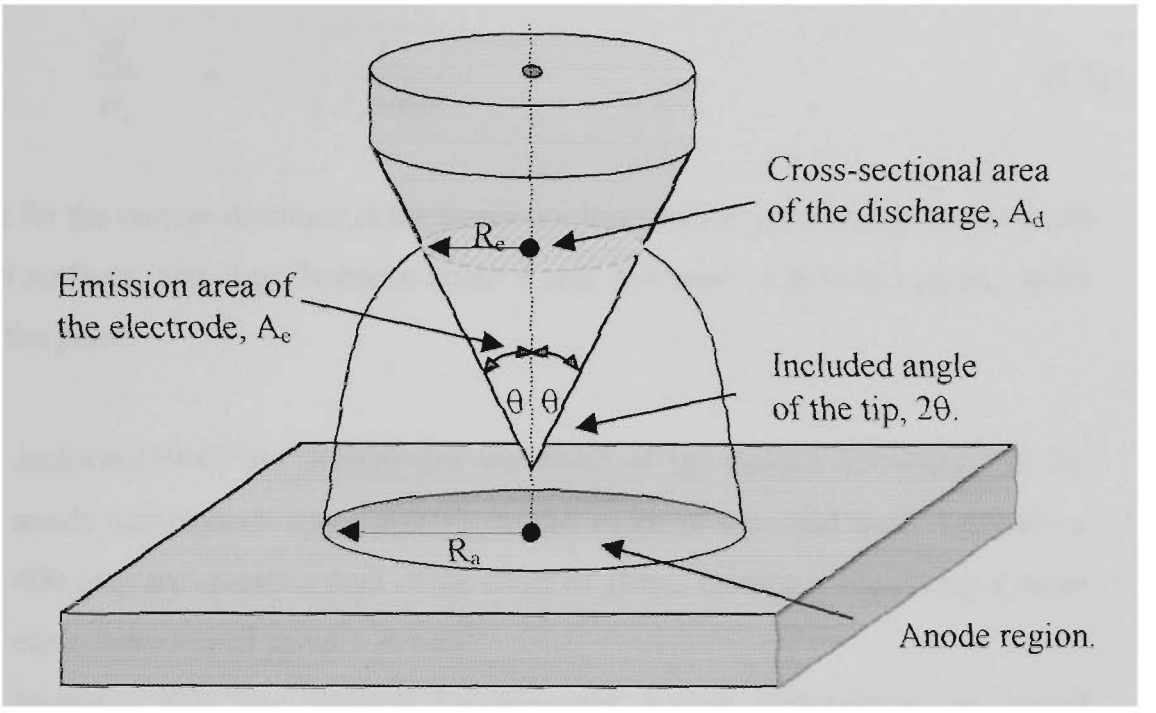

Figure 5.6. Schematic illustrating parameters used in the estimation of arc force.

The emitting area may also be expressed as I_0/J_e where I_0 is the total current. Thus, at the cathode

$$\frac{I_0}{J_e} = \frac{\pi R_e^2}{\sin\theta}$$

And

$$R_e^2 = \frac{I_0 \sin\theta}{\pi J_e}$$

Similarly if the anode region has a radius R_2 then

$$\frac{I_0}{J_a} = \pi R_a^2$$

And

$$R_a^2 = \frac{I_0}{\pi J_a}$$

Therefore Converti's model allows the estimation of the arc expansion ratio in terms of tip angle and current densities:

$$\frac{R_a}{R_e} = \sqrt{\frac{J_e}{J_a \sin\theta}} \qquad (5.11)$$

Estimates for the current densities at the anode are less precise, particularly for distorted weld pool surfaces, and range between about 4 and 30A/mm^2. The following examples illustrate the point.

- Jackson (1960) has argued that the width of the current distribution at the anode corresponds approximately to the width of the weld pool. Typically a 400 amp arc creates a pool of the order of 10mm diameter, suggesting a mean current density of about 5 A/mm^2.
- Nestor (1962) has reported Gaussian-like current distributions on cooled copper anodes, with central values as high as 24 A/mm^2, and mean values of between about 7 and 10 A/mm^2 at typical weld pool radii (Lancaster 1986).
- Lin and Eagar (1985) have suggested that the arc expansion ratio is about 4, corresponding to a higher effective current density of about 12 A/mm^2.

The effect of varying the anode current density over the range suggested by these estimates is evident in Table 5.1. The data was generated assuming that the arc expansion ratio, R_a/R_e, is given by (5.11), the cathode had a 60° taper, and the emission current density was 150 amps/mm^2. Recalling (5.4), the arc force is proportional to the product of the term $[1 + 2\ln(R_a/R_e)]$ and the welding current squared.

As a practical example, the estimated arc force for a 300A arc current, assuming an anode current density of 8 A/mm^2 and a cathode current density of 150 A/mm^2 and a 60° taper on the cathode, the would be

$$F \approx 24x10^{-6} I^2 \; grams$$

$$\approx 2.2 \; grams$$

This force would be expected to increase to about 6 grams at 500 amps.

Table 5.1. Calculated values of R_a/R_e and $[1 + 2\ln(R_a/R_e)]$ for various anode current densities, assuming a cathode with a 60° taper and J_e equal to 150 amps/mm^2 (refer to Figure 5.3).

J_a *(amps/mm^2)*	R_a/R_e	$1 + 2\ln(R_a/R_e)$
5	7.75	5.09
7	6.55	4.76
8	6.12	4.62
10	5.48	4.40
12	5.00	4.22
24	3.54	3.53

5.2. Arc pressure

5.2.1. A change of variables

In the following discussion it will be convenient on occasion to introduce a change in variables. Since the interest is the force and pressure acting on the weld pool the variables R_e and R_a may be replaced by R and α, where R is the pool radius and α is the arc expansion ratio. Furthermore, it will be useful to introduce a dimensionless radius, p, such that p ranges between zero and one. Specifically,

$$\begin{aligned} R &= R_a & \alpha &= \frac{R}{R_e} \\ p &= \frac{r}{R} & R_e &= \frac{R}{\alpha} \\ r &= pR & \frac{r}{R_e} &= \alpha p \end{aligned} \qquad (5.12)$$

It follows that

$$\begin{aligned} p=0 \quad & when \quad r=0 \\ p=1 \quad & when \quad r=R_a \\ p=\frac{1}{\alpha} \quad & when \quad r=R_e \end{aligned}$$

5.2.2. The pinch pressure

The force acting on an electrode due to the self-compression, or magnetic pinching of the arc was derived in Section 5.1.6. In that section the radial increment in pressure, dP, due to the magnetic pinch effect was found to be

$$dP = \frac{df}{2\pi r}$$

where

$$df = \frac{\mu I(r)}{2\pi r} dI(r)$$

Consequently

$$dP = \frac{\mu I(r)}{4\pi^2 r^2} dI(r)$$

and

$$P = \int_R^r \frac{\mu I(r')}{4\pi^2 r'^2} \frac{dI(r')}{dr'} dr' \qquad (5.13)$$

That derivation will now be retraced using the new variable p. (Refer to Section 5.1.6 and Figure 5.4 for clarification).

The current enclosed by p is I(p). The strength of the associated magnetic field is derived from this current and the radius at p, namely pR. Thus

$$B_\theta = \frac{\mu I(p)}{2\pi pR}$$

If we consider the compressive force generated by this field acting on the current dI, (= (dI/dp) dp) passing through an annulus, thickness dp and radius pR, one has

$$df = \frac{\mu I(p)}{2\pi pR} \frac{dI(p)}{dp} dp$$

This force is distributed around a circumference of $2\pi r$, which in terms of p is $2\pi pR$. Therefore the incremental pressure rise inside the annulus is $df/2\pi pR$, so

$$dP = \frac{\mu I(p)}{4\pi^2 p^2 R^2}\frac{dI(p)}{dp}dp$$

The pressure at p is obtained by integrating dp between p and the outer boundary, p=1:

$$P_{pinch} = \int_1^p \frac{\mu I(p')}{4\pi^2 p'^2 R^2}\frac{dI(p')}{dp'}dp' \qquad (5.14)$$

Equations (5.13) and (5.14) are equivalent.

5.2.3. Pressure due to geometric divergence of current.

The derivation of the force on the weld pool due to the arc expansion, given in the preceding section, will now be complimented by an examination of the corresponding component of arc pressure. This is the 'stagnation' or dynamic pressure of the gas. This pressure is not isotropic and only acts on surfaces that modify the gas flow.

The arc pressure due to the $J_r x B_\theta$ acceleration of the plasma will be derived using the following strategy. First, the appropriate JxB force acting on an element of a thin cylinder coaxial with the arc will be determined. This result will then be integrated between z=e and z=a to give a total force acting on an annulus at the pool surface. The pressure contribution is then found by dividing this force by the area of the annulus. The analysis omits the inertial terms of the momentum equations, so results give only an approximate indication of the variation of pressure with radius.

Consider a thin cylinder, radius r, thickness dr, coaxial with the arc. Now consider a thin ring, depth dz, which forms a part of this cylinder. This ring encloses a current I, = I(r,z). Also note that

$$I(r,e) = I_0 \quad \text{if } r \geq R_e$$

and (5.15)

$$I(r,a) = I_0 \quad \text{if } r \geq R_a$$

Now the radial current flow through this ring, in the direction of increasing r, is

$$I_r(r,z) = -\frac{\partial I(r,z)}{\partial z}dz$$

The strength of the magnetic field, $B_\theta(r,z)$ with which this current interacts is

$$B_\theta(r,z) = \frac{\mu I(r,z)}{2\pi r}$$

Finally, the path length for the interaction is dr, hence the incremental force, df, is

$$df = -\frac{\mu I(r,z)}{2\pi r}\frac{\partial I(r,z)}{\partial z}dz\,dr$$

The total force exerted by this cylinder is obtained by integrating over z from e to a. Note the integration has been reversed (ie from a to e) to eliminate the minus sign, arising because a radially outward flow of current corresponds to a negative value of $\partial I/\partial z$.

$$dF = dr\int_a^e \frac{\mu I(r,z)}{2\pi r}\frac{\partial I(r,z)}{\partial z}dz$$

$$= \frac{\mu dr}{2\pi r}\int_{I(r,a)}^{I(r,e)} I(r,z)dI \qquad (5.16)$$

and

$$P(r) = \frac{\mu}{4\pi^2 r^2}\int_{I(r,a)}^{I(r,e)} I(r,z)dI \qquad (5.17)$$

P(r) in (5.17) is to be understood to mean the pressure at the pool surface (ie z=a). In carrying out this integral the conditions of (5.15) must be remembered. For convenience

rather than necessity assume that $R_a > R_e$, as would be anticipated in all welding situations. Then, conducting the integral in (5.17) gives

$$P(r)_{JrxB} = \frac{\mu}{8\pi^2 r^2}\left(I^2(r,e) - I^2(r,a)\right) \qquad r \le R_e$$

$$= \frac{\mu}{8\pi^2 r^2}\left(I_0^2 - I^2(r,a)\right) \qquad R_e \le r \le R_a$$

$$= 0 \qquad r \ge R_a \qquad (5.18)$$

The arc expansion pressure (JrxB) can be written directly for the new variable p, noting that r = pR. Thus (5.18) becomes

$$P(p)_{JrxB} = \frac{\mu}{8\pi^2 p^2 R^2}\left(I^2(p,e) - I^2(p,a)\right) \qquad p \le \frac{1}{\alpha}$$

$$= \frac{\mu}{8\pi^2 p^2 R^2}\left(I_0^2 - I^2(p,a)\right) \qquad \frac{1}{\alpha} \le p \le 1 \qquad (5.19)$$

The pressure distribution on the pool is the sum of (5.6) and (5.18),

$$P(r) = \int_r^{Re} \frac{\mu I(r',b)}{4\pi^2 r'^2}\frac{dI(r',b)}{dr'}dr' + \frac{\mu}{8\pi^2 r^2}\left(I^2(r,e) - I^2(r,a)\right) \qquad r \le R_e$$

$$= \int_r^{Re} \frac{\mu I(r',b)}{4\pi^2 r'^2}\frac{dI(r',b)}{dr'}dr' + \frac{\mu}{8\pi^2 r^2}\left(I_0^2 - I^2(r,a)\right) \qquad R_e \le r \le R_a$$

$$= 0 \qquad r \ge R_a \qquad (5.20)$$

Or, in terms of the variable p,

$$P = \int_1^p \frac{\mu I(p')}{4\pi^2 p'^2 R^2}\frac{dI(p')}{dp'}dp' + \frac{\mu}{8\pi^2 p^2 R^2}\left(I^2(p,e) - I^2(p,a)\right) \qquad p \le \frac{1}{\alpha}$$

$$= \int_1^p \frac{\mu I(p')}{4\pi^2 p'^2 R^2}\frac{dI(p')}{dp'}dp' + \frac{\mu}{8\pi^2 p^2 R^2}\left(I_0^2 - I^2(p,a)\right) \qquad \frac{1}{\alpha} \le p \le 1 \qquad (5.21)$$

5.2.4. Derivation of arc force from arc pressure

It is a useful check to use (5.20) to determine the total arc force acting on the weld pool, and thereby confirm consistency with (5.5) and (5.6). Consider the magnetic pinch first. Since this pressure is isotropic an incremental change in pressure, dP, at a radius r, adds to the force exerted over the face of the enclosed disc by an amount dF equal to $\pi r^2 dP$. The total pinch force is obtained by integrating dF over the radius:

$$P = \int_R^r \frac{\mu I(r')}{4\pi^2 r'^2}\frac{dI(r')}{dr'}dr'$$

$$dP = \frac{dP}{dr}dr$$

$$= \frac{\mu I(r)}{4\pi^2 r^2}\frac{dI(r)}{dr}dr$$

Consequently

$$dF = \pi r^2 \frac{\mu I(r)}{4\pi^2 r^2}\frac{dI(r)}{dr}dr$$

and

$$F = \int_0^R \frac{\mu I(r)}{4\pi}\frac{dI(r)}{dr}dr$$

$$= \int_0^{I_0} \frac{\mu I(r)}{4\pi}dI$$

ie

$$F_{pinch} = \frac{\mu I_0^2}{8\pi}$$

This is the pinch component of the arc force given by (5.5).

The total J_rxB force is given by

$$F_{JrxB} = \int_0^{R_a} P(r)\,2\pi r\,dr$$

$$= \frac{\mu}{4\pi}\int_0^{R_a}\left(I^2(r,e)-I^2(r,a)\right)\frac{1}{r}\,dr$$

Now since I(r,e) is a constant for r>R_e it is convenient to split the integral into pieces, as

$$F = \frac{\mu}{4\pi}\left(\int_0^{R_e}\frac{I^2(r,a)}{r}\,dr+\int_{R_e}^{R_a}\frac{I_0^2}{r}\,dr-\int_0^{R_e}\frac{I^2(r,b)}{r}\,dr\right)$$

Evaluating the second integral leaves

$$F = \frac{\mu I_0^2}{4\pi}\ln\frac{R_a}{R_e}+\frac{\mu}{4\pi}\int_0^{R_e}\frac{I^2(r,e)}{r}\,dr-\frac{\mu}{4\pi}\int_0^{R_a}\frac{I^2(r,a)}{r}\,dr$$

This is the second component as given in (5.6), as required.

In situations where the current density is assumed uniform over R_e

$$I = I_0\left(\frac{r}{R_1}\right)^2$$

Therefore

$$\frac{\mu}{4\pi}\int_0^{R_e}\frac{I^2(r,e)}{r}\,dr = \frac{\mu}{4\pi}\int_0^{R_e}\frac{I_0^2 r^3}{R^4}\,dr$$

$$= \frac{\mu I_0^2}{16\pi}$$

And the total arc force becomes

$$F = \frac{\mu I_0^2}{8\pi}\left(\frac{3}{2}+2\ln\left(\frac{R_a}{R_e}\right)\right)-\frac{\mu}{4\pi}\int_0^{R_a}\frac{I^2(r,a)}{r}dr \qquad (5.22)$$

5.2.5. Arc pressure in the Converti model

As an initial example of the arc pressure over a weld pool, consider the Converti model with its uniform current distribution and total current I_0 enclosed within the arc radius R. The pressure distribution at the anode is obtained from (5.21), where P is given as the sum of the pinch and expansion pressures. To evaluate these two terms note that the current enclosed within the dimensionless radius p ($p<1$) at the anode is

$$I(p) = I_0 p^2 \quad (p\le 1)$$

Consequently the pinch pressure (5.14) is given by

$$P_{pinch} = \int_1^p \frac{\mu I_0 p'^2}{4\pi^2 p'^2 R^2} 2I_0 p' dp'$$

$$= \frac{\mu I_0^2 (1-p^2)}{4\pi^2 R^2} \qquad (5.23)$$

The expansion term is obtained from (5.19) with the usual conditions,

$$P_{JrxB} = \frac{\mu}{8\pi^2 p^2 R^2}\left(I^2(p,e)-I^2(p,a)\right)$$

Where

$$I(p,e) = I_0(\alpha p)^2 \qquad (p\le\frac{1}{\alpha})$$

$$= I_0 \qquad (p>\frac{1}{\alpha})$$

and

$$I(p,a) = \quad I_0 p^2 \qquad (p \le 1)$$

$$= \quad I_0 \qquad (p > 1)$$

Inserting the functions for I(p,e) and I(p,a) gives

$$P_{JrxB} = \frac{\mu}{8\pi^2 p^2 R^2}\left(I_0^2 \alpha^4 p^4 - I_0^2 p^4\right)$$

$$= \frac{\mu I_0^2 \left(\alpha^4 - 1\right)}{8\pi^2 R^2} p^2 \qquad p \le \frac{1}{\alpha} \qquad (5.24a)$$

and if $p \ge \frac{1}{\alpha}$

$$P_{JrxB} = \frac{\mu}{8\pi^2 p^2 R^2}\left(I_0^2 - I_0^2 p^4\right)$$

$$= \frac{\mu I_0^2}{8\pi^2 p^2 R^2}\left(1 - p^4\right)$$

$$= \frac{\mu I_0^2}{8\pi^2 R^2}\left(\frac{1}{p^2} - p^2\right) \qquad \frac{1}{\alpha} \le p \le 1 \qquad (5.24b)$$

The total pressure acting on the anode is the sum of (5.23) and (5.24):

$$P = \frac{\mu I_0^2}{8\pi^2 R^2}\left(2 + \left(\alpha^4 - 3\right) p^2\right) \qquad p \le \frac{1}{\alpha}$$

$$= \frac{\mu I_0^2}{8\pi^2 R^2}\left(2 + \frac{1}{p^2} - 3p^2\right) \qquad \frac{1}{\alpha} \le p \le 1 \qquad (5.25)$$

Graphical representations of such pressure distributions, for several different arc expansion ratios (α's) are presented in Figure 5.7.

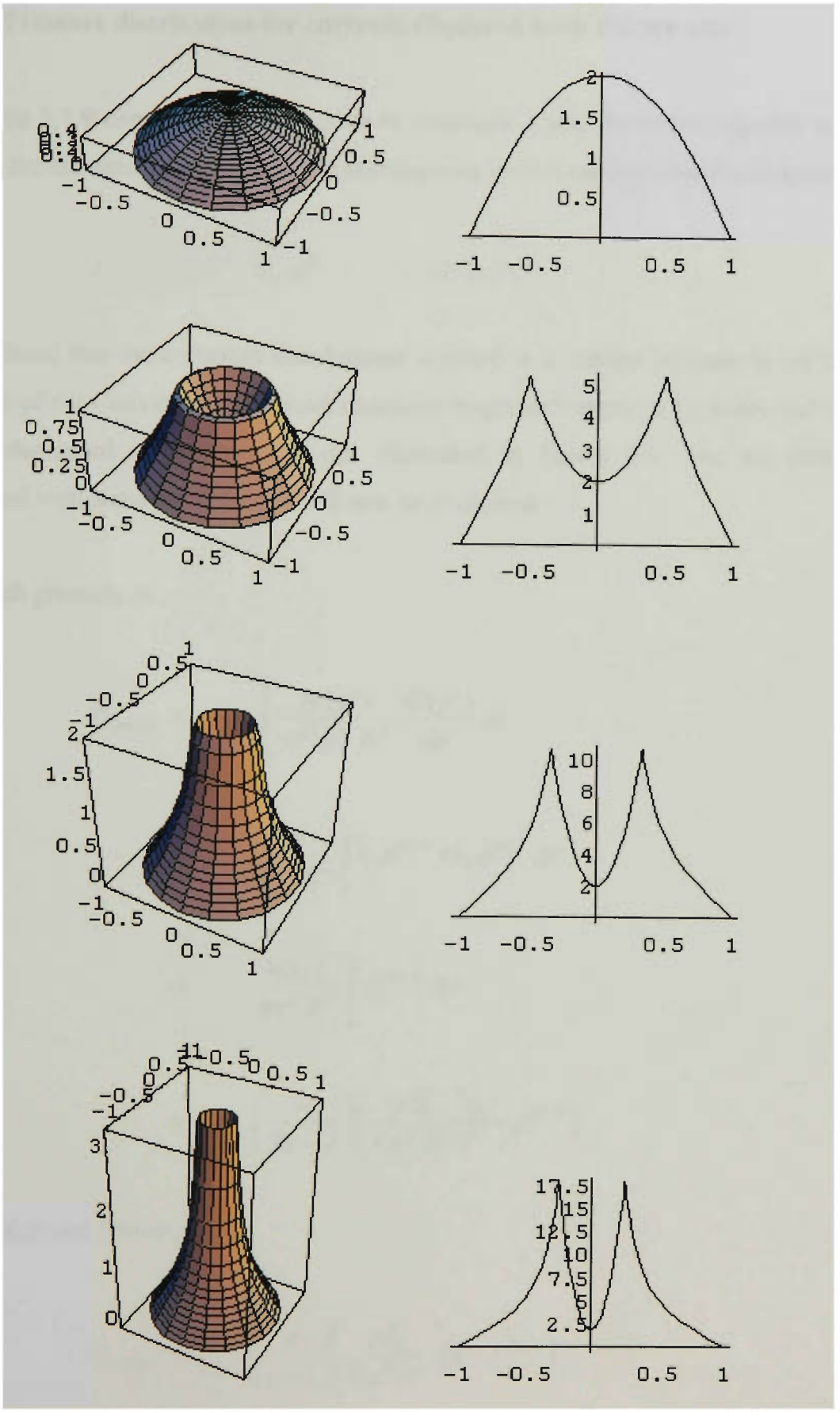

Figure 5.7. Changing total pressure distributions (static plus dynamic components, arbitrary units) with increasing arc expansion. Arc expansion (from top): 1, 2, 3 and 4.

5.2.6. Pressure distribution for currents displaced from the arc axis

In Section 5.1.9 consideration was given to situations where the current density is low close to the arc axis. In particular such distributions were modelled with the function

$$I = I_0 p^n \qquad n \geq 2, p \leq 1$$

It was found that these current distributions resulted in a modest increase in arc force over that of the Converti model. Such situations might well apply to keyholes and other deeply depressed weld pools, as was illustrated in Figure 5.5. The arc pressure associated with these distributions will now be evaluated.

The pinch pressure is

$$P_{(pinch)} = \int_p^1 \frac{\mu I(p')}{4\pi^2 p'^2 R^2} \frac{dI(p')}{dp'} dp'$$

$$= \frac{\mu}{4\pi^2 R^2} \int_p^1 I_0 p'^{n-2} n I_0 p'^{n-1} dp'$$

$$= \frac{n\mu I_0^2}{4\pi^2 R^2} \int_p^1 p'^{2n-3} dp'$$

$$= \left(\frac{n}{2n-2}\right)\left(\frac{\mu I_0^2}{4\pi^2 R^2}\right)\left(1 - p^{2n-2}\right)$$

From which one obtains

$$P_{(pinch)} = \left(\frac{n}{n-1}\right)\left(\frac{\mu I_0^2}{8\pi^2 R^2}\right)\left(1 - p^{2n-2}\right)$$

The pressure due to arc expansion is given by substitution into (5.19). Thus inside the radius of the cathode emission

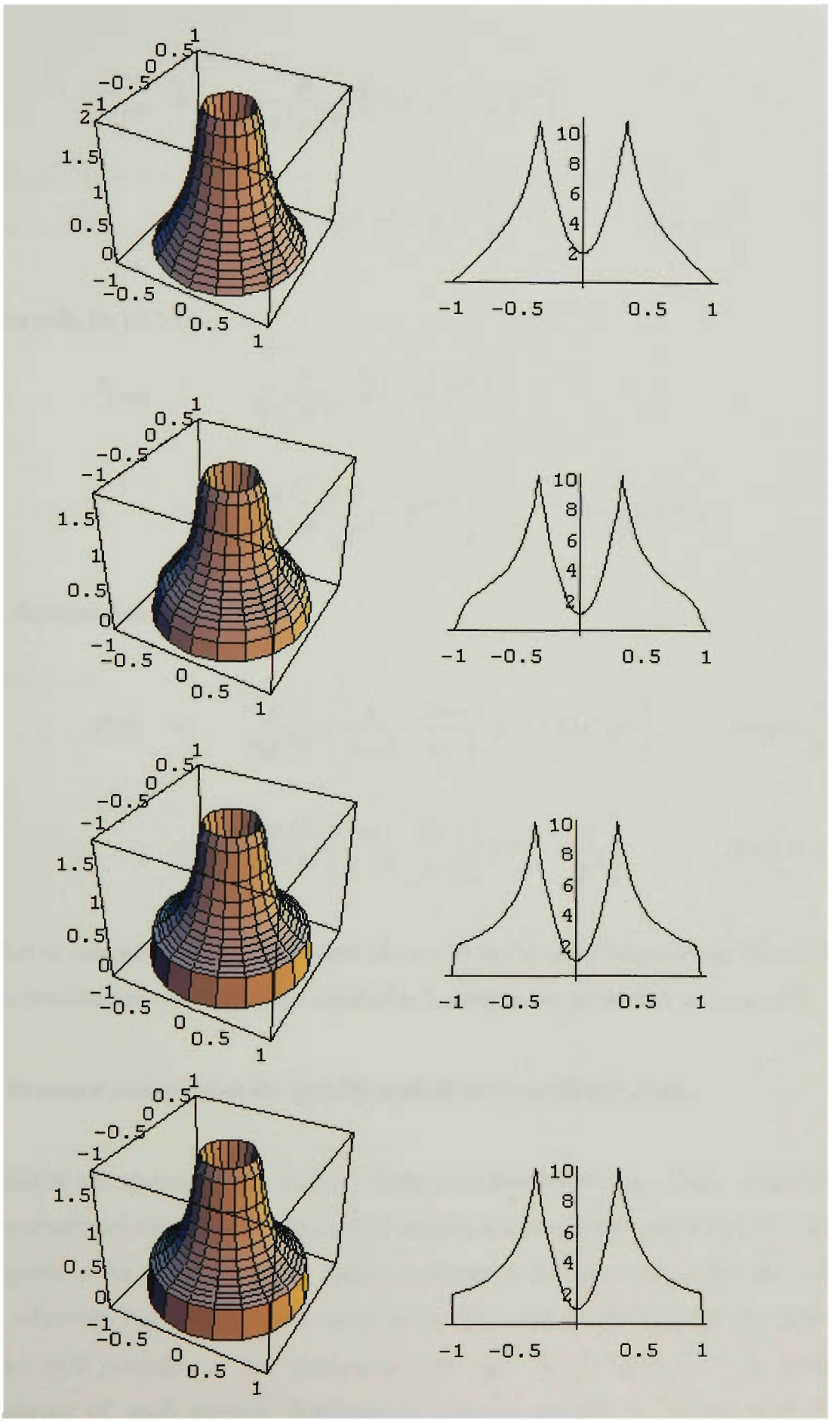

Figure 5.8. The effect on total arc pressure of welding current diverging to the rim of the anode region. Model assumes $I_0 = p^n$ where (from top) n=2, 8, 32 and1000. $\alpha = 3$, arbitrary units. (Refer 5.2.6).

$$P_{(JrxB)} = \frac{\mu}{8\pi^2 p^2 R^2}\left[I_0^2 \alpha^4 p^4 - I_0^2 p^{2n}\right]$$

$$= \frac{\mu I_0^2}{8\pi^2 R^2}\left[\alpha^4 p^2 - p^{2n-2}\right] \qquad for\ p \le \frac{1}{\alpha}$$

While for $r > R_e$ (ie $p > 1/\alpha$)

$$P_{(JrxB)} = \frac{\mu}{8\pi^2 p^2 R^2}\left[I_0^2 - I_0^2 p^{2n}\right]$$

$$= \frac{\mu I_0^2}{8\pi^2 R^2}\left[\frac{1}{p^2} - p^{2n-2}\right] \qquad for\ \frac{1}{\alpha} \le p \le 1$$

Finally, the total pressure is

$$P(r) = \frac{\mu I_0^2}{8\pi^2 R^2}\left[\frac{n}{n-1} - \frac{2n-1}{n-1} p^{2n-2} + \alpha^4 p^2\right] \qquad for\ p \le \frac{1}{\alpha}$$

$$= \frac{\mu I_0^2}{8\pi^2 R^2}\left[\frac{n}{n-1} - \frac{2n-1}{n-1} p^{2n-2} + \frac{1}{p^2}\right] \qquad for\ \frac{1}{\alpha} \le p \le 1$$

The effect of increasing the displacement of current to the outer boundary of the anode region is modelled by increasing the value of n. Examples are presented in Figure 5.8.

5.2.7. Pressure distribution for axially peaked current distributions

In contrast to the above, results such as those provided by Nestor (1962) show that there are situations where the anode current density is a maximum on the arc axis, and drops rapidly in the radial direction. These situations are likely to arise when the weld pool is relatively flat, or localised vaporisation from the anode reduces the sheath resistance and provides a low resistance path for the arc current. The likely consequences of such current distributions can be gauged by considering the representative example:

$$J(p) = \frac{2I_0}{\pi}\left(1-p^2\right)$$

The constant $2I_0/\pi$ ensures that a current of I_0 is enclosed by the radius R. In fact the enclosed current is

$$I = \frac{2I_0}{\pi}\int_0^p \left(1-p'^2\right) 2\pi p'\, dp'$$

ie

$$I = I_0\left(2p^2-p^4\right)$$

and

$$\frac{dI}{dp} = 4I_0\left(p-p^3\right)$$

Hence the pinch pressure is given by

$$P_{pinch} = \frac{\mu I_0^2}{\pi^2 R^2}\int_p^1 \frac{\left(2p'^2-p'^4\right)\left(p'-p'^3\right)}{p'^2}\, dp'$$

$$= \frac{\mu I_0^2}{\pi^2 R^2}\int_p^1 \left(2p'-3p'^3+p'^5\right)dp'$$

$$= \frac{\mu I_0^2}{\pi^2 R^2}\left[\frac{5}{12}-p^2+\frac{3}{4}p^4-\frac{1}{6}p^6\right]$$

The arc expansion term is more readily obtained. If $p<1/\alpha$ then:

$$P_{JrxB} = \frac{\mu}{8\pi^2 p^2 R^2}\left[I_0^2\alpha^4 p^4 - I_0^2\left(4p^4-4p^6+p^8\right)\right]$$

$$= \frac{\mu I_0^2}{8\pi^2 R^2}\left(\left(\alpha^2-4\right)p^2+4p^4-p^6\right) \qquad p\le\frac{1}{\alpha}$$

While if $p > 1/\alpha$ then

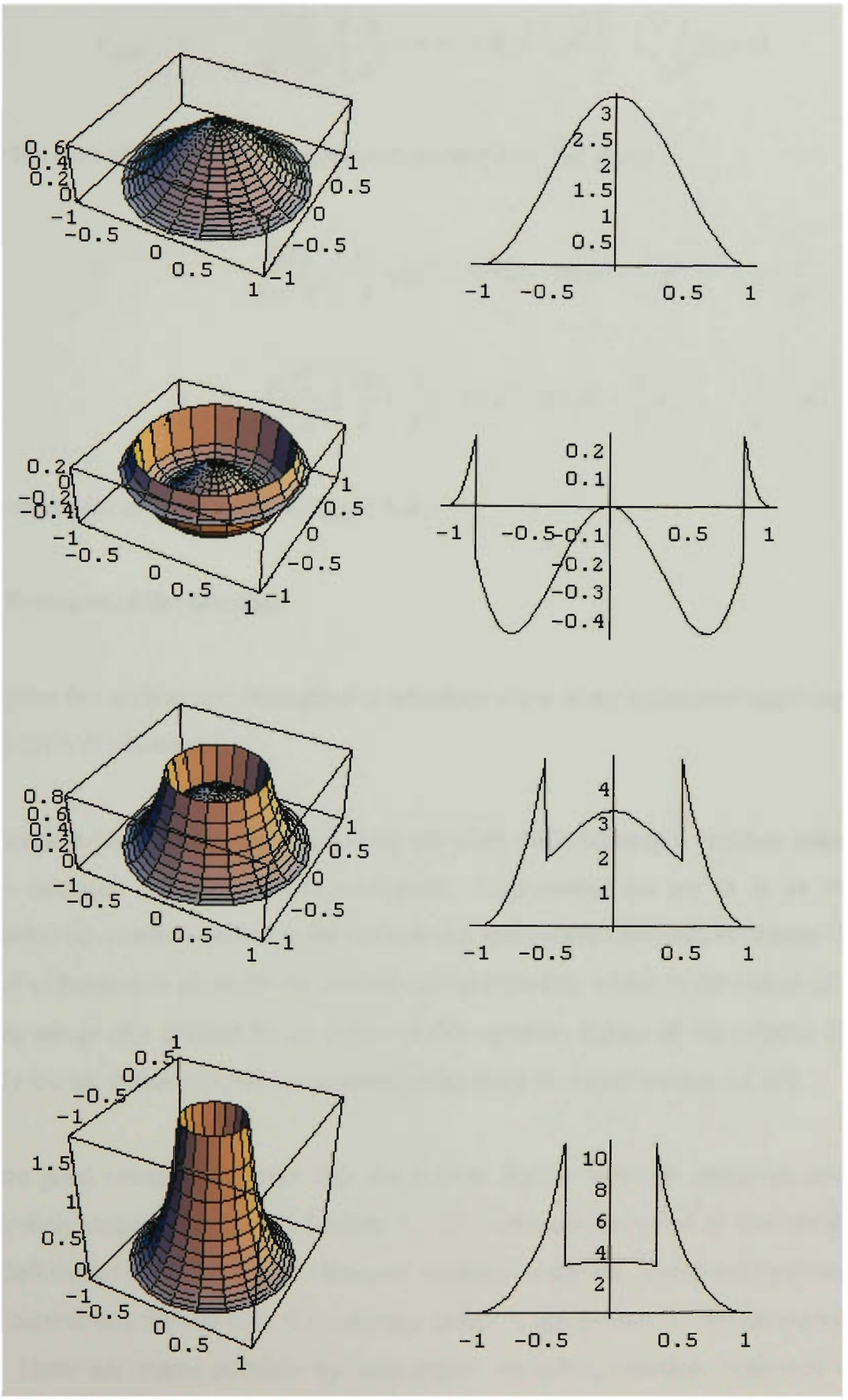

Figure 5.9. Arc pressure distributions for a gaussian-like current distribution at the anode (refer 5.2.7). From top, pinch component, dynamic component for $\alpha = 1.2$ and total arc pressure for $\alpha = 2$, and $\alpha = 3$ (arbitrary units).

$$P_{JxB} = \frac{\mu I_0^2}{8\pi^2 R^2}\left(\frac{1}{p^2} - 4p^2 + 4p^4 - p^6\right) \qquad \frac{1}{\alpha} \le p \le 1$$

Writing the sum of the pinch and expansion pressures in full gives

$$P = \frac{\mu I_0^2}{8\pi^2 R^2}\left(\frac{10}{3} + (\alpha^2 - 12)p^2 + 10p^4 - \frac{7}{3}p^6\right) \qquad p \le \frac{1}{\alpha}$$

and

$$= \frac{\mu I_0^2}{8\pi^2 R^2}\left(\frac{10}{3} + \frac{1}{p^2} - 12p^2 + 10p^4 - \frac{7}{3}p^6\right) \qquad \frac{1}{\alpha} \le p \le 1$$

Several examples are presented in Figure 5.9.

5.2.8. Pressure at the arc core

To complete this section it is instructive to introduce some of the constraints applying to practical GTAW situations.

This discussion has already assumed that the arc takes place between a negative polarity tungsten electrode and the positive workpiece. Furthermore the arc is at its most concentrated (ie smallest radius) at the cathode tip, and expands towards the anode. The degree of expansion is given by the arc expansion ratio (α), which is the radius of the arc at the anode (R_a) divided by its radius of the emission region of the cathode (R_e). Typically the arc expansion ratio is expected to be about four (see section 5.1.10).

There are good reasons to expect that the current density over the emission area is approximately constant (again see Section 5.1.10), although the value of that constant may be influenced by the particular choice of welding conditions. This constraint means that the current distribution over the emission radius is determined by the geometry of the tip. There are many possible tip geometries, including rounded, hollowed and truncated designs. Corresponding current distributions for each can be determined by a straight forward application of geometric principles. However, the normal shape for keyhole GTAW is a conical tip, where

$$I = I_0\left(\frac{r}{R_e}\right)^2$$

If it is assumed that this condition applies, then (5.7) and (5.21) become

$$F = \frac{\mu I_0^2}{8\pi}\left(\frac{3}{2}+2\ln\alpha\right) - \frac{\mu}{4\pi}\int_0^{R_a}\frac{I^2(r,a)}{r}dr$$

And

$$P = \int_1^p \frac{\mu I(p')}{4\pi^2 p'^2 R^2}\frac{dI(p')}{dp'}dp' + \frac{\mu}{8\pi^2 p^2 R^2}\left(I_0^2(\alpha p)^4 - I^2(p,a)\right) \qquad p \le \frac{1}{\alpha}$$

$$= \int_1^p \frac{\mu I(p')}{4\pi^2 p'^2 R^2}\frac{dI(p')}{dp'}dp' + \frac{\mu}{8\pi^2 p^2 R^2}\left(I_0^2 - I^2(p,a)\right) \qquad p \le 1$$

$$= 0 \qquad p > 1$$

A second observation is that the anode current density near the arc axis is significantly less than it is at the cathode. In fact it is unlikely to exceed about 20% of J_e (Section 5.1.10), and it is likely to approach zero in keyhole mode welding. Therefore for $p \le 1/\alpha$ the arc pressure is, quite accurately,

$$P = \int_1^p \frac{\mu I(p')}{4\pi^2 p'^2 R^2}\frac{dI(p')}{dp'}dp' + \frac{\mu I_0^2 \alpha^4 p^4}{8\pi^2 p^2 R^2} \qquad p \le \frac{1}{\alpha}$$

The second term is the pressure due to the arc expansion. This component of pressure is a maximum for $p = 1/\alpha$, for which it has the value

$$P_{JrxB,\max} = \frac{\mu I_0^2}{8\pi^2 p^2 R^2} \qquad (5.26)$$

But pR is nothing other than the emission radius at the cathode. In other words, the peak pressure due to arc expansion is dependent only on the total current and the radius of

the emission area. (Recall of course that this is valid only if the assumption of significant arc expansion is true).

The other contribution to the arc pressure comes from the pinch pressure. The examples of the previous sections indicate that the pinch pressure decreases as the current distribution progresses from one concentrated around the axis, to uniform, to dispersed to the outer boundary of the anode region. Numerically, if the expansion pressure at ($p = 1/\alpha$) is α^2 then the pinch pressure would be approximately 3.3 for the gaussian-like distribution ($I=I_0(2p^2-p^4)$), 2 for the uniform current density distribution and 1 for the circumferential distribution. Given that α^2 is likely to be greater than at least 10, the respective pinch contributions will be relatively small, but not necessarily negligible. The expansion pressure is therefore at least the dominant term.

A final argument for the reduced importance of pinch pressure relative to the expansion pressure arises from the pool shape. In the situations of practical interest the weld pool surface will be highly distorted and current density near the arc axis is likely to be very low. This would be sufficient to make the expansion pressure alone as a good approximation to the peak pressure of the arc for the proposed model. Nevertheless, one could argue further that in situations of significant surface depression the pinch pressure may reduce with depth within the crater. The reason is that the original derivation has assumed the arc to be impinging on a flat surface. In practice however, once inside the weld pool crater the outer portions of the arc are progressively stripped away. But this process also progressively reduces the contributions to the pinch pressure. Therefore it would seem that (5.12) is at least a good approximation to the peak arc pressure, and it may indeed be very nearly exact.

In the preceding discussions viscosity has been largely neglected. Viscosity acts to reduce velocity gradients, and can be described as a diffusion of momentum. Its effect on welding arcs is therefore to cause a dampening and radial spreading of any high velocity gradients. This constitutes a de-coupling of the velocity and current distributions.

At low temperatures viscosity increases with temperature, but at the elevated temperatures within arcs the effects of ionisation are important, and viscosity decreases with increasing temperature. For example, the viscosity of argon reaches a peak value of about $2.3x10^{-4}$ kg/ms at about 10000K and drops to about one-tenth this value at 25,000K (Lancaster 1986). Helium is more viscous than argon between about 12,000K and at least 25,000K. Consequently a jet at the core of a helium arc should be more heavily damped than one within an argon arc, and peak arc pressures in helium should be relatively low.

The analysis in fact indicates that the arc pressure due to the arc expansion (Jr x B) is zero on the arc axis, but may attain its maximum value within a very short distance (approximately equal to R_e). Physically this seems unrealistic, given the very high velocity gradient that would be involved. A more likely result would be that the axial velocity, and therefore the stagnation pressure, would be rendered relatively close to the maximum because of viscous drag. This observation, and that of the recurrence of the dimension R_e suggest the identification of an arc 'core'. This core has several notable characteristics, namely:

- The core has a radius of R_e
- The peak arc pressure is attained at its boundary, and will be referred to as the core pressure.
- The pressure of the core will be a minimum on the axis, but the plasma viscosity and the core radius will regulate the depth of this minimum.
- The core pressure is proportional to I_0^2/R_e.
- Under typical welding conditions the core pressure is independent of arc length (except for some losses due to viscous damping).
- The core pressure is approximately equal to the mean pinch pressure for an arc radius of R_e, and approximates the pressure at the tip of the cathode.

5.3. Experimental investigation of cathodic influences

5.3.1. Introduction

To complete this investigation the characteristic behaviour of the arc force was examined by direct measurement of the force exerted on the samples during welding. Although the method included the use of 'short-circuit' determinations, these corrections differed to that employed by other workers (eg Lin and Eagar 1985). Specifically, only differences in short-circuit measurements were used, and then only to correct for geometrical and material variations resulting from different measurement points and plate materials. This approach was intended to reduce the external contributions to the measurements to a constant, although undetermined, value. In the terminology of the preceding discussion, the method aimed to make R_a constant for all trials, without determining its value. In so far as this was successful the subsequent variances reported were due to changes in the welding current and its distribution over the cathode emission region. To distinguish these measurements from the true arc force the quantity determined in these experiments will be referred to as a 'fixed anode force' (FAF). Provided the current distribution over the cathode emission region is relatively uniform, the Converti model (5.4) offers an accurate description of the FAF regardless of how the current may be distributed at the anode region. However, it does not necessarily provide a good description of the arc force since this does have a dependence of the anode conditions. Nevertheless, it is reasonable to assume that influences that generate changes in the FAF will generate similar changes in arc force, provided that they do not significantly alter the behaviour of the weld pool.

5.3.2. In-situ weighing method

Since the current flow is continuous through the arc, weld pool and solid plate, Lorentz forces are generated throughout welding the circuit, and the isolation of the 'arc force' is difficult. In particular, Lorentz forces are generated in the cathode as the current flow converges in the tip and then diverges through the arc, weld pool and solid plate. Therefore the first component of the experimental strategy was to mechanically isolate the welding sample from the rest of the welding circuit, and measure the force exerted

on this element. In the experimental arrangement to be described below the isolation points were a liquid gallium contact between the welding platform and the return circuit, and the interface between the arc and the cathode tip (see Figures 5.10 and 5.11). To compliment this approach additional measurements were made to allow corrections for coupling to different parts of the circuit that made the measurements position sensitive. The result was that the corrected measurements were due to the current diverging from R_e to a constant, but unknown R_a.

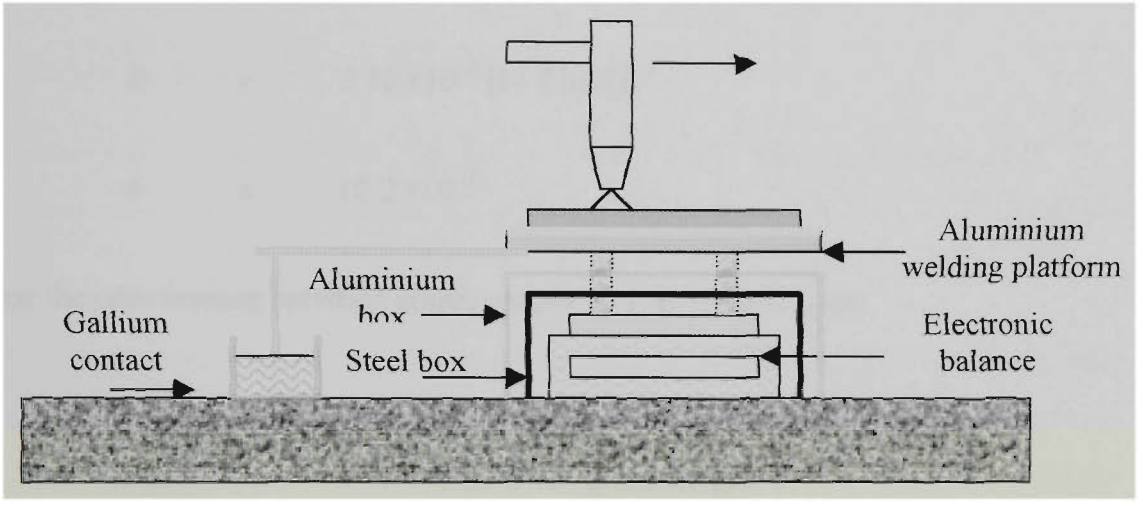

Figure 5.10. Schematic of the arrangement employed for measuring aspects of the arc force.

If R_e and R_a are interpreted as the two radii identified in Converti's model, (5.4), then rearrangement gives

$$F = \frac{\mu I^2}{8\pi}\left(1+2\ln R_a - 2\ln R_e\right)$$

Furthermore, if R_a is artificially fixed to some unknown value Λ, the measurement becomes an FAF measurement and

$$F = \frac{\mu}{8\pi}\left(1+2\ln \Lambda - 2\ln R_e\right)I^2 \qquad (5.27)$$

$$= \left(a+b\ln R_e\right)I^2$$

where

$$a = \frac{\mu}{8\pi}(1+2\ln\Lambda)$$

$$b = \frac{\mu}{4\pi}$$

If the FAF is measured in grams weight, current in amps, and R_e and Λ in millimetres then the anticipated values for a and b are

$$a = 5.10x10^{-6}(1+2\ln\Lambda)$$

$$b = 10.2x10^{-6}$$

Note that the conversions between grams weight and newtons (N) are

1 gram weight = 9.8×10^{-3} N

1 N = 1.02×10^{2} gram weight

Where there is no confusion the symbol 'g' will be used for the force 'gram weight'.

In the experiments force was read directly from a digital balance to a computer-based logging system. The balance maintained zero displacement of the pan during operation. This type of operation prevented any changes in arc length, and also minimised variations in any of the forces that were geometry-sensitive. The experimental set-up was carefully shielded against electrical disturbances generated by the welding process. The welding current flowed into the plate through a metal arm terminating in a rod that dipped into a metal container filled with liquid gallium. This so-called 'floating contact' provided both electrical continuity and mechanical isolation.

The torch was track-mounted and set for a welding speed of 150 mm/min. The torch was held vertically, and the separation between the plate and the electrode tip was adjusted manually using feeler gauges. The range of welding conditions used in the experiments is shown in Table 5.2.

Table 5.2. The range of conditions considered in the arc force experiments.

Parameter	Selections
Welding current (A):	100, 200, 300, 400 and 500.
Plate material:	C-Mn steel, AISI 304 stainless steel, AA5083 and AA6060 aluminium and DHP copper.
Shielding gas:	Helium, argon and a 75% helium-25% argon mix (He-25Ar).
Electrode diameter (mm):	1.6, 2.4, 3.2, 4.0, 4.8 and 6.35.
Electrode tip angle (°):	30, 45, 60, 75 and 90.
Electrode elevation (mm):	+2.0, 0.0, -2.0 and –4.0 (relative to plate surface)

The raw measurements were obtained in the following manner. Plates of each material were cut into 150x150mm squares. Each plate was clamped to the aluminium platform with copper clamps at each corner. A layer of insulation between the plate and platform ensured that the entire current was confined to the sample as it flowed radially through and away from the weld pool. Three easily identified positions were marked at 40mm separation on the aluminium platform. Six readings were automatically logged and averaged as the arc traversed each of these positions (ie TP1, TP2 and TP3). The use of three sampling points increased the total number of readings, and also helped warn of damage to the electrode. GTAW electrodes are easily damaged if the welding parameters are inappropriate for a particular material. The arrangement is illustrated in Figure 5.11.

The averaged readings were corrected for positional and material effects. These corrections were made as follows. Short circuits measurements were made for each combination of position, current and material used in the trials. These measurements were then compared to that corresponding to the same current at position 1 (TP1) on an unused aluminium sample. The differences were registered as the required corrections. At no stage were the absolute values of the short circuit measurements used to correct the raw data. For clarification, let the short circuit measurement corresponding to a particular position TPx, current I and material M be S(TPx, I, M). Similarly let the

weight registered during the corresponding trial be W(TPx, I, M). Then the correction C(TPx, I, M) is given by

$$C(TPx, I, M) = S(TPx, I, M) - S(TP1, I, Aluminium)$$

And

$$FAF(TPx, I, M) = W(TPx, I, M) - C(TPx, I, M)$$

A second gallium-filled container was required for the short circuit measurements. This container was machined from a 25mm diameter copper bar. It was filled to a depth of about 20mm with liquid gallium. The short-circuiting electrode was 3.2mm diameter, and was dipped deeply enough into the gallium to completely submerge the entire tip. Care was taken to ensure the gallium thoroughly wet the electrode to well above its tapered section to ensure that the current diverged from a constant radius into the detection region.

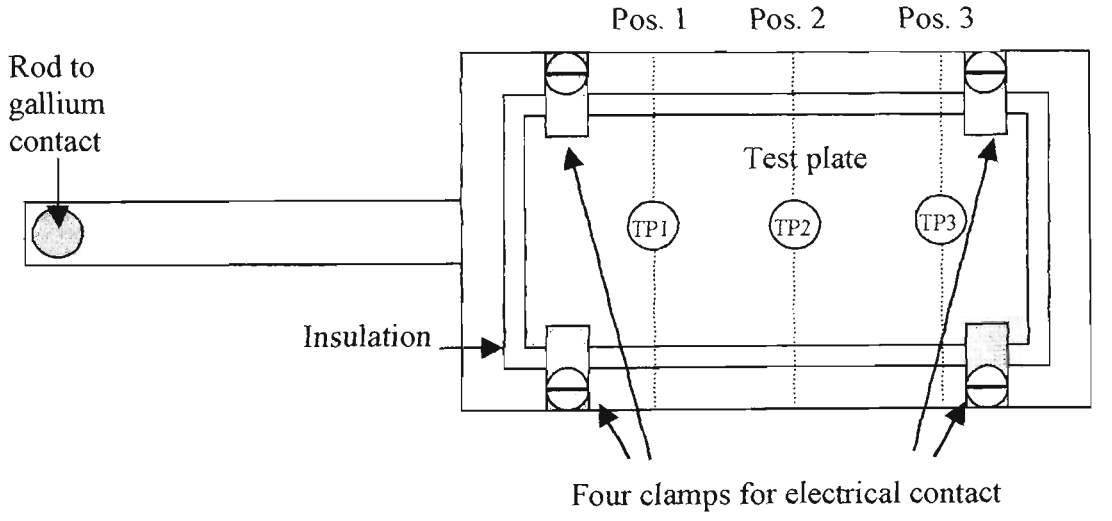

Figure 5.11. Schematic showing plate placement and measurement points used in the measurements.

Further corrections were made for weight changes during each weld, and for the thrust exerted by the shielding gas. Weight change was determined by recording the difference in sample weight immediately before and after welding. The difference was

due to a combination of oxidation and possibly the reaction to the expansion of the gas in contact with the heated surface. The corrections were of the order of +1.5 milligram per millimetre of weld, and were assumed to have increased linearly along the length of the weld. Finally the results were corrected for the thrust associated with each shielding gas. The argon flow produced a thrust of 0.10 gram, while the other two gases contributed a thrust of only 0.01 gram.

Table 5.3. Table of arc force measurements

No.	Material	Shield gas	Arc Current amps	Arc voltage volts	Arc gap *mm*	Tip $2\theta°$	Elect. Dia. *mm*	Fused area mm^2	FAF *Grams*
1	C-Mn Steel	Ar	500	15.89	+2.0	45	3.2	68.4	10.59 ± .07
2	C-Mn Steel	Ar	500	13.29	0.0	45	3.2	57.6	10.08 ± .06
3	C-Mn Steel	Ar	500	9.82	-2.0	45	3.2	47.7	10.58 ± .07
4	C-Mn Steel	Ar	300	9.91	0.0	45	3.2	24.2	3.98 ± .13
5	C-Mn Steel	Ar	100	7.12	0.0	45	3.2	6.2	0.62 ± .00
6	AA5083	Ar	300	10.07	0.0	45	3.2	29.6	3.93 ± .04
7	AA5083	Ar	100	7.88	0.0	45	3.2	2.4	0.66 ± .04
8	AA6060	Ar	200	8.42	0.0	45	3.2	4.3	1.69 ± .08
9	AA5083	Ar	400	14.56	0.0	45	3.2	113.2	7.05 ± .01
10	AA5083	He-25Ar	300	14.57	0.0	45	3.2	68.4	3.89 ± .06
11	AA6060	He	300	17.25	0.0	45	3.2	58.5	3.80 ± .04
12	AA5083	He	300	18.02	0.0	45	3.2	83.9	3.74 ± .05
13	*Aborted*								
14	C-Mn Steel	He-25Ar	300	11.90	0.0	45	3.2	28.4	3.81 ± .08
15	AA5083	Ar	200	9.39	0.0	45	3.2	12.2	1.65 ± .11
16	AA6060	He	300	23.39	+2.0	45	3.2	98.6	4.13 ± .05
17	AA6060	He	500	21.41	-2.0	45	3.2	257.3	9.31 ± .05
18	AA6060	He	500	16.70	-4.0	45	3.2	155.6	9.35 ± .11
19	C-Mn Steel	He	300	13.07	0.0	45	3.2	31.5	3.72 ± .05
20	AISI304	He	300	14.39	0.0	45	3.2	36.5	3.71 ± .05
21	Copper	He	300	13.11	0.0	45	3.2	5.7	3.74 ± .01
22	Copper	He	400	14.69	0.0	45	3.2	18.8	6.94 ± .00
23	AISI304	He	400	19.35	0.0	45	3.2	89.2	7.10 ± .25
24	C-Mn Steel	He	400	15.62	0.0	45	3.2	52.9	6.69 ± .02
25	C-Mn Steel	Ar	400	11.63	0.0	45	2.4	33.8	6.65 ± .07
26	C-Mn Steel	Ar	400	11.61	0.0	45	3.2	37.4	6.87 ± .08
27	C-Mn Steel	Ar	400	11.83	0.0	45	4.0	45.3	6.93 ± .03
28	C-Mn Steel	Ar	400	13.17	0.0	45	4.8	48.0	6.92 ± .08
29	C-Mn Steel	Ar	400	13.77	0.0	45	6.4	51.3	7.24 ± .07
30	C-Mn Steel	Ar	400	13.31	0.0	30	3.2	44.6	7.14 ± .07
31	C-Mn Steel	Ar	400	10.77	0.0	60	3.2	33.6	6.59 ± .03
32	C-Mn Steel	Ar	400	10.24	0.0	75	3.2	29.7	6.50 ± .05
33	C-Mn Steel	Ar	400	10.00	0.0	90	3.2	27.6	6.43 ± .01

The maximum combined corrections were less than 10% of the uncorrected measurements, and the corrected values showed a high degree of consistency. The details of each trial, including the standard deviations determined for each set of measurements, are presented in Table 5.3.

After welding, the plates were cross-sectioned, polished and etched so that the profiles of the fusion zones could be inspected and the fused areas determined. Where possible, three cross sections were extracted from each plate so that area measurements could be averaged. These results are also shown in Table 5.3.

5.3.3. Welding current

The FAF results (in grams weight) were consistent with a quadratic dependence on current, as expected from (5.1). A least squares fit of all the measurements in Table 5.3 gave a correlation coefficient (R^2) of 0.985 with the constant of proportionality, k, equal to 41.7 x 10^{-6} g/A^2 (see Figure 5.12). The correlation was not noticeably improved by allowing constant and linear terms in the regression:

$$FAF = 41.73 \times 10^{-6} A^2 \qquad R^2 = 0.985$$

$$FAF = 0.258 + 40.20 \times 10^{-6} A^2 \qquad R^2 = 0.986$$

$$FAF = -0.198 + 3.042 \times 10^{-3} A + 35.63 \times 10^{-6} A^2 \qquad R^2 = 0.987$$

Least squares fitting was also applied to the subset of the data that excluded trials dealing with the effects of electrode geometry and arc length. The trials considered included variations in current, material and gas mixture. The correlation between FAF and current squared was higher for these data. R^2 had a value of 0.993, and the best-fit value for k was 42.3 x 10^{-6} g/A^2.

It could be argued that the high correlation of force to current squared might have been due to the inclusion of forces external to the arc. To test this scenario 50% of the measured force was assumed to be external and exactly proportional to the square of the current. Even after subtraction of this 'component' the correlation remained strong with $R^2 = 0.9697$. The choice of 50% was based on the expectation that k was likely be about

20-25 x 10^{-6} g/A^2 *(see section 5.2.4). This further illustrates the consistency between the* theoretical prediction of (5.4) and (5.27) and the experimental results.

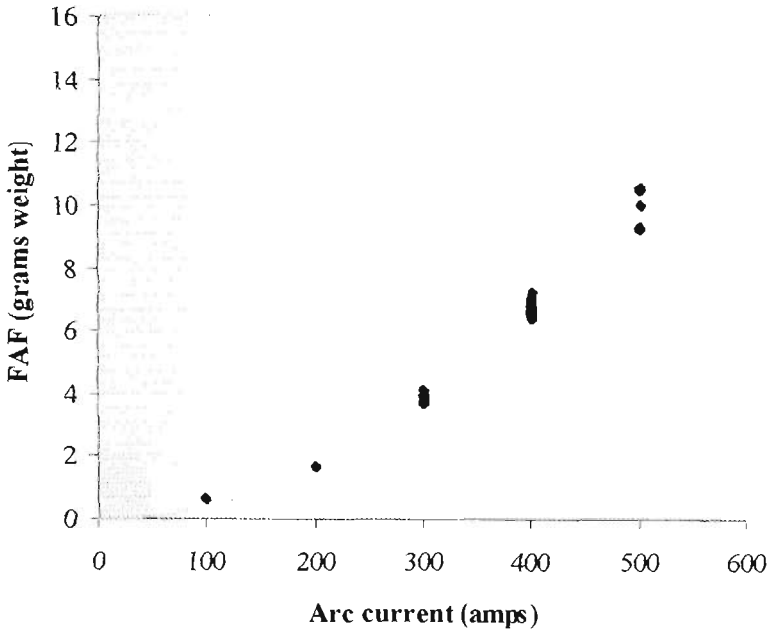

Figure 5.12. Graph showing all FAF measurements (points) and the quadratic curve FAF = 41.7x10^{-6} A^2.

5.3.4. Independence from anodic influence

Table 5.4. Relationship between variations at the anode and the 'fixed anode' force.

Plate No.	Material	Current *(amps)*	Voltage *(volts)*	Fused area *(mm^2)*	FAF *(grams)*
11	AA6060 Al.	300	17.25	58.5	3.80 ± .04
12	AA5083 Al.	300	18.02	83.9	3.74 ± .05
19	C-Mn steel	300	13.07	31.5	3.72 ± .05
20	AISI 304	300	14.39	36.5	3.71 ± .05
21	DHP Copper	300	13.11	5.73	3.74 ± .01

Comparing FAF results for different materials tested the measurements' independence from anodic (ie weld pool) influences. Five different materials had been welded under the same conditions of 300 amps, helium shielding gas, zero electrode elevation, and a

3.2mm electrode with a 45° electrode tip angle. Results for these trials are shown in Table 5.4.

The data show a very large variation in measured arc voltage. The variance in fusion areas was even greater, ranging over more than an order of magnitude. It followed that a wide range of anode conditions was encountered in these trials. Nevertheless, the measured FAF appeared generally unaffected (see Figure 5.13), providing strong evidence that the measurements were independent of anode conditions, as anticipated. The variation that was observed was not statistically significant, as can be inferred from the standard deviations of the individual measurements.

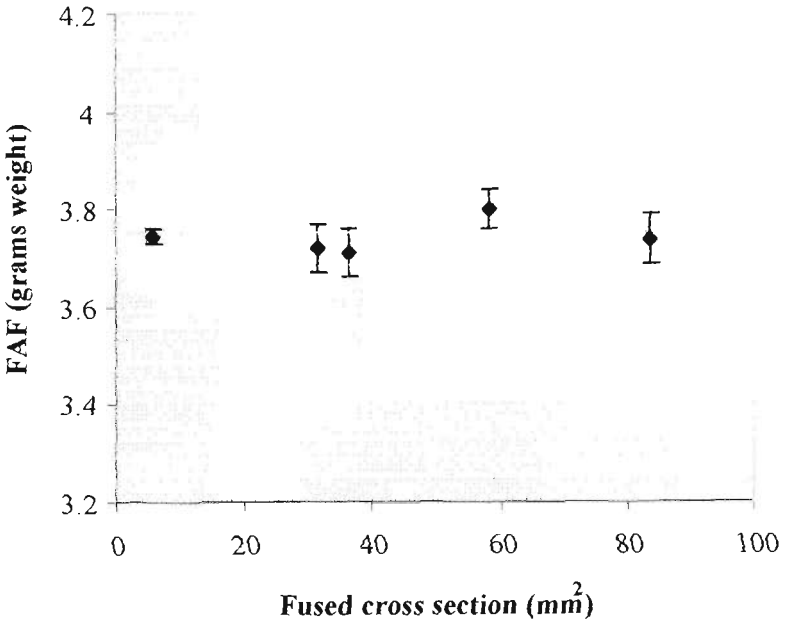

Figure 5.13. Graphical illustration of the almost constant value of the FAF for experiments in which the fused cross sectional areas varied by more than an order of magnitude.

It should be noted that it was not possible to guarantee total elimination of effects due to tip deterioration during the welding process. Many welding conditions were not ideal, and tip damage did occur from time to time. When visible damage occurred the readings were eliminated, but more subtle deterioration may have gone undetected. The importance of the tip condition was explored by deliberately varying the electrode tip angle, the effects of which will now be discussed.

5.3.5. Electrode tip angle

The effects of the electrode tip angle on the FAF, welding voltage and fusion cross section are illustrated by the data for plates 26, 30, 31, 32 and 33. Those effects were an 11% increase in the FAF, a 33% increase in welding voltage and a 62% increase in fused area as the tip angle was reduced from 90° to 30°. The data is presented graphically in Figure 5.14 and numerically in Table 5.5. (Conditions associated with the 90° included angle were used as a reference for the calculations of percentage variations.) These trials were performed on C-Mn steel using a welding current of 400 amps and argon as the shielding gas. It is to be appreciated that the percentage variations in arc force and arc voltage should be larger than for the FAF and welding voltage, respectively, because the latter measurements include external contributions.

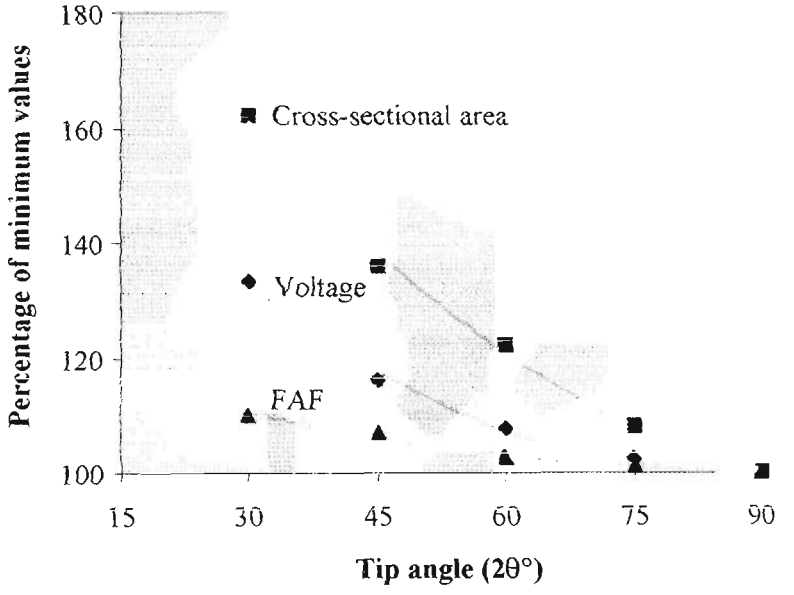

Figure 5.14. Illustration of the relative effects of variations in tip angle on FAF, welding voltage and cross sectional area of the weld bead.

Table 5.5. Variations in welding voltage, FAF and fused area with tip angle.

Plate No.	Tip Angle ($2\theta°$)	Voltage (volts)	Fused area (mm^2)	FAF (grams)
33	90	10.00	27.5	6.43 ± .01
32	75	10.24	29.7	6.50 ± .05
31	60	10.77	33.6	6.59 ± .03
26	45	11.61	37.4	6.87 ± .08
30	30	13.31	44.6	7.14 ± .07

The arc force, arc voltage and fused area are all fundamental parameters for any GTAW system, but take on extra importance for automated, high current applications such as keyhole GTAW, where operating windows can be relatively small. Therefore an understanding of the sensitivity of these parameters to electrode tip angle is of great practical importance. In the following discussion the behaviour of the FAF and voltage will be examined in some detail. Discussion of fused area will be taken up in Chapter 6.

5.3.6. Relationship of the FAF and arc voltage to tip angle

The principle relationship between the FAF and the angle of the tip can be deduced if the emission current distribution is known. Since available information suggests that the current density is relatively uniform over the surface of the emission region (eg Savage, Strunck and Ishikawa 1965) it will be assumed that the Converti approximation of (5.27) can be used. This equation can be rearranged as

$$F = \frac{\mu}{8\pi}\left(1+\ln\left(\frac{\Lambda^2}{R_e^2}\right)\right)I^2$$

Recalling (5.10) and noting that $A_d = \pi R_e^2$:

$$R_e^2 = \frac{A_e \sin\theta}{\pi}$$

Substituting this result into (5.27) and rearranging gives

$$FAF = \frac{\mu}{8\pi}\left(1+\ln\left(\frac{\pi\Lambda^2}{A_e}\right)-\ln\sin\theta\right)I^2$$

The product $\pi\Lambda^2$ is the effective anode area (and a constant) and will be symbolised as A_a, allowing the above expression to be expressed as

$$FAF = \frac{\mu}{8\pi}\left(1+\ln\left(\frac{A_a^{\,2}}{A_e}\right)-\ln\sin\theta\right)I^2 \qquad (5.28)$$

With the assumption that the cathode emission area is independent of tip angle:

$$FAF = (f_0 - f_1 \ln\sin\theta)I^2 \qquad (5.29)$$

Where

$$f_0 = \frac{\mu}{8\pi}\left(1+\ln\frac{A_a}{A_e}\right)$$

$$f_1 = \frac{\mu}{8\pi}$$

If the FAF is measured in grams then f_1 should have a value of 5.10×10^{-6} g/A^2 (cf a and b in Section 5.3.2).

The most common specification of any arc system is its current-to-voltage characteristics. Now, it is well known that for arcs conducting more than about 100A the arc voltage is approximately independent of the current, given that the arc length, electrode geometry and gas are unaltered (Lancaster 1986). It follows that, given the above constraints, the electrical resistance of high current and keyhole GTAW arcs must be very nearly inversely proportional to current.

To model this assume that the arc resistance Ω, which excludes the fall regions, can be expressed conventionally in terms of a resistivity ω_g, an arc length L and effective cross sectional area A_{eff}:

$$\Omega = \frac{\omega_g L}{A_{eff}}$$

The subscript 'g' is used to signify that the resistivity is dependent on the choice of shielding gas. Now it will be assumed that for a given arc length the effective cross sectional area is proportional to the cross sectional area of the cathode emission region A_d. Therefore

$$\Omega = \frac{\omega_g L}{A_d}$$

However, by (5.10) $A_d = A_e \sin\theta$. Furthermore, since A_e (the emission area of the cathode) is proportional to the arc current I,

$$\Omega = \frac{\omega_g L}{A_e \sin\theta}$$

$$\approx \frac{\omega_g L}{I \sin\theta}$$

$$\approx \frac{V_1}{I \sin\theta}$$

The value of V_1 in the final relation is dependent on the choice of gas and the arc length. The arc voltage can now be estimated as the sum of the cathode and anode falls, V_0 say, and the ohmic component $I\Omega$:

$$V = V_0 + I\left(\frac{V_1}{I \sin\theta}\right)$$

$$= V_0 + \frac{V_1}{\sin\theta} \qquad (5.30)$$

This result describes the arc voltage as dependent on tip angle but independent of current, as required.

The predictions of (5.29) and (5.30) for the FAF and arc voltage respectively can be compared to the experimental results provided in Table 5.5. For convenience the current has been combined with the coefficients in (5.29) since for these experiments it was constant. Thus $F_0 = f_0 I^2$ and $F_1 = f_1 I^2$. Least squares error values for the coefficients F_0, F_1, V_0, and V_1 were determined by regression and yielded the following equations:

$$FAF = 6.146 - 0.728 \ln \sin\theta \qquad RMS\ error = 0.034 g$$

$$V = 8.039 + \frac{1.364}{\sin\theta} \qquad RMS\ error = 0.023 V$$

The voltages and forces for each tip predicted by these equations are shown in Table 5.6. The agreement between the measured and best-fit values is very good for both FAF and welding voltage. The discrepancies in voltages in particular are less than 1% of the total variance.

Table 5.6. Least-squares fit predictions of voltage and FAF as functions of tip angle.

Tip angle *(2θ°)*	**Meas. Volts** *(volts))*	**Best-fit** *(volts)*	**Meas. Force** *(grams)*	**Best-fit** *(grams)*
90	10.00	9.97	6.43 ± .01	6.40
75	10.24	10.28	6.50 ± .05	6.51
60	10.77	10.77	6.59 ± .03	6.65
45	11.61	11.60	6.87 ± .08	6.84
30	13.31	13.31	7.14 ± .07	7.13

The above results are encouraging but the best-fit value for F_1 differs slightly from that of the model. In fact f_1 evaluation of F_1 for a welding current of 400 amps gives,

$$F_1 = 0.816 g$$

Accordingly, one would have expected

$$FAF = F_0 - 0.816 \ln \sin\theta \qquad (5.31)$$

The reason for the discrepancy could be the assumption that the emission current density is independent of tip angle (see 5.3.8). At present however, it is useful to use the theoretical value of F_1 and redo the regression for F_0 only. The result is still a good fit:

$$FAF = 6.078 - 0.816 \ln(\sin\theta) \qquad RMS\ error = 0.047\ g$$

The least-squares error estimates and the measured FAF values are shown numerically in Table 5.7 and graphically in Figure 5.15.

Table 5.7. Predictions of FAF using least squares error estimates of both F_0 and F_1 Pred.1) and only F_1 (Pred. 2).

Tip angle *(2θ °)*	**Meas. FAF** *(grams)*	**Pred. 1** *(grams)*	Pred. 2 *(grams)*
90	6.43 ± .01	6.40	6.36
75	6.50 ± .05	6.51	6.48
60	6.59 ± .03	6.65	6.64
45	6.87 ± .08	6.84	6.86
30	7.14 ± .07	7.13	7.18

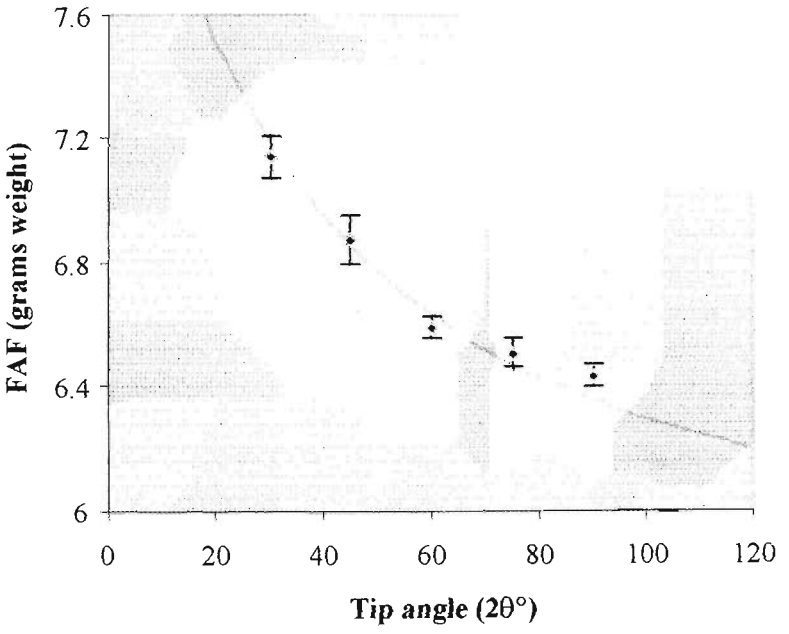

Figure 5.15. FAF values measured for various tip angles compared with the prediction: FAF = 6.078 – 0.81 ln(sin 2θ).

The predictions based on a theoretical value of F_1 appear to slightly underestimate the FAF at large tip angles, and overestimate it at small angles. Nevertheless the agreement between the measurements and the predictions is sufficient to justify acceptance of the underlying description as a useful approximation. In doing so it draws attention to several important issues. Most importantly, the arc force, arc voltage and total fusion cross section all show significant sensitivity to the condition of the electrode tip, and this has obvious practical implications for the various welding processes. In particular, penetration in melt-in mode welding is dependent on fusion area, while in the keyhole GTAW process it is sensitive to changes in arc force. Neither of these parameters is easily measured during welding, and therefore the associated changes in voltage, which are readily monitored, take on added significance. For example, in the above case the FAF has a simple dependence on voltage. Rearranging (5.30) to express $\sin\theta$ in terms of voltages, and then substituting into (5.29) gives

$$\sin\theta = \frac{V_1}{V - V_0}$$

$$FAF = \left(f_0 - f_1 \ln \frac{V_1}{V - V_0} \right) I^2 \qquad (5.32)$$

Inserting the theoretical value for F_1 and using the determined values of V_0 and V_1 gives

$$FAF = F_0 - 0.816 \ln \frac{1.364}{V - 8.039} \qquad (5.33)$$

Finally the limited scope of the semi-empirical formulae (eg (5.29) and (5.30)) need to be appreciated. Specifically both relations are built on assumptions of constant current density over the cathode emission regions, fixed arc lengths at changing tip angles, and the general independence of arc voltage from arc current, all of which are approximations.

5.3.7. Electrode diameter

The electrode diameter was varied between 2.4 and 6.35 mm in the trials 25 to 29. The welds were made on C-Mn steel using argon as the shielding gas. Relevant results taken from Table 5.3 are presented numerically in Table 5.8 (see also Figure 5.16 below).

Table 5.8. Variation of voltage and arc force with electrode (cathode) diameter.

Plate No.	**Cathode dia.** *(mm)*	**Voltage** *(volts)*	**FAF** *(grams)*	**Fused area** *(mm^2)*
25	2.4	11.63	6.65 ± .07	33.8
26	3.2	11.61	6.87 ± .08	37.4
27	4.0	11.83	6.93 ± .03	45.3
28	4.8	13.17	6.92 ± .08	48.0
29	6.35	13.77	7.24 ± .07	51.3

The data show that the changing of the electrode diameter has a significant effect on welding voltage, FAF and fusion area. The measured FAF increased from 6.65 to 7.24 grams, or about 9%, with increasing electrode diameter. Arc voltage increased by 18% (from 11.63 to 13.77 V), and fused area by 51%, for the same experiments. The increase in voltage was not very uniform, and in particular, showed a step as the electrode increased from 4.0 to 4.8 mm.

Consistency between the data and the proposed model requires that the emission region of the cathode contracted as the electrode diameter increased (see (5.28)). Such a relationship between the emission region and electrode diameter has been reported in the literature, for example in the work of Savage, Nippes and Agusa (1979). This effect might be attributed to improving heat extraction from the tip as the electrode diameter increases since the thermal conduction of the electrode increases with its cross-sectional area. The consequences of a contraction of the emission region would be similar to a reduction of the tip angle.

If increasing the electrode diameter has a similar effect on the arc to a reduction in tip angle, then the respective voltage behaviours should also be similar. However, the

voltage measurements include the voltage drop due to the resistance of the electrode, and in this case that would reduce as the diameter is increased. In fact measurements have indicated that the voltage drop associated with a 3.2mm electrode and a welding current of 400 amps is approximately one volt. Furthermore, the voltage drop across the electrode should have halved as it was increased from 2.4 to 3.2 mm diameter, possibly masking other effects.

5.3.8. Results in terms of emission current density

The contraction of the emission region with increasing electrode diameter is a very useful finding. It would be even better if the resultant current densities over the respective emission areas of the electrodes could be estimated. Unfortunately there is insufficient information available to achieve this, but the current densities can be presented as ratios to a selected reference condition. This can be done as follows.

Suppose one has a pair of FAF determinations, FAF(1) and FAF(R), the latter to be used as the reference. Then by (5.28)

$$FAF_1 = \frac{\mu}{8\pi}\left(1+\ln\left(\frac{A_a^{\,2}}{A_{e1}}\right)-\ln\sin\theta_1\right)I_1^2$$

and

$$FAF_R = \frac{\mu}{8\pi}\left(1+\ln\left(\frac{A_a^{\,2}}{A_{eR}}\right)-\ln\sin\theta_R\right)I_R^2$$

Before proceeding it is noted that if the FAF measurements are in grams weight instead of newtons then the constant ($\mu/8\pi$) is replaced by the value 5.10×10^{-6}. For convenience the appropriate constant will be identified by the constant 'a'. Then

$$\frac{FAF_1}{I_1^2}-\frac{FAF_R}{I_R^2} = a\left[\left(1+\ln\frac{A_a}{A_{e1}}-\ln\sin\theta_1\right)-\left(1+\ln\frac{A_a}{A_{eR}}-\ln\sin\theta_R\right)\right]$$

After some rearranging and cancellation:

$$\frac{FAF_1}{I_1^2} - \frac{FAF_R}{I_R^2} = a\left(\ln\frac{A_{eR}}{A_{e1}} - \ln\frac{\sin\theta_1}{\sin\theta_R}\right)$$

Now the surface area of the emission region, A_e, can be found by dividing the total current by J_e, the mean current density on the surface,

$$A_e = \frac{I}{J_e}$$

Substituting for A_{eR} and A_{e1} gives

$$\frac{FAF_1}{I_1^2} - \frac{FAF_R}{I_R^2} = a\left(\ln\frac{J_{e1}I_R}{J_{eR}I_1} - \ln\frac{\sin\theta_1}{\sin\theta_R}\right)$$

With some rearrangement

$$\ln\frac{J_{e1}I_R}{J_{eR}I_1} = \frac{1}{a}\left(\frac{FAF_1}{I_1^2} - \frac{FAF_R}{I_R^2}\right) + \ln\frac{\sin\theta_1}{\sin\theta_R}$$

Taking the exponential of each side,

$$\frac{J_{e1}I_R}{J_{eR}I_1} = Exp\left[\frac{1}{a}\left(\frac{FAF_1}{I_1^2} - \frac{FAF_R}{I_R^2}\right)\right]\frac{\sin\theta_1}{\sin\theta_R}$$

Or finally

$$\frac{J_{e1}}{J_{eR}} = \frac{I_1\sin\theta_1}{I_R\sin\theta_R}Exp\left[\frac{1}{a}\left(\frac{FAF_1}{I_1^2} - \frac{FAF_R}{I_R^2}\right)\right] \qquad (5.33)$$

where

$$a = \frac{\mu}{8\pi} \qquad \textit{if the FAF is in newtons}$$

$$= 5.10x10^{-6} \qquad \textit{if the FAF is in grams weight}$$

This result was applied to the data presented in Table 5.3. For this exercise the FAF result for Trial 26 was used as the reference. The calculated ratios J_{en}/J_{e26} are presented in Table 5.9.

Table 5.9. Table of emission current density determinations.

No.	Material	Shield gas	Arc current *(amps)*	Arc Gap *(mm)*	Tip *(2θ°)*	Elect. Dia. *(mm)*	J_{en}/J_{26}
1	C-Mn Steel	Ar	500	+2.0	45	3.2	1.12
2	C-Mn Steel	Ar	500	0.0	45	3.2	0.75
3	C-Mn Steel	Ar	500	-2.0	45	3.2	1.11
4	C-Mn Steel	Ar	300	0.0	45	3.2	0.96
5	C-Mn Steel	Ar	100	0.0	45	3.2	10.49
6	AA5083	Ar	300	0.0	45	3.2	0.87
7	AA5083	Ar	100	0.0	45	3.2	22.96
8	AA6060	Ar	200	0.0	45	3.2	0.44
9	AA5083	Ar	400	0.0	45	3.2	1.25
10	AA5083	He-25Ar	300	0.0	45	3.2	0.79
11	AA6060	He	300	0.0	45	3.2	0.65
12	AA5083	He	300	0.0	45	3.2	0.57
13	*Aborted*						
14	C-Mn Steel	He-25Ar	300	0.0	45	3.2	0.67
15	AA5083	Ar	200	0.0	45	3.2	0.36
16	AA6060	He	300	+2.0	45	3.2	1.34
17	AA6060	He	500	-2.0	45	3.2	0.41
18	AA6060	He	500	-4.0	45	3.2	0.42
19	C-Mn Steel	He	300	0.0	45	3.2	0.55
20	AISI304	He	300	0.0	45	3.2	0.54
21	Copper	He	300	0.0	45	3.2	0.57
22	Copper	He	400	0.0	45	3.2	1.09
23	AISI304	He	400	0.0	45	3.2	1.33
24	C-Mn Steel	He	400	0.0	45	3.2	0.80
25	C-Mn Steel	Ar	400	0.0	45	2.4	0.76
26	C-Mn Steel	Ar	400	0.0	45	3.2	1.00
27	C-Mn Steel	Ar	400	0.0	45	4.0	1.08
28	C-Mn Steel	Ar	400	0.0	45	4.8	1.06
29	C-Mn Steel	Ar	400	0.0	45	6.4	1.57
30	C-Mn Steel	Ar	400	0.0	30	3.2	0.94
31	C-Mn Steel	Ar	400	0.0	60	3.2	0.93
32	C-Mn Steel	Ar	400	0.0	75	3.2	1.01
33	C-Mn Steel	Ar	400	0.0	90	3.2	1.08

Physically the emission current density of the electrode is dependent on the electrode work function and the surface temperature, as described by the Richardson-Dushman equation (Lancaster 1986). Since all electrodes were of the same material in these experiments, an increase in the emission current density must correspond to an increase in temperature over the emission region. Consequently the postulated contraction of the

emission region with increasing electrode diameter must be accompanied by an increase in its temperature. Put another way, improving the heat extraction from the tip causes the emission region to get smaller and hotter.

If the above results are applied to Table 5.7 if will be found that the required increase in emission current density is quite large. In fact the current density would appear to have doubled as the electrode diameter was increased from 2.4 to 6.4mm, as shown in numerically Table 5.10 and graphically in Figure 5.16.

Table 5.10. Dimensionless emission current densities calculated for the FAF values in Table 5.7.

Electrode dia. *(mm)*	**FAF** *(grams)*	J_e/J_r
2.4	6.65 ± .07	0.76
3.2	6.87 ± .08	1.00
4.0	6.93 ± .03	1.08
4.8	6.92 ± .08	1.06
6.35	7.24 ± .07	1.57

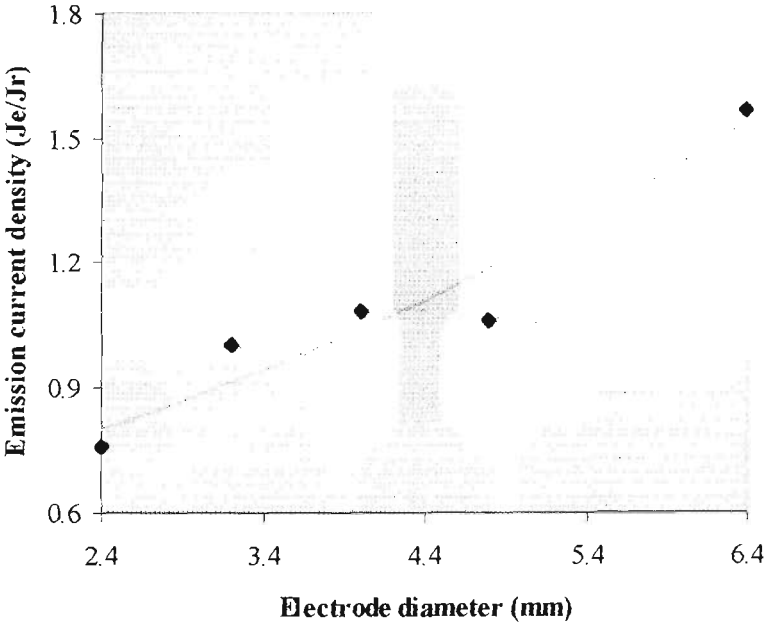

Figure 5.16. Current densities (points) inferred from FAF measurements for various diameter electrodes. The solid line is the trend line.

The result that improving the heat extraction from the cathode tip increases the emission current density suggests a correction to the relationship between FAF and tip angle (5.29). Specifically as the tip angle is increased the heat extraction should improve and increase the emission current density. The assumption of a constant emission current density would then overestimate the current density at low tip and underestimate it at large angles. The current densities required to provide perfect matching to the data are shown in Table 5.11. The results show that the current densities are approximately constant, as originally assumed. However, there is a small variation that is consistent with the expected consequences of the changing heat conduction from the tip. The data is presented graphically in Figure 5.17, using the same vertical scale as in Figure 5.16 for ease of comparison.

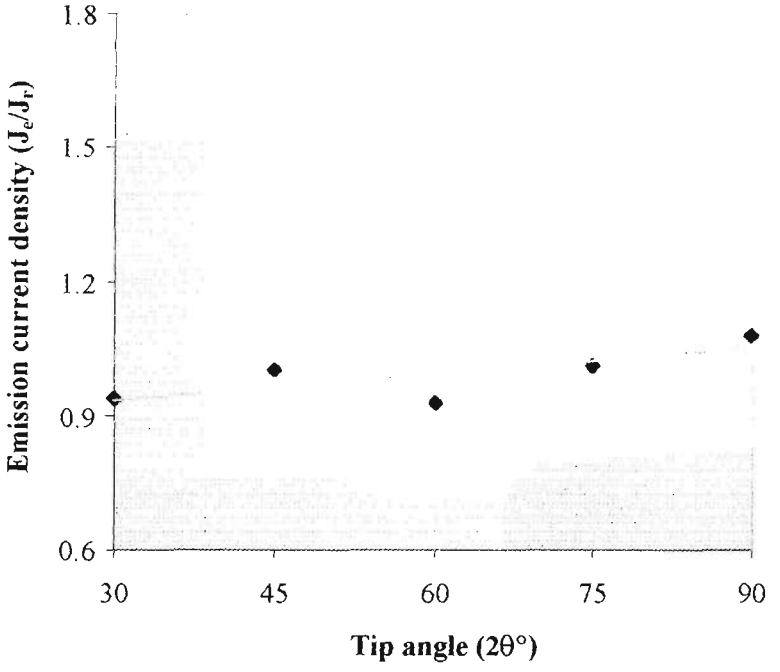

Figure 5.17. Current densities (points) inferred from FAF measurements for various electrode tip angles. The solid line is the trend line.

Table 5.11. Variations in emission current density with tip angle that would be required to account for the discrepancies between FAF measurements and predictions presented in Table 5.6.

Tip angle. *(2θ °)*	**FAF** *(grams)*	**Required** J_e/J_r
90	6.43 ± .01	1.08
75	6.50 ± .05	1.01
60	6.59 ± .03	0.93
45	6.87 ± .08	1.00
30	7.14 ± .07	0.94

5.3.9. Shielding gas composition

Only three shielding gases were used: argon, helium and a mix of 25% argon in helium. The effects of the different gases were examined in the trials 4, 14 and 19 for steel, and 6, 10 and 12 for aluminium. The results are presented in Table 5.12 and Figure 5.18.

Table 5.12. Variation of voltage, arc force and emission current density with shielding gas composition.

Plate No.	**Material**	**Shield gas**	**Voltage** *(volts)*	**FAF** *(grams)*	J_e/J_r
4	C-Mn steel	Ar	9.91	3.98	0.96
14	C-Mn steel	He-25Ar	11.90	3.81	0.67
19	C-Mn steel	He	13.07	3.72	0.55
6	AA5083 Al	Ar	10.07	3.93	0.87
10	AA5083 Al	He-25Ar	14.57	3.89	0.79
12	AA5083 Al	He	18.02	3.74	0.57

The major effect was an increase in welding voltage with helium concentration. This increase amounted to 32% for steel and almost 80% for aluminium. The more rapid increase in voltage with helium concentration found with aluminium may have been due to a greater displacement of the aluminium pool (and consequent lengthening of the arc) as the heat input increased, as would be consistent with previous discussions.

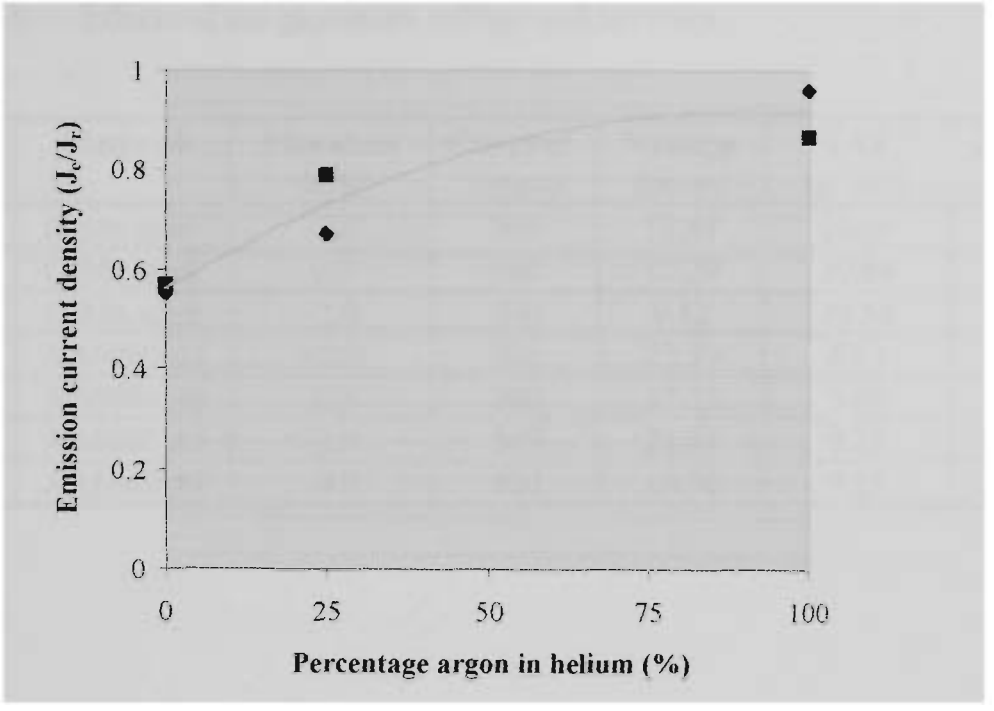

Figure 5.18. Inferred variation in emission current density with change in shielding gas composition. Diamond symbols are for steel, squares are for aluminium. The solid line indicates the trend.

The data reveal a decrease in arc force with increasing helium concentration in the shielding gas. Since the current was fixed, this trend must be associated with an increase in R_e, and equivalently a decrease in the emission current density. Such an effect is plausible because helium has a much greater thermal conductivity than argon, and so would provide increased heat transport from the plasma to the tip. An increase in heat flowing into the tip will have the same consequence as a reduction in heat being removed from it, and would therefore lead to a reduction in the emission current density. This can be seen as an extension of the argument concerning the influence of the electrode diameter.

5.3.10. Electrode elevation

The final variable was electrode elevation. Unfortunately, it was not possible to cover the range of elevations chosen without varying other conditions due to difficulties in maintaining a stable arc and weld pool crater. Results from C-Mn steel and AA6060 aluminium are presented below in Table 5.13 and graphically in Figure 5.19.

Table 5.13. Effects of arc gap on arc voltage and arc force.

Plate No.	Material	Elevation *(mm)*	Current *(amps)*	Voltage *(volts)*	FAF *(grams)*	J_e/J_R
1	C-Mn steel	+2.0	500	15.89	10.59	1.12
2	C-Mn steel	0.0	500	13.29	10.08	0.75
3	C-Mn steel	-2.0	500	9.82	10.58	1.11
16	AA6060 Al	+2.0	300	23.39	4.13	1.34
11	AA6060 Al	0.0	300	17.25	3.80	0.65
17	AA6060 Al	-2.0	500	21.41	9.31	0.41
18	AA6060 Al	-4.0	500	16.70	9.35	0.42

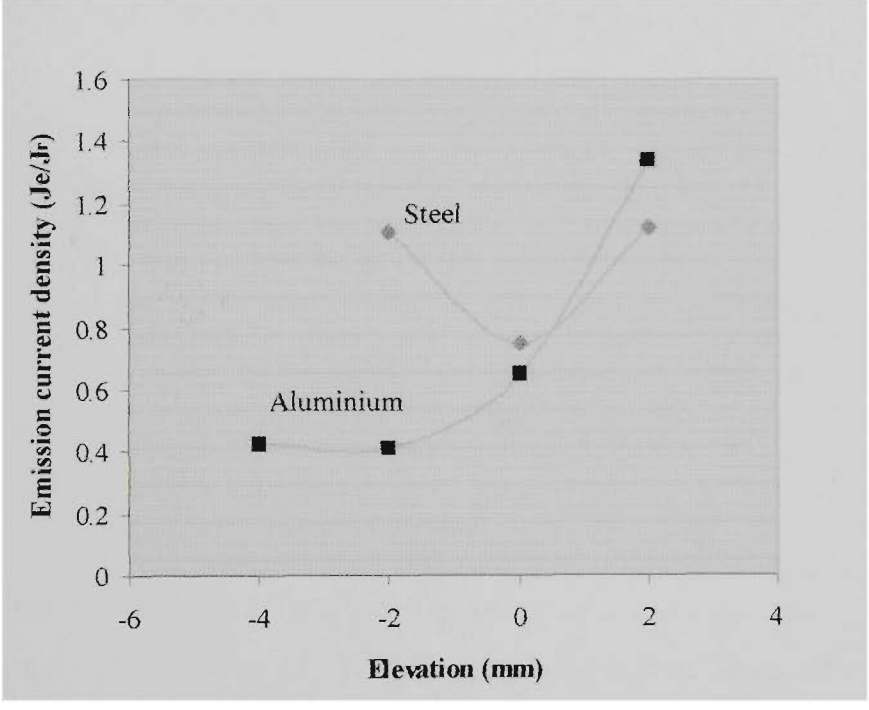

Figure 5.19. Inferred variation in emission current density with change in electrode elevation. Negative elevation means the electrode tip was immersed into the weld pool crater.

In all cases reducing elevation reduced the arc voltage and hence the heat input. The forces measured for the steel at +2.0, 0.0 and -2.0 mm showed the force to be lowest (by about 5%) at 0 mm elevation. Correspondingly, the emission current density dropped by one-third as the electrode elevation was changed from +2.0 to 0.0, but subsequently increased with submersion. The results for aluminium are not entirely similar. Although the maximum emission current density occurred for the elevated

position, and dropped rapidly as the electrode approached the plate, no significant reversal was observed with continued submersion.

The implication appears to be that the electrode position affects the emission current density. The observation of a minimum in the case of the steel substrate may indicate the action of two mechanisms. For example, the emission region may initially expand as the electrode tip approaches the plate due to increased geometrical divergence of the electric field surrounding the tip and an expansion of the area in contact with the plasma. Eventually, however, the energy transfer to the tip must succumb to the falling energy within the arc with increasing submersion (as indicated by falling arc voltage) and the emission area must begin to contract.

6. The role of the arc in keyhole GTAW

6.1. Review

6.1.1. Conduction through an arc

Under standard conditions all shielding gases are extremely good electrical insulators. The current densities typical of welding arcs (of the order of tens of amps per square millimetre) can only be achieved if a high concentration of charged particles can be generated and maintained in the conducting channel. In arcs the necessary populations of electrons and ions are maintained by thermal ionisation, and this requires temperatures of about 10,000K and above.

The degree of ionisation of a gas can be expressed as a function of temperature by the Saha equation (Lancaster 1986), and the resultant conductivity is then determined from consideration of the charge mobilities, as can be found in standard texts, eg (Lorraine and Corson 1970) and (Papoular 1965). An example of how the conductivity varies with temperature is tabulated in Table 6.1 and presented graphically in Figure 6.1. The data is taken from Lancaster (1986), and is for argon at atmospheric pressure.

It is well established that the current density in an arc column has a limiting value under normal conditions. Once this limit is reached further increases in total current only distribute the current over larger areas of the anode, with no appreciable change in peak current density on the arc axis (Jackson 1960). In the case of argon the conductivity increases until doubly ionised argon appears at about 22000 K. These ions impede electrons more that the extra number of electrons can compensate for, and there is a local maximum (see Figure 6.1). Once this condition has been reached in a particular region further increases in current will tend to generate a spreading of the current distribution into the adjacent, slightly cooler regions (Shaw February 1975). A useful rule is that 'the most stable and reproducible condition is that which allows the arc to operate at the lowest possible voltage' (Jackson 1960).

Table 6.1. The electrical conductivity of argon from 3000K to 30000K, at one atmosphere pressure.

Temperature *(degrees K)*	**Electrical conductivity** *(mho/m)*
3000	0.00006
4000	0.127
5000	10.3
6000	101
7000	361
8000	923
9000	1770
10000	2730
12000	4740
14000	6670
16000	8200
18000	9430
20000	10400
22000	10800
24000	10500
26000	10200
28000	10400
30000	10900

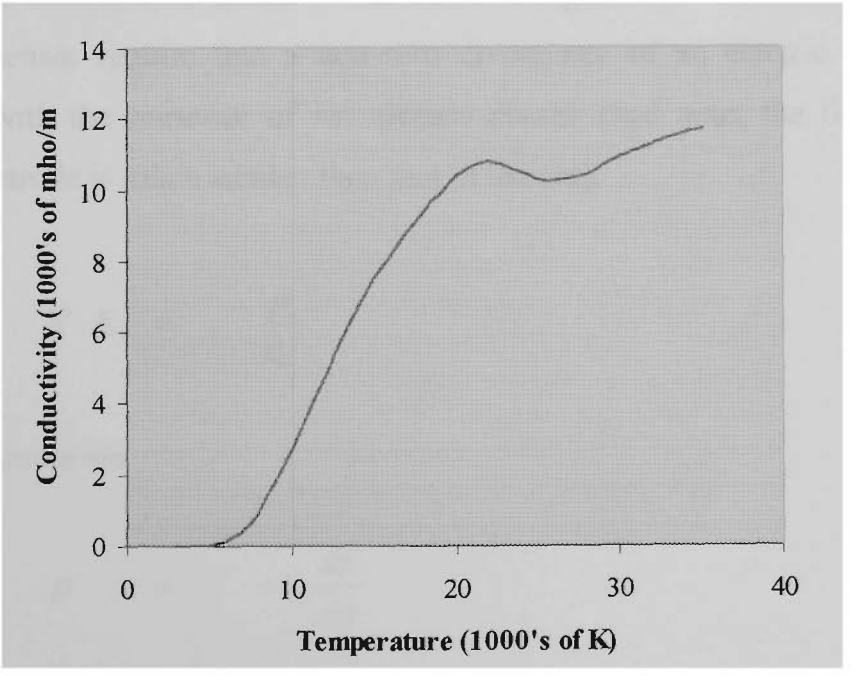

Figure 6.1. Plot of the electrical conductivity of argon from 3,000K to 30,000K.

6.1.2. Sheath regions

The temperatures of the order of 10,000K needed for good electrical conductivity cannot be met at all points between the electrodes. Convection, conduction and radiation losses limit the conduction path to a relatively narrow channel. In addition, the gases close to the electrode surfaces must approach the temperatures of those surfaces (Jackson 1960). Even if the electrodes were vaporising the temperature would still be thousands of degrees below that required for significant ionisation of the shielding gas. In other words the regions immediately adjacent the electrodes are too cold for the thermal generation of ions, and the conductivity should be relatively low. This situation may be moderated by the presence of the more readily ionised metallic vapours, but the formation of a non-conductive transition region remains inevitable. These near-surface regions are known as the anode and cathode sheaths, depending on the electrode with which they are to be associated.

The generation of the sheath regions has several consequences. Of particular importance is that a significant fraction of the total arc resistance can be attributed to the resistivity of these two regions. It also follows that the electric field of the arc cannot be uniform, but should be relatively much stronger close to the electrodes. An idealised one-dimensional model is illustrated in Figure 6.2. Maxwell's equations for electromagnetism require that a non-zero divergence of an electric field must be associated with the presence of net electric charge (and note, the field inside the metallic electrode is much weaker than that in the arc):

$$\nabla \cdot E = \frac{\rho}{\varepsilon_0}$$

Or, in one dimension

$$\rho = -\varepsilon_0 \frac{dE}{dx} \tag{6.1}$$

The physical implication is that each sheath region is bounded by regions of charge, one on the electrode surface and the other at the interface with the plasma. This latter constitutes a region of space charge.

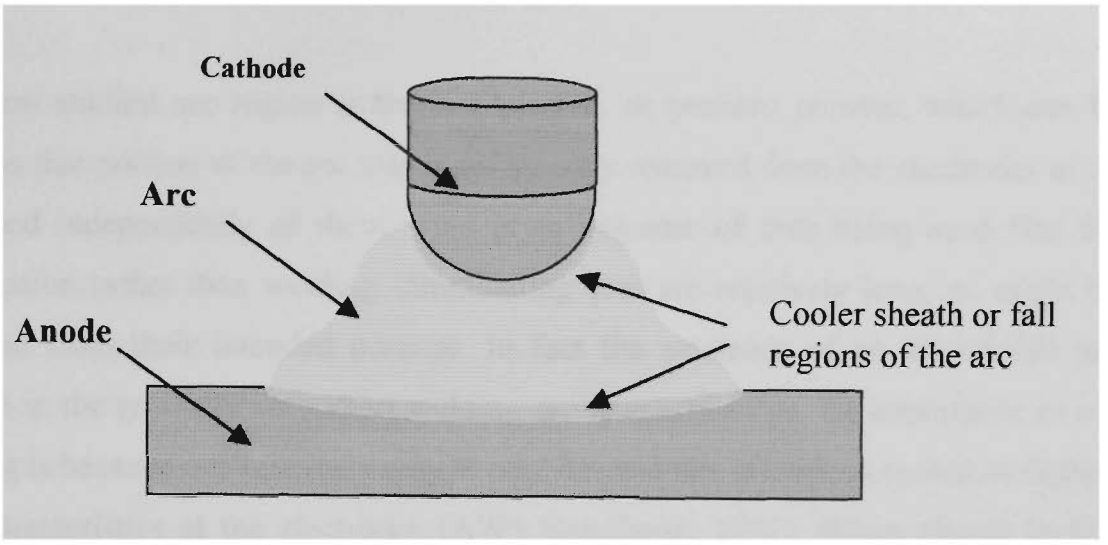

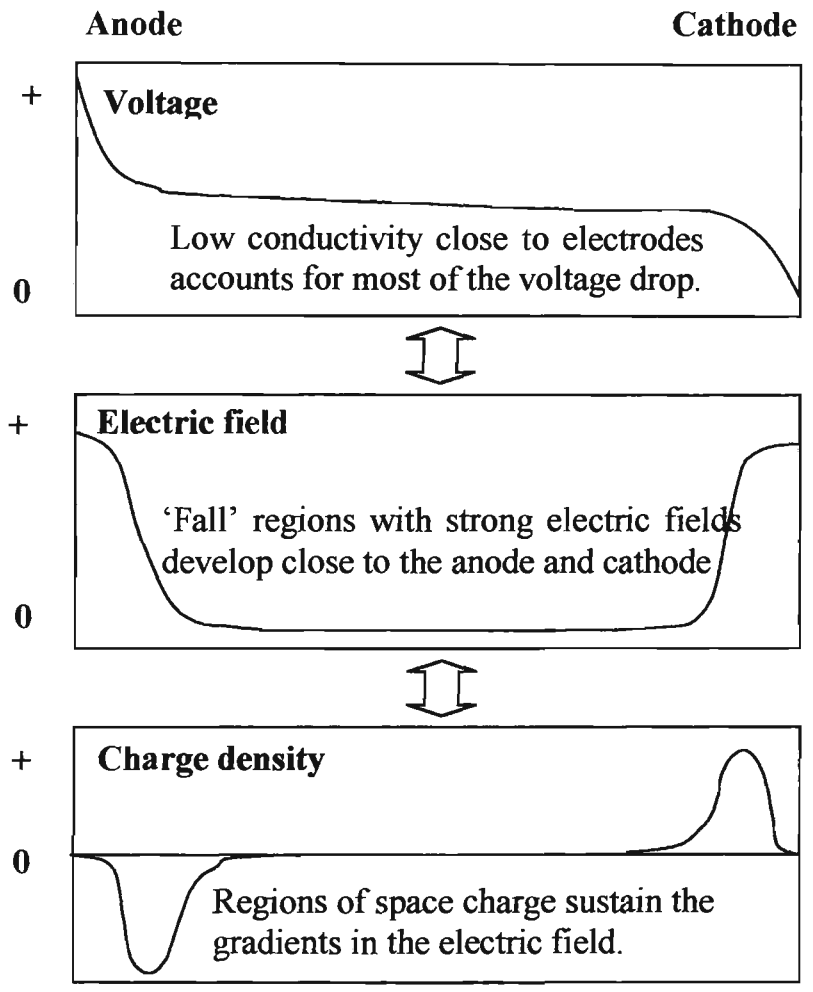

Figure 6.2. Schematic illustrations of the variation in voltage, electric field and charge densities with position along an arc discharge.

6.1.3. Arc column

The most-studied arc region is the arc, plasma, or positive column, which can be taken as that portion of the arc that is sufficiently removed from the electrodes to be described independently of them. This is an outcome of arcs being used first for illumination rather than welding. Illuminating arcs are relatively long, as might be expected from their intended purpose. In fact the existence of an identifiable arc column in the typically very short welding arc is questionable. Its importance in arc welding is because it is relatively easy to analyse, and this provides a means to deduce arc characteristics at the electrodes (AWS Handbook, 1991). When placed in this context the contributions of Glickstein (1981) represented a significant development in the understanding of welding arcs. He introduced electric field strength measurements as an aid to estimating gross arc behaviour and showed that the shape of the electrode has a strong influence on the electric fields within the arc and on the discharge configuration.

In developing this approach Glickstein introduced a simple 1-D model for the positive column in which he equated ohmic heating to radial thermal conduction:

$$\sigma E^2 = \frac{-1}{r}\frac{d}{dr}\left(rk\frac{dT}{dr}\right)dr \qquad (6.2)$$

where σ is the electrical conductivity, E the electric field, r the radius from the arc axis, k the thermal conductivity and T the temperature. Equation (6.2) is known as the Elenbaas-Heller equation.

The electrical and thermal conductivities of shielding gases have complicated temperature dependencies. However, Glickstein was able to find numerical solutions to equation (6.2) for those cases where the appropriate thermo-physical data was available. The approach proved to be very useful. For example, his solutions predicted that helium arcs should be much broader than argon, but that the peak temperatures and current density distributions would be similar. Glickstein used this result to argue that helium arcs should require higher voltages than argon arcs - as is observed - since the energy is derived from the electric field. The model also correctly predicted that

vapour contamination would significantly alter the arc configuration. Even minor addition of a gas of lower ionisation potential was shown to enhance electrical conductivity over a limited range of temperature. The interpretation was that such additives would begin to ionise at a much lower temperature than the carrier gas (usually argon or helium) and thereby increase the conductivity at that temperature. On increasing the temperature the conductivity would continue to rise until the additive is fully ionised. Further increases in conductivity must then result from ionisation of the carrier gas, and this may not become significant until much higher temperatures are reached. As a practical matter however, the temperatures at issue are still high relative to pool temperatures. For example, the ion population in iron vapour at 4000K is about 100,000 times greater than that in argon at the same temperature, but is still only about one part in 10,000 (Lancaster, 1986).

Despite the success of Glickstein's model it is nevertheless a considerable over-simplification of the situation. In particular, the Elenbaas-Heller equation does not allow for energy losses through radiation, and because of this it is only justified for currents below 100 amps (Lancaster 1986). However, if S(T) is the energy loss by radiation per unit volume the 'corrected Elenbaas-Heller' equation becomes

$$\sigma E^2 = \frac{-1}{r}\frac{d}{dr}\left(rk\frac{dT}{dr}\right)dr + S(T) \qquad (6.3)$$

It turns out that this refined description is also over-simplistic. For example, as Lancaster (1986) pointed out, cylindrical free burning arcs are unstable and must be stabilised by external means such convection into the weld pool. Therefore equations that consider conduction and radiation only may not be appropriate for modelling arc behaviour. In fact, it is now believed that free-burning arc properties, such as size, shape and temperature, are largely dominated by convective flow (Zhu et al, 1992). Zhu attributed convective flow to Lorentz forces for currents over about 40 amps, and thereby further limited the validity of both (6.2) and (6.3). The linking of convection to Lorentz forces is suggestive of the importance of both in the high current and keyhole modes of GTAW.

6.1.4. The anode region

The anode region is often studied to gain insight into heat transfer to the weldment and the factors that influence it. In particular, the heat balance at the anode determines the overall efficiency of the welding process. Some factors identified as contributing to the heat balance include the action of vaporised material on work function, the anode fall (the voltage drop across the anode sheath) and temperature gradient close to the anode (Quigley et al 1973).

In 1973 Quigley et al reported the results of a spectroscopic study of a gas-tungsten arc on steel (Quigley et al 1973). They began their analysis by identifying the energy transport processes occurring at the anode. These are shown in Table 6.2. One of their primary objectives was to include the impact of a molten weld pool. In this regard they discovered that a significant amount of metal was vaporised by the intense localised heat flux. However, the bulk of this material recondensed on cooler regions of the pool with only a small net loss of metal. A significant effect of the vaporisation was therefore to provide an effective mechanism for the redistribution of the heat flux over a wider area, thereby complimenting the effects of conduction, convection and radiation.

Their study further showed that the spectrum near to the anode was due entirely to iron; near the cathode it was entirely due to argon; and at intermediate positions both species were present. This was strong evidence for vapours from the anode diffusing into the arc and modifying its properties. They anticipated that this would have important consequences for the process behaviour. Such an expectation would appear well founded, especially in light of the subsequent work of Glickstein (1981). Their conclusion was that the presence and consequence of iron vapour in the plasma was a compelling reason to reject previous results obtained on chilled copper anodes (Quigley et al 1973). In addition, these observations highlighted the limitations (and perhaps dangers) of studying aspects of the welding process in isolation, and this has become a recurrent warning throughout the literature (Jackson 1960, Quigley 1973, Shaw 1975, Glickstein 1981 and many others). Despite these dangers however, studies of specific effects in isolation remain essential steps to the formulation of a complete description of welding processes.

Table 6.2. Energy transport mechanisms at an arc anode (Quigley et al 1973).

Mechanism	Mathematical form
Heating	
Electron work function	$I.\phi$
Thermal energy of electrons	$I.(3k_B/2e)(Te-Ta)$
Current crossing anode fall	I.Va
Conduction	kAdT/dx
Convection	k'AdT/dx
Radiation	$\varepsilon\sigma T^4$
Cooling	
Surface radiation	$\varepsilon\sigma T^4$
Vaporisation	Log W = A-B/T - ½ log T + C

In this table:

I = current,	V_a = anode fall voltage
ε = emissivity	T = temperature
ϕ = work function	T_e = electron temperature
σ = Stefans constant	T_a = anode temperature
k_B = Boltzman's constant	k = thermal conductivity
e = electronic charge	k' = effective thermal conductivity
W = weight	A, B and C are constants.

The first three energy transport processes identified in Table 6.2 are associated with the passage of electrons from the plasma to the anode. Put another way, the energy transported by each of these three processes is proportional to the current, and their total contribution is:

$$E(I) = \left(\phi + V_a + \frac{3k_B}{2e}(T_e - T_a)\right)I \qquad (6.4)$$

The largest of these contributions is due to release of electron binding energy, $I\phi$, as the electrons are absorbed into the anode. The work function, ϕ, is typically about 4.5 volts (Nestor 1962). The second term ($I.V_a$) is due to the energy gained by the electrons crossing the anode fall. Again according to Nestor, V_a is between about 1 and 5 volts. The final term is the electron thermal energy carried from the plasma to the anode, and is equal to $(3k_B/2)(T_e-T_a)$ per electron (this is otherwise known as the Thomson effect). Taking the temperature of the plasma as 10,000K and the anode as

3,000K, this term can be equated to a further voltage drop of about 0.9 volts. Conservatively the effective voltage drop for these three mechanisms is at least 6 volts and likely higher.

In Quigley et al's study the overall transfer efficiency was 44.4%. This was for a 100 amp, 1600W arc in argon, impinging on a steel plate. It can be inferred that the arc voltage must have been 16V, and that the heat transfer efficiency due to the three current-dependent mechanisms alone would have been about 37.5%. Furthermore, since this electronic contribution is apparently independent of parameters such as electrode configuration, shielding gas and arc length, the conclusion must be that conduction, convection and radiation played only a minor role in the above case. More generally, in so far as these other parameters affect the heat transfer they must do so by altering either conduction or convection within the arc since anode losses to radiation and vaporisation are both small.

Although it has long been recognised that the anode composition influences the arc characteristics, studies have tended to focus their attentions elsewhere. This is a situation that may need to be addressed in the future. An indication that this may be so is the development of so-called active fluxes for GTAW by the E. O. Paton Institute of Electric Welding. These fluxes may be produced as a powder suspended in a volatile liquid such as acetone. The suspension is painted or sprayed along the weld joint immediately before welding and then allowed to dry. The original flux compositions were based on fluorides, although more recent formulations are apparently mixtures of oxides (Tanaka et al, 2000). A very small amount of the flux is required, and this is ultimately vaporised by the arc. It is claimed to be equally suitable for both GTAW and plasma keyhole welding.

According to Lucas and Howse (1996) the effects are very significant. In particular, the flux causes a very significant increase in penetration. Increases in penetration of between 1.5 and 2.5 times have been claimed for stainless steels. Despite its potential benefits however, the mechanisms underlying the process are still under discussion. One proposition is that the flux introduces vapours into the periphery of the arc (Eroshenko et al 1997), and these reduce the free electron concentrations (Lucas and

Howse 1996). The implication is that this effect would concentrate the anode root, and this would result in deeper penetration.

However, the fusion profiles associated with this process show depth-to-width ratios significantly greater than one. Such profiles cannot be generated by conduction alone, even if the heat source were constricted to a single point. Other mechanisms must be involved to efficiently transport the transferred energy from the surface to the bottom of the pool. Consequently the prevailing view is that an altered fluid flow is involved. In particular, if the flux were surface active (as oxides tend to be) but was vaporised from the central regions of the pool, then the surface tension would increase from the edges towards the centre of the pool. The fluid would then flow across the surface from the edges to the centre, then to the bottom, to return across the floor of the crater to the outer edges.

The reported effects of activating fluxes illustrate that changes in the anode environment can have quite dramatic consequences for process performance. This realisation raises the possibility that the high current weld pool, and more specifically the GTAW keyhole, may also present environments that generate significantly altered transfer characteristics to those of more conventional arc processes. For example, surface distortion increases the area available for conductive heat transfer and may also alter vapour concentrations in the arc. In addition the geometry of a keyhole would radically alter the flow characteristics of the arc gases, with potential consequences for convective heat transfer.

6.1.5. Influence of the cathode tip on arc properties

The implications of the electrode tip angle, or taper, have been discussed extensively in Chapter 5. However, further review of the literature is worthwhile to gain an appreciation of some wider implications.

The role of arc forces in welding has been recognised for many years. Certainly by 1960 Jackson was linking arc pressure to penetration, and by extension through theoretical arguments, to current density. Simply put, decreasing the electrode angle was expected to increase in current density, and result in increased penetration for a

given current. However, this apparently straightforward reasoning has not always been borne out by experiment.

Savage, Strunck and Ishikawa presented a benchmark investigation into electrode effects in 1965 (Savage et al 1965). Their experiments dealt with electrode angles of between 30° and 120°, and currents from 100 to 300 amps. Notable among their findings was a significant and reproducible increase in bead width, with a corresponding decrease in penetration, as the electrode angle was reduced from 120° to 30° - quite the contrary to Jackson's predictions. They also found that the relation between width and penetration was such that the fused area remained approximately constant, for a given current and arc length. Another important result was that the arc voltage was strongly dependent on tip geometry as well as on current and arc length. Only this latter result was consistent with theoretical predictions.

Subsequent investigations, such as that by Key (1980), have qualified these results. Key found that penetration increased with increasing electrode angle, as had Savage et al before him. However, in Key's study the effect was shown to be moderated by changes in shielding gas. For example helium additions caused a large (273%) increase in penetration when used with a 30° tip, but the increase was much less significant at larger angles. He also found that the electrode tip and groove dimensions (ie the weld preparation) interact to establish the path length to ground, and they must be compatible to ensure arc stability. One outcome of his work was the practical recommendation that sharp tips (ie relatively small included angles) be used for greater reliability and reproducibility.

In apparent contradiction to the above investigations, Petrie and Pfender (1970) confirmed the anticipated theoretical relations between tip angle and arc behaviour. They provided evidence to show that the severe constriction of the arc near the cathode resulting from small included angles produced up to a 50% increase in the plasma velocity. They also suspected that the peak current density could be increased by a similar amount, although there were no confirming measurements. In any case the heat flux distribution at the anode became narrower and had a higher peak value. The peak arc pressure was also increased significantly, as might be anticipated from

the higher jet velocity. Arc reproducibility was very much improved for sharply pointed cathodes compared to those with large included angles. Like Jackson, their investigations led them to conclude that a sharply pointed cathode would be expected to produce a deeper and narrower penetration of the work piece.

The results of Petrie and Pfender were obtained with the aid of a chilled copper anode arrangement whereas Savage et al and Key dealt with actual weld pools. It may be supposed therefore that the difference between the predicted and observed penetration behaviour could be attributed to coupling between the arc and the weld pool. This coupling has the capacity to stimulate other mechanisms such as Marangoni flow, surface deformation, plasma shear and electromagnetic pumping. More recently it has been established that the geometry of weld pools deeper that about 1 to 2mm is strongly influenced by convective motion within the pool (Choo and Szekely 1992).

Fortunately however, the situation may be less complex in the cases of high current and keyhole GTAW. In these processes the arc forces are strong enough to displace almost all the liquid from the leading portion of the weld pool, and when this does happen convection within the melt will not have a significant effect on penetration. This may not be true for bead width however, because convection in the trailing portion of the pool may well be significant, and in the absence of direct arc influence will be outwards across the pool surface (see Figure 2.2). Consequently the expected influence of tip angle on penetration that either was not found, or was ambiguous, in conventional GTAW may be realised in keyhole, and perhaps high current, GTAW.

The chemical composition of cathodes also influences arc properties. Matsuda, Ushio and Sadek (1990) have studied electrodes activated with single and multiple metal oxides. In their investigations the tip operating temperature decreased with decreasing work function. The order for single species additions was thorium, (3600°C), yttrium (3400°C), cerium (3100°C) and lanthanum (2700°C). Lanthanated electrodes also produced the highest emission current densities. Other results for the single additives included an increase in work function, but little change in current density, with increasing current.

6.1.6. Gas composition

Despite the incorrect terminology, shielding gases are often referred to in terms of their 'hotness', and for example, helium-rich arcs would be regarded as being hotter than argon arcs. In fact the temperatures achieved in the different gases do not differ significantly, although the heat transferred to the weldment certainly may do so. This well-known aspect of shielding gas formulations implicates the gas in the energy transfer process.

In 1983 Key et al (Key et al 1983) produced a study in which they characterised welding arcs shielded by mixtures of argon and helium or argon and hydrogen, and operated with a variety of electrode tip geometries. They were concerned with the effect of process variables on the temperature distribution in the arc.

One significant result was that helium additions did not increase the peak temperature in the arc, but did increase its plasma radius enormously. For instance, they observed that an arc in He-10Ar had a plasma radius approximately three times that of pure argon (here the plasma radius was equated to the visible radius which would indicate a temperature exceeding about 8000k). The addition of hydrogen to argon resulted in a slight decrease in peak temperature and increased the plasma radius by approximately 50% (at 150amps). They also drew attention to the fact that the thermal conductivity and heat capacity of helium are an order of magnitude greater than for argon at temperatures between 5000K and 10000K. These differences were considered sufficient to change the ranking of effective heat transfer mechanisms in helium arcs compared to argon arcs.

Eagar (1989) was another who challenged the concept of arc temperatures. He argued that in an argon arc the electrons carry approximately 80% of the energy transferred to the anode. In this sense arc temperature is not a dominating factor since the electrons transfer the same amount of energy, regardless of shielding gas. Exploring this example further, one has 20 'units' of heat conducted to the anode for every 80 units transported by the electrons. However, the thermal conductivity of helium is approximately three times that of argon. Therefore in a helium environment one could expect 60 units to be transferred through conduction (ie three times that in argon) for

every 80 units of heat transported by electron flow. Consequently the greater heat delivery from the helium arc is easily understood in terms of an increased thermal conduction across the anode sheath, without postulating different arc temperatures. This is illustrated in Table 6.3. In other words, it had often been assumed that the thermal conductivity of the shielding gas was not a major factor in regulating the heat flux into the anode since this was the case for the usual shielding gas, argon. However, this reasoning is flawed because the thermal conductivity of argon is very low and not typical of other shielding gases.

Table 6.3. Comparison of conductive heat transfer in argon and helium (arbitrary units).

Shielding gas	Heat transferred by current	Heat transferred by conduction	Heat transfer due to conduction (%)
Argon	80	20	20
Helium	80	60	43

This argument applied equally well to mixtures of argon and helium, and also diatomic gases. Diatomic gases such as hydrogen have an enhanced thermal conductivity due to the energy absorbed during the dissociation of the gas. This is known as reactive thermal conductivity. Eagar saw this description as fitting well with his rule that an arc will seek the lowest possible temperature for which sufficient electrons are available to carry the current.

More recently, Onsoin, Peters, Olsen and Liu (1995) have addressed the effect hydrogen additions to shielding gases have on arc behaviour. By 1995 it was known that an addition of hydrogen to argon or helium gives an arc a wider temperature distribution, a larger heat input and a slightly reducing atmosphere. In addition, the reducing atmosphere had been reported to increase the surface tension of liquid stainless steel because of a decrease in surface oxygen concentration (Onsoin et al 1995). All of these effects are likely to have important consequences for the keyhole GTAW process.

Onsoin et al argued that more energy is required to generate hydrogen ions than argon ions because the hydrogen must first be dissociated. The authors used this fact to show that for a particular set of welding parameters, the number of charge carriers in

an argon shielding gas with hydrogen additions is decreased, and the welding voltage increased. They then provided evidence demonstrating that additions of hydrogen to argon shielding gas can lead to increases in penetration of over 50%. In these same experiments the bead widths also increased, although only slightly. The significant conclusion of the paper was that this increased penetration was due to influences on the heat generating processes and not through influences on Marangoni flow behaviour.

6.1.7. Numerical simulations

Numerical simulations have contributed significantly to the understanding of arc behaviour since the work of Glickstein. For example, in 1983 Cram published results of a simulation of the cathode in which he concluded that the important processes for the energy balance were thermal conduction throughout the tip, electron emission and the contribution of an ion current slightly above the tip (Cram 1983). His work helped to establish that the heating of the electrode tip was due to interactions with the plasma, and ohmic heating of the electrode was relatively unimportant.

The current distribution at the cathode was predefined in Crams' simulation. More recently, Zhu, Lowke and Morrow (1992) have been able to avoid this assumption by adjusting the internal boundary conditions to energy and current conservation. As they pointed out, having to specify the current distribution is a disadvantage because free burning arc properties, such as arc radius and central temperature, are largely dominated by convective flow. In arcs the convective flow is mainly driven by the pinch pressure of the self magnetic field, which in turn is determined by the current density at the electrodes, particularly the cathode.

The calculations of Zhu et al for a 200 amp arc showed the two dominant heat transfer processes at the cathode tip to be heating by thermal conduction from the arc and cooling by thermionic emission. In the region to 0.7mm above the tip cooling by thermionic emission dominated over conduction through the electrode, and the cathode surface was actually cooler than its interior by about 5°. This region accounted for virtually the entire emission. The simulation also predicted a maximum

plasma velocity of about 500 m/sec, with the pressure near the cathode tip about 2% above ambient. These findings are in agreement with earlier work by Savage et al and others, and clearly identify the importance of convective flow.

In another simulation Lee and Na (1996) assessed the effects of varying the electrode angle. Their approach was to revert to an assumed current distribution at the cathode surface in order to calculate current and heat flux distributions at the anode, subject to a variety of influencing parameters. Their predictions were subsequently compared to experimental results. They are summarised below.

- The maximum current density at the cathode is about 135 A/mm^2 for a work function of 3.4 V.
- The heat flux to the anode decreased with increasing arc length but was not sensitive to electrode angle. It ranged from 23 W/mm^2 at 12.7mm to 90 W/mm^2 at 3.2mm, at 200 amps.
- Current density at the anode decreased with increasing arc length but was not sensitive to electrode angle. Results varied from 2 A/mm^2 at 12.7mm to 9 A/mm^2 at 3.2mm, at 200 amps.
- Peak arc pressure at the anode increased as angle decreased, but was not sensitive to arc length. Values ranged from 1800 Pa at 30° degrees dropping to 800 Pa at 120° degrees, at 300 amps.
- Peak shear stress increased with decreasing electrode angle but was insensitive to arc length. Values began at $260N/m^2$ at 30° and dropped to 110 N/m^2 at 120°, at 300 amps.

They further found that the peak arc pressure occurred on the arc axis, and was approximately the same at the anode and cathode. The agreement became closer at higher currents. This finding was in agreement with earlier work by Halmoy (1994), John Lowke (private communication 2001), and the theoretical analysis presented in the previous chapter.

There is some variation between the predictions of Lee and Na and available experimental data. As an example, Petrie and Pfender (1970) measured significant

increases in peak heat flux with decreasing electrode angles whereas Lee and Na predicted a relatively small effect. This may be attributable to the assumed current distributions at the cathode (see Zhu et al 1992). On the other hand there is agreement that the peak arc pressure increases with decreasing angle, and that convective heat transfer is important. In addition, a subsequent study has eliminated gas shear as a significant factor, at least for currents below 200 amps (Choo and Szekely, September 1991).

The issue the surface geometry of the pool has been difficult to introduce into numerical simulations. However, Choo, Szekely and Westhoff have taken significant steps in this direction by introducing predefined pool surface deformation into their model (Choo et al 1990). Their models accurately predict the behaviour of arcs impinging on flat surfaces, and suggest that the heat and current flux distributions are markedly modified for deformed pool surfaces. In fact, their calculations predicted bimodal distributions of current and heat flux for deformed surfaces, in contrast to the Gaussian distributions observed for flat plates. This distribution was more pronounced for current than for heat flux as convection continued to add some heat to the centre of the pool. As they concluded, "the previously employed procedure of independent specification of arc characteristics (notably heat flux distribution) is proven questionable".

The work of Choo, Szekely and Westhoff (1990) may have a particular relevance to keyhole mode welding with its prediction of bimodal current distributions. The possibility of such distributions has been raised in the previous chapter. The analysis in Chapter 5 indicated that such distributions tend to increase the total arc force and increase the pressure over the outer region of he pool surface. Choo's prediction that the heat flux to the centre of the pool would be partially maintained by convection confirms a level of decoupling between the plasma and current flow, and thereby further develops the role of viscosity.

6.1.8. Alternative models

The literature is very supportive of the notion that models are useful in terms of their potential to capture and provide insight into specific characteristics. Often very simple

models prove to be very fruitful in this regard. For example Jackson (1960) proposed a model for arc voltage-current characteristics based on just two series resistances. One of these represented the arc column, which required a potential more or less proportional to the current. The other represented the sheath resistance that he associated with the power required to maintain the arc action at the cathode. He argued that this latter resistance should decrease as the cathode temperature increased with current. Supporting evidence was the observation that the cathode drop was independent of arc length. This simple model captured the apparent 'negative resistance' observed at low currents, and provided researchers with a useful means of 'visualising' the electrical behaviour.

Shaw (March 1975) has also demonstrated the use of simplified models in his pursuit of a practical appreciation of welding arcs. For example he made use of prolate spherical coordinates to more easily approximate the equipotential close to a tapered cathode. This strategy enabled him to explain his observation that arc voltage increases significantly as the electrode angle (or taper) decreases. Shaw was concerned with a view of the arc as part of a more complex phenomenon, and his concept of diagnostic parameters presupposes one is dealing with a system rather than isolated decoupled components of it. He intended a diagnostic parameter to refer to a parameter that is not of intrinsic interest but is symptomatic of the degree to which the system is functioning in a desired manner.

6.1.9. Arc characteristics and keyhole welding

In conventional GTAW convection dominates heat transport within the arc, is the mechanism for transferring the arc force to the anode, and ultimately determines the anode pressure distribution. It is also an important, although perhaps not the dominant, mechanism for transferring heat to the anode. Since the heat flux and arc pressure distributions are central issues in keyhole welding it is anticipated that flow within the arc gases will be even more significant than is the case in conventional welding. This reinforces the role of electrode geometry in keyhole formation, and places added significance to the choice of shielding gas. The finding that the pressure on the arc axis at the cathode is closely reproduced at the anode may prove important in defining the conditions required for keyhole formation.

In early work Apps and Milner (1955) contended that convection, conduction and radiation conveyed a significant heat flux to the weldment, but that this contribution was relatively diffuse, and much fell outside the boundaries of the weld pool. In the GTAW keyhole the plasma gas flow is predominantly through the plate, and under these circumstances it may be that much of this heat flux is recovered due to the altered flow pattern. In addition, as extension to the arguments of Eagar (1989), the surface area of the pool exposed to the arc will be significantly increased for keyhole geometries and again the heat transfer should be improved. There is therefore reason to anticipate that the keyhole GTAW process may benefit from improved arc efficiency when compared to the conventional process.

Finally the prediction of bimodal current distributions for distorted weld pool surface geometries would impact on keyhole GTAW in at least two ways. Firstly it would generate an intensification of arc forces, as has been discussed in Chapter 5. Secondly it would reduce the heat flux near the arc axis. Fortunately this is modified by the effects of convection, but it may still have significant consequences for the temperatures generated in the metal at the bases of keyhole and high current GTAW weld pools. One may speculate that insufficient heat flux in this region might result in premature freezing of the metal, thereby increasing the potential for defects such as tunnel porosity and worm holes.

6.2. Cathode - keyhole relationships

6.2.1. The effect of electrode geometry on the fused area

In melt-in mode trials concerned with the effects of the tip angle, the current, travel speed and electrode position were fixed, allowing the resultant fused areas to be related to tip angle (see section 5.3.5). The results are shown below in Table 6.4. Possible correlations between the two variables, voltage and fused area, were examined using regression analysis, and results suggested a linear relationship. The predictions of this linear relationship are presented numerically in Table 6.4, and graphically in Figure 6.3.

Table 6.4. Variation of fused area against arc voltage.

Tip angle ($2\theta°$)	Voltage (V)	Measured area (mm^2)	Best-fit area (mm^2)
30	13.31	44.6	45.2
45	11.61	37.4	36.7
60	10.77	33.6	32.5
75	10.24	29.7	29.8
90	10.00	27.6	28.6

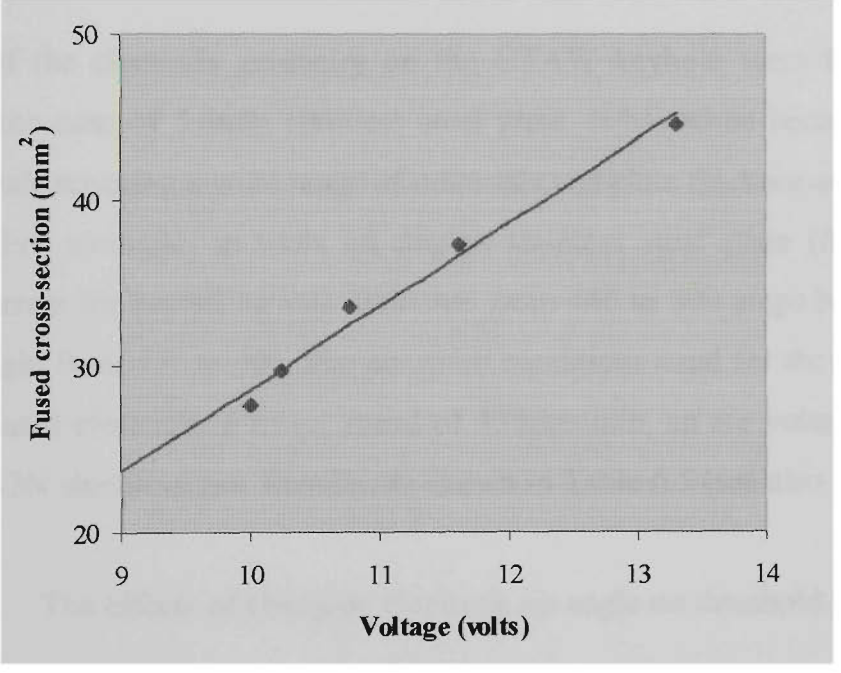

Figure 6.3. An illustration of the variations in fused area with welding voltage. Points are measured values and solid line is the regression line A = 5.015(V – 4.29).

Specifically, the relationship was

$$Area = 5.015(V - 4.29)$$

with a correlation coefficient (r^2) of 0.982. This result can be interpreted as signifying that a component of the voltage (4.3V) was unrelated to the energy delivered to the anode. This could be associated with cable losses and the cathode fall. More importantly however, the result links the tip angle to the heat delivered to the anode.

Since it has been established that changes to the tip angle affects the velocity field of the arc it is supposed that the variation in heat input is mediated by convection.

6.2.2. The effect of electrode geometry on threshold current

The ease with which a keyhole was formed was strongly influenced by the geometry of the electrode. In particular, either decreasing the included angle of the electrode tip or increasing the electrode diameter had the effect of reducing the threshold current. This is consistent with a strong relationship between keyhole formation and core arc pressure.

Influences of the electrode geometry on the GTAW keyhole were first noted and studied for the case of 5.6mm stainless steel plate. It has since been confirmed by numerous trials covering a wide range of materials and plate thicknesses. The effect is significant. For example, in trials on duplex stainless steel plate (SAF 2205) the threshold current for keyholing was increased from 440 to 590 amps by changing the electrode angle from 45° to 90°. The common conditions used for these trials were a 3.2 mm ceriated electrode, a travel speed of 450mm/min, an arc voltage of 14V and an Ar-10He-2N shielding gas. Results are shown in Table 6.5 (see also Figure 6.6).

Table 6.5. The effects of changing electrode tip angle on threshold current.

Electrode angle *(2θ°)*	**Threshold current** *(amps)*
45	440
60	511
75	560
90	590

To form a keyhole the arc plasma must be able to generate a pressure within the cavity at least sufficient to overcome the net effects of the 'hydrostatic' pressure and surface tension. While the exact pressure is difficult to estimate for generalised condition, there will be a minimum pressure threshold for a given plate, and this will not be less than the hydrostatic pressure of the weld pool at the root face. Assuming

that the plasma jet supplies this pressure, the results imply a relationship between arc pressure and tip angle.

The model developed in the previous chapter (Sections 5.1 and 5.2) has addressed the issue of arc pressure over the anode surface. In particular, the identification and characterisation of the arc core in Section 5.2.8 clearly specifies the pressure at its boundary. In fact this pressure is given by (5.26). This can be presented in the form:

$$P = \frac{\mu I_0^2}{8\pi^2 R_e^2}$$

$$= \frac{\mu I_0^2}{8\pi A_d} \qquad (6.6)$$

where R_e is the radius of the emission cross-section A_d (refer to Figure 6.4). This equation implies that the pressure of the core arc is (approximately) independent of arc length and also independent of the size of the anode region. This is in agreement with previous researchers, as discussed in Section 6.1.7.

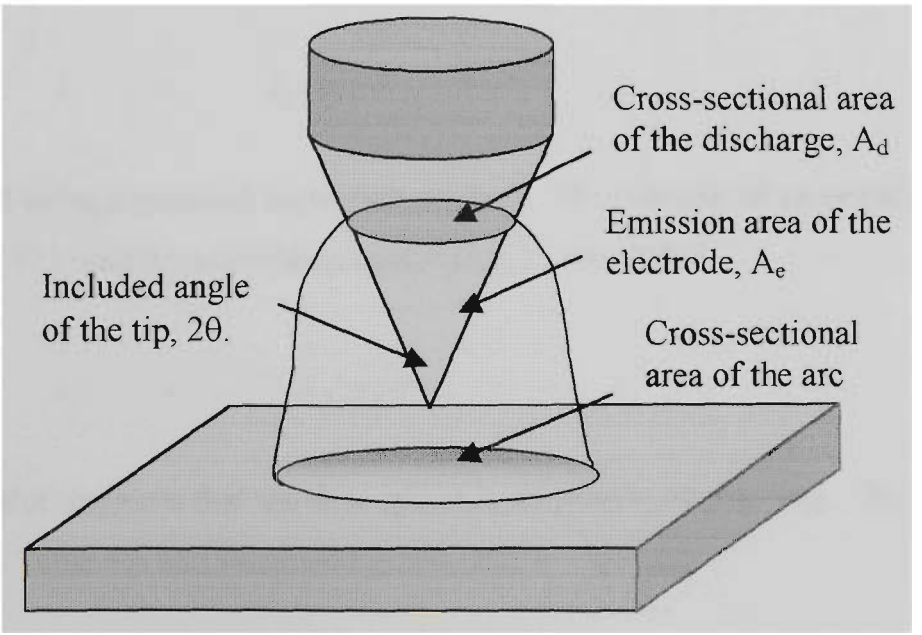

Figure 6.4. Schematic diagram illustrating the parameters used to examine the effects of electrode geometry on threshold current.

Since the ratio of A_d to the surface area of the emission region, A_e, is given by

$$\frac{A_d}{A_e} = \sin\theta$$

It follows that for a given current and emission characteristic, A_d, must vary as $\sin\theta$. Substituting this in (6.6) leads to the result

$$P \sim \frac{I^2}{\sin\theta}$$

Now the current necessary to provide this minimum pressure is readily identifiable as the threshold current, I_t, and for a particular thickness of plate:

$$I_t \sim \sqrt{\sin\theta}$$

This prediction has been compared with the experimental results obtained with 5.6mm SAF2205 (see Table 6.5). The predicted values were obtained by choosing a single constant I_p that gave the least squares error for the equation

$$I_t = I_P\sqrt{\sin\theta}$$

I_p was found using a standard regression package. The constant of proportionality had the value of 713, and the correlation coefficient, r^2, was 0.988:

$$I_t = 713\sqrt{\sin\theta}$$

This high value suggests that the description agrees well with the data. The results are presented in Table 6.6 and illustrated graphically in Figure 6.5.

Table 6.6. Data illustrating the correlation between tip angle and threshold current.

Tip angle *(2θ°)*	**$Sin^{1/2}\theta$**	**Threshold** *(amps)*	**Predicted** *(amps)*
0*	0	0*	0
45	0.619	440 ±5	441
60	0.707	511 ±5	504
75	0.780	560 ±5	556
90	0.841	590 ±5	599

* The condition that current was zero at zero angle was imposed as a constraint.

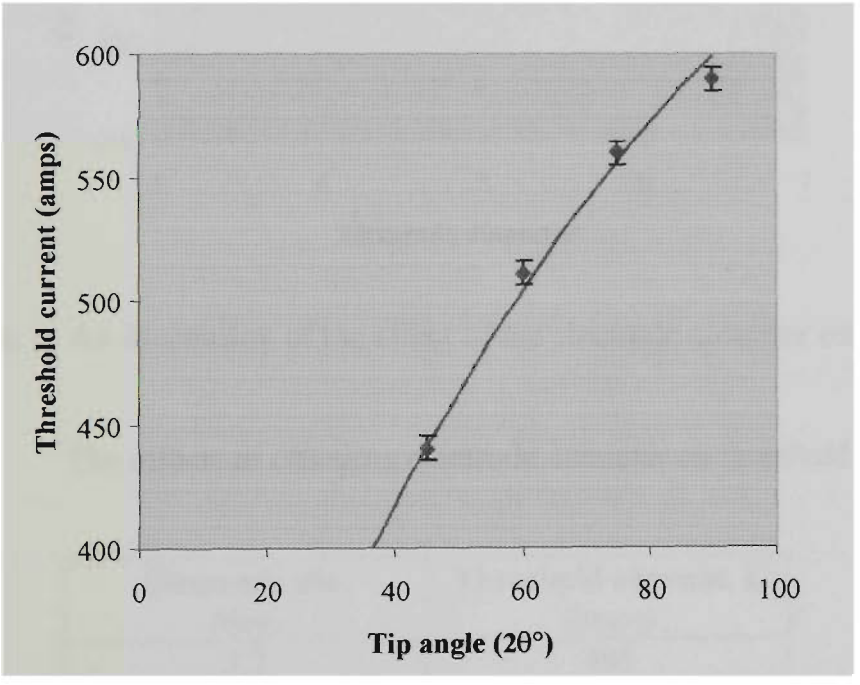

Figure 6.5. Graphical presentation of threshold current variations with tip angle. Points are measured values and solid line is the regression line: $I_t = 712.6 \sin^{1/2}\theta$.

It has also been established that the emission area of the tip decreases with increasing electrode diameter at a given current (Savage et al 1965, Savage et al 1979 and Chapter 3). It is therefore expected that larger diameter electrodes should give lower threshold currents for a given plate. Experiments have confirmed this expectation. For example, in one set of experiments on SAF 2205 plate the threshold current reduced

from 495 amps to 438 amps as the electrode diameter was increased from 3.2 to 6.35 mm. The results, presented graphically in Figure 6.6, and numerically in Table 6.7, were obtained using ceriated electrodes ground to have a 60° tip. The arc voltage was kept constant at 14 volts and the travel speed was 450mm/min. The shielding gas was Ar-3.5N.

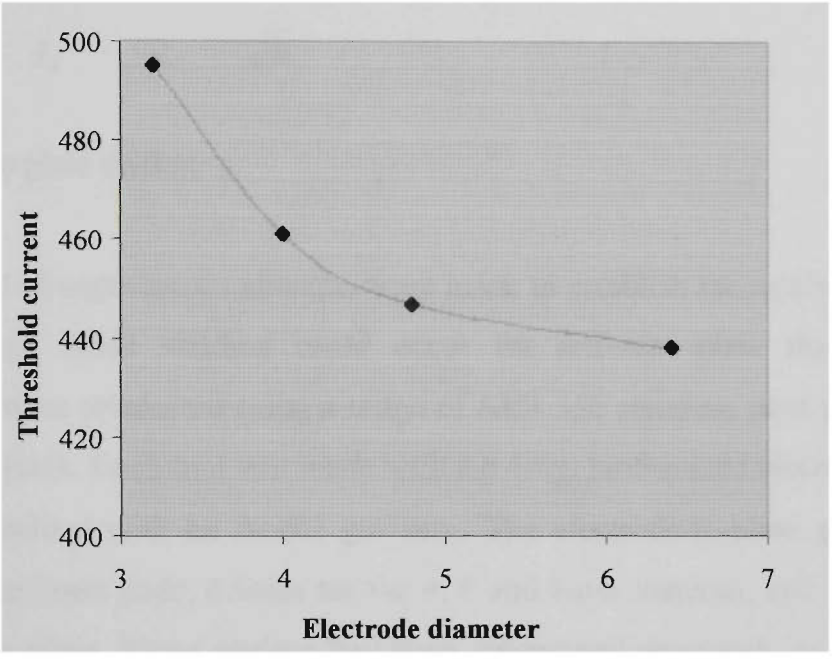

Figure 6.6. An illustration of the effect of the electrode diameter on threshold current.

Table 6.7. The effects of changing electrode diameter on threshold current.

Electrode dia. *(mm)*	**Threshold current, I_t** *(amps)*
3.2	495
4.0	461
4.8	447
6.4	438

6.2.3. The effect of plate thickness on threshold current

A simple extension of the preceding argument is that the peak pressure required to keyhole should be proportional to the plate thickness. This would follow from an

expectation that the peak pressure is equal to, or at least proportional to the maximum pressure that can be exerted by the weld pool. If this were the case then since

$$P \quad \sim \quad I^2$$

One has

$$I_t \quad \sim \quad \sqrt{h}$$

where h is the plate thickness.

In another set of experiments attempts were made to establish the minimum current at which keyhole mode welding could occur for different plate thicknesses. The experiments were conducted using a range of AISI 316 stainless steel plates between 3 and 12mm thick. Each trial was made with a 6.4mm lanthanated electrode ground to a 60° tip, shielded with an Ar-5H gas mix. The electrode-to-plate gap was set at 0.3mm for the 3mm plate, 0.6mm for the 4, 6 and 8mm material, and 1.0mm for the 10 and 12mm plate. These settings had been determined previously as being optimal for the respective thicknesses. All welds were bead-on-plate. The minimum threshold current was established by incremental changing of the welding speed and determining the corresponding threshold current (when keyhole formation was possible). The travel speed was adjusted in increments of 25mm/min. The threshold current at the minimum successful travel speed constitutes the data for this discussion.

The data is presented in Table 6.8 and again in Figure 6.7. The 'estimated threshold' in the right hand column was derived using the simple relation

$$I_t \quad = \quad 132\sqrt{h}$$

The agreement is quite good with the exception of the 3mm plate. During many trials it has been established that this plate thickness represented the lower limit for the process. It is also significant that the minimum current found for this plate was greater than for the 4mm material and the welding speed was also higher. This would imply that the conditions for keyholing were not dictated by arc pressure but by some other

agent. Possible limiting mechanisms have been discussed in Chapter 4. In that context the minimum measured current was not the threshold current under consideration here. It was presumed that this was related to the effects of plate thickness on heat flow and resultant fusion profiles – a subject to be discussed later. The results for threshold current with respect to both tip angle and plate thickness are therefore consistent with the requirement of a minimum peak arc pressure, where

$$P \sim \frac{I^2}{\sin\theta}$$

Table 6.8. Minimum travel speeds and currents for keyhole GTAW in AISI 316.

Plate thickness *(mm)*	**Travel speed** *(mm/min)*	**Minimum I_t** *(amps)*	**Estimated Min. I_t** *(amps)*
3	550	300	228
4	325	285	264
6	250	325	324
8	225	390	374
10	200	420	416
12	175	450	457

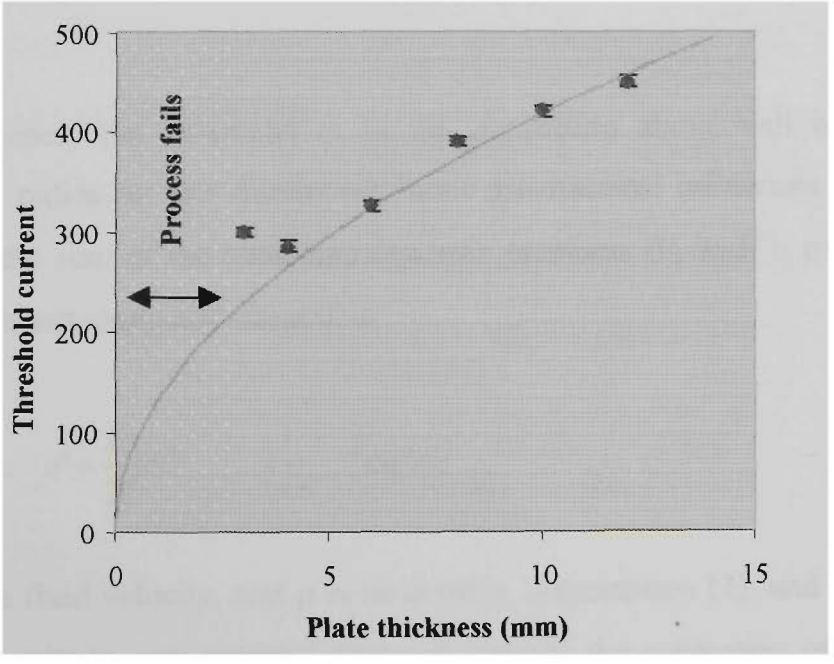

Figure 6.7. Minimum achievable threshold currents obtained for various thicknesses of AISI 316 material. Solid points are measured values, the line is a theoretical relationship: $I_t = 132\sqrt{h}$.

6.3. Arc - keyhole relationships

6.3.1. Minimum throat size

One constraint on GTAW keyholes is that they must be open to allow the arc plasma gases to flow through the keyhole. This requirement for venting places a limit on the minimum cross-section of a keyhole with a given size entrance. It is useful to construct a simple model that can express this more formally. The aims of this model are to establish the credibility of a minimum throat size, and to provide a rough estimate of its value. The model is constructed on three assumptions:

1. The stagnation pressure in the throat of the keyhole is the maximum arc stagnation pressure.
2. All gas entering the keyhole exits through the vent.
3. The stagnation pressure of the arc at the plate surface has a Gaussian distribution,

$$P(r) = P_m \exp\left[-\left(\frac{r}{r_0}\right)^2\right]$$

For convenience, the parameter r_0 in the expression above will be taken as an effective arc radius for this discussion. Since gravitational influences on the gas can be ignored, the sum of the static and dynamic pressures (P, and $^1/_2\ \rho v^2$ respectively) will be a constant along any streamline.

$$P + \frac{1}{2}\rho v^2 = const.$$

Here v is the fluid velocity, and ρ is its density. Assumption (1), and the expectation that the gas exits to zero external pressure, permits the estimation of the exhaust or efflux velocity:

$$v_e = \sqrt{\frac{2P_m}{\rho_e}}$$

The subscript 'e' has been introduced to indicate the exiting flow properties. The rate at which the plasma flows from the keyhole, f_e, is simply $\rho_e v_e A$, where A is the throat cross-sectional area, so substituting for v_e relates the flow to the flow constant P_m:

$$f_e = A\sqrt{\frac{2P_m}{\rho_e}}$$

By assumption (2) that this flow must be equal to the flow entering the keyhole. Again, if the excess static pressure is zero outside the keyhole entrance the pressure is entirely dynamic and, by (3):

$$\rho v^2(r) = P_m \exp\left[-\left(\frac{r}{r_0}\right)^2\right]$$

and

$$v_i(r) = \sqrt{\frac{2P_m}{\rho_i}}\exp\left[-\frac{1}{2}\left(\frac{r}{r_0}\right)^2\right]$$

where the subscript indicates conditions for the in-flowing gas. The mass flow from the arc, f_i, can be calculated by integration:

$$f_i = \int_0^\infty \rho_i \sqrt{\frac{2P_m}{\rho_i}}\exp\left[-\frac{1}{2}\left(\frac{r}{r_0}\right)^2\right]2\pi r dr$$

$$= 2\pi r_0^2 \sqrt{\frac{2P_m}{\rho_i}}\left(1-\exp\left[-\frac{1}{2}\left(\frac{r}{r_0}\right)^2\right]\right)$$

If $r_i >\sim 2r_0$ the exponential term can be ignored, and

$$f_i = 2\pi r_0^2 \sqrt{\frac{2P_m}{\rho_i}}$$

Equating the two flow rates f_i and f_e,

$$A\sqrt{2P_m\rho_e} = 2\pi r_0^2 \sqrt{2P_m\rho_i}$$

whence

$$A = 2\pi r_0^2 \sqrt{\frac{\rho_i}{\rho_e}}$$

The exit radius is approximately

$$r_e = 1.4 r_0 \left(\frac{\rho_i}{\rho_e}\right)^{\frac{1}{4}}$$

Since density is inversely proportional to temperature,

$$r_e = 1.4 r_0 \left(\frac{T_e}{T_i}\right)^{\frac{1}{4}}$$

T_i is about 12000K. T_e is unknown but must be between 12000K and about 3000K since it cannot be colder than the metal. Hence the temperature ratio is between 1 and 0.25. So

$$r_0 < r_e < 1.4 r_0$$

Finally therefore, the throat radius is approximately the same as the arc radius (as defined in (3)).

This very approximate result imposes a limit on the throat size of the keyhole. Specifically a keyhole vent will reach a minimum size for a given set of electrode and shielding gas conditions, and this cannot be reduced however finely the welding current is trimmed. Physically any contraction of the throat beyond this limit will restrict the gas flow to the extent that some will be forced to exit via the front face or

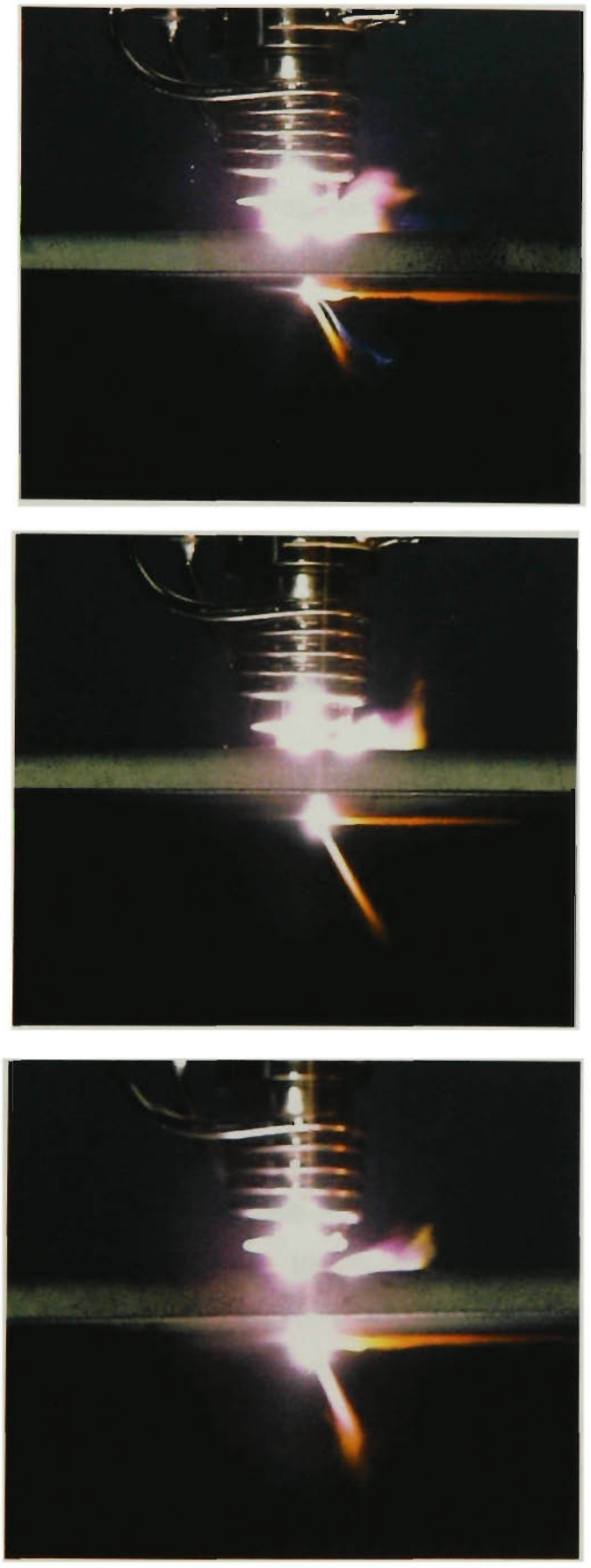

Figure 6.8. Photographs illustrating the changes in the strength and direction of the efflux plasma emerging from both the front and root faces as the current is increased (top to bottom).

entrance. This will result in turbulence and other instabilities in the flow and weld pool.

Operation in this transition range can be identified in thicker plate by the presence of a strong, steeply angled plasma jet exiting the keyhole immediately behind the welding arc (see Figure 6.8). This jet can be detected with a simple voltage probe, and such a technique may prove useful in monitoring the state of the process. The condition has been associated with the generation of worm-hole porosity near the root of the weld. This unstable regime appears to be restricted to plates and pipes thicker than about 7mm. The 'immunity' of thinner material is possibly related to hysteresis effects although this has not been firmly established. In any case increasing the current eliminates both the rebounding (front face) jet and the porosity.

6.3.2. Influence of the shielding gas composition

The parameter r_0 in Section 6.3.1 is a measure of arc constriction, and the smaller its value the more localised is the property being described. (The same can be said for the parameter R_e characterising the pressure distribution. However, the very specific meaning of this parameter makes it inappropriate for the present purposes). In the past considerable effort has been given to establishing the radial dependence of current density, heat flux and arc pressure on arc parameters such as electrode geometry and gas composition. It is important to note that these distributions are of fluxes to the anode, and therefore may differ from expectations based on visual observations of the arcs. For example, additions of hydrogen to argon are known to broaden the temperature distribution, and visibly widen the arc. However, direct measurements by Nestor (1962) have established that the flux distributions to the anode actually contract slightly. More generally his measurements have shown that the distributions in question are broadest for helium shielding gas, approximately equal for argon and argon-nitrogen mixtures, and narrowest for argon-hydrogen shielding gases. On the other hand he suggested that total power delivery decreases in the order helium, argon-nitrogen, argon-hydrogen, pure argon (Nestor 1962). The broadest distributions imply the largest value for r_0, and therefore the greatest degree of difficulty in maintaining the small exit vent required for keyhole stability. In Nestor's work the

implied values of r_0 for the various combinations of argon, nitrogen and hydrogen varied only slightly, but were all much less than for helium

It is not surprising that the shielding gas was found to be important in keyhole GTAW. The choice not only had a pronounced effect on the threshold current, but, for the case of 5.6mm SAF 2205 plate for example, it also determined whether or not the keyhole could be formed at all. Data from these experiments is shown in Table 6.9. The gas compositions used were constrained by availability, and by detrimental reactions with either the electrode or the weld metal. The data shown is from a series of trials on the 5.6mm SAF 2205 plate. All these welds were made with a travel speed of 450mm/min, an arc voltage of 14V, and with the electrode ground to a 60° included angle. There was no backing or trailing gas, and no filler wire addition.

Table 6.9. The effect of gas composition on keyhole formation in 5.6mm duplex stainless steel.

Gas composition	**Threshold current** *(amps)*
Helium	Melted at 520A, no keyhole
Argon	Would not keyhole
Ar-1H	528
Ar-3.2H	486
Ar-10He-2N	513
Ar-3.5N	475
Ar-5H-5N	457
Ar-10N	435

These results indicate that nitrogen was the most effective shielding gas addition for reducing the keyhole threshold current, whereas helium was the least effective. Nitrogen and hydrogen are both diatomic at normal temperatures, but dissociate within the arc. Since their dissociation energies are large, dissociation will increase the heat content per unit volume of gas. However, the dissociation energy of nitrogen is more than twice that of hydrogen, and accordingly it could be expected to provide a higher total thermal delivery, in agreement with Nestor's results.

The difficulties of generating keyholes with helium shielding gas are consistent with a large value of r_0. However, if this were the only consideration then argon-hydrogen

mixtures would produce better results than argon-nitrogen compositions. One interpretation would be that both the degree of constriction (r_0) and the absolute thermal flux combine to establish the condition for the onset of keyholing. In particular the value of r_0 distinguishes helium from the argon-based shielding gases, whereas the latter have similar r_0 values and are therefore separated on the basis of thermal yield at the anode.

6.3.3. The effect arc length on threshold current

The influences of arc voltage can be appreciated by reference to two examples: 5.6mm SAF 2205 and 12mm austenitic stainless steel (AISI 304). In the former situation there was a minimum voltage (11.3V for the particular conditions applying to the experiment) below which a keyhole would not form. For that case, increasing the current only led to the collapse of the pool as the root face of the plate gave way. Increasing the voltage from this value resulted in a reduction of the threshold current, reaching an apparent minimum at about 14V. Increasing the voltage to 16 volts had little further effect other than to increase the undercut. The reduction in threshold current was not particularly smooth, and could be interpreted as involving a transition between two levels, as shown in Figure 6.9 (also Figure 3.4)

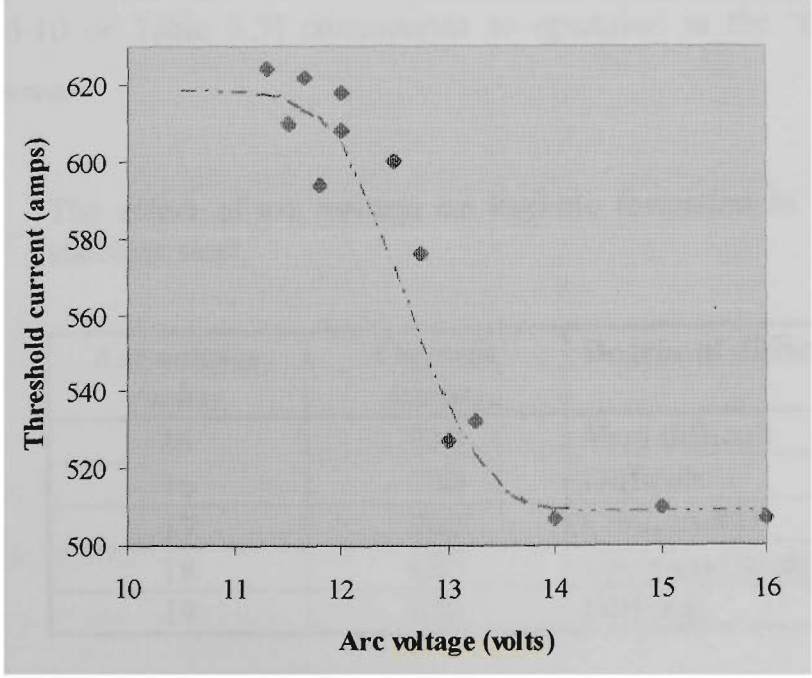

Figure 6.9. Threshold current as a function of voltage for 5.6mm SAF 2205.

It is supposed that a keyhole is stable only between two extreme voltage conditions. At low voltages the electrode becomes submerged. Under such conditions radial current flow to the cavity walls becomes more likely. Consequences would include a reduction in peak arc pressure due to an increased emission area, and a redistribution of heat flux from the base of the cavity to the sides. Both can be interpreted as an increase in the respective r_0 values and increase the risk of a 'melt-through' rather than the formation of a small exit vent in the bottom of the plate.

At the other extreme increasing the voltage will simply add to the overall heat input, because the keyhole current cannot be reduced below that level which provides enough force to displace the liquid metal from the cavity. In other words, increasing the voltage eventually results in excessive fusion, and this will destabilise the process by increasing the width of the root.

This scenario is consistent with the observations for both the SAF 2205 and AISI 304. It is to be appreciated however, that the thickness of the SAF 2205 material was such that the operating window for the keyhole process was very wide. This provided an ideal opportunity to explore a wide range of voltage conditions. On the other hand, 12mm corresponds to the limiting thickness for AISI 304 and consequently the operating window was quite restricted. It is postulated that the behaviour observed (see Table 6.10 or Table 3.3) corresponds to operation in the 'transition' region described above.

Table 6.10. The effect of arc voltage on keyhole formation in 12mm austenitic stainless steel.

Arc voltage *(volts)*	**Current** *(amps)*	**Degree of difficulty**
15	750	Very difficult
16	730	Difficult
17	700	Comfortable
18	680	Becoming harder
19	650	Difficult

7. Conductive heat flow

7.1. Analytic models of conductive heat flow

7.1.1. Introduction

The prediction of weld pool dimensions and thermal cycles has received sustained attention since the pioneering work of Rosenthal (1941). Specific reasons for this include the need to estimate cooling rates in order to predict the resultant weld microstructures and, following the introduction of laser welding, to specify the relationship between beam power and penetration depth in beam welding. It is important in the present case for the additional reason that the keyhole stability is critically dependent on the pool's size and shape. Therefore the development of this technology is reliant on an appreciation of the heat flow, particularly with respect to the generation of the fusion boundary.

7.1.2. Quasi-stationary temperature fields.

Rosenthal (1941, 1946) is generally credited with providing the first comprehensive mathematical description of the temperature field associated with welding and cutting processes, although, as Wells (1952) pointed out, Roberts had given a solution for a moving point source in 1923.

Rosenthal's model involved several simplifying assumptions. In particular he assumed that:

- The thermal conductivity (k) and diffusivity (α) of the metal did not change with temperature;
- The heat source speed, v, and power, q, were constant;
- The heat source could be considered to be a point source;
- The temperature distribution did not change with time relative to the heat source, ie the temperature field was in a 'quasi-stationary' state.

His treatment proceeded as follows. First the heat equation was presented in rectangular coordinates. For constant k and α, and with T representing the excess temperature (sometimes written as $T-T_0$, where T_0 is the ambient temperature) this is

$$\alpha\left(\frac{\partial^2 T}{\partial X^2}+\frac{\partial^2 T}{\partial Y^2}+\frac{\partial^2 T}{\partial Z^2}\right) = \frac{\partial T}{\partial t} \qquad (7.1)$$

Rosenthal then represented this equation in the frame of the moving heat source. In this frame the temperature field does not change over time, that is $\partial T/\partial t = 0$. In doing this he chose the X-axis to be in the welding direction, and introduced a new variable, E, such that a point, distance X along the X-axis, will be a distance E = X - vt from the moving source. Transformation to the frame of the heat source then gave the differential equation:

$$\frac{\partial^2 T}{\partial E^2}+\frac{\partial^2 T}{\partial Y^2}+\frac{\partial^2 T}{\partial Z^2} = -\frac{v}{\alpha}\frac{\partial T}{\partial E} \qquad (7.2)$$

Rosenthal (1941) presented solutions for point sources in one, two and three dimensions. The solution for one dimension (1-D) corresponds to a heat source moving along a metal filament, and was used to approximate the heat flow in a consumable electrode. The two dimensional solution (2-D) describes a point heat source moving across a very thin sheet, or alternatively, a line source, strength Q/G power per unit thickness, acting through the thickness, G, of a plate. Rosenthal applied it to both thermal cutting and the welding of very thin plate. The three dimensional solution (3-D) corresponds to a point source moving across the surface of a plate of great thickness.

To begin, let R symbolise the radial distance from the heat source, such that

$$R = \sqrt{E^2+Y^2} \qquad 2D$$

$$R = \sqrt{E^2+Y^2+Z^2} \qquad 3D$$

Two boundary conditions are required to uniquely specify a solution to the temperature field. The boundary conditions chosen by Rosenthal were that the gradient of the temperature field goes to zero at large distances from the source, and that the heat leaving a region enclosing the source must converge to that of the source as the radius of that region shrinks to zero. This latter condition is expressed as:

$$k\,2\pi R\frac{\partial T}{\partial R}\rightarrow -\frac{Q}{G} \qquad as \qquad R\rightarrow 0 \qquad 2D$$

$$k\,2\pi R\frac{\partial T}{\partial R}\rightarrow -Q \qquad as \qquad R\rightarrow 0 \qquad 3D$$

The required solutions were found to be

$$T = \frac{Q}{2\pi kG}\exp\left(-\frac{vE}{2\alpha}\right)K_0\left(\frac{vR}{2\alpha}\right) \qquad 2D \qquad (7.3)$$

and

$$T = \frac{Q}{2\pi kR}\exp\left(-\frac{vE}{2\alpha}\right)\exp\left(-\frac{vR}{2\alpha}\right) \qquad 3D \qquad (7.4)$$

where $K_0\left(\frac{vR}{2\alpha}\right)$ is the modified Bessel function of the second kind and zero order.

In his later paper (1946) Rosenthal showed how thermal fields for plates of intermediate thickness, G, may be determined using the method of images. The result was expressed as the sum of an infinite series ($-\infty<n<\infty$) as shown below:

$$T = \frac{Q}{2\pi kR}\exp\left(-\frac{vE}{2\alpha}\right)\sum_{n=-\infty}^{n=\infty}\frac{\exp\left(-\frac{vR_n}{2\alpha}\right)}{R_n} \qquad (7.5)$$

where

$$R_n = \sqrt{E^2+Y^2+(Z+2nG)^2}$$

7.1.3. Melting efficiency in 2-D (thin plate or keyhole).

Rosenthal was interested in describing the temperature fields and thermal cycles associated with welding and cutting. However, his work also provided a basis for the estimation of weld pool dimensions, and Wells took this up in one of his papers (Wells 1952). Wells also made the important discovery that two-dimensional (eg thin plate or keyhole) fusion processes have maximum fusion efficiency of about 50%, achievable at high speed. His predictions have been supported experimentally.

Wells began by equating the weld pool boundary with the melting point isotherm, T_c. This, or any other isotherm, is at its maximum width when its tangent is parallel to the E-axis (dT/dE = 0). If this condition is applied to (7.3), it turns out that the losses inherent in the fusion process can be estimated. Wells did this by introducing a 'melting ratio', M, which was the ratio of total heat supplied to the plate to that required to melt an amount of material equal to that in the nugget. Details of his arguments are presented below. First however, it will be useful to introduce several dimensionless variables.

The parameter v/2α occurs repeatedly in analyses of heat flow from moving sources, and since it has the dimensions of 1/length terms such as vR/2α, vE/2α and vY/2α are dimensionless. For convenience dimensionless or scaled distances will be written in lower case and the upper case symbols will be reserved for the original unscaled parameters. The parameter D is taken to be the width (or diameter) of the weld bead.

$$x = \frac{v}{2\alpha}X \qquad \xi = \frac{v}{2\alpha}E$$

$$y = \frac{v}{2\alpha}Y \qquad r = \frac{v}{2\alpha}R$$

$$z = \frac{v}{2\alpha}Z \qquad d = \frac{v}{2\alpha}D$$

Now, following Wells arguments, the condition applying at the position at which any chosen isotherm reaches its maximum width is

$$\frac{dT}{d\xi} = \frac{\partial T}{\partial \xi} + \frac{\partial T}{\partial r}\frac{\partial r}{\partial \xi} = 0 \qquad (7.6)$$

The expression (7.6) can be evaluated using (7.3) for T. The result can be presented in the following form:

$$\frac{\xi_m}{r_m} = \frac{K_0(r_m)}{K_1(r_m)} \qquad (7.7)$$

The subscript 'm' has been introduced to indicate values at the point where the isotherm has maximum width. Note also that $dK_0(x)/dx = K_1(x)$, where K_0 and K_1 are modified Bessel functions of the second kind, zero and first order, respectively.

Setting $T = T_c$, substituting for ξ_m in (7.3), and rearranging gives an expression for Q:

$$\frac{Q}{G} = \frac{2\pi k T_c}{K_0(r_m)} \exp\left(-\frac{r_m K_0(r_m)}{K_1(r_m)}\right) \qquad (7.8)$$

while y_m, the bead half-width, is obtained from (7.7) using the definition of R:

$$y_m = \sqrt{r_m^2 - \xi_m^2}$$

and

$$y_m = r_m \sqrt{\left(1 - \left(\frac{K_0(r_m)}{K_1(r_m)}\right)^2\right)} \qquad (7.9)$$

Since both power input and bead width are now known as functions of r_m, it is possible to examine the behaviour of M, the ratio of the heat input to the heat required by the nugget:

$$M = \frac{Q}{v\rho c G D T_c} \qquad (7.10)$$

where ρ is the mean density of the metal and c its heat capacity. Substitution for Q and D, where $D = Y_m$, and $d = y_m$, allows M to be expressed as a function of r_m

$$M = \frac{\pi}{r_m K_0(r_m)\sqrt{\left(1-\left(\frac{K_0(r_m)}{K_1(r_m)}\right)^2\right)}} \exp\left(-\frac{r_m K_0(r_m)}{K_1(r_m)}\right) \qquad (7.11)$$

When d is small r_m is also small. Further, it can be shown that $K_0(x)/K_1(x) \rightarrow 0$ as $x \rightarrow 0$. Therefore $r_m \rightarrow y_m$, and (7.11) reduces to

$$M = \frac{\pi}{dK_0(d)} \qquad (7.12)$$

This situation is the limit of low welding speeds, low heat input or high thermal diffusivity. At the other extreme as d becomes large, as would be the case at high welding speeds, (7.11) simplifies to

$$M = \sqrt{\frac{\pi e}{2}} \qquad (7.13)$$

This latter expression has the value of about 2.07. In other words, the melting process becomes extremely inefficient as d becomes small, and approaches a maximum of approximately 50% as d increases. An approximate solution for both M and Q, valid to within 6% for $d > 0.1$, is

$$M = 2\left(1+\frac{1}{5d}\right)$$

or

$$\frac{Q}{G} = 8kT_c\left(\frac{1}{5}+d\right)$$

Evidently, $d = 2$ implies an M within about 10% of its minimum possible value.

7.1.4. Melting efficiency in 3-D (thick plate).

Christensen et al (1965) and others took up the discussion of pool geometry for the 3-D solution. Christensen, like Wells, was concerned with making and testing predictions covering the whole range of materials and welding processes then

available. His predictions were based on the 3-D solution provided by Rosenthal. The mathematical component of his work is summarised below.

Christensen began by converting the variables in (7.4) to dimensionless form. Dimensionless distances, ξ, y, z, r, were defined as above (ie $\xi = vE/2\alpha$, etc.). A dimensionless temperature, θ, was defined as $(T-T_0)/(T_c-T_0)$ where T_0 is the ambient temperature and T_c was some specific reference temperature, such as the melting point. Substitution into (7.4) gave

$$\theta = \frac{Qv}{4\pi\alpha k(T_c - T_0)} \frac{\exp(-(\xi + r))}{r}$$

Noting that $k\delta T = \alpha\delta H$, where δT and δH are the respective changes in temperature and enthalpy in a unit volume of material,

$$\theta = \frac{Qv}{4\pi\alpha^2 \delta H} \frac{\exp(-(\xi + r))}{r} \tag{7.14}$$

The factor, $Qv/4\pi\alpha^2\delta H$, is dimensionless, and Christensen identified it as the 'operating parameter', n, for the process

$$n = \frac{Qv}{4\pi\alpha^2 \delta H}$$

Hence, (7.4) becomes

$$\frac{\theta}{n} = \frac{\exp(-(\xi + r))}{r} \tag{7.15}$$

'n' can be thought of as a ratio between the rate at which heat is being injected into the joint, (Q), to the rate at which it is diffusing away. An increase in the operating parameter is then associated with either an increased power input, or better retention of the heat by the weld zone.

Isotherm dimensions were determined as follows. First, the condition identifying the point of maximum width, $d(\theta/n)/d\xi = 0$, was applied to (7.14) to give a relation between ξ and r (at maximum width):

$$\xi_m = -\frac{r_m^2}{1+r_m} \tag{7.16}$$

Following Wells' approach, the width can be determined from the Pythagorean relationship between ξ, r and y:

$$y_m = \frac{r_m\sqrt{1+2r_m}}{1+r_m} \tag{7.17}$$

Since y_m and z_m are equal, the cross-sectional area, a_m, is $\pi y_m^2/2$, or

$$a_m = \frac{\pi r_m^2(1+2r_m)}{2(1+r_m)^2} \tag{7.18}$$

Again as in the 2-D case, ξ_m is eliminated from (7.14) to provide a relationship between the operating parameter (the analogue of Q) and r_m:

$$n = \theta_m r_m \exp\left(\frac{r_m}{1+r_m}\right) \tag{7.19}$$

Although Christensen did not derive the melting ratio from his calculations it is straightforward to do so. Substitution of the expression for ξ_m in (7.16) into (7.14) and selection of the melting isotherm ($\theta = 1$) leads to the expression:

$$\frac{1}{Q} = \frac{v\exp\left(-\frac{r_m}{1+r_m}\right)}{4\pi\alpha^2\delta H r_m}$$

The power required for melting is given by $vA\delta H$, where A is the cross sectional area of the bead. Since $A = (4\alpha^2/v^2)a_m$

$$vA\delta H = \frac{2\pi\alpha^2\delta H r_m^2(1+2r_m)}{v(1+r_m)^2}$$

The ratio of power required for melting to total input power is then vAδH/Q, or

$$\frac{vA\delta H}{Q} = \frac{2\pi\alpha^2\delta H r_m^2(1+2r_m)}{4\pi v\alpha^2\delta H r_m(1+2r_m)^2}\exp\left(\frac{-r_m}{1+r_m}\right)$$

which simplifies to

$$\frac{vA\delta H}{Q} = \frac{r_m(1+2r_m)}{2(1+2r_m)^2}\exp\left(\frac{-r_m}{1+r_m}\right) \qquad (7.20)$$

As r_m becomes small this approaches $r_m/2$, and for large values of r_m it approaches e^{-1}.

The ratio of power required for melting to total input power is referred to as the melting efficiency, ME, and is more commonly used than Wells' melting ratio. It is generally expressed as a percentage. The melting efficiencies for both the 2- and 3-D solutions asymptotically approach limiting values with increasing welding speeds, and the limiting efficiency for the 2-D weld is significantly higher than for the 3-D welds. The respective values are:

$$ME = 100\sqrt{\frac{2}{\pi e}} \sim 48.4\% \quad (2D)$$

$$ME = \frac{100}{e} \sim 36.8\% \quad (3D) \qquad (7.21)$$

7.1.5. The heat function

Shortly after the introduction of laser welding Swift-Hook and Gick (1973) provided a fresh analysis for keyhole welding for the prediction of the penetrating power of laser and electron beam processes. Their analysis had much in common with that of Wells (1952). Significant differences included the introduction of the so-called 'heat

function', the use of dimensionless parameters, and the presentation of new experimental data generated with these beam processes.

In previous analyses it had been convenient to take the thermal properties of the metal as being independent of temperature. In fact this is quite unrealistic (Rosenthal 1941), and the normal approach has been to select appropriate 'average' values, which in practice provides considerable latitude to select values that give the 'best fit' to the data (Rosenthal 1941 and 1946, Solomon and Levi 1982, Easterling 1992). One of the most temperature-sensitive properties is the thermal conductivity, k, and Swift-Hook and Gick accommodated this with the introduction of a heat function (S) (see Condon and Odishaw 1958). S is defined by

$$\begin{aligned} S &= \int_0^T k(T')dT' \\ &= k_{av}T \end{aligned} \qquad (7.22)$$

S can be thought of in several ways: it is the amount of heat associated with a given temperature rise (per unit of material), or alternatively, it may be taken as defining a new temperature scale T_s

$$T_s = \frac{k_{av}}{k_0}T$$

such that

$$S = k_0 T_s \qquad (7.23)$$

where k_0 is the value of k at some specified temperature. The use of S gives equations identical in form to those developed by Rosenthal, and so no extra complexity is introduced. The other critical property, thermal diffusivity, is much less variable than k, and changes smoothly and gradually against the new temperature scale (Swift-Hook and Gick 1973).

Swift-Hook and Gick also worked with dimensionless quantities. They formed the new variables X and Y where

$$X = \frac{Q}{GS} \quad (= \frac{Q}{Gk_0T_s})$$

and

$$Y = 2\frac{vy}{2\alpha} \quad (= d\,in(7.12))$$

It is readily shown that 100 (Y/X) is the melting efficiency for the process, and Swift-Hook and Gick carefully explored the relationship between these two variables. They derived approximate expressions for both the low-speed and high-speed regimes. At low speeds

$$Y \cong \exp\left(\ln 8 - \gamma - \frac{2\pi}{X}\right)$$

$$\cong 4.5\exp\left(-\frac{2\pi}{X}\right)$$

where γ = Euler's constant ~ 0.577. At high speeds,

$$Y \cong \sqrt{\frac{2}{\pi e}}X$$

$$\cong 0.483X$$

in agreement with the earlier findings of Wells.

7.1.6. Recent investigations

The importance of the above analyses, and ultimately predictions of heat inputs and penetrations for various welding schedules, is emphasised by the continuing scrutiny to which they have been subjected. Such studies help to highlight deficiencies, and to close the gap between abstracted models and practical experience.

The work of Fuerschback is one example. In 1991 Fuerschback and Knorovsky presented a detailed study of melting efficiencies in 2-D geometry (as applicable to keyholes). They paid particular attention to the determinations of arc efficiencies for

the processes investigated, thereby raising an important consideration: in processes such as PAW and GTAW very significant, and possibly even the greater part, of the input electrical power is dissipated without generating heat within the weldment.

Fuerschback and Knorovsky's results led them to propose that the dimensionless group $Qv/\alpha^2\delta H$ (see (7.14)) be replaced by $Qv/\nu\alpha\delta H$, where ν is the kinematic viscosity of the molten material. This was claimed to provide better agreement with experimental data, a finding suported by DuPont and Marder (1995).

It was certainly plausible that viscosity should play a role in heat transfer within the weld pool, and perhaps surprising that it had not been introduced earlier. However, the difficulty in accepting this alternative group was that it lacked any theoretical justification. Indeed, in more recent papers Fuerschback (1995, 1996) has shown that the discrepancies that he was observing could be resolved by ensuring that the values for thermal diffusivity used were those applying to the respective materials at or near their melting points.

Fuerschback concluded by proposing two key parameters for the development of welding schedules. These were consistent with the work of earlier researchers, and he has proposed that they be named accordingly:

$$Ry = \frac{Qv}{\alpha^2 \delta H} \qquad (after\ Rykalin) \tag{7.24}$$

and

$$Ch = \frac{v^2 A}{\alpha^2} \qquad (after\ Christensen) \tag{7.25}$$

'A' refers to the area of the fusion bead. Fueschbach observed that the melting efficiency is given by Ch/Ry. Numerical approximations were also developed. For keyhole welding he suggested

$$Ch = Ry\left(0.48 - 0.29\exp\left(-\frac{Ry}{6.8}\right) - 0.17\exp\left(-\frac{Ry}{59}\right)\right) \tag{7.26}$$

while for VPPAW and GTAW he found the following expression useful:

$$Ch = 0.44\,Ry \exp\left(-\frac{3.6}{Ry}\right) \tag{7.27}$$

7.1.7. Dimensional analysis and its implications for keyhole shape

One objective of this work was to determine how the weld pool dimensions are affected by changes in material or welding parameters. This information is formally presented in the equations derived from the different models. Nevertheless it is useful to illustrate some of the consequences through reference to practical applications. These insights will be derived through dimensional considerations and therefore could be expected to hold beyond the idealised conditions assumed by the original models. On the other hand keyhole behaviour is subject to mechanisms in addition to conductive heat flow, and therefore the limitations of the present context should be appreciated.

The temperature field associated with a point source on a plate of intermediate thickness, (7.5), is

$$T = \frac{Q}{2\pi kR}\exp\left(-\frac{vE}{2\alpha}\right)\sum_{n=-\infty}^{n=\infty}\frac{\exp\left(-\frac{vR_n}{2\alpha}\right)}{R_n}$$

where

$$R_n = \sqrt{E^2 + Y^2 + (Z + 2nG)^2}$$

Suppose a change is made in the physical dimensions of the plate such that G' = ωG, where G' is the new plate thickness, and it is desired to maintain the same scaling for the other dimensions. Then other lengths must be scaled accordingly, hence X' = ωX, Y' = ωY and Z' = ωZ. However, to scale E, v must also be scaled (v' = ωv), since E' = ω(X-vt). Therefore (vE)' = ω^2 vE and vR = ω^2 vR, and consequently α' = ω^2 α in order to preserve the value of the dimensionless quantities vE/2α and vR/2α. Finally the factor (Q/2πkG) or (Q/2πkR) requires Q' = ω^3 Q (since k = αcρ, the diffusivity by the product of heat capacity and density). Thus, writing L for any of the length dimensions:

$$
\begin{aligned}
L' &\sim \omega L \\
v' &\sim \omega v \\
\alpha' &\sim \omega^2 \alpha \\
k' &\sim \omega^2 k \\
Q' &\sim \omega^3 Q
\end{aligned} \tag{7.28}
$$

The significance of this is that it is impossible to completely compensate for the change in one of the parameters (length, travel speed, thermal conductivity or power input, without changing all the other three. This implies, for example, that the temperature field produced in 12mm 304 cannot be reproduced in 6mm 304 (albeit at a reduced size) no matter how heat input and travel speed are adjusted. Similarly, the temperature field in 3mm AISI 304 cannot be reproduced in carbon steel of the same thickness.

In reality it is unlikely that a 'scaled' version of a keyhole in 12mm material would be appropriate for thinner plate. One reason for this, the limit on minimum throat size, has already been presented. A less ambitious but practical aim would be to duplicate the transverse fusion profiles in different materials of the same thickness. Specifically it could be argued that the transverse fusion profile is more critical to keyhole stability than the temperature distribution along the welding axis. This objective is more easily met because it does not require that the isotherms be reproduced exactly. In fact the transverse profile may be maintained simply by varying the welding speed in proportion to the diffusivity such that

$$
\frac{v}{2\alpha} = \text{constant}
$$

Let the established profile correspond to a material diffusivity α and welded at a travel speed of v. Suppose the new material has a different diffusivity α'. If

$$
v' = v\frac{\alpha'}{\alpha}
$$

Then

$$y' = y$$
$$z' = z$$
$$g' = g$$

but

$$\xi' \neq \xi$$

The result is that identical transverse temperature distributions exist in each plate, but occur at different positions along the weld axis.

Unfortunately it is not possible to vary the welding speed greatly before the consequences of the necessarily increased power levels introduce further complications. For example, increasing the welding current causes the arc to expand, and this automatically widens the temperature distribution – counteracting to some degree the intended benefits. Other issues such as excessive arc force or arc pressure, and unachievable power density requirements may also arise.

Nevertheless it can be concluded that increasing the thermal diffusivity of the material is equivalent to reducing the welding speed, at least in respect to the influence of conduction on the fusion profile. Therefore there is some equivalence between failure due to high diffusivity and failure due to low welding speed. In either case failure can be linked to excessive melting of the root face.

7.2. Heat distributions in the high-speed welding regime

7.2.1. Approximations for high welding speeds

At sufficiently high welding speeds Rosenthal's equations can be simplified by introducing limiting relationships:

$$E = X - vt \quad \rightarrow \quad -vt \tag{7.29}$$

$$R = \sqrt{(vt)^2 + Y^2 + Z^2} \quad \rightarrow \quad vt \tag{7.30}$$

Since the sum E+R involves the difference between approximately equal terms it requires expansion of R:

$$E+R = -vt+\sqrt{(vt)^2+Y^2+Z^2}$$

$$= vt\left(-1+\sqrt{1+\frac{R^{*2}}{(vt)^2}}\right) \qquad (where\ R^{*2}=Y^2+Z^2)$$

$$= vt\left(-1+1+\frac{1}{2}\frac{R^{*2}}{(vt)^2}+\cdots\right)$$

$$\rightarrow \frac{R^{*2}}{2vt} \qquad (7.31)$$

It will be convenient to rewrite Rosenthal's equations in terms of α only rather than both α and k. Since $\alpha = k/\rho c$ where ρ is the density and c the thermal capacity his equations are then

$$T = \frac{Q}{2\pi\alpha\rho cG}\exp\left(-\frac{vE}{2\alpha}\right)K_0\left(\frac{vR}{2\alpha}\right) \qquad 2D \qquad (7.3')$$

and

$$T = \frac{Q}{2\pi\alpha\rho cR}\exp\left(-\frac{v(E+R)}{2\alpha}\right) \qquad 3D \qquad (7.4')$$

Noting that for large z, $K_0(z) \sim \sqrt{(\pi/2z)}\ e^{-z}\ [1 + O(1/z)]$(Handbook of Mathematical Functions) and substituting $vR/2\alpha$ for z

$$K_0\left(\frac{vR}{2\alpha}\right) \approx v\sqrt{\frac{\alpha\pi}{t}}\exp\left(-\frac{vR}{2\alpha}\right)$$

and

$$T = \frac{Q}{2\rho cvG\sqrt{\pi\alpha t}}\exp\left(-\frac{Y^2}{4\alpha t}\right) \qquad 2D \qquad (7.32)$$

Applying the high travel speed approximations to (7.4) and dropping the '*' gives

$$T = \frac{Q}{2\pi\alpha\rho cvt}\exp\left(-\frac{R^2}{4\alpha t}\right) \qquad 3D \qquad (7.33)$$

These two equations represent the limiting behaviour of Rosenthal's temperature fields with increasing welding speed. It may be noted that the heat flow has become entirely radial.

7.2.2. Instantaneous application of heat at a point

The situation at high welding speed can be compared to that of an instantaneous application of heat at the origin of a half-plane (for the 3-D problem) or at the centre of a linear filament (for the 2-D problem). The connection between these various solutions is illustrated in Figure 7.1 and Figure 7.2.

Solutions are well known, and can be found in standard mathematics texts such as Margenau and Murphy (1956). They are:

$$T = \frac{m}{\sqrt{t}}\exp\left(-\frac{Y^2}{4\alpha t}\right) \qquad (7.34)$$

for a point source on a filament and

$$T = \frac{b}{t}\exp\left(-\frac{R^2}{4\alpha t}\right) \qquad (7.35)$$

for a point on a plane (see Figure 7.1). 'b' and 'm' are constants, α the thermal diffusivity, t time after the application of the heat input, and R and Y are distances from the origin. The constants b and m can be determined by integration. To do this the total energy input per unit length will be determined by integration of ρcT over the appropriate space.

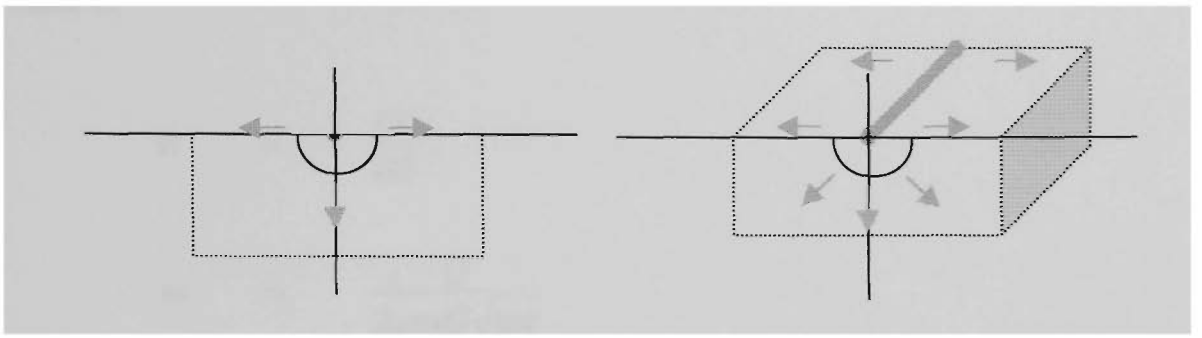

Figure 7.1. Schematic illustrating the equivalence between a point source on a half-plane and a line source on the surface of a semi-infinite block.

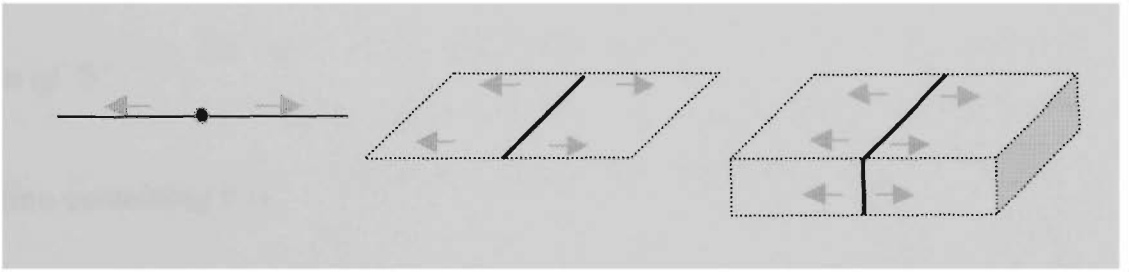

Figure 7.2. Schematic illustrating the equivalence between a point source on a line, line source on a plane and a planar source in a semi-infinite block.

Evaluation of m

To evaluate m the total heat input (per unit cross section) is first found by integrating ρcT over the entire length of the filament,

$$H = \int_{-\infty}^{\infty} \rho c T \, dY$$

$$= \frac{\rho c m}{\sqrt{t}} \int_{-\infty}^{\infty} \exp\left(-\frac{Y^2}{4\alpha t}\right) dY$$

ie

$$H = 2\rho c m \sqrt{\alpha \pi} \qquad (7.36)$$

For the physical situation of an instantaneous application of heat over the face of a weld seam is

$$H = \frac{Q}{vG}$$

$\therefore$

$$m = \frac{Q}{2\rho cvG\sqrt{\alpha\pi}}$$

and

$$T = \frac{Q}{2\rho cvG\sqrt{\alpha\pi t}}\exp\left(-\frac{Y^2}{4\alpha t}\right)$$

This is identical to (7.32), the limiting form of Rosenthal's 2-D solution.

Evaluation of 'b'.

The equation containing b is

$$T = \frac{b}{t}\exp\left(-\frac{R^2}{4\alpha t}\right)$$

The total energy H in the half plane surrounding the point source can be expressed by the integral of ρcT over the half plane,

$$H = \frac{\rho cb}{t}\int_0^\infty \exp\left(-\frac{R^2}{4\alpha t}\right)\pi R\,dR$$

$$H = 2\pi\alpha\rho cb \qquad (7.37)$$

This relates the total linear heat input into the system to the constant b. It is to be appreciated that H can also be expressed as power divided by travel speed, Q/v, in which case

$$b = \frac{Q}{2\pi\alpha\rho cv}$$

and

$$T = \frac{Q}{2\pi\alpha\rho cvt}\exp\left(-\frac{R^2}{4\alpha t}\right)$$

This is identical to the limiting form of Rosenthal's 3-D solution (7.33).

7.2.3. Re-calculation of melting efficiencies

It will now be shown that these equations can be used to determine the limiting melting efficiencies for the respective geometries. To do this, the time at which the maximum temperature at an arbitrary distance r_0 (or y_0) is reached will be determined and used to calculate the value of the peak temperature. Then the energy per unit length required to raise all the material bounded by r_0 (or $\pm y_0$) to that temperature will be calculated and compared to the total heat input. This ratio is the melting efficiency.

2-D limit

The time at which the temperature at any distance y_0 reaches a maximum is identified by the condition $dT(y_0)/dt = 0$. Differentiating (7.22) and solving for t gives

$$t = \frac{y_0^2}{2\alpha}$$

Substituting this value of t in (7.22) provides the peak temperature

$$T(\max at\ y_0) = \frac{m}{y_0}\sqrt{\frac{2\alpha}{e}}$$

The heat required to raise the material between $-y_0$ and y_0 to this temperature is

$$H(\min) = 2\rho cm\sqrt{\frac{2\alpha}{e}}$$

and the melting efficiency is H(min)/H, where H is given by (7.36):

$$ME = \frac{2\rho cm}{2\rho cm}\frac{\sqrt{\frac{2\alpha}{e}}}{\sqrt{\pi\alpha}}$$

so

$$ME = \sqrt{\frac{2}{\pi e}}$$

This is the result obtained by Wells and later by Swift-Hook and Gick.

3-D limit

The time at which the temperature at any radius r_0 reaches a maximum is found in exactly the same way as for the 2-D limiting case, and as before

$$t = \frac{r_0^2}{4\alpha}$$

The peak temperature at r_0 is therefore

$$T(\max at\, r_0) = \frac{4\alpha b}{r_0^2 e}$$

The heat required to raise all the material within the half-circle bounded by r_0 to the maximum temperature reached at r_0 is

$$H(\min) = \frac{1}{2}\pi r_0^2 . \rho c \frac{4\alpha b}{r_0^2 e}$$

$$= \frac{2\pi\alpha\rho ct}{e}$$

and so the melting efficiency is

$$\frac{H(\min)}{H} = \frac{2\pi\alpha\rho cb}{e2\pi\alpha\rho cb}$$

$$= \frac{1}{e}$$

As required.

7.2.4. Energy partitioning

Equations (7.34) and (7.35) permit easy inspection of the radial temperature and heat distributions. First, the solutions indicate that the temperatures on the weld axis will be considerably higher than on an isotherm at the time when that isotherm reaches its maximum width. The extent of this difference is calculated by substituting for t. The results are:

$$T_{Y=0} = \sqrt{e}\,T_{Y=y0} \qquad (2D\ case\ where\ t=\frac{y_0^2}{2\alpha})$$

$$T_{R=0} = eT_{R=r0} \qquad (3D\ case\ where\ t=\frac{r_0^2}{4\alpha})$$

Evidently a significant amount of 'excess energy' is still enclosed by any isothermal boundary, such as the fusion line, when it reaches its maximum width. For example, for steel with a melting point of 1500°C the central temperature would be over 4000°C when the pool reaches its maximum width for a 3-D geometry, and close to 2500°C for a keyhole. It is noted that the boiling point of iron is 2750°C (CRC handbook). The extent of this excess heat will now be determined.

In the limiting 2-D case.

$$H = \frac{\rho cm}{\sqrt{t}}\int_{-\infty}^{\infty}\exp\left(-\frac{Y^2}{4\alpha t}\right)dY$$

To determine the heat contained within an isothermal boundary set $t = y_0^2/4\alpha$, and integrate from $-y_0$ to y_0:

$$H = \frac{\sqrt{2\alpha}\,\rho cm}{y_0}\int_{-y_0}^{y_0}\exp\left(-\frac{Y^2}{2y_0^2}\right)dY$$

$$H_{-y0<Y<yo} = 2\rho cm\sqrt{\alpha\pi}\,Erf\left(\frac{1}{\sqrt{2}}\right)$$

Comparing this with $H(\min) = 2\rho cm\sqrt{(2\alpha/e)}$ shows that

$$H_{-y0<Y<yo} = \sqrt{\frac{e\pi}{2}}\,Erf\left(\frac{1}{\sqrt{2}}\right)H_{\min}$$

$$\approx 1.41H_{\min}$$

Also, since the total heat is $\sqrt{(\pi e/2)}$ H(min), the heat outside the isotherm must be [1-Erf($1/\sqrt{2}$)] times H(min), or about 0.317 H(min). So, if for example, the weld pool was well-mixed to give a uniform melting temperature, the maximum efficiency would be 1/(1.317) or about 76%, and higher still if allowance was made for the latent heat of fusion.

In the 3-D limit

$$H = \frac{\rho ck}{t}\int_0^{\infty}\exp\left(-\frac{R^2}{4\alpha t}\right)\pi R\,dR$$

Setting $t = r_0^2/4\alpha$, and integrating between 0 and r_0 gives

$$H_{R<r0} = 2\pi\alpha\rho cb\left(1-\frac{1}{e}\right)$$

Compare this to the heat required to melt the material,

$$H_{\min} = \frac{2\pi\alpha\rho cb}{e}$$

and it is evident that the material within the isotherm contains (e-1) or approximately 1.72 times the heat necessary to achieve the boundary temperature:

$$H_{R<r0} = (e-1)H_{\min}$$

Also, since the total heat input is e times H(min),

$$H_{R<r0} + H_{R>r0} = eH_{\min}$$

the heat outside the isotherm is exactly equal to H(min). One implication is that if the thermal gradients within the pool could be eliminated the melting efficiency would approach 50%. Furthermore, since real fusion processes absorb heat without increasing the temperature, the minimum actual heat within the pool would exceed that outside it, and the efficiency would exceed 50%.

7.2.5. The onset of the high-speed regime

The parameter $v/2\alpha$ is used to scale the length dimensions, and the value of the resultant dimensionless quantity is critical in determining the resultant behaviour of the process. For example, when $(v/2\alpha)$ times the width of the puddle exceeds about 2, a keyhole process will have achieved about 90% of its theoretical efficiency. Table 7.1 presents calculated values for a variety of materials and welding speeds, and can be used as a guide for determining the operating regime for a particular application.

If the limiting 2-D solution is used as a reference the meaning of specific values of the parameter $vD/2\alpha$ can be made a little clearer. It has been established that any chosen isotherm reaches its maximum extent at a time

$$t = \frac{Y^2}{2\alpha}$$

Now if this time is applied to the motion of a finite-speed heat source, that heat source will have travelled a distance X given by

$$X = \frac{vY^2}{2\alpha}$$

Comparing the distance travelled by the source to the extent of the isotherm gives

$$\frac{X}{Y} = \frac{vY}{2\alpha} = \frac{d}{2}$$

So for example, if d = 2 then the source will have travelled a distance equal to the maximum radius of the isotherm in the time required for this maximum width to be achieved. In other words, if one imagines a 'temperature wave' travelling radially out from the source, the 'speed' of this wave is equal to the speed of the source. In the limiting 3-D solution the time for any point R to reach its maximum temperature is

$$t = \frac{R^2}{4\alpha}$$

and so

$$\frac{X}{R} = \frac{d}{4}$$

Table 7.1. 2-D puddle diameters for 90% maximum melting efficiency for various materials and travel speeds. Diffusivity values are taken at approximately one third of the melting temperature (Easterling, 1992)

Material	**Diffusivity**	**Travel speed** *mm/min*						
	mm²/sec	*100*	*200*	*400*	*800*	*1600*	*3200*	*6400*
Aluminium	100	240	120	60	30	15	7.5	3.8
Copper	96	230	115	58	29	14	7.2	3.6
Ni steel	11	26.4	13.2	6.6	3.3	1.6	0.83	0.41
Mild steel	9.1	21.8	10.9	5.5	2.7	1.4	0.68	0.34
Titanium	9.0	21.6	10.8	5.4	2.7	1.4	0.68	0.34
Monel 400	8.0	19.2	9.6	4.8	2.4	1.2	0.60	0.30
AISI 304	5.3	12.7	6.4	3.2	1.6	0.8	0.40	0.20
Inconel 600	4.7	11.3	5.6	2.8	1.4	0.7	0.35	0.18

7.2.6. Implications for heat flow from keyholes

The concept of melting efficiency and its relationship to travel speed and puddle diameter provides another means of appreciating the consequences of travel speed on keyhole shape. Suppose a keyhole takes on a conical shape at a 'suitably high welding speed'. A 'suitably high welding speed' can be defined as meaning that the maximum melting efficiency is achieved over the keyhole's entire depth. The fusion profile will therefore not change no matter how much the travel speed is increased, provided the heat input per unit length is constant.

However, suppose the travel speed is slowly decreased. If only heat flow is considered the consequences will be a progressive decrease in melting efficiency. The interesting aspect to this is that the loss of efficiency will be greatest where the puddle is narrowest. Consequently the keyhole radius will begin to contract, and the rate of contraction will be greatest where the radius is smallest. Even if the heat input is increased to maintain full penetration, the fusion depth-to-width ratio will decrease, until eventually the root penetration becomes uncontrollable.

7.3. Modelling the thermal field associated with keyholes

7.3.1. Solution by separation of variables

Following Rosenthal (1941, 1946) the equation for the temperature field (under his assumptions of constant thermal properties) is (7.2)

$$\frac{\partial^2 T}{\partial E^2}+\frac{\partial^2 T}{\partial Y^2}+\frac{\partial^2 T}{\partial Z^2} \quad = \quad -\frac{v}{\alpha}\frac{\partial T}{\partial E}$$

Putting $\xi = (v/2\alpha)\,E$, $y = (v/2\alpha)\,Y$, $z = (v/2\alpha)\,Z$

$$\frac{\partial^2 T}{\partial \xi^2}+\frac{\partial^2 T}{\partial y^2}+\frac{\partial^2 T}{\partial z^2} \quad = \quad -\frac{v}{\alpha}\frac{\partial T}{\partial \xi} \tag{7.38}$$

Setting $T = e^{-\xi}\Gamma$ one finds that Γ satisfies:

$$\frac{\partial^2\Gamma}{\partial\xi^2}+\frac{\partial^2\Gamma}{\partial y^2}+\frac{\partial^2\Gamma}{\partial z^2} = \Gamma \tag{7.39}$$

In cylindrical coordinates this is

$$\frac{\partial^2\Gamma}{\partial r^2}+\frac{1}{r}\frac{\partial\Gamma}{\partial r}+\frac{\partial^2\Gamma}{\partial z^2}-\Gamma = 0 \tag{7.40}$$

where $r = \sqrt{(\xi^2+y^2+z^2)}$, and it is assumed that Γ has no angular dependence. This equation can be solved by separation of variables. Assume $\Gamma = P(r)\,S(z)$, then

$$\frac{1}{P}\left(\frac{\partial^2 P}{\partial r^2}+\frac{1}{r}\frac{\partial P}{\partial r}\right)-1 = \frac{1}{S}\frac{\partial^2 S}{\partial z^2}$$

Equate both sides to a constant, $-w^2$, (since the LHS is a function of r and the RHS is a function of z) and obtain

$$\frac{\partial^2 P}{\partial r^2}+\frac{1}{r}\frac{\partial P}{\partial r}-\left(1+w^2\right)P = 0$$

$$\frac{\partial^2 S}{\partial z^2}+w^2 S = 0 \tag{7.41}$$

7.3.2. Boundary conditions

The solution to the first of these equations is the modified Bessel function of the second kind, zero order, for the reasons given by Rosenthal (1941). That is

$$P_w = K_0(w'r) \qquad where\ w' = \sqrt{1+w^2} \tag{7.42}$$

The solution for S is

$$S_w = a\cos(wz)+b\sin(wz) \tag{7.43}$$

The solution for the temperature field in a plate thickness G can be expressed as a series:

$$T = e^{-\xi}\sum c_w P_w S_w \tag{7.44}$$

where the coefficients c_w are chosen so that the boundary conditions are satisfied. For consistency let g = (v/2α)G.

Since the temperatures above and below the plate do not enter the problem it is convenient to define the temperature to be periodic, period 2g (if Z=G then z=g). An advantage of this device is that the temperature gradients across each surface can readily be made equal to zero, providing compliance with the surface boundary conditions. If z=0 is taken as the front face of the plate the temperature is an even function of z and all sine terms vanish. Also, since the temperature has a period of 2g

$$\cos(wz) = \cos(w(z+2g))$$

for all w. Thus 2wg = 2nπ or w = nπ/g. As a result, T can be simplified to

$$T = e^{-\xi}\sum_{n=0}^{\infty} a_n K_0(r_n)\cos\left(\frac{n\pi z}{g}\right) \tag{7.45}$$

$$where\, r_n = \sqrt{1+\left(\frac{n\pi z}{g}\right)^2}\; r$$

The behaviour of T is now correct for large r, and at the plate surfaces. It remains to ensure that the temperature field corresponds to the specified distribution of the heat source.

Consider the case where the heat is deposited along the Z axis (R=0) and is given by Q(Z). Now, the heat crossing a circle radius R equals $2\pi Rk\partial T/\partial R$ (Rosenthal 1941) and as R approaches zero this quantity approaches the heat input, Q(Z). Further, $\partial T/\partial R = (\partial T/\partial r)(\partial r/\partial R)$ and $R\partial r/\partial R = r$, hence

$$2\pi Rk\frac{\partial T}{\partial R} \quad = \quad 2\pi rk\frac{\partial T}{\partial r}$$

For small x, $K_0(x) \cong \ln(x) + \gamma$ where γ is Euler's constant, so $\partial K_0(r_n)/\partial r$ goes to 1/r. Therefore,

$$Q(Z) \quad = \quad Lim_{r\to 0}\, 2\pi k\frac{\partial}{\partial r}\left(e^{-\xi}\sum_{n=0}^{\infty}a_n K_0(r_n)\cos\left(\frac{n\pi z}{g}\right)\right)$$

$$= \quad 2\pi k\sum_{n=0}^{\infty}a_n \cos\left(\frac{n\pi z}{g}\right)$$

Before continuing it is convenient to define normalised power distribution functions F(Z) and f(z) by dividing the corresponding power distributions by the total power Q:

$$F(Z) \quad = \quad \frac{Q(Z)}{Q}$$

$$f(z) \quad = \quad \frac{q(z)}{Q} \qquad (7.46)$$

It remains to determine how the description of the power distribution (F(Z)) should be expressed as a function of z (ie f(z)). Noting that the integral of either function over the thickness of the plate is one, then:

$$\int_0^G F(Z)dZ \quad = \quad \int_0^g f(z)dz$$

Now the right hand side can be re-written

$$\int_0^g f(z)dz = \int_0^g f(z)d\frac{vZ}{2\alpha}$$

$$= \int_0^G \frac{v}{2\alpha} f(z)dZ$$

Whence

$$F(Z) = \frac{v}{2\alpha} f(z)$$

And

$$f(z) = \frac{4\pi\alpha k}{Qv} \sum_{n=0}^{\infty} a_n \cos\left(\frac{n\pi z}{g}\right) \qquad (7.47)$$

The coefficients can be determined readily since the set of functions cos(nπz/g) (n=0, 1, 2, ...) are orthogonal on the interval -g to g. Multiplying both sides by cos(mπz/g) and integrating between -g and g gives

$$\int_{-g}^{g} f(z)\cos\left(\frac{m\pi z}{g}\right)dz = \frac{4\pi\alpha k}{Qv} a_m \int_{-g}^{g} \cos^2\left(\frac{m\pi z}{g}\right)dz$$

$$= \frac{8\pi\alpha k}{Qv} a_0 \qquad for\ m=0$$

$$= \frac{4\pi\alpha k}{Qv} a_m \qquad for\ m>0$$

That is:

$$a_0 = \frac{Q}{4\pi kG} \int_{-g}^{g} f(z)dz$$

$$= \frac{Q}{2\pi kG}$$

Therefore we have

$$a_0 = \frac{Q}{4\pi kG}$$

$$a_n = \frac{Q}{2\pi kG}\int_{-g}^{g} f(z)\cos\left(\frac{n\pi z}{g}\right)dz \qquad (7.48)$$

7.3.4. Special cases

If f(z) is a constant, say 1/g, then $a_0 = Q/(2\pi kG)$ and all other coefficients are zero, and hence:

$$T = \frac{Q}{2\pi kG}e^{-\xi}K_0(r)$$

as required. The other extreme, the temperature surrounding a point source can also be determined. For this consider a heat source such that

$$f(z) = \frac{1}{z_0} \quad for\ -z_0 \le z \le z_0$$

$$= 0 \quad \text{elsewhere on the interval.}$$

This represents a fixed quantity of heat distributed over a fraction of the plate thickness z_0/g. The coefficient a_0 is

$$a_0 = \frac{Q}{2\pi kG}$$

The coefficient for a_n is

$$a_n = \frac{Q}{\pi kG}\frac{\sin\left(\frac{n\pi z_0}{g}\right)}{\left(\frac{n\pi z_0}{g}\right)}$$

Now the interval z_0 over which the source is distributed is allowed to approach zero. Since the limit of sin(x)/x as x approaches 0 is 1

$$a_n = \frac{Q}{\pi k G}$$

And .

$$T = \frac{Q}{2\pi k G} e^{-\xi} \left(K_0(r) + 2 \sum_{n=1}^{\infty} K_0(r_n) \cos\left(\frac{n\pi z}{g} \right) \right)$$

This is the same result as that obtained by Rosenthal using the method of images. In particular, however, this formulation allows the determination of the temperature field for an arbitrary heat distributions along the vertical axis of the weld.

Descriptions such as that presented here are useful for inferring general properties of the temperature fields, and for providing quick but approximate estimates of the cooling cycles. However, they are not good at providing detail close to the heat source because of the various approximations built into the model. For example this model does not allow the heat source to have any radial extent or angular dependence. In addition, important phenomena such as latent heats for different phase changes, and convection, have been ignored. Such detailed solutions can only be attempted using computer-based numerical simulations. Nevertheless, when these limitations are appreciated, the model can provide valuable insights into the process in question. This can be seen from the plots in Figure 7.3, where only the first two terms in the series solution (7.45) have been used, and in the concluding considerations of pool shape.

7.3.5. The effect of heat distribution on root face pool shape

The foregoing arguments show how the temperature fields associated with a certain class of heat distributions can be calculated. It will be noted that the expansion for the temperature field is reduced to only two terms if the heat distribution along the axis has the form (1 + a cos(πz/g)) (see Figure 7.3). This choice allows variation of the

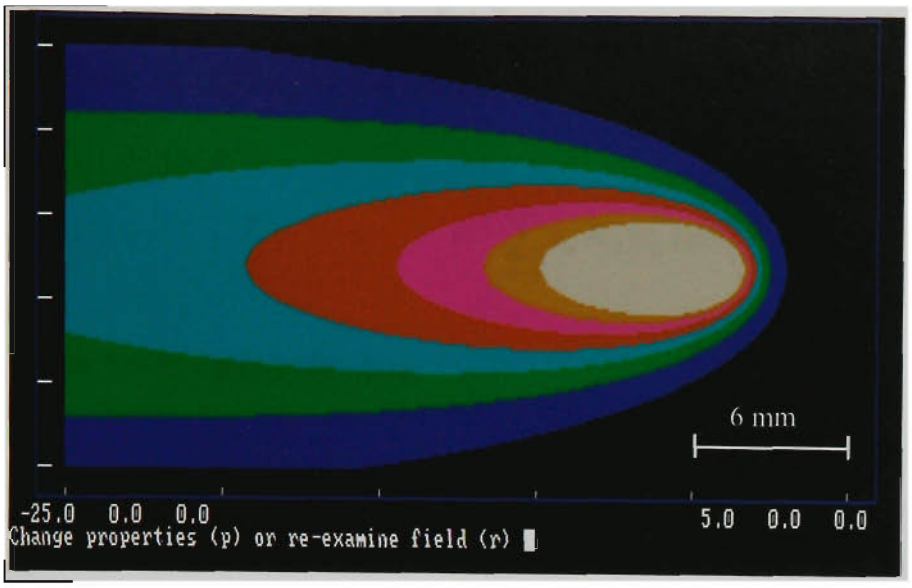

Simulation Example:

AISI 304
10mm plate

Front face

Length 30mm
Width 20mm
Bands 200°C
Melt White

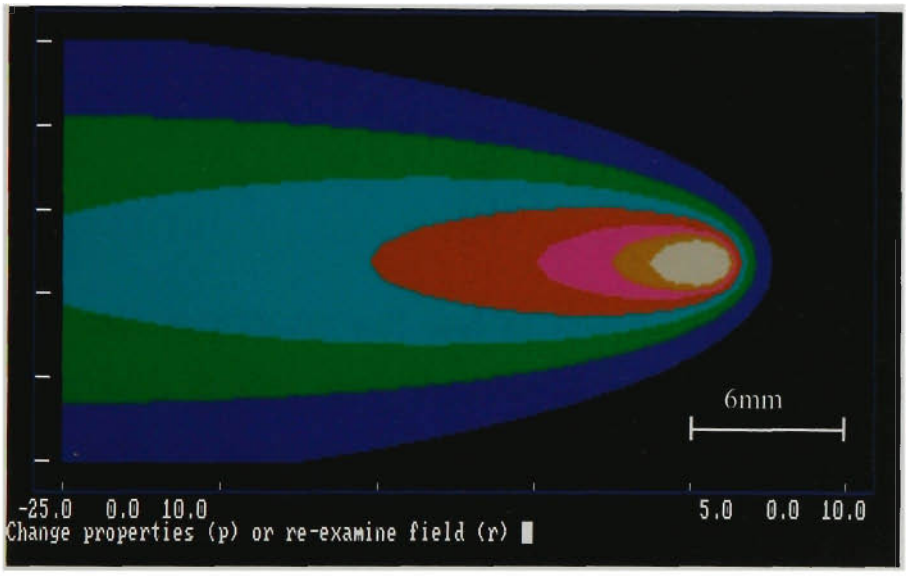

Simulation Example:

AISI 304
10mm plate

Root face

Length 30mm
Width 20mm
Bands 200°C
Melt Grey

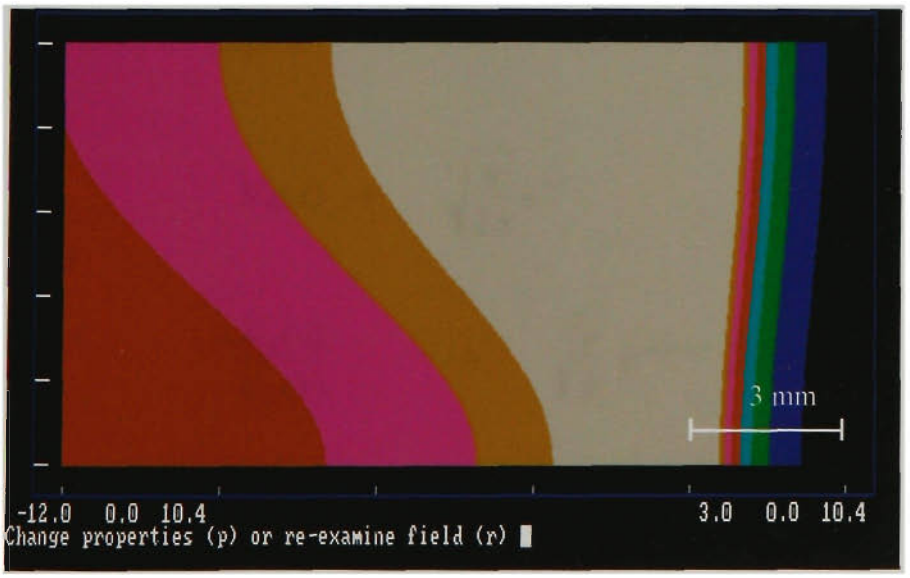

Simulation Example:

AISI 304
10mm plate

Fraying face

Length 15mm
Depth 10mm
Bands 200°C
Melt Grey

Figure 7.3. Examples of temperature fields for a simulated keyhole weld on 10mm stainless steel (600 A, 18V, 300mm/min). $f(z) = Q[1 + 0.35\cos(\pi z/g))]$. Refer to (7.45) and (7.47) for discussion.

heat input from uniformly distributed to concentrated at the top or bottom of the keyhole, depending on the choice for a. Since

$$T = e^{-\xi}\sum_{n=0}^{\infty} a_n K_0(r_n)\cos\left(\frac{n\pi z}{g}\right)$$

Then for this particular case

$$T = \frac{Q}{2\pi kG}e^{-\xi}\left(K_0(r)+aK_0(r_1)\cos\left(\frac{\pi z}{g}\right)\right)$$

If the solution is rewritten as

$$T = \frac{Q}{2\pi kG}e^{-\xi}K_0(r)\left(1+a\frac{K_0(r_1)}{K_0(r)}\cos\left(\frac{\pi z}{g}\right)\right)$$

the ratio $K_0(r_1)/K_0(r)$ will tend to zero for large r (Handbook of Mathematical Functions). In other words the z-variation in temperature tends to insignificance as r increases. Furthermore, this argument holds for all the cosine terms in the more general expansion.

The rate at which the z-variation is attenuated is dictated by the ratio $K_0(r_n)/K_0(r)$. For example, for large x

$$K_0(x) \rightarrow \sqrt{\frac{\pi}{2x}}e^{-x}$$

And

$$\frac{K_0(x)}{K_0(y)} \rightarrow \sqrt{\frac{y}{x}}\,e^{-(x-y)}$$

Now

$$r_n = \sqrt{1+\left(\frac{n\pi}{g}\right)^2}\,r$$

Therefore as r_n becomes large

$$r_n \cong \frac{n\pi r}{g}$$

and

$$\frac{K_0(r_n)}{K_0(r)} \rightarrow \sqrt{\frac{n\pi}{g}} \exp\left(-r\left(\frac{n\pi}{g}-1\right)\right)$$

This example illustrates the more general result that the smaller the value of g the more rapidly the z-distribution in temperature is attenuated and the more difficult it becomes to maintain a small root bead relative to the front face bead. Since

$$g = \frac{vG}{2\alpha}$$

favourable keyhole profiles are promoted by increasing plate thickness or welding speed, and selecting materials of lower thermal diffusivity. This result is in agreement with expectations. In fact it reaches the same conclusions as the preceding section, re control of the root bead, through a more formal mathematical process.

8. Conclusions

8.1. Review

8.1.1. Thesis

It will be recalled from Chapter 1 that the thesis being presented is that:

"GTAW can be operated in a keyhole mode to provide a process having some significant advantages over established welding methods."

The defence of this claim required not only the demonstration that such a mode of operation was possible, but that it was both practical and well-understood. Having completed the proposed study the case for the thesis can now be reviewed.

8.1.2. Practical appraisal

The appraisal of Chapter 3 introduced a novel GTAW process variant, known as keyhole GTAW. In fact, the novelty has been recognised with the issuing of international patents (Jarvis et al, 1999). The novelty arises because the keyhole is generated through the peculiar choice of operating conditions rather than the introduction of specific enhancements. For example, it uses a conventional high current GTAW torch designed to provide good and reliable cooling of the electrode. The process can be implemented using 'off-the-shelf' GTAW power sources of suitable rating (a 600 amp supply would be suitable for most applications). It does not use enhancements, such as dual shielding or orifices, to pinch or otherwise constrict the arc.

It was further demonstrated that keyhole GTAW is easy and inexpensive to implement, and can be used within broad operating windows. Qualified procedures were developed for a selection of stainless steel plates ranging between 3 and 12mm thick. Procedures have also been developed for titanium plate and pipe to 14mm (wall) thickness. These procedures all call for simple square-butt joint configurations, and joints are completed

in a single pass with little of no filler additions. This performance represents a significant advantage over GMAW and conventional GTAW for such applications.

Similar performance might be obtained with plasma arc welding, but implementation costs are considerably greater, and process operation is more complex. Laser and electron beam processes are capable of superior performance, but both capital and operational costs are very much greater.

The research covered in this chapter has shown that practical control over the process can be exercised through variations to the electrode geometry, voltage, current, travel speed and shielding gas composition. In general use however, variation of only travel speed and current is sufficient for access to most of the process operating window. Furthermore, keyhole operation is readily confirmed through observation of the efflux plasma emerging from the root face, and this has been used as a very simple but effective control strategy.

8.1.3. Keyhole stability

In Chapter 4 it was shown that GTAW keyhole structures must be presented in three dimensions. More specifically, these surfaces are closely related to minimal surfaces, familiar in such phenomena as soap films. Implicit in this description is the critical, stabilising role accorded to surface tension. This is in sharp contrast to traditional models for laser and electron beam keyholes, where the keyhole is usually modelled in two dimensions. In these 2-D models surface tension is always destabilising, and acts to collapse the keyhole.

Elementary analyses of the forces acting on the root bead were used to provide an understanding of how the weld pool is supported while it solidifies. This investigation resulted in the so-called first stability criterion that specifies the maximum allowable root bead width for a given material type and plate thickness. Among the implications are that the process operates to a limiting plate thickness, and that the welding speed must be reduced as this limit is approached.

It was further shown that surface tension limits the minimum thickness of plate that can be welded. This finding might conveniently be referred to as the second stability criterion. In this case the limit is established by purely geometric considerations and is not directly dependent on material properties.

Surface tension is involved in the generation of the surface structure of the pool, and this was examined initially through the novel concept of weld pool deficit. This proved to be fruitful, and led to the identification of different welding regimes. In particular, it was found that prior to keyhole formation the surface geometry can switch between one dominated by surface tension to one limited by displacement, as the arc force increases. The latter condition was equated to a deep penetration mode. The transition was found to be abrupt, and a precursor to the development of a keyhole.

The discussion was then directed to the geometry of the weld pool surface. Equations were developed using an energy minimisation strategy, and solutions for specific examples demonstrated that keyholes could be anticipated for a wide variety of conditions. The identification of keyhole solutions is offered as strong evidence that the source of GTAW keyhole stability has been identified. Furthermore, the tendency for the pool surface to settle into these minimum energy states was used to explain the forces inducing flow from the leading to trailing regions of the pool in moving systems. This, coupled with the identification of a mechanism to regulate the deficit, provided a useful introduction to the pool dynamics.

An interesting aspect of the process is that keyhole generation involves the transition through fundamentally different surface topologies. Considerations of this provided additional insights into issues such as hysteresis and the generation of porosity.

8.1.4. Arc forces and pool displacement

It has long been appreciated that the arc force is dependent on the square of the current, and the current distributions at the anode and cathode. The analysis of Chapter 5 developed an electrodynamic model that generalised the results proposed by Converti (1981). Both models consider the arc force as having two components, namely those

due to radial compression and axial acceleration. Mathematically these can be identified as components of a Navier-Stokes equation for the arc:

$$J_z \, x \, B_\theta - \nabla P = 0$$

and

$$J \, x \, B_\theta = \rho \frac{dv}{dt}$$

The model that was developed not only provided a generalised expression for the arc force, but also one for the arc pressure distribution. It was particularly interesting to find that, if viscosity is ignored, the arc exhibits a well-defined core. This core has the radius of the cathode emission region, and the peak arc pressure is found approximately at its boundary. In addition, the peak arc pressure is equal to the mean pressure at the cathode emission region, and does not vary with arc length or continued arc expansion. It was noted that the pressure due to axial acceleration of the plasma constitutes a stagnation pressure, and therefore is not isotropic. The force (or pressure) exerted on the weld pool crater is dependent on the extent to which the wall affects the velocity of the plasma.

Attention was then directed towards experimental measurements of arc forces. Unfortunately however, the experimental techniques did not provide a measurement of the actual force exerted on the weld pool surface but only a related quantity, the FAF. The FAF responds only to variations at the cathode. Estimates based on the work of other researchers, and inferred from measured pool deficits, suggested that the actual arc forces were approximately 50% of the FAF values.

The experimental data were used to further qualify the understanding of the arc properties. For example, the assumption that the surface area for electron emission is independent of tip angle was used to explain the relationship between the FAF and the electrode tip angle. This same assumption, and the published results suggesting arc voltage changes only gradually with current, was then used to link arc voltage to the tip angle, and thereby establish a relationship between arc voltage and arc force. The existence of such a relationship may prove important for process monitoring and control since the arc force is difficult to monitor directly.

The developing understanding of the behaviour of the cathode emission region in physical situations was then called upon to qualitatively understand the mechanisms for the influences of electrode diameter and gas composition. Finally, the behaviour of arc force with electrode position was also connected to variations in the emission region, although the mechanisms for this were more speculative.

8.1.5. Arc-keyhole relations

From a functional point of view arcs transport heat and momentum to the weldment. The heat is conveyed by the electrons, gas and radiation, although the latter is generally relatively small. The literature suggests that the electrons may transport as much as 80% of the total energy transferred. The plasma gas may also contribute a significant heat flux through conduction and convection. Conduction is dependent on the choice of shielding gas and the contact area between the arc and weld pool. Keyholes expose relatively large surface areas to the arc, and consequently the geometry will enhance role of conduction relative to other energy transfer mechanisms. The plasma gas is also the vehicle for conveying momentum to the weld pool, and therefore its characteristics are important in relating the pool displacement to the specific welding conditions.

This published information provided the starting point for the discussion of the role of the arc in keyhole welding developed in Chapter 6. The first issue covered was the link between electrode geometry and fused area. This was found to be a result of convection within the arc. Since convection is driven by Lorentz forces, it is therefore dependent on current and electrode geometry.

The discussion subsequently moved on to examine the link between electrode geometry and the threshold current for keyhole generation. The peak arc pressure was identified as the critical parameter in determining this threshold current. Recalling the work of the preceding chapter, a simple model was advanced that related threshold current to electrode geometry and plate thickness:

$$I_t \quad \sim \quad \sqrt{h \sin\theta}$$

An important implication of this model was that the weld behaviour may be significantly affected by variations in the area of the cathode emission region, which in turn is sensitive to the heat flow within the electrode. Thus changing the electrode stick-out, taper, diameter, or composition are all means of altering the point of transition to keyhole mode. Choosing large diameter electrodes is one of several simple strategies for reducing the threshold current.

The influence of shielding gas and arc length on threshold current was also examined. Although helium-rich arcs are very effective in transferring thermal energy they were not desirable for keyhole welding because, apparently, the high viscosity of helium dampened the action of the arc core. On the other hand, diatomic gases absorb substantial amounts of energy in dissociation, and this provided an alternative, highly efficient energy transport mechanism known as 'reactive thermal conductivity'. This gave better keyholing potential than pure argon because heat input was increased without sacrificing high core pressure. Although the addition of gases such as hydrogen or nitrogen to an argon shielding gas gave the lowest threshold currents, their detrimental interaction with some metals and alloys limit their use.

The final parameter discussed in this chapter was arc length. Arc length had a significant effect on keyhole behaviour when operation was near the limits of the process envelope. For example, keyholes were not observed in situations where the electrode was submerged. However, when the electrode was incrementally raised from a submerged position the threshold current was at first high, but on continuing increase in arc length it displayed an abrupt transition to a significantly lower value. This lower level then remained relatively constant on continued raising of the electrode. The practical implication was that operation with too short an arc length can give inconsistent performance, with the threshold current either becoming random between the two levels, or the process failing completely. At the other extreme of arc length the weld pool may also broaden, this time due to expansion of the arc. Thinner (eg 6mm) plate did not appear sensitive to this but thicker sections did show a quite well defined upper as well as lower limits to arc length, and by association, arc voltage.

8.1.6. Conductive heat flow in the weldment

The final investigative chapter, Chapter 7, addressed conductive heat flow in the weldment. The purpose of this study was to review the available literature and to develop some tools for modelling the GTAW form of keyhole. Nevertheless, there were some pertinent findings. For example, it was concluded that there is equivalence between failure due to high thermal diffusivity and failure due to low welding speed. In either case failure can be linked to excessive melting of the root face.

The failure mechanism is due to a progressive loss in melting efficiency, beginning at the root of the keyhole. (It was shown in the discussion that the melting efficiency increases with increasing pool diameter). Continued loss in efficiency causes the keyhole to become ever more rounded or concave until penetration becomes uncontrollable and the keyhole collapses. The only counter to this is to reshape the heat source to deliver more energy to the root. This can be interpreted as a requirement for a more constricted arc.

8.2. Conclusions

8.2.1. Summary

The research presented in the preceding chapters has introduced an original variant of the GTAW process. The granting of international patents supports this claim (Jarvis, Barton, Ahmed, CRC-MWJ 1999). While it could be argued that alternate forms of the GTAW process have also achieved keyhole performance, these involve very significant modifications to the welding equipment, and deliver pronounced enhancement of the power density within the arc. More particularly, in such processes the enhancements are emphasised to provide valid differentiation from GTAW. Examples include plasma arc welding and dual shielded GTAW. Keyhole GTAW is as readily differentiated from these processes as they are from one another.

The research has demonstrated that this welding mode is suitable for commercial use. Procedures for a significant range of plate and pipe material have been developed and

qualified. These procedures have been found to be robust and easily implemented. In particular the process accepts square butt joint configurations with reasonable tolerance to gap and mismatch. Where the process can be used it has been found to offer considerable savings when compared to conventional GMAW and GTAW alternatives. The reduced joint preparation, single pass full penetration performance, and almost total elimination of filler wire generate these economies. The several companies who have already introduced the process into their production support these claims.

The final observation to be made is that the process has been described at both practical and mechanistic levels, thereby providing a broad appreciation of the process parameters. In this regard the identification of the source of the keyhole stability has been very satisfying. More importantly the impact of specific operating conditions can now be estimated from fundamental considerations with confidence. This level of understanding was necessary before this welding method could be regarded as a 'process' and supported in industrial applications.

It is therefore proposed that the thesis has been justified.

8.2.2. Future work

This research has covered a broad range of issues relating to keyhole GTAW. Unfortunately however, this has not allowed individual topics to be treated in great detail. It would appear that all areas would benefit from further investigation. Nevertheless some areas present themselves as priorities.

The process itself has several opportunities for development. Perhaps the two most valuable extensions relate to operation out-of-position, and the use of keyhole root passes for very thick sections. The immediate target for out-of-position welding would be operation in the horizontal position. This would create new opportunities, such as in applications for tanks and pressure vessels. The development of keyhole welding for root passes in heavy sections also has the potential for major benefits. For example, it would seem realistic to complete a full penetration joint in say 20mm plate in two passes if the joint were prepared with a 10mm root face. It may well eventuate that

keyholing into such a prepared joint would also enhance the possibilities of welding out-of-position.

Another area for further research is the keyhole surface. Observation of the process demonstrates that these surfaces are very stable and can be almost ripple-free. This raises the tantalising prospect of almost perfect realisations of well-defined mathematical surfaces. It is unusual for high-power welding processes to be so well behaved.

A third priority is the development of on-line monitoring and control for the process. Observations in this work suggest front-face as well as root face detection is possible. Control via front face detection would be a particularly attractive development, since there are many critical applications where the root face of the weldment is not readily observed.

It is hoped that research into this process will continue and that the work presented here will serve as a useful foundation for future developments.

9. References

Adonyi-Bucurdiu, I. 1989: *"A study of arc force effects during submerged gas tungsten-arc welding"*, PhD dissertation, The Ohio State University.

Adonyi, Y., Richardson, R.W. and Baeslack III, W.A., 1992: *"Investigation of arc force effects in subsurface GTA welding"* Welding Journal, Vol 71 (9) pp 321s-330s.

Akhter, R., Davis, M., Dowden, J., Kapadia, P., Ley, M. and Steen, W.M., 1989: *"A method for calculating the fused zone profile of laser keyhole welds"*, Journal of Physics D: Applied Physics, Vol 22, pp 23-28.

Albright, C., 1982: *"Pulsed CO2 laser welding"*, Trends in welding in the United States, Conf. Proc. American Society for Metals, Nov. 1982.

American Welding Society 1991: Welding Handbook, 8th Edition, Vol 2.

Andrews, J.G. and Atthey, D.R., 1976: *"Hydrodynamic limit to penetration of a material by a high-power beam"*, Journal of Physics D: Applied Physics, Vol 9, pp 2181-2194.

Apps, R.L. and Milner, D.R., 1955: *"Heat flow in argon-arc welding."* British Welding Journal, October 1955, pp 475-485.

Arata, Y., Terai, K. and Matsuda, S., 1973: *"Study on characteristics of weld defects and its prevention in electron beam welding - characteristics of weld porosity"*. Trans. JWRI 2 1973, 103. IIW Document IV-114-73.

Arata, Y., Maruo, H., Miyamoto, I. and Takeuchi, S., 1977: *"Dynamic behaviour of laser welding"*, IIW Document IV-22-77.

Arata, Y., Abe, N. and Oda, T., 1983: *"Beam hole behaviour during laser welding"*. ICALEO '83. IIW Document IV-339-83.

Arata, Y. and Inoue, K., 1974: *"Generation of point arc and its characteristics"*, Trans. JWRI 3, 1974, 201.

Arata, Y. and Kobayashi, A., 1983: *"Fundamental characteristics of stationary plasma arc in gas tunnel"*, Trans. JWRI 13, 1984, 173.

Arata, Y. Abe, N. Oda, T. and Tsujii, N. 1984: *"Fundamental phenomena during vacuum laser welding"*, ICALEO '84.

Arata, Y. and Tomie, M., 1984: *"Development and application of a strong focusing electron beam gun with multi-stage electromagnetic accelerating units"*, Journal of the High Temperature Society, 10, 1984.

Arata, Y. and Kobayashi, A.,1985: *"Development of gas tunnel type high power plasma jet"*, J. High Temp. Soc. II, 1985.

ASM International 1993: ASM Handbook Vol 6, pp 195 – 199.

Baeslack III, W.A., Davis, J.R. and Cross, C.E., *"Selection and weldability of conventional titanium alloys"*, ASM Handbook, 1993, Vol. 6, Welding ,brazing and soldering

Beesley, M.J., 1976*: "Lasers and their applications"*, Publ. Taylor and Francis Ltd, London.

Bibby, M.J., Goldak, J.A.. and Shing, G.Y., 1985: *"A model for predicting the fusion and heat-affected zone sizes of deep penetration welds"*, Canadian Metallurgical Quarterly, Vol 24, (1), pp 101-105, 1985.

Burleigh, T. and Eagar, T.W. 1983: *"Measurement of the force exerted by a welding arc"* Metallurgical Transactions, 14A (6), 1223-1224.

Chalmers, B. 1953: *"Progress in Metal Physics, 4"*, (book), Pergamon Press, London, pp 358-359.

Champion, F.C. and Davy, N., 1947: *"Properties of matter"*, Published by Blackie & Son Ltd, London.

Choo, R.T.C. Szekely,J. Westhoff, R.C.1990: *"Modelling of high current arcs with emphasis on free surface phenomena in the weld pool"*. Welding Journal 69 (9), pp 346s – 361s

Choo, R.T.C. and Szekely, J. 1992: *"Vaporisation kinetics and surface temperature in a mutually coupled spot gas tungsten arc weld and weld pool."* Welding Journal 71 (3) pp 77s – 93s.

Choo, T.C. and Szekely, J.1991: *"The effect of gas shear stress on Marangoni flows in arc welding"* Welding Journal 71 (9): pp 223s - 233s.

Christensen, N., Davies, V. de L., and Gjermundsen, K. 1965: *"Distribution of temperatures in arc welding"*, British Welding Journal, Feb. 1965.

Clegg, J.C., 1968: *"Calculus of Variations"*, Oliver and Boyd Ltd. Edinburgh

Converti, J. 1981: *"Plasma jets in welding arcs"*, Ph.D. Thesis, Mechanical Engineering, M.I.T., Cambridge, MA.

Cram, L.E. 1983. *"A model of the cathode of a thermionic arc."* Journal of Physics D: Applied Physics, 16 (1983) pp1643 – 1650.

CSIRO, 1995: *"GTA welding torch design"*, International Patent Application PCT/AU95/00269

Davis, M., Kapadia, P. and Dowden, J., 1985: *"Solution of a Stefan problem in the theory of laser welding by the method of lines"*, Journal of Computational Physics, 60, pp 534-548, 1985.

Do Carmo, M.P., 1976: *"Differential Geometry of Curves and Surfaces"*, Prentice-Hall inc., Englewood Cliffs, New Jersey.

Dowden, J., Davis, M. and Kapadia, P. 1983: *"Some aspects of the fluid dynamics of laser welding"*, Journal of Fluid Mechanics, Vol 126, pp 123-146.

Dowden, J., Postacioglu, N., Davis, M. and Kapadia, P., 1987: *"A keyhole model in penetration welding with a laser"*, Journal of Physics D: Applied Physics, Vol 20, pp 36-44, 1987

Dowden, J., Kapadia, P. and Postacioglu, N., 1989: *"An analysis of the laser-plasma interaction in laser keyhole welding"*, Journal of Physics D: Applied Physics, Vol 22, pp 741-749, 1989

Dowden, J., Sheng, W., Kapadia, P. and Strange, C. 1991: *"Dynamics of the vapour flow in the keyhole in penetration welding with a laser at medium welding speed"*, Journal of Physics D: Applied Physics, Vol 24, pp 519-532.

Duley, W.W., 1987: *"A comparison of keyhole absorption processes in laser and electron beam welding"*, Report M3JIP3, Laser Processing Laboratory, York University, Ontario.

DuPont, J,N. and Marder, A.R. 1995: *"A comparative study of the arc and melting efficiencies of arc welding processes."* Trends in Welding Research, Proceedings of the 4th International Conference, 5-8 June 1995, Gatlinburg, Tennessee.

Eagar, T.W. 1989: *"An iconoclast's view of the physics of welding – rethinking old ideas"*. Keynote address, Trends in Welding in the United States, Conf. Proc. American Society for Metals.

Easterling, K., 1992: *"Introduction to the physical metallurgy of welding"* 2nd Edition, Butterworth Heineman.

Erokhin, A.A. 1979: *"Force exerted by the arc on the metal being melted"*, Avtom. Svarka, (7), 21-26.

Eroshenko, L.E. Prilutskii, V.P. and Zamkov, V.N., 1997: *"Examination of the glow of anode vapours in the arc in TIG welding titanium in argon through a flux layer."* Paton Welding Journal, 1997, 9,(11), pp 601 - 605.

Fuerschback, P.W. and Knorovsky, G. A. 1991: *"A study of melting efficiency in plasma arc and gas tungsten arc welding"* Welding Journal, October 1991, pp 287s-297s.

Fuerschback, P.W. 1995: *"A dimensionless parameter model for arc welding processes"* Trends in Welding Research, Proceedings of the 4th International Conference, 5-8 June 1995, Gatlinburg, Tennessee.

Fuerschback, P.W. 1996: *"Measurement and prediction of energy transfer efficiency in laser beam welding"* Welding Journal, January 1996, pp 24s-34s.

Giedt, W.H., 1982: *"Heat transfer and fluid flow in electron beam welding"*, Trends in Welding in the United States, Conf. Proc. American Society for Metals, Nov. 1981.

Glickstein, S.S.,1981: *"Basic studies of the arc welding process"*, Trends in Welding in the United States, Conf. Proc. American Society for Metals, Nov. 1981.

Goryachev, A.P. and Zelenin, V.A. 1964: Autom. weld., 17, (12), 21-26.

Grimsehl, E., 1947: *"A textbook of physics"*, Vol 1, Mechanics, Published by Blackie & Son Ltd, London.

Guu, A.C. and Roklin, S.I. 1992: Weld. J., 71 (12), 473s-482s.

Handbook of Mathematical Functions with Formulas, Graphs and Mathematical Tables, 1955: US Department of Commerce, National Bureau of Standards.

Halmoy, E., 1994: *"New applications of plasma keyhole welding"*, Welding in the World, Vol 34, pp 285–291.

Houldcroft, P., 1991: *"Lasers in materials processing"*, TWI Supplement to Welding Abstracts Vol 4. 1991.

Howse, D, 1998: *"Developments in A-TIG welding"*, TWI International Conference, Exploiting Advances in Arc Welding Technology, Cambridge UK. Abington Publications.

Iida, T. and Guthrie, R. I. L., 1993: *"The physical properties of liquid metals"*, Oxford University Press.

Ireland, C.L.M., 1989: *"Deep penetration welding with kW YAG laser beams"*, Welding Review, Feb. 1989, pp 39-42.

Irving, B., 1995: *"U.S. Navy maintains high interest in funding for welding research."* Welding Journal, March, 1995, pp 41 - 47.

Jackson, C.E., 1960: *"The science of arc welding"*. Welding Journal, 39 (4), pp 129s - 140s and 39 (6), pp 225s - 230s.

Jarvis, B.L., Viano, D.M., Zhu, J.H., Dunne, D., and Ahmed, N.U., *"Final report for project 93-06,"* Open Technical Report No. MTA 365, CRC for Materials Welding and Joining, 1995

Jarvis, B.L., Barton, K. J., Ahmed, N.U. CRC-MWJ, 1999: World Intellectual Property Organisation Publication of International Application WO9921677A1.

Kapadia, P., and Dowden, J., 1994: *"Review of mathematical models of deep penetration laser welding,"* Lasers in Engineering, Vol 3, pp 187-281, 1994.

Kaye, G.W.C. and Laby T.H., 1966: *"Tables of Physical and Chemical Constants"*, Longmans, Green and Co. Ltd, London.

Key, J.F. 1980: *"Anode/cathode geometry and shielding gas interrelationships in GTAW."* Welding Journal, 59 (12), pp 364s – 370s.

Key, J.f., Chan, J.W., and McIlwain, M.E. 1983. *"Process variable influence on arc temperature distribution."* Welding Journal 63 (7): pp179s - 184s.

Key, J.F. 1993. *"Arc physics of gas-tungsten arc welding."* ASM Handbook, Vol. 6. ASM International.

Kristensen, T., Olsen, F.O. 1992: *"A transient model of laser-plasma interactions during keyhole welding"*, Proceedings of LAMP '92, Nagaoka. pp 317-322.

Kroos, J., Gratzke, U., Vicanek, M. and Simon, G., 1993: *"Dynamic behaviour of the keyhole in laser welding"*, Journal of Physics D: Applied Physics, Vol 26, pp 481-486, 1993.

Kroos, J., Gratzke, U., and Simon, G., 1993: *"Towards a self consistent model of the keyhole in penetration laser beam welding"*, Journal of Physics D: Applied Physics, Vol 26, pp 44-48, 1993

Lancaster, J.F. 1986: *"The physics of welding."* Second edition, IIW publication, Pergamon Press.

Lambrakos, S.G., Metzbower, E.A., Dunn, J.H., and Moore, P.G., 1992: *"A numerical model of deep penetration laser welding"*, Proc. Int. Trends in Welding Research, TWR 1992

Lee, S.-Y. and Na, S.-J. 1996: *"A numerical analysis of a stationary gas tungsten welding arc considering various electrode angles."* Welding Journal 75 (9): pp 269s - 279s.

Lim, S.Y. and Chatwin, C.R.,1994: *"Spatial chaos aspects of laser-material interaction"*, Optics and Lasers in Engineering, 20, 1994, pp 341-356.

Lin, M.L. and T.W. Eagar, T.W. 1985: *"Influence of arc pressure on weld pool geometry"*, Welding Journal, 64 (6), 163s-169s.

Lin, M.L. and T.W. Eagar, T.W., 1986: *"Pressures produced by gas tungsten arcs"*, Metallurgical Transactions B, Vol 17B, pp 601-607.

Liptak, J.A., 1965: *"Gas tungsten arc welding heavy aluminium plate"*, Welding Journal, 44, (6), 276s-281s.

Locke, E., Hella, R., and Westra, L., 1971: *"Performance of an unstable oscillator on a 30 kW CW GDL"*, IEEE Journal of Quan. Elect., December 1971.

Locke, E., Hoag, E., and Hella. R., 1972: *"Deep penetration welding with high power CO2 lasers"*, Welding Journal, May 1972, pp 245s - 249s.

Locke, J. 1993: private communication.

Lorrain, P. and Corson, D., 1970: *"Electromagnetic fields and waves"*, Publ. W.H. Freeman and Co.

Lucas, W and Howse D., 1996: *"Activating flux – increasing the performance of the TIG and plasma processes."* Welding and Metal Fabrication, January 1996, pp 11 – 17.

Maecker, H., *"Plasma streaming in arcs as a result of self-induced magnetic compression"*, Z. Physics, Vol 141, 1955, pp198-216

Margenau, H. and Murphy, G.M. 1956: *"The mathematics of physics and chemistry"* Book, 2nd Edition, D.Van Nostrand Co.

Martinez, L.F., Marques, R.E., McClure, J.C. and Nunes Jr, A.C., 1992: *"Front side keyhole detection in aluminium alloys"*, Welding Journal, May 1992.

Matsuda, F., Ushio, M. and Sadek, A. 1990: *"Development of GTA electrode materials."* The 5th International Symposium of the Japanese Welding Society. Tokyo, April 1990.

Matsunawa. A., 1992: *"Modelling of heat and fluid flow in arc welding"*, keynote address, International Trends in Welding Conf. Gattlingburg, 1992.

Matsunawa, A., Kim, J-D., Seto, N., Mizutani, M. and Katayama, S., 1998: *"Dynamics of keyhole and molten pool in laser welding"*, Laser Applications, Vol 10, No.6, 1998, pp 247-254.

Meier, J.W., 1963: *"Recent advances in electron beam welding"*, Welding Journal, 42 (12), pp 963-7.

Meleka, A. H., 1971: *"Electron beam welding: principles and practice"*, McGraw-Hill, London 1971.

Metcalfe, J.C. and Quigley, M.B.C., 1975: *"Keyhole stability in plasma arc welding"*, Welding Journal, Nov. 1975, pp 401s-404s.

Mills, K.C., and others, 1984: *"Surface tension of 304 and 316 type stainless steels and their effect on weld penetration"*, Report of the National Physical Laboratory, Teddington, Middlesex, U.K., 1984.

Miyazaki, T. and Giedt, W.H., 1982: *"Heat transfer from an elliptical cylinder moving through an infinite plate applied to electron beam welding"*, Int. J. Heat Mass Transfer. Vol 25, (6), pp 807-814, 1982.

Moon, D.W. and Metzbower, E.A., 1986: *"Effects of alloying elements of low boiling point on the keyhole mechanism during laser beam welding"*, Naval Research Laboratory, Washington D.C. U.S.A. 1986.

Nestor, O.H. 1962: *"Heat intensity and current distributions at the anode of high current inert gas arcs"*, Journal of Applied Physics, 33,(5) pp 1638-1648.

Nesterov, A.F. Bulgachev, E.A. and Boitsev, N.B. 1987: *"Increasing the stability of the process of welding structures of aluminium and magnesium alloys using an immersed arc"*, Weld. Int., 1 (7), 659-660.

Norrish, J. 1992: *"Advanced welding processes"*, Bristol, IOP Publishing Ltd.

Ocana, J.L., 1994: *"Review on the physics and calculational methods for the modelling of the laser-matter interaction in high intensity laser processing applications,"* Lasers in Engineering, Vol. 3, pp 301-345, 1994.

Olsen, H.N. 1958: *"Thermal and electrical properties of high current argon arc plasmas."* Eleventh annual gaseous electronics conference, New York.

Onsoien, M., Peters, R., Olsen, D.L. and Liu, S., 1995: *"Effect of hydrogen in an argon GTAW shielding gas: arc charateristics and bead morphology"*, Welding Journal, January 1995, pp 10s-15s.

Painter, M.J., Davies, M.H., Battersby, S., Jarvis, L., and Wahab, M., 1993: *"Numerical modelling the gas metal arc process: a literature review"*, Report MTA283, Cooperative Research Center for Materials Welding and Joining, project No. 93.04. October 1993.

Papoular, R. 1965. *"Electrical phenomena in gases."* Iliffe Books Ltd, London.

Petrie, T.W. and Pfender, E., 1970: *"The influence of the cathode tip on temperature and velocity in a gas-tungsten arc"*, Welding Journal, December 1970, pp 588s – 596s.

Postacioglu, N., Kapadia, P., Davis, M. and Dowden, J. 1987: *"Upwelling in the liquid region surrounding the keyhole in penetration welding with a laser"*, Journal of Physics D: Applied Physics, Vol 20, pp 340-345, 1987

Quigley, M.B.C., Richards, P.H., Swift-Hook, D.T. and Gick, A.E.F. 1973. *"Heat flow to the workpiece from a TIG welding arc."* Journal of Physics D: Applied Physics. Vol 6. 1973, pp 2250 - 2258.

Roklin, S.I. and Guu, A.C. 1993: Weld. J., 72 (8), 381s-390s.

Rosenthal, D. 1941: *"Mathematical theory of heat distribution during welding and cutting"*, Welding Journal, 1941, pp 220s - 234s.

Rosenthal, D., 1946: *"Theory of moving sources of heat and its application to metal treatments."* Transactions of the A.S.M.E., November, 1946.

Savage, W.F., Nippes, E. F., and Agusa, K, 1979: *"Effect of arc force on defect formation in GTA welding"*, Welding Journal, Vol 58 (7), pp 212s – 224s.

Savage, F., Strunck, S.S. and Ishlkawa, Y. 1965. *"The effect of electrode geometry in gas tungsten-arc welding."* Welding Journal, Nov. 1965. Pp489s – 496s.

Schebesta, W., 1975: *"A contribution to explain the deep penetration of high-power-density electron-beams in metals"*, Journal of Vacuum Science and Technology, Vol 12, (6) 1975.

Shaw, Jr, C.B. 1975: *"Diagnostic studies of the GTAW arc, Pt. 1"*. Welding Journal, 54 (2) pp 33s – 44s.

Shaw, Jr, C.B. 1975: *"Diagnostic studies of the GTAW arc, Pt. 2"*. Welding Journal, 54 (3) pp 81s – 86s.

Solomon, H.D. and Levy, S. 1982: *"HAZ temperatures and cooling rates as determined by a simple computer program", ASM Publication.*

Squire, H.B.1951: *"The round laminar jet"*, Quarterly Journal of Mechanics and Applied Mathematics, 1951(4), pp 321-29

Staff report, 1970: *"State of the art in continuous Nd:YAG welding"*, Metal Progress, Nov. 1970.

Steen, W.M., Dowden, J., Davis, M. and Kapadia, P., 1988: *"A point and line source model of laser keyhole welding"*, Journal of Physics D: Applied Physics, Vol 21, pp 1255-1260, 1988

Steigerwald, K.H., 1983: *"25 years of deep penetration electron beam welding"*, Schweiben und Schneiden, Dec. 1983.

Suzdalev I.V., and Yavno E.I., 1981: *"The effect of arc length and the form of the non-consumable electrode on the distribution of the force effect of the welding arc on the surface of the active spot"*, Welding Production, 28 (11), pp 13-15

Swift-Hook, D.T., and Gick, A.E.F., 1973: *"Penetration welding with lasers"*, Welding Journal, Nov. 1973, pp 492s-499s.

Tanaka, M., Shimizu, T., Terasaki, H., Ushio, M., Koshi-ishi, K, and Yang, C.L. 2000: *"Effects of activating flux on arc phenomena in TIG welding"*, IIW Asian Pacific International Congress, Melbourne. Paper 54.

Tomie, M., Abe, N., and Arata, Y., 1990: *"Characteristics of 500kV ultra high voltage electron beam heat source (Report II)"*, Transactions of JWRI, Vol 19, No. 2, 1990.

Tomsic, M.J., and Jackson, C.E., 1974: *"Energy distribution in keyhole mode plasma arc welding"*, Welding Journal, March 1974.

Viano, D.M., Jarvis, B.L., and Ahmed, N.U. 1993: CRC for Materials Welding and Joining, Project No. 93-06 Report No. MTA265.

Vertrag Irving Rossi 1952: Suddeutsche Laboratorien vom 26.1.1952.

Walsh, D.W., and Nunes, A.C., 1989: *"Keyhole flow phenomena in VPPA weldments"*, Proc. TWR, 1989.

Weber, C.M., 1982: *"New developments in electron beam welding"*, Trends in Welding in the United States, Conf. Proc. American Society for Metals, Nov. 1982.

Webster, J., 1970: *"Welding at high-speed with the CO2 laser"*, Metal Progress, Nov. 1970.

Wei, P.S. and Giedt, W.H., 1985: *"Surface tension gradient-driven flow around an electron beam welding cavity"*, Welding Journal, pp 251s-259s, Sept. 1985.

Wells, A., 1952: *"Heat flow in welding"*, Welding Journal, May 1952, pp 263s-267s

Wirth, P., 1995: *"Types of lasers suitable for industrial processing and their means of power generation."* WTIA Laser applications in manufacturing seminar, Melbourne, May 1995.

Woolcock, A. and Ruck, R.J.,1978: *"Keyhole plasma welding of titanium plate"*, Metal Construction, December 1978.

Yamauchi, N., Taka, T. and Oh-I, M., 1981: *"Development and application of high current TIG process (SHOLTA) welding process"*, The Sumitomo Search, No 25 May 1981, pp 87-100.

Zhu, P., Lowke, J.J. and Morrow, R. 1992. *"A unified theory of free burning arcs, cathode sheaths and cathodes."* Journal of Physics D: Applied Physics 25: pp1221 - 1230.

Appendix A

For further clarification CSIRO metallurgist Mr D. Viano has provided the following assessment of the results for the AISI304 and AISI 316L samples listed in Table 3.7 of Section 3.4.

Tensile Test Requirements

AS 3992 –1998 and ASME IX-1998 state that the transverse tensile strength must exceed the minimum specified tensile strength (MSTS) of the base material. If the specimen breaks outside the weld in the base material the test shall be accepted provided that the tensile strength is not less than 95% of the MSTS.

The MSTS for grade 304 is 515 MPa and the MSTS for grade 316L is 485 MPa. Therefore all tensile tests comply with AS 3992 and ASME IX.

Bend Test Requirements:

The bend test specimens shall have no open defects in the weld or heat affected zone exceeding 3 mm (AS 3992) or 3.2 mm (ASME IX) measured in any direction.

No defects had a length exceeding 3mm so all bend tests comply with AS 3992 and ASME IX.

Impact Tests:

ASME: Not specified in section IX

In AS3992 the requirement for impact tests for austenitic stainless steels is 0.38 mm minimum lateral expansion at material design minimum temperature (MDMT). All impact samples had a lateral expansion greater than 0.38 mm at a test temperature of minus 40 °C and therefore comply.

Hardness:

AS 3992 does not require hardness survey on austenitic stainless steels. However some clients may specify a maximum hardness for corrosive service applications. The maximum specified hardness for grades 304 and 316L are 92 HRB (~200 HV) and 95 HRB (~217 HV) respectively (source: ASTM). Most weld procedures comply with these maximum hardness values except for 304 pipe and 304 8mm which are only just above the limit.

Intergranular Corrosion

ASTM A262 Practice E comprises of immersing a bend test sample in boiling $CuSO_4$ – 16% H_2SO_4 with copper contact for 24 hours and then conducting a bend test. The samples are then examined x20 magnification to check for any cracking. All welds complied with this test.

Delta ferrite Content

Summary from AS 1554.6 Appendix F:

Hot Cracking:
The introduction of 5 to 15% ferrite to the weld metal effectively prevents hot cracking while maintaining high strength and ductility of the joint.

High Temperatures:
In high temperature applications, where the material is exposed to continuos service in the range 700 to 900°C, any ferrite in the weld metal may transform to sigma phase. In order to reduce the negative effects of sigma phase it is common practice to specify a tighter tolerance of 3 to 7% ferrite. Since elements Mo, Ti, and Nb significantly accelerate the formation of sigma phase from ferrite, these elements are sometimes also restricted.

Cryogenic Temperatures:

At cryogenic temperatures, (-196°C) ferrite becomes brittle, thus reducing the notch toughness of austenitic stainless steels at these low temperatures. For this reason ferrite contents may be restricted in the range 3 to 7%.

Zero Ferrite – Special Applications

Certain specific applications may require restricted or zero ferrite contents.

Corrosion in nitric acid, urea solutions and even molten zinc can actively attack ferrite. In this case zero ferrite consumables, usually with high nickel contents can be used.

Ferrite content measured in the Key hole welds

The measured ferrite contents of the qualification welds range between 7 and 14%. Whilst this would be acceptable for most applications there are some situations where the ferrite content may be deemed too high. On the other hand, the tear drop shape weld pool and high cooling rate characteristic of key-hole welding produces a more hot crack sensitive microstructure. Thus, lowering the ferrite content below 7% may result in hot cracking.